A Progress Report

July 1, 1991 to December 31, 1991

NASA-UVA LIGHT AEROSPACE ALLOY AND STRUCTURES TECHNOLOGY PROGRAM (LA^2ST)

NASA-LaRC Grant NAG-1-745

Submitted to:

National Aeronautics and Space Administration
Langley Research Center
Hampton, Virginia 23665

LANGLEY GRANT

Attention:

For Review by:

Mr. Dennis L. Dicus
Grant Monitor
Metallic Materials Branch
MS 188A

Submitted by:

Richard P. Gangloff
Professor

SEAS Report No. UVA/528266/MS92/109
January 30, 1992

SCHOOL OF
ENGINEERING & APPLIED SCIENCE

DEPARTMENT OF MATERIALS SCIENCE AND ENGINEERING

University of Virginia
Thornton Hall
Charlottesville, VA 22903

UNIVERSITY OF VIRGINIA
School of Engineering and Applied Science

The University of Virginia's School of Engineering and Applied Science has an undergraduate enrollment of approximately 1,500 students with a graduate enrollment of approximately 600. There are 160 faculty members, a majority of whom conduct research in addition to teaching.

Research is a vital part of the educational program and interests parallel academic specialties. These range from the classical engineering disciplines of Chemical, Civil, Electrical, and Mechanical and Aerospace to newer, more specialized fields of Applied Mechanics, Biomedical Engineering, Systems Engineering, Materials Science, Nuclear Engineering and Engineering Physics, Applied Mathematics and Computer Science. Within these disciplines there are well equipped laboratories for conducting highly specialized research. All departments offer the doctorate; Biomedical and Materials Science grant only graduate degrees. In addition, courses in the humanities are offered within the School.

The University of Virginia (which includes approximately 2,000 faculty and a total of full-time student enrollment of about 17,000), also offers professional degrees under the schools of Architecture, Law, Medicine, Nursing, Commerce, Business Administration, and Education. In addition, the College of Arts and Sciences houses departments of Mathematics, Physics, Chemistry and others relevant to the engineering research program. The School of Engineering and Applied Science is an integral part of this University community which provides opportunities for interdisciplinary work in pursuit of the basic goals of education, research, and public service.

NASA-UVA LIGHT AEROSPACE ALLOY AND STRUCTURES TECHNOLOGY PROGRAM

LA^2ST

Program Director:

Richard P. Gangloff

Co-principal Investigators:

Richard P. Gangloff
John K. Haviland
Carl T. Herakovich
Walter D. Pilkey
Marek-Jerzy Pindera
John R. Scully
Edgar A. Starke, Jr.
Glenn E. Stoner
Earl A. Thornton
Franklin E. Wawner, Jr.
John A. Wert

NASA-LaRC Grant Monitor:

Dennis L. Dicus

TABLE OF CONTENTS

		Page
Executive Summary		v
Introduction		1
Summary Statistics		5
Grant Publications (Cumulative, Refereed)		11
Completed Projects		13
Administrative Progress		15
Current Projects		17
Research Progress and Plans		23
Project 1	Environmental Fatigue Crack Growth and Cracking Mechanisms in Al-Li-Cu Alloy 2090 D.C. Slavik and R.P. Gangloff	23
Project 2	Environmental Effects in Fatigue Life Prediction Sang Kim and R.P. Gangloff	45
Project 3	Elevated Temperature Fracture of an Advanced Powder Metallurgy Aluminum Alloy W.C. Porr and R.P. Gangloff	49
	Elevated Temperature Crack Growth in Advanced Aluminum Alloys Yang Leng and R.P. Gangloff	65
Project 4	Elevated Temperature Damage Tolerance of Advanced Aluminum Alloys Sang Kim and R.P. Gangloff	67
Project 5	Cryogenic Temperature Effects on the Deformation and Fracture of Al-Li-Cu-In Alloys J.A. Wagner and R.P. Gangloff	69

TABLE OF CONTENTS (continued)

		Page
Project 6	The Effect of Temperature on the Fracture Toughness of Weldalite™ 049 C.L. Lach and R.P. Gangloff	81
Project 7	Mechanisms of Localized Corrosion in Al-Cu-Li-Mg-Ag Alloy X2095 and Compositional Variations F. Douglas Wall and G.E. Stoner	97
Project 8	The Effects of Zinc Additions on Precipitation and SCC in Alloy 8090 R.J. Kilmer and G.E. Stoner	101
Project 9	Hydrogen Interactions in Aluminum-Lithium Alloy 2090 and Model Alloys S.W. Smith and J.R. Scully	111
Project 10	Investigation of the Effect of Thermal Exposure on the Mechanical Properties of Ti/SiC Composites D.B. Gundel and F.E. Wawner	121
Project 11	Quantitative Characterization of the Spatial Distribution of Particles in Materials: Application to Materials Processing J.B. Parse and J.A. Wert	133
Project 12	Processing and SPF Properties of Weldalite Sheet M. Lyttle and J.A. Wert	157
Project 13	Development of Low Alloy High Strength Aluminum Alloys A.K. Mukhopadhyay and E.A. Starke, Jr.	165
Project 14	Inelastic Response of Metal Matrix Composites Under Biaxial Loading C.J. Lissenden, M.-J. Pindera and C.T. Herakovich	185
Project 15	Effect of Temperature on the Response of Metallic Shell Structures C. Copper, K. McCarthy, T. Johnson, W.D. Pilkey and J.K. Haviland	199

TABLE OF CONTENTS (continued)

		Page
Project 16	Experimental Study of the Nonlinear Viscoplastic Response of High Temperature Structures M.F. Coyle and E.A. Thornton	211
	Experimental Study of the Nonlinear Viscoplastic Response of High Temperature Structures Mark A. Rawley and E.A. Thornton	219
Appendix I:	Grant Publications	227
Appendix II:	Grant Presentations	
Appendix III:	Abstracts of Grant Publications	
Appendix IV:	Grant Progress Reports	

NASA-UVA LIGHT AEROSPACE ALLOY AND STRUCTURES TECHNOLOGY PROGRAM

EXECUTIVE SUMMARY

The NASA-UVa Light Aerospace Alloy and Structures Technology (LA^2ST) Program has achieved a high level of activity in 1991, with projects being conducted by graduate students and faculty advisors in the Departments of Materials Science and Engineering, Civil Engineering and Applied Mechanics, and Mechanical and Aerospace Engineering at the University of Virginia. This work is funded by the NASA-Langley Research Center under Grant NAG-1-745. Here, we report on progress achieved between July 1 and December 31, 1991. The previous progress report summarized the work presented at the Second Annual LA^2ST Grant Review Meeting held at the Langley Research Center in July of 1991.

The general objective of the LA^2ST Program is to conduct interdisciplinary graduate student research on the performance of next generation, light weight aerospace alloys, composites and thermal gradient structures in collaboration with Langley researchers. Specific technical objectives are established for each research project. We aim to produce relevant data and basic understanding of material behavior and microstructure, new monolithic and composite alloys, advanced processing methods, new solid and fluid mechanics analyses, measurement advances, and critically, a pool of educated graduate students for aerospace technologies.

The accomplishments presented in this report are:

- oo Four research areas are being actively investigated, including: (1) Mechanical and Environmental Degradation Mechanisms in Advanced Light Metals and Composites, (2) Aerospace Materials Science, (3) Mechanics of Materials and Composites for Aerospace Structures, and (4) Thermal Gradient Structures.

- oo Sixteen research projects are being conducted by 12 PhD and 3 MS graduate students, 11 faculty members, and 1 research associate from three departments in the Engineering School at UVa. Each project is planned and executed in conjunction with a specific branch and technical monitor at LaRC.

- oo Four new graduate students were recruited into the LA^2ST Program; 3 during the first half of 1991 and 1 during this reporting period.

- oo The undergraduate program, initiated with four students working at LaRC during the

Summer of 1990, was not conducted in 1991 because of a lack of qualified applicants. Recruiting efforts were intensified for 1992 and a successful program is anticipated.

oo Dean E.A. Starke, Jr. initiated a large NASA funded University-industry collaboration on "Aluminum Based Materials for High Speed Aircraft", as a supplement to the LA^{2}ST Program. This work, involving 4 UVa faculty and engineering-scientists from 6 industrial laboratories, will begin in January of 1992.

oo Reporting accomplishments between January and December of 1991 include 23 journal or proceedings publications, 1 PhD dissertation, 2 NASA progress reports, and 15 presentations at technical meetings. The LA^{2}ST totals since 1986 are 46 publications, 6 dissertations/theses, 48 external presentations and 11 NASA progress reports. Since 1986, 21 graduate students, including 20 United States citizens, have been involved with LA^{2}ST research.

oo ***Research on environmental fatigue of advanced Al-Li-Cu alloys*** determined similar fatigue crack growth rate behavior for peak aged unrecrystallized 2090 sheet and plate (Vintage III) in inert vacuum, and in embrittling moist air and aqueous NaCl environments. A dissertation proposal is presented with the objective to understand and model crack growth rates and microscopic fatigue damage processes, based on experiments with both commercial and model recrystallized large grain microstructures, the latter produced by novel thermomechanical processing. (Project 1)

oo ***Research on mechanisms of localized corrosion in Al-Cu-Li-Mg-Ag alloy X2095 and compositional variations*** suggests a continuing role of T_1 precipitates in stress corrosion cracking of Weldalite™ in aqueous chloride, consistent with previous results for alloy 2090. For each alloy, SCC is most severe within a "window" of applied electrode potential, consistent with the need for active T_1 dissolution but a passive aluminum matrix to sustain crack growth. (Project 7)

oo ***Research on the effects of zinc additions on the precipitation and stress corrosion cracking behavior of alloy 8090*** demonstrates that low Zn additions to this commercial alloy cause markedly improved aqueous chloride SCC resistance, even at low aging times. Specific windows of SCC resistance are defined and it is shown that S' (Al_2CuMg) is not integrally necessary for SCC performance. These results suggest an approach to improving the environmental compatibility of higher lithium alloys. This work is cosponsored by the Alcoa Technical Center; the graduate student spent several months at this laboratory conducting dissertation research. (Project 8)

oo *Research on hydrogen interactions with Al-Li alloys* successfully developed a method that produces sufficient hydrogen uptake to cause significant hydrogen damage in 7075-T6. A method to examine hydrogen fugacities present at crack tips during film rupture has also been developed. (Project 9)

oo *Research on the fracture of Al-Cu-Li-In alloys* demonstrated that the initiation and growth toughnesses of Vintage III alloy 2090 (K_{IC} and tearing modulus, T_R) and experimental 2090 + In (T_R only) increase with decreasing temperature to cryogenic levels for both plane strain and plane stress deformation. High angle boundary delamination increases at cryogenic temperatures and contributes to increased toughness, independent of whether the microscopic fracture mode is transgranular slip plane cracking (2090) or intersubgranular (2090 + In). In contrast to 2090, subgrain boundary precipitation of T_1 occurs in the In-bearing composition after short aging times at 160°C and degrades fracture toughness by promoting intersubgranular cracking. (Project 5)

oo *Research on the fracture toughness of Weldalite™* indicates that, for loading at 25°C, both K_{IC} and T_R decrease with increasing aging time at constant temperature, with increasing aging temperature at constant yield strength, and with increasing copper content favoring primary T_1 or T_B phases. Work is planned to systematically confirm and explain these trends, and to examine cryogenic fracture. (Project 6)

oo *Research on elevated temperature fracture of PM Al-Fe-Si-V alloy 8009* suggests four possible causes for the elevated temperature (175°C) embrittlement of 8009: (1) Extrinsic delamination toughening, (2) Oxygen or hydrogen embrittlement from reactions with moist air or from process-introduced water, (3) Dynamic strain aging, or (4) Localized plastic deformation. Neither delamination, hydrogen embrittlement nor macroscopic plastic instability are the causes of decreased cracking resistance. Rather, either dynamic strain aging or dislocation interactions with solute and dispersoid or oxide laden boundaries are likely damage mechanisms. (Project 3)

oo *Research on Ti alloy matrix-SiC fiber reinforced composites* employed thermal cycling experiments to show that cycling up to 800°C, repeated 500 times, causes a reduction in the tensile properties of Ti-1100/SCS-6 composites; while the equivalent isothermal exposure, cycling to 700°C, or cycling in argon does not. A large degree of matrix-environment interaction in the composite cycled to 800°C (not present in similarly exposed monolithic Ti-1100 samples) may be responsible for the property degradation. (Project 10)

- oo ***Research on quantifying the spatial distribution and homogeneity of microstructure*** demonstrates that newly established microstructural analysis methods, applied to a PM aluminum alloy, provide a rational basis for selecting deformation processing methods to optimize dispersal of oxide particles. In particular direct rolling of compacted billets is a less effective method for break-up and dispersal of the oxide particles than processes involving forging prior to rolling. (Project 11)

- oo ***Research on superplastic forming of Weldalite™*** demonstrated modest differences in microstructure and texture between two superplastic Weldalite™ alloys. Future research will establish the effect of these microstructures and texture differences on the variability of superplastic properties. (Project 12)

- oo ***Research to develop low alloy high strength aluminum alloys*** is focusing on a low to medium strength Al-1Si-1Ge-1at%Cu alloy produced by ingot metallurgy. This alloy exhibits superior microstructural stability at typical commercial aging temperatures (150 to 200°C) and is in the process of further development. (Project 13)

- oo ***Research on the deformation of SCS-6/Ti-15-3 metal matrix composite tubulars under biaxial loading*** demonstrated a stiffness degradation with increasing load, based on both experimental measurements and micromechanics model predictions. The results indicate that axial stiffness falls within the bounds of predictions based upon bonding parameters that vary between perfect bond and total debond, however, measured shear stiffness values are well below the value predicted for total debond. (Project 14)

- oo ***Research on finite element analysis of the effect of temperature on metallic shell structures*** analytically demonstrated the feasibility of a simple and less expensive method to stabilize tanks for large launch vehicles. It was found that tanks with external hot stiffeners could be subject to buckling; internal cold stiffeners appear to lead to stability. (Project 15)

- oo ***Research on the thermoviscoplastic behavior*** of high temperature alloy panels demonstrated material and geometric nonlinearities. Hastelloy-X panels were instrumented with thermocouples, strain gages and displacement gages. Initial tests of Hastelloy-X provided elastic and inelastic temperature and displacement data for the thermal buckling of the panel. A heat lamp characterization program was initiated. In 1992 the Hastelloy-X test series and the lamp characterization program will be completed, and a test series with 8009 aluminum alloy panels will be initiated. (Project 16)

INTRODUCTION

Background

In 1986 the Metallic Materials Branch in the Materials Division of the NASA-Langley Research Center initiated sponsorship of graduate student engineering and scientific research in the Department of Materials Science and Engineering at the University of Virginia. This work emphasized the mechanical and corrosion behavior of light aerospace alloys, particularly Al-Li-Cu based compositions, in aggressive aerospace environments[1]. Results are documented in three progress reports[2-4].

In the Fall of 1988 this program was increased in scope to incorporate materials science research at UVa on the development and processing of advanced aerospace materials[5]. Funding was provided by the Metallic Materials and Mechanics of Materials Branches. In early 1989 the program was further enhanced to include interdisciplinary work on solid mechanics and thermal structures, with funding from several Divisions within the Structures Directorate at NASA-LaRC[6]. The Department of Civil Engineering and the Department of Mechanical and Aerospace Engineering at UVa participated in this expanded program. With this growth, the NASA-UVa Light Aerospace Alloy and Structures Technology Program (LA^2ST) was formed within the School of Engineering and Applied Science at UVa.

The first progress report for the LA^2ST program was published in August of 1989[7]. Research efforts in solid mechanics were in a state of infancy and were not represented at that time. Since then, graduate students have been recruited into the structural mechanics programs and several new projects have been initiated. Since July of 1989, the LA^2ST program has operated with full participation from all faculty and graduate students, as outlined in the last four progress reports[8-11] and three grant renewal proposals[12-14]. Two 2-day Grant Review Meetings were held in June of 1990 and 1991 at the Langley Research Center, with over 25 faculty and graduate students from UVa participating.

In October of 1991, Dean E.A. Starke proposed a substantial enhancement to the base LA^2ST Program[15]. The objective of this supplement is to involve UVa faculty with engineering scientists from aluminum alloy producers and airframe manufacturers in a broad research program to develop aluminum alloys and composites for elevated temperature high speed civil transport applications. This research will begin in January of 1992.

Problem and Needs

Future aerospace structures require high performance light alloys and metal matrix composites with associated processing and fabrication techniques; new structural design methods and concepts with experimental evaluations; component reliability/durability/damage tolerance prediction procedures; and a pool of masters and doctoral level engineers and scientists. Work on advanced materials and structures must be interdisciplinary and integrated. The thermal and chemical effects of aerospace environments are particularly important to material performance. Nationally, academic efforts in these areas are limited. The NASA-UVa Light Aerospace Alloy and Structures Technology Program addresses these needs.

LA^{2}ST Program

As detailed in the original proposal[6] and affirmed in the most recent renewal document[14], faculty from the Departments of Materials Science and Engineering, Mechanical and Aerospace Engineering, and Civil Engineering and Applied Mechanics at UVa are participating in the LA^{2}ST research and education program focused on high performance, light weight, aerospace alloys and structures. We aim to develop long term and interdisciplinary collaborations between graduate students, UVa faculty, and NASA-Langley researchers.

Our research efforts are producing basic understanding of materials performance, new monolithic and composite alloys, advanced processing methods, solid and fluid mechanics analyses, and measurement advances. A major product of the LA^{2}ST program is graduate students with interdisciplinary education and research experience in materials science, mechanics and mathematics. These advances should enable various NASA technologies.

The scope of the LA^{2}ST Program is broad. Four research areas are being investigated, including:

- oo Mechanical and Environmental Degradation Mechanisms in Advanced Light Metals and Composites,
- oo Aerospace Materials Science,
- oo Mechanics of Materials and Composites for Aerospace Structures,
- oo Thermal Gradient Structures.

Sixteen specific research projects are ongoing within these four areas and are reported here. These projects involve 11 faculty, 1 research associate and 15 graduate students. The majority of the graduate students are at the doctoral level (12 of 15) and all are citizens of the United States. In each case the research provides the basis for the thesis or dissertation requirement of graduate studies at the University of Virginia. Each project is developed in conjunction with a specific LaRC researcher. Research is conducted at either UVa or LaRC, and under the guidance of UVa faculty and NASA staff. Participating students and faculty are closely identified with a NASA-LaRC branch.

A primary goal of the LA^{2}ST Program is to foster interdisciplinary research. To this end, many of the research projects share a common focus on the same next generation light alloys and composites, and on light and reusable aerospace structures which will be subjected to aggressive terrestrial and space environments. Emphasis is placed on both cryogenic and elevated temperature conditions, with severe thermal gradients typical of tankage structures.

Organization of Progress Report

This progress report first provides LA^{2}ST Program administrative information including statistics on the productivity of faculty and graduate student participants, a history of current and graduated students, refereed or archival publications, and a list of ongoing projects with NASA and UVa advisors. Sixteen sections summarize the technical accomplishments of each research project, emphasizing the period from July 1st to December 31, 1991. Appendices document grant-sponsored publications, conference participation, abstracts of technical papers published during this reporting period, and citations of all LA^{2}ST Progress Reports.

References

1. R.P. Gangloff, G.E. Stoner and M.R. Louthan, Jr., "Environment Assisted Degradation Mechanisms in Al-Li Alloys", University of Virginia, Proposal No. MS-NASA/LaRC-3545-87, October, 1986.

2. R.P. Gangloff, G.E. Stoner and R.E. Swanson, "Environment Assisted Degradation Mechanisms in Al-Li Alloys", University of Virginia, Report No. UVA/528266/MS88/101, January, 1988.

3. R.P. Gangloff, G.E. Stoner and R.E. Swanson, "Environment Assisted Degradation Mechanisms in Advanced Light Metals", University of Virginia, Report No. UVA/528266/MS88/102, June, 1988.

4. R.P. Gangloff, G.E. Stoner and R.E. Swanson, "Environment Assisted Degradation Mechanisms in Advanced Light Metals", University of Virginia, Report No. UVA/528266/MS89/103, January, 1989.

5. T.H. Courtney, R.P. Gangloff, G.E. Stoner and H.G.F. Wilsdorf, "The NASA-UVa Light Alloy Technology Program", University of Virginia, Proposal No. MS NASA/LaRC-3937-88, March, 1988.

6. R.P. Gangloff, "NASA-UVa Light Aerospace Alloy and Structures Technology Program", University of Virginia, Proposal No. MS NASA/LaRC-4278-89, January, 1989.

7. R.P. Gangloff, "NASA-UVa Light Aerospace Alloy and Structures Technology Program", University of Virginia, Report No. UVA/528266/MS90/104, August, 1989.

8. R.P. Gangloff, "NASA-UVa Light Aerospace Alloy and Structures Technology Program", University of Virginia, Report No. UVA/528266/MS90/105, December, 1989.

9. R.P. Gangloff, "NASA-UVa Light Aerospace Alloy and Structures Technology Program", UVa Report No. UVA/528266/MS90/106, June, 1990.

10. R.P. Gangloff, "NASA-UVa Light Aerospace Alloy and Structures Technology Program", UVa Report No. UVA/528266/MS91/107, January, 1991.

11. R.P. Gangloff, "NASA-UVa Light Aerospace Alloy and Structures Technology Program", UVa Report No. UVA/528266/MS91/108, July, 1991.

12. R.P. Gangloff, "NASA-UVa Light Aerospace Alloy and Structures Technology Program", University of Virginia, Proposal No. MS NASA/LaRC-4512-90, November, 1989.

13. R.P. Gangloff, "NASA-UVa Light Aerospace Alloy and Structures Technology Program", University of Virginia, Proposal No. MS NASA/LaRC-4841-91, September, 1990.

14. R.P. Gangloff, "NASA-UVa Light Aerospace Alloy and Structures Technology Program", University of Virginia, Proposal No. MS NASA/LaRC-5219-92, October, 1991.

15. R.P. Gangloff, E.A. Starke, Jr., J.M. Howe and F.E. Wawner, "NASA-UVa Light Aerospace Alloy and Structures Technology Program: Supplement on Aluminum Based Materials for High Speed Aircraft", University of Virginia, Proposal No. MS NASA/LaRC-5215-92, October, 1991.

SUMMARY STATISTICS

Table I documents the numbers of students and faculty who participated in the LA^{2}ST Program, both during this reporting period and since the program inception in 1986. Academic and research accomplishments are indicated by the degrees awarded, publications and presentations. Specific graduate students and research associates who participated in the LA^{2}ST Program are named in Tables II and III, respectively.

TABLE I: LA^{2}ST Program Statistics

	Current 7/1/91 to 12/31/91	Cumulative 1986 to 12/31/91
PhD Students--UVa:	11	14
--NASA-LaRC:	1	1
MS Students--UVa:	2	4
--NASA:	1	1
--VPI:	0	1
Undergraduates--UVa:	1	4
--NASA-LaRC:	0	4
Faculty--UVa:	11	11
--VPI:	0	1
Research Associates--UVa:	1	4
PhD Awarded:	0	3
MS Awarded:	0	3

TABLE I: LA^{2}ST Program Statistics (continued)

	Current 1/1/91 to 6/30/91	Cumulative 1986 to 6/30/91
Employers--NASA:	0	1
--Federal:	0	1
--University:	0	0
--Industry:	0	1
--Next degree:	0	2
Publications:	14	46
Presentations:	9	48
Dissertations/Theses:	0	6
NASA Reports:	1	11

TABLE II

GRADUATE STUDENT PARTICIPATION IN THE NASA-UVa LA^{2}ST PROGRAM

January, 1992

POS #	GRADUATE STUDENT EMPLOYER	ENTERED PROGRAM	DEGREE COMPLETED	LANGLEY RESIDENCY	RESEARCH TOPIC	UVa/NASA-LaRC ADVISORS
1.	R. S. Piascik NASA-Langley	6/86	Ph.D. 10/89		Damage Localization Mechanisms in Corrosion Fatigue of Aluminum-Lithium Alloys	R. P. Gangloff D. L. Dicus
2.	J. P. Moran NIST	9/88	Ph.D. 12/89		An Investigation of the Localized Corrosion and Stress Corrosion Cracking Behavior of Alloy 2090	G. E. Stoner W. B. Lisagor
3.	R. G. Buchheit Sandia National Laboratories	6/87	Ph.D. 12/90		Measurements and Mechanisms of Localized Aqueous Corrosion in Aluminum-Lithium Alloys	G. E. Stoner D. L. Dicus
4.	D. B. Gundel Ph.D.-UVa	9/88	M.S. 12/90		Investigation of the Reaction Kinetics Between SiC Fibers and Titanium Matrix Composites	F. E. Wawner W. B. Brewer
5.	F. Rivet (VPI)	9/88	M.S. 12/90		Deformation and Fracture of Aluminum-Lithium Alloys: The Effect of Dissolved Hydrogen	R. E. Swanson (VPI) D. L. Dicus
6.	C. Copper Ph.D.-UVa	4/89	M.S. 12/90		Design of Cryogenic Tanks for Space Vehicles	W. D. Pilkey J. K. Haviland D. R. Rummler M.J. Shuart
7.	J. A. Wagner NASA-Langley	6/87	Ph.D.	PhD Research @ LaRC	Temperature Effects on the Deformation and Fracture of Al-Li-Cu-In Alloys	R. P. Gangloff W. B. Lisagor J. C. Newman
8.	W. C. Porr, Jr.	1/88	Ph.D.		Elevated Temperature Facture of an Advanced Powder Metallurgy Aluminum Alloy	R. P. Gangloff C. E. Harris

TABLE II (continued)

GRADUATE STUDENT PARTICIPATION IN THE NASA-UVa LA^{2}ST PROGRAM

(continued)

POS #	GRADUATE STUDENT EMPLOYER	ENTERED PROGRAM	DEGREE COMPLETED	LANGLEY RESIDENCY	RESEARCH TOPIC	UVa/NASA-LaRC ADVISORS
9.	J. B. Parse	9/88	Ph.D.		Quantitative Characterization of the Spatial Distribution of Particles in Materials	J. A. Wert D. R. Tenney
10.	D. C. Slavik	9/89	Ph.D.		Environment Enhanced Fatigue of Advanced Aluminum Alloys and Composites	R. P. Gangloff D. L. Dicus
11.	C. L. Lach NASA-Langley	9/89	M.S.	MS Research @LaRC	Effect of Temperature on the Fracture Toughness of Weldalite^{TM} 049	R.P. Gangloff W. B. Lisagor
12.	R. J. Kilmer	11/89	Ph.D.		Effect of Zn Additions on the Environmental Stability of Alloy 8090	G. E. Stoner W. B. Lisagor
13.	M. F. Coyle	12/89	Ph.D.		Visoplastic Response of High Temperature Structures	E. A. Thornton J.H. Starnes
14.	C.J. Lissenden	9/90	Ph.D.		Inelastic Response of Metal Matrix Composites Under Biaxial Loading	C.T. Herakovich M.J. Pindera W.S. Johnson
15.	C. Cooper	1/91	Ph.D.		Shell Structures Analytical Modeling	W. D. Pilkey J. K. Haviland M. Shuart J. Stroud

TABLE II (continued)

GRADUATE STUDENT PARTICIPATION IN THE NASA-UVa LA^{2}ST PROGRAM

(continued)

16.	Douglas Wall	4/91	Ph.D.		Measurements and Mechanisms of Localized Corrosion in Al-Li-Cu Alloys	G. E. Stoner D. L. Dicus
17.	S. W. Smith	4/91	Ph.D.		Hydrogen Interactions with Al-Li Alloys	J. R. Scully W. B. Lisagor
18.	D. B. Gundel	4/91	Ph.D.		Effect of Thermal Exposure on the Mechanical Properties of Titanium/SiC Composites	F. E. Wawner W. B. Brewer
19.	K. McCarthy	5/91	MS		Shell Structures Analytical Modeling	W. D. Pilkey M. J. Shuart J. Stroud
20.	M. Lyttle	12/91	MS		Superplasticity in Al-Li-Cu Alloys	J. A. Wert T. Bayles
21.	T. Johnson	12/91	Ph.D.	(NASA Minority Grantee)	Shell Structures Analytical Modeling	W. D. Pilkey M. J. Shuart J. Stroud

TABLE III

Post-Doctoral Research Associate Participation

in NASA-UVA LA^{2}ST Program

Pos #	Res. Assoc. Employer	Tenure	Research	Supervisor
1.	Yang Leng	3/89 to 12/91	Elevated Temperature Deformation and Fracture of PM AL Alloys and Composites	R. P. Gangloff
2.	Farshad Mizadeh	7/89 to 12/91	Deformation of Metal Matrix Composites	C. T. Herakovich and Marek-Jerzy Pindera
3.	A.K.Mukhopadhyay	6/91 to 6/92	Aluminum Alloy Development	E. A. Starke, Jr.
4.	Sang-Shik Kim	12/91	Environmental Fatigue Life Prediction	R. P. Gangloff

GRANT PUBLICATIONS (REFEREED JOURNALS AND ARCHIVAL PROCEEDINGS)

The following papers were based on research conducted under LA^{2}ST Program support, and were published in the referred or archival literature.

19. R.P. Gangloff, R.S. Piascik, D.L. Dicus and J.C. Newman, "Fatigue Crack Propagation in Aerospace Aluminum Alloys", Journal of Aircraft, in press (1991).

18. R.G. Buchheit, Jr., J.P. Moran, F.D. Wall, and G.E. Stoner, "Rapid Anodic Dissolution Based SCC of 2090 (Al-Li-Cu) by Isolated Pit Solutions," Proceedings, Parkins Symposium on Stress Corrosion Cracking, TMS-AIME, Warrendale, PA, in press (1991).

17. R.J. Kilmer, T.J. Witters and G.E. Stoner, "Effect of Zn Additions on the Precipitation Events and Implications to Stress Corrosion Cracking Behavior in Al-Li-Cu-Mg-Zn Alloys", Proceedings of the Sixth International Al-Li Conference, in press (1991).

16. C.J. Lissenden, M-J. Pindera, and C.T. Herakovich, "Stiffness Degradation of SiC/Ti Tubes Subjected to Biaxial Loading with Damage", Int. J. Composites Science and Technology, in press (1991).

15. E.A. Thornton and J.D. Kolenski, "Viscoplastic Response of Structures with Intense Local Heating", Journal of Aerospace Engineering, in press (1991).

14. C.T. Herakovich and J.S. Hidde, "Response of Metal Matrix Composites with Imperfect Bonding", Ultramicroscopy, in press (1991).

13. R.P. Gangloff, D.C. Slavik, R.S. Piascik and R.H. Van Stone, "Direct Current Electrical Potential Measurement of the Growth of Small Fatigue Cracks", in Small Crack Test Methods, ASTM STP, J.M. Larsen and J.E. Allison, eds., ASTM, Philadelphia, PA, in press (1991).

12. R.J. Kilmer and G.E. Stoner, "The Effect of Trace Additions of Zn on the Precipitation Behavior of Alloy 8090 During Artificial Aging", Proceedings, Light Weight Alloys for Aerospace Applications II, E.W. Lee, ed., TMS-AIME, Warrendale, PA, pp. 3-15, 1991.

11. W.C. Porr, Jr., Anthony Reynolds, Yang Leng and R.P. Gangloff, "Elevated Temperature Cracking of RSP Aluminum Alloy 8009: Characterization of the Environmental Effect", Scripta Metallurgica et Materialia, Vol. 25, pp. 2627-2632 (1991).

10. J. Aboudi, J.S. Hidde and C.T. Herakovich, "Thermo-mechanical Response Predictions for Metal Matrix Composites", in Mechanics of Composites at Elevated and Cryogenic Temperatures, S.N. Singhal, W.F. Jones and C.T. Herakovich, eds., ASME AMD, Vol. 118, pp. 1-18 (1991).

9. R.S. Piascik and R.P. Gangloff, "Environmental Fatigue of an Al-Li-Cu Alloy: Part I - Intrinsic Crack Propagation Kinetics in Hydrogenous Environments", Metall. Trans. A, Vol. 22A, pp. 2415-2428 (1991).

8. W.C. Porr, Jr., Y. Leng, and R.P. Gangloff, "Elevated Temperature Fracture Toughness of P/M Al-Fe-V-Si", in Low Density, High Temperature Powder Metallurgy Alloys, W.E. Frazier, M.J. Koczak, and P.W. Lee, eds., TMS-AIME, Warrendale, PA, pp. 129-155 (1991).

7. Yang Leng, William C. Porr, Jr. and Richard P. Gangloff, "Time Dependent Crack Growth in P/M Al-Fe-V-Si at Elevated Temperatures", Scripta Metallurgica et Materialia, Vol. 25, pp. 895-900 (1991).

6. R.J. Kilmer and G.E. Stoner, "Effect of Zn Additions on Precipitation During Aging of Alloy 8090", Scripta Metallurgica et Materialia, Vol. 25, pp. 243-248 (1991).

5. D.B. Gundel and F.E. Wawner, "Interfacial Reaction Kinetics of Coated SiC Fibers", Scripta Metallurgica et Materialia, Vol. 25, pp. 437-441 (1991).

4. R.G. Buchheit, Jr., J.P. Moran and G.E. Stoner, "Localized Corrosion Behavior of Alloy 2090-The Role of Microstructural Heterogeneity", Corrosion, Vol. 46, pp. 610-617 (1990).

3. Y. Leng, W.C. Porr, Jr. and R.P. Gangloff, "Tensile Deformation of 2618 and Al-Fe-Si-V Aluminum Alloys at Elevated Temperatures", Scripta Metallurgica et Materialia, Vol. 24, pp. 2163-2168 (1990).

2. R.P. Gangloff, "Corrosion Fatigue Crack Propagation in Metals", in Environment Induced Cracking of Metals, R.P. Gangloff and M.B. Ives, eds., NACE, Houston, TX, pp. 55-109 (1990).

1. R.S. Piascik and R.P. Gangloff, "Aqueous Environment Effects on Intrinsic Corrosion Fatigue Crack Propagation in an Al-Li-Cu Alloy", in Environment Induced Cracking of Metals, R.P. Gangloff and M.B. Ives, eds., NACE, Houston, TX, pp. 233-239 (1990).

COMPLETED PROJECTS

1. DAMAGE LOCALIZATION MECHANISMS IN CORROSION FATIGUE OF ALUMINUM-LITHIUM ALLOYS
   Faculty Investigator: R.P. Gangloff
   Graduate Student: Robert S. Piascik
   Degree: PhD
   UVa Department: Materials Science
   NASA-LaRC Contact: D. L. Dicus (Metallic Materials)
   Start Date: June, 1986
   Completion Date: November, 1989
   Employment: NASA-Langley Research Center

2. AN INVESTIGATION OF THE LOCALIZED CORROSION AND STRESS CORROSION CRACKING BEHAVIOR OF ALLOY 2090 (Al-Li-Cu)
   Faculty Investigator: Glenn E. Stoner
   Graduate Student: James P. Moran
   Degree: PhD
   UVa Department: Materials Science
   NASA-LaRC Contact: W.B. Lisagor (Metallic Materials)
   Start Date: September, 1988
   Completion Date: December, 1989
   Co-Sponsor: ALCOA
   Employment: ALCOA Laboratories

3. MECHANISMS OF LOCALIZED CORROSION IN AL-LI-CU ALLOY 2090
   Faculty Investigator: G.E. Stoner
   Graduate Student: R.G. Buchheit
   Degree: PhD
   UVa Department: Materials Science
   NASA-LaRC Contact: D.L. Dicus (Metallic Materials)
   Start Date: June, 1987
   Completion Date: December, 1990
   Cosponsor: Alcoa
   Employment: Sandia National Laboratories

4. DEFORMATION AND FRACTURE OF ALUMINUM-LITHIUM ALLOYS: THE EFFECT OF DISSOLVED HYDROGEN
   Faculty Investigator: R.E. Swanson (VPI)
   Graduate Student: Frederic C. Rivet
   Degree: MS
   VPI Department: Materials Engineering at VPI
   NASA-LaRC Contact: D.L. Dicus (Metallic Materials)
   Start Date: September, 1988
   Completion Date: December, 1990
   Employment: Not determined

5. INVESTIGATION OF THE REACTION KINETICS BETWEEN SiC FIBERS AND SELECTIVELY ALLOYED TITANIUM MATRIX COMPOSITES AND DETERMINATION OF THEIR MECHANICAL PROPERTIES
   Faculty Investigator: F.E. Wawner
   Graduate Student: Douglas B. Gundel
   Degree: MS
   UVa Department: Materials Science
   NASA-LaRC Contact: D.L. Dicus and W.B. Brewer (Metallic Materials)
   Start Date: January, 1989
   Completion Date: December, 1990
   Employment: Graduate School, University of Virginia; PhD candidate on LA^{2}ST Program; Department of Materials Science

6. DESIGN OF CRYOGENIC TANKS FOR SPACE VEHICLES
   Faculty Investigators: W.D. Pilkey and J.K. Haviland
   Graduate Student: Charles Copper
   Degree: MS
   UVa Department: Mechanical and Aerospace Engineering
   NASA-LaRC Contact: Drs. D.R. Rummler (Structural Mechanics Division), R.C. Davis and M.J. Shuart (Aircraft Structures)
   Start Date: April, 1989
   Completion Date: December, 1990
   Employment: Graduate School, University of Virginia; PhD candidate on NASA-Headquarters sponsored program; Department of Mechanical and Aerospace Engineering

ADMINISTRATIVE PROGRESS

Faculty Participation

Professor Edgar A. Starke, Jr., Dean of the School of Engineering and Applied Science, initiated a major research and engineering program on "Aluminum Based Materials for High Speed Aircraft", as a supplement to the LA^{2}ST Program.[1] This work, involving four UVa faculty and engineering-scientists from six industrial laboratories, will begin in January of 1992.

Brochure

A brochure was prepared in March of 1991 to advertise the LA^{2}ST program. Our aim is to nationally distribute this information to Universities and industries in the aerospace materials and mechanics communities. 250 copies have been circulated to date. All layout, printing and mailing costs were paid by the School of Engineering and Applied Science, and by the Materials Science Department at UVa.

Student Recruitment

The LA^{2}ST Program continues to recruit the best graduate students entering the participating Departments at UVa, and in sufficient numbers to achieve our education and research objectives. Three graduate students were recruited during the first half of 1991 and one new graduate student, Mr. Mark Lyttle, was recruited by Professor Wert during this reporting period to work on superplasticity in Al-Li-Cu alloys.

In April of 1990, the LA^{2}ST Program was increased in scope to include undergraduate engineering students[2]. While four students from North Carolina State and California Polytechnic State Universities, worked at NASA-LaRC during the Summer of 1990, there were no qualified applicants for the 1991 program. Efforts to recruit undergraduates for the Summer of 1992 have been intensified. The brochure was mailed to about 60 materials and mechanics departments in December of 1991; applications are beginning to arrive at UVa.

Complementary Programs at UVa

The School of Engineering and Applied Science at UVa has targeted materials and structures research for aerospace applications as an important area for broad future growth. The LA^{2}ST Program is an element of this thrust. Several additional programs are of benefit to LA^{2}ST work.

The Board of Visitors at UVa awarded SEAS an Academic Enhancement Program Grant in the area of Light Thermal Structures. The aim is to use University funds to seed

the establishment of a world-class center of excellence which incorporates several SEAS Departments. This program is lead by Professor Thornton and should directly benefit NASA.

The Light Metals Center has existed within the Department of Materials Science at UVa for the past several years under the leadership of Professor H.G.F. Wilsdorf, and upon his retirement, by Dean Starke. A Virginia Center for Innovative Technology Development Center in Electrochemical Science and Engineering was established in 1988 with Professor G.E. Stoner as Director. Professors Pilkey, Thornton and Gangloff are conducting research under NASA-Headquarters Grant sponsorship to examine "Advanced Concepts for Metallic Cryo-thermal Space Structures"[3,4]. Research within this program is complementing LA^{2}ST studies.

References

1. R.P. Gangloff, E.A. Starke, Jr., J.M. Howe and F.E. Wawner, "NASA-UVa Light Aerospace Alloy and Structures Technology Program: Supplement on Aluminum Based Materials for High Speed Aircraft", University of Virginia, Proposal No. MS NASA/LaRC-5215-92, October, 1991.

2. R.P. Gangloff, "NASA-UVa Light Aerospace Alloy and Structures Technology Program: A Supplementary Proposal", University of Virginia, Proposal No. MS NASA/LaRC-4677-90, April, 1990.

3. W.P. Pilkey, "Advanced Concepts for Metallic Cryo-thermal Space Structures", University of Virginia Proposal No. MAE-NASA/HQ-4462-90, August, 1989.

4. W.P. Pilkey, "Advanced Concepts for Metallic Cryo-thermal Space Structures", University of Virginia Report No. UVA/528345/MAE91/101, February, 1991.

CURRENT PROJECTS

MECHANICAL AND ENVIRONMENTAL DEGRADATION MECHANISMS IN ADVANCED LIGHT METALS AND COMPOSITES

1. ENVIRONMENTAL FATIGUE CRACK GROWTH AND CRACKING MECHANISMS IN Al-Li-Cu Alloy 2090
   Faculty Investigator: R.P. Gangloff
   Graduate Student: Donald Slavik; PhD Candidate.
   UVa Department: Materials Science and Engineering (MS&E)
   NASA-LaRC Contact: D.L. Dicus (Metallic Materials)
   Start Date: September, 1989
   Anticipated Completion Date: December, 1992
   Project #1

2. ENVIRONMENTAL EFFECTS IN FATIGUE LIFE PREDICTION: MODELING CRACK PROPAGATION IN TITANIUM ALLOYS
   Faculty Investigator: R.P. Gangloff
   Graduate Student: To be appointed in 6/92
   Post Doctoral Research Associate: Dr. Sang Kim
   UVa Department: MS&E
   NASA-LaRC Contact: R.S. Piascik (Mechanics of Materials)
   Start Date: January, 1992 (New project not reported here)
   Anticipated Completion Date: December, 1994
   Project #2

3. ELEVATED TEMPERATURE FRACTURE OF AN ADVANCED RAPIDLY SOLIDIFIED, POWDER METALLURGY ALUMINUM ALLOY
   Faculty Investigator: R.P. Gangloff
   Graduate Student: William C. Porr, Jr.; PhD candidate
   UVa Department: MS&E
   NASA-LaRC Contact: C.E. Harris (Mechanics of Materials)
   Start Date: January, 1988
   Anticipated Completion Date: June, 1992
   Project #3

4. ELEVATED TEMPERATURE CRACK GROWTH IN ADVANCED ALUMINUM ALLOYS

   Faculty Investigator: R.P. Gangloff
   Research Associate: Dr. Yang Leng
   Graduate Student: None
   UVa Department: Materials Science
   NASA-LaRC Contact: C.E. Harris (Mechanics of Materials)
   Start Date: March, 1989
   Completion Date: December, 1991
   Project # 3

5. ELEVATED TEMPERATURE DAMAGE TOLERANCE OF ADVANCED POWDER METALLURGY ALUMINUM ALLOYS

   Faculty Investigator: R.P. Gangloff
   Graduate Student: To be appointed
   UVa Department: MS&E
   NASA-LaRC Contact: To be named (Mechanics of Materials)
   Start Date: July, 1992 (New project not reported here)
   Completion Date: July, 1995
   Project #4

6. CRYOGENIC TEMPERATURE EFFECTS ON THE DEFORMATION AND FRACTURE OF Al-Li-Cu-In ALLOYS

   Faculty Investigator: R.P. Gangloff
   Graduate Student: John A. Wagner; PhD candidate and NASA-LaRC employee
   UVa Department: MS&E
   NASA-LaRC Contacts: W.B. Lisagor (Metallic Materials) and J.C. Newman (Mechanics of Materials)
   Start Date: June, 1987
   Anticipated Completion Date: May, 1993
   Project #5

7. THE EFFECT OF CRYOGENIC TEMPERATURE ON THE FRACTURE TOUGHNESS OF WELDALITE™

   Faculty Investigator: R.P. Gangloff
   Graduate Student: Cynthia L. Lach; MS candidate and NASA-LaRC employee
   UVa Department: MS&E
   NASA-LaRC Contacts: W.B. Lisagor (Metallic Materials)
   Start Date: August, 1990
   Anticipated Completion Date: May, 1993
   Project #6

8. MECHANISMS OF LOCALIZED CORROSION IN Al-Cu-Li-Mg-Ag ALLOY X2095 AND COMPOSITIONAL VARIATIONS
   Faculty Investigator: G.E. Stoner
   Graduate Student: Douglas Wall; PhD candidate
   UVa Department: MS&E
   NASA-LaRC Contact: D.L. Dicus (Metallic Materials)
   Start Date: April, 1991
   Completion Date: May, 1994
   Cosponsor: Reynolds Metals Company
   Project #7

9. EFFECTS OF Zn ADDITIONS ON THE PRECIPITATION AND STRESS CORROSION CRACKING BEHAVIOR OF ALLOY 8090
   Faculty Investigator: Glenn E. Stoner
   Graduate Student: Raymond J. Kilmer; PhD candidate
   Department: MS&E
   NASA-LaRC Contact: W.B. Lisagor (Metallic Materials)
   Start Date: September, 1989
   Anticipated Completion Date: December, 1992
   Cosponsor: Alcoa
   Project #8

10. HYDROGEN INTERACTIONS IN ALUMINUM-LITHIUM ALLOY 2090 AND SELECTED COMPLIMENTARY MODEL ALLOYS
   Faculty Investigator: John R. Scully
   Graduate Student: Stephen W. Smith; PhD Candidate
   Department: MS&E
   NASA-LaRC Contact: W.B. Lisagor and D.L. Dicus (Metallic Materials)
   Start Date: April, 1991
   Anticipated Completion Date: To be determined
   Cosponsor: Virginia CIT
   Project #9

AEROSPACE MATERIALS SCIENCE

11. INVESTIGATION OF THE EFFECT OF THERMAL TREATMENT ON THE MECHANICAL PROPERTIES OF Ti-1100/SCS-6 COMPOSITES
   Faculty Investigator: F.E. Wawner
   Graduate Student: Douglas B. Gundel; PhD candidate
   UVa Department: MS&E
   NASA-LaRC Contact: D.L. Dicus and W.B. Brewer (Metallic Materials)
   Start Date: April, 1991
   Anticipated Completion Date: June, 1993
   Project #10

12. QUANTITATIVE CHARACTERIZATION OF THE SPATIAL DISTRIBUTION OF PARTICLES IN MATERIALS: APPLICATION TO MATERIALS PROCESSING
    Faculty Investigator: John A. Wert
    Graduate Student: Joseph Parse; PhD candidate
    UVa Department: Materials Science
    NASA-LaRC Contact: D.R. Tenney (Materials Division)
    Start Date: September, 1988
    Anticipated Completion Date: December, 1991
    Project #11

13. PROCESSING AND SPF PROPERTIES OF WELDALITE™ SHEET
    Faculty Investigator: John A. Wert
    Graduate Student: Mark Lyttle; MS Candidate
    UVa Department: MS&E
    NASA-LaRC Contact: T. Bayles (Metallic Materials)
    Start Date: September, 1991
    Anticipated Completion Date: September, 1993
    Project #12

14. DEVELOPMENT OF LOW ALLOY HIGH STRENGTH ALUMINUM
    Faculty Investigator: E.A. Starke, Jr.
    Post Doctoral Research Associate: A.K. Mukhopadhyay
    UVa Department: MS&E
    NASA-LaRC Contact: W.B. Lisagor (Metallic Materials)
    Start Date: April, 1991
    Anticipated Completion Date: Transferred to Grant Supplement on High Speed Civil Transport Alloys; Completion is projected for December of 1994.
    Project #13

MECHANICS OF MATERIALS FOR AEROSPACE STRUCTURES

14. INELASTIC RESPONSE OF METAL MATRIX COMPOSITES UNDER BIAXIAL LOADING
    Faculty Investigators: Carl T. Herakovich and Marek-Jerzy Pindera
    Graduate Student: Mr. Clifford J. Lissenden, PhD Candidate
    UVa Department: Civil Engineering and the Applied Mechanics Program
    NASA-LaRC Contact: W.S. Johnson (Mechanics of Materials)
    Start Date: September, 1990
    Anticipated Completion Date: May, 1993
    Project #14

THERMAL GRADIENT STRUCTURES

15. EFFECT OF TEMPERATURE ON THE RESPONSE OF METALLIC SHELL STRUCTURES

Faculty Investigators: W.D. Pilkey and J.K. Haviland
Graduate Student: Karen McCarthy; MS candidate
Graduate Student: Theodore Johnson; PhD candidate (NASA Minority Grantee)
Graduate Student: Charles Copper; PhD Candidate
UVa Department: Mechanical and Aerospace Engineering
NASA-LaRC Contact: Drs. M.J. Shuart and Jeffrey Stroud (Aircraft Structures)
Start Date: April, 1991
Anticipated Completion Date: December, 1992
Project #15

16. EXPERIMENTAL STUDY OF THE NONLINEAR VISCOPLASTIC RESPONSE OF HIGH TEMPERATURE STRUCTURES

Faculty Investigator: Earl A. Thornton
Graduate Student: Marshall F. Coyle; PhD candidate
Undergraduate Student: Ms. Yool Kim
UVa Department: Mechanical and Aerospace Engineering
NASA-LaRC Contact: James H. Starnes, Jr. (Aircraft Structures)
Start Date: January, 1990
Anticipated Completion Date: To be determined
Project #16

RESEARCH PROGRESS AND PLANS (July 1 to December 31 , 1991)

Research progress, recorded during the period from July 1, 1991 to December 31, 1991, is summarized by Project in the following sections.

Project 1 Environmental Fatigue Crack Growth and Cracking Mechanisms in Al-Li-Cu Alloy 2090

Donald C. Slavik and Richard P. Gangloff

Objective

The broad objectives of this PhD research are: (a) to expand the environmental fatigue data base with intrinsic and chemically correct FCP data for Al-Li-Cu alloys, (b) to physically understand intrinsic process zone damage, and (c) to incorporate observations into an environmental fatigue crack growth rate model. Mr. Slavik recently completed the formal Proposal for his PhD research. This report, presented here, identifies critical uncertainties, summarizes experimental and analytical approaches and data obtained to date, and outlines the tasks remaining to complete the PhD degree.

Background--Fatigue Crack Growth Behavior

Crack growth rates for Al-Li-Cu-X alloys are dramatically affected by environment[1] and crack closure[2,3]. Microstructural interactions with environmental crack growth are equally important, but are not well understood.

Crack Closure, the premature contact of fatigue crack faces during unloading, dominates FCP in Al-Li alloys at low stress intensity ranges and low R-ratios ($R = K_{min}/K_{max}$)[2,3]. The influence of environment and microstructure on intrinsic fatigue crack growth rates can only be established when crack closure is understood. Crack closure must be precisely measured and interpreted, which is difficult[4,5], or minimized with high mean stress experiments[1,6]. The majority of such work has focused on FCP in the Al-Li-Cu/moist air system, without regard for environment-closure interactions.

Environment dramatically affects fatigue cracking in Al-Li-Cu alloys; Figure 1[1]. Intrinsic growth rates were measured for peak aged 2090 in inert, moist air, and aqueous

NaCl environments. Moist air is aggressive compared to vacuum, and aqueous NaCl is aggressive compared to moist air. It is not known if Weldalite or other Al-Li-Cu alloys behave similarly. Microstructure should affect environment-sensitive intrinsic crack growth rates, but this has not been substantiated.

Microstructure can be dramatically changed in Al-Li alloys with alloying elements or by thermomechanical processing[7,8]. The role of microstructure on FCP in Al-Li was documented for FCP in moist air[8-10] and inert environments[11], and for stress corrosion cracking in aqueous NaCl[7,12-13]. Microstructure has not, however, been varied systematically to understand environmental fatigue crack growth rates; particularly intrinsic properties and causal damage mechanisms.

Environmental Fatigue Behavior-Questions and Needs The following uncertainties must be resolved.

(1) How do environmental fatigue crack growth rates compare for unrecrystallized 2090 sheet, 2090 plate, and Weldalite?

(2) Are crack growth rates and microscopic crack paths different for recrystallized and unrecrystallized grain structures? Can model systems be developed to expand understanding of corrosion fatigue in Al-Li-Cu?

(3) How is crack closure effectively eliminated to establish intrinsic fatigue crack growth rate data?

Background-Process Zone Damage and Crack Growth Rate Modelling

Process Zone Damage Models Prediction of environmental fatigue crack growth rates requires an understanding of crack tip damage mechanisms. During fatigue cycling, intense reverse plastic flow at the crack tip produces a cyclic plastic zone. Stable crack extension defines the process zone, consuming a portion of the cyclic plastic zone; the definition of the precise process zone is unclear. Crack growth rate calculations require the process zone stress gradient, the plastic strain gradient, and a stress/strain-life relationship. Finite element methods established monotonic stress and strain distributions, and cyclic plastic zone sizes and estimates of crack tip plastic strain range[14]. Crack tip fields and the process zone may be affected by environment.

Direct crack tip damage measurements are extremely difficult, thus limiting model development. The process zone is small (0.1 to 50 μm size), stress/strain gradients are large,

and crack tip damage is difficult to directly probe.

Since process zone measurements are not available, assumptions are required. Mechanical FCP models assume either a constant process zone size of microstructural dimensions[15,16], or a process zone size based on a critical strain[17]. The role of environment in process zone damage, be it hydrogen embrittlement or anodic dissolution and repassivation, is not well understood.

Inert Environment Crack Growth Modelling {111} crack paths have been identified for 2090 FCP in inert[17] and moist air[18] environments. Localized and intense slip bands form in 2090 due to easy shearing of the coherent δ' (Al_3Li) precipitate. Once δ' is sheared, further dislocation motion progresses on the slip plane resulting in local strain accumulation and eventual {111} cracking. A single damage mechanism is activated and a single Paris Law exponent is observed (Figure 1).

Microstructure generally does not influence intrinsic FCP rates for metals in truly inert environments[19], but this has not been established for Al-Li-Cu alloys. Changes in slip length due to the subgrain size, the grain size, dispersoids (Al_3Zr), and perhaps T_1 (Al_2CuLi) have not been considered in establishing microstructural influences on inert environment fatigue crack growth. It is not known how cracking proceeds in an Al-Li-Cu alloy without the δ' precipitate (e.g., Weldalite[9]).

Hydrogen Producing Environments and Crack Growth Modelling Aggressive environments control damage within the process zone for alloys and microstructure that are susceptible. Selective anodic dissolution of the electrochemically active T_1 precipitate was found for 2090 in aqueous NaCl[13]. Since hydrogen production accompanies anodic dissolution in aluminum alloys at most electrode potentials, either mechanism may explain crack growth in 2090. For example, at low ΔK, hydrogen embrittlement, including brittle hydride formation[20] perhaps produces {100} cleavage cracks[17]. For larger ΔK and process zone size, dislocation transport hydrogen to subboundary T_1 may supply hydrogen for intersubgranular cracking.

Varying amounts of unique microscopic cracking mechanisms are the cause for changes in da/dN-ΔK slopes for 2090 plate in moist air and NaCl[17] (Figure 1). Different cracking mechanisms, with individual growth kinetics, can operate in parallel for corrosion fatigue[21]. The measured crack growth rate is a superposition of the FCP kinetics for each mechanism times the area fraction of each process (Θ_i)[17]:

$$da/dN \;\alpha\; \Theta_{\{111\}}\Delta K^{n\{111\}} + \Theta_{\{100\}}\Delta K^{n\{100\}} + \Theta_{subgrain}\Delta K^{n(subgrain)}$$

where n{111}, n{100}, and n(subgrain) correspond to the exponents representative of slip band cracking, cleavage cracking, and intersubgranular cracking, respectively. The challenge is to develop microscopic mechanism-based models for n_i and Θ_i. This crack growth rate modeling framework was proposed for 2090 plate. The existing model is speculative, applicable to a single 2090 microstructure, requires adjustable parameters, and does not include a quantitative failure criteria for hydrogen environments. Further work is needed.

Process Zone Modeling-Questions and Needs The following uncertainties must be resolved in order to model environmental FCP.

(1) What determines the process zone? Is process zone size a constant based on microstructural features and slip length, or does the size increase with ΔK on a critical plastic strain basis? Are "striations" observed in Al-Li-Cu alloys? Why are striations formed and do they correspond to the process zone size?

(2) How does cracking proceed within the process zone: continuously per load cycles or discontinuously after damage accumulation?

(3) Why do {100} cleavage facets form? Do hydrides with a {100} habit form in 2090 or Weldalite? Is the {100} facet orientation consistent with unrecrystallized textures? What causes intersubgranular cracking? Does it occur in unrecrystallized 2090 sheet, 2090 plate, and Weldalite? What are the cracking mechanisms for a recrystallized microstructure with no subgrain path?

(4) Do precipitates affect environmental FCP mechanisms? Does a $\delta' + \Theta' + T_1$ alloy (2090) behave differently than a $\Theta' + T_1 + S'$ alloy (Weldalite)?

(5) What causes a change in the slope of da/dN versus ΔK? Do fractographic mode changes correlate to Paris slope transitions for different environments and microstructures?

(6) What controls damage or life within the process zone for inert and aggressive environments? Is uniaxial smooth bar fatigue life at a given strain representative of the process zone? How are environmental effects correctly included in a process zone failure criterion?

Objectives

To achieve the broad objectives of the research, specific goals are to: (a) characterize commercial unrecrystallized peak aged 2090 sheet, 2090 plate, and Weldalite with intrinsic

closure-free FCP data for controlled inert and hydrogen bearing environments, (b) establish microscopic fracture modes, including crystallographic facet orientations, (c) determine the effect of varying fractions of T_1 and δ' on environmental FCP rates and cracking modes, (d) produce model microstructures to provide FCP damage mechanism insight, and (e) establish a process zone hydrogen embrittlement model.

Approach

The approach to the proposed research was previously detailed[22]. In summary global fatigue crack growth rates will be measured for alloy 2090 and Weldalite in inert and hydrogen producing environments with compact tension and single edge notch specimens. High mean stress constant K_{max} experiments will be utilized to minimize the influence of crack closure. The inert environment is a dynamic vacuum at better than 1μPa total pressure. The aggressive environment is a deaerated 1 wt% salt solution at -840 mV_{SCE}. Potential-current density measurements will be performed on all microstructures to ensure that this potential is below the pitting potential.

The materials are commercially produced (Vintage III) unrecrystallized 2090 sheet, 2090 plate, and Weldalite (obtained from Marshall Space Flight Center through NASA-LaRC). Low temperature ages and near peak aged (T8) tempers will be considered. Transmission electron microscopy (TEM) will be used to identify the type, size, and distribution of precipitates and subgrains. Texture analysis will be performed to determine preferred crystallographic orientations.

Recrystallized fine and coarse grain microstructures will be produced with novel thermomechanical processing techniques[23]. Such model structures will be used to probe microstructural and environmental effects on fatigue crack growth rates and microscopic cracking processes.

High magnification scanning electron fractography will be used to characterize microscopic fracture modes. Facet orientations will be determined with quantitative stereo-pairs, crack plane sections, and electron channelling patterns. Resolved shear and normal stresses on observed cracking planes will be calculated to establish possible failure criteria. Striations will be identified on crack facets to establish the process zone size and character.

A fatigue crack growth rate model will be developed based on observed crack growth rates and microscopic cracking modes. Process zone stress and strain distributions will be

taken from the literature[14]. A process zone failure criteria will be proposed, based on environmental fatigue crack growth rates and microscopic cracking modes, and perhaps independently evaluated.

Results to Date

Crack closure measurements are ideally needed to verify that high mean stress experiments are closure-free. A small strain gauged plexiglass structure, capable of salt water submersion, was manufactured and glued to the specimen front face bridging the crack mouth. Load displacement data from the plexiglass gauge were nonlinear, indicative of crack closure, but the trends did not agree with a conventional clip gauge for an experiment in air casting doubt on the reliability of the plexiglass clip gauge. This technique has not been pursued, particularly since interpretation of the closure measurements are controversial[4,5].

Crack closure levels can be estimated with low R and high K_{max} experiments. Assuming that high R-ratio data are intrinsic, and that the shift of low R (0.1) data is due to crack closure:

$$K_{open} = K_{max} - \Delta K_{eff}$$

K_{max} is the R = 0.1 maximum stress intensity, and ΔK_{eff} is the intrinsic stress intensity range. A crack growth rate of 6 x 10^{-7} mm/cycle was chosen for the calculation. For inert environments where closure is likely to be highest due to tortuous {111} cracking, K_{open} equals 2.3 MPa$\sqrt{m}$ for 2090 sheet and plate. For the high K_{max} experiments, stress intensities are well above this and other calculated crack closure levels.

Intrinsic crack growth rates of peak aged (155°C for 18 hours) Vintage III 2090 sheet and plate were established for inert vacuum, moist air and 1 wt% aqueous NaCl as shown in Figure 2. Sheet and plate possess similar intrinsic growth rates. Moist air is significantly more damaging as compared to inert environments with a 3-fold reduction in ΔK_{th}. Aqueous solutions are mildly more aggressive compared to moist air.

The shapes of the intrinsic growth rate curves are environment dependent. For vacuum a steep and linear Paris regime is observed. In moist air and salt water, a steep slope is observed for $\Delta K < 2$ MPa$\sqrt{m}$. The slope decreases for 2 MPa$\sqrt{m} < \Delta K < 5$ MPa$\sqrt{m}$, before increasing for higher ΔK.

Microstructural characterizations of peak aged 2090 sheet and plate were performed on planes normal to the T direction with optical and transmission electron metallography.

An optical micrograph of the grain structure, and a TEM micrograph of subboundary and matrix T_1 are shown in figure 3. Average grain widths (S direction) and subgrain sizes are:

	Grain Width S-Direction (μm)	Subgrain Size S x T (μm)
2090 Plate	10 to 200	3 x 13
2090 Sheet	10	1 x 5

Subgrains are elongated in the T direction and are somewhat smaller in sheet compared to plate. Grains sizes vary considerably in plate, but are reasonably uniform in sheet. The grains are very long in the L and T directions for sheet and plate (order of millimeters). A full {111} pole figure provided by the Alcoa Technical Center established that 2090 sheet is unrecrystallized, exhibiting S, brass and copper texture elements similar to 2090 plate[17].

T_1 nucleates on subgrain boundaries and within the matrix on {111} habit planes. More T_1 nucleated on subgrain boundaries, but matrix and subgrain T_1 are typically the same size. Large subgrain T_1 plates are occasionally observed. The precipitation of δ' is uniform, with minimal precipitate free zones near subboundaries. The precipitate morphologies of sheet and plate 2090 are similar.

Microscopic fatigue crack paths were determined for sheet and plate in vacuum and in 1 wt.% NaCl. Large slip band facets were produced by FCP in 2090 plate in inert environments (Figure 4a) as reported in the literature[17]. The facets in 2090 sheet are smaller, and on multiple planes (Figure 4b) which are possibly different {111} variants. Facets are reasonably smooth with no visible striations and fracture modes are not dependent on ΔK for 2090 in inert environments, consistent with the single Paris slope.

Cracking mechanisms in the 2090/NaCl system are significantly more complex. SEM fractographs at selected ΔK are shown for 2090 plate in Figure 5. Large facets are observed (ΔK = 1.3 MPa$\sqrt{m}$); Figure 5a. Stereo viewing and metallographic T-plane sections establish that the facets are stepped in the L-T plane. The T-plane section is shown in figure 6 with a 30° tilt toward the fracture surface. These facets are distinctly different from {111} facets and have been tentatively identified as {100}[17]. Channelling patterns[24,25] will be taken directly from the facet and the sectioned T-plane to determine the precise facet crystallography. The large grain size model alloys will enable study of crystallographic FCP.

At higher ΔK, narrow (possibly {100}) facets form on parallel planes with interface tearing (Figure 5b). Increased tearing and slip plane cracking are observed for 2090 plate at ΔK = 8.5MPa$\sqrt{m}$ (Figure 5c).

2090 sheet/NaCl fractography is shown in Figure 7. Small flat pitted regions are observed for ΔK = 1.3 MPa$\sqrt{m}$; these are possible {100} facets. Flat facets and intersubgranular crack paths are observed for 2.3 MPa$\sqrt{m} \leq \Delta K \leq$ 8.5 Mpa$\sqrt{m}$. 2090 sheet has significantly more intersubgranular cracking than 2090 plate. It is not understood why the fracture mechanisms in 2090 sheet and plate are apparently different, while measured growth rates are similar. It is possible that microscopic mechanisms do not strongly influence intrinsic crack growth rates in aggressive hydrogen producing environments. It is also possible that the fracture modes in sheet and plate are more similar than they first appear. If T_1 dominates corrosion fatigue behavior, transgranular and intergranular fracture may be equivalent cracking mechanisms since matrix and subgrain T_1 are similar.

Model recrystallized microstructures were developed by overaging, warm rolling, and solutionizing Vintage III plate 2090[23]. The over age was 4 to 16 hours at 400°C followed by a furnace cool, and was designed to coarsen precipitates that focus highly local deformation regions during subsequent rolling. The plate was warm rolled at 300 to 320°C to $\epsilon_{eff} \approx -2$. This temperature was chosen to minimize edge cracking and dynamic recovery. A slow 10^{-3} °C/second temperature ramp from 250°C to 510°C produced the coarse grain recrystallized microstructure. The fine grain size was produced by rapid salt bath solutionizing at 540°C.

Recrystallized microstructures are shown in Figure 8 (Barker's etch and polarized light). The fine grains are approximately 25 μm x 25 μm. The coarse grains are approximately 200 μm x 7000 μm (S x T directions). Recrystallization was complete with uniform through thickness grains. Rolled model microstructures were all resolutioned at 540°C for 1/2 hour, quenched in cold water, stretched to $\epsilon p \approx 6\%$, and aged at 155°C for 18 hours. T_1 precipitation in the recrystallized microstructures is similar to the conventional peak aged unrecrystallized microstructures.

Process zone failure criteria are being considered with high magnification fractography and process zone calculations. High magnification fractography is needed to find striations. Striations in aluminum alloys in aqueous chloride were hypothesized to correspond to process zone size[26]. The stationary crack tip is believed to corrode while the

process zone accumulates cyclic damage and embrittling hydrogen. The process zone material fails and damage accumulation repeats. A striated plate fracture facet (2090 plate in NaCl) is shown in Figure 9. Striations have not been observed for high stress intensity ranges, possibly due to subgrain tearing. A model system without subgrains will be examined for striations to aid in process zone evaluation.

Shear and tensile stresses, resolved with respect to crystallographic facets, were predicted with a model that incorporates facet orientation from a metallographic section, grain orientation from X-ray diffraction, and process zone continuum triaxial stress distributions. Fatigue facets appear to form along those {111} planes that are oriented to produce the maximum shear stress. {100} type facets appear to form along planes oriented to produce maximum tensile stress. If broadly true, these results suggest that the failure criteria for inert environments is shear based for cracking along slip planes, while the failure criteria is normal stress based for the aggressive environments, typical of hydrogen embrittlement.

Proposed Research

The following research is proposed to complete the PhD degree.

Basic material properties will be established with moist air tensile tests, aqueous chloride polarization scans, and texture analysis. The monotonic yield stress, elastic modulus, ultimate stress, fracture strain, and strain hardening exponent will be measured for all microstructures. Polarization scans will be used to determine pitting potentials. Full {200} and {111} pole figures will establish common texture components and crystallographic orientations.

Alloy composition and aging treatment will be varied to determine if precipitate characteristics affect environmental FCP and microscopic cracking mechanisms in the Al-Li-Cu system. T_1, which controls intersubgranular and {100} cracking in peak aged 2090 ($\delta' + T_1 + \Theta'$) in aggressive environments, will be eliminated by low temperature aging of Vintage III 2090 plate. Aging at low temperatures produces $\delta' + \Theta'$ precipitates. δ', which causes slip band cracking in under to peak aged 2090 in inert environments, will be eliminated with different Cu/Li ratios; specifically Weldalite compositions. For the 4.0 wt% Cu - 1 wt% Li composition of Weldalite, the precipitates are $\Theta' + T_1 + S'$[9]. Apart from precipitate effects, the environmental FCP behavior of Weldalite has not been characterized.

Unfortunately, yield strength/work hardening and precipitate type cannot be varied

independently with commercial alloys. Since both factors may affect FCP, future experiments may be proposed as needed.

Recrystallized model grain structures were successfully produced in Vintage III 2090. Environmental FCP will be measured for inert and aggressive environments and for fine subgrain unrecrystallized, fine grain recrystallized, and coarse grain recrystallized microstructures. The aim here is not to produce FCP resistant microstructures, but rather is to simplify the microstructure in order to test mechanistic ideas regarding environmental effects.

Microscopic cracking mechanisms in aqueous NaCl have been tentatively identified for unrecrystallized microstructures. Quantitative stereo-pair microscopy and electron channelling patterns will conclusively determine facet crystallography for low ΔK FCP in NaCl; such facets were tentatively identified as {100}[17,27]. Facet orientations produced by FCP at increasing ΔK will be established with stereo-pair microscopy[28]. Large grain size microstructures will enable these experiments.

Potential problems involve recording an electron channelling pattern of sufficient detail to identify the crystallographic orientation, but in the presence of significant crack wake plasticity. Irrefutable facet crystallography could be determined by comparing facet orientation with T_1 on {111} habit planes. This technique is under consideration, but may not be pursued since corrosive films and highly active surface T_1 may obscure the precipitate.

High magnification fractography will be employed to identify important fracture surface features. Particular emphasis is placed on striations and facet roughness. If observed, striation spacings will be measured for different stress intensity ranges and environments. Corrosive debris may limit high magnification observations.

Mean stress effects on intrinsic rates of environmental FCP, above crack closure levels, have not been addressed. Modeling suggests that K_{max} has not influence on da/dN enhanced by process zone hydrogen embrittlement[17]. Variations in K_{max} above crack closure levels can be probed with multiple R-ratios. As an example, FCP will be measured for R = 0.75 for ΔK = 1.3 to 4.5 MPa$\sqrt{m}$ (K_{max} = 3.9 to 18 MPa$\sqrt{m}$). Da/dN-ΔK shapes and crack growth rates of constant R experiments will be compared to constant K_{max} (17 MPa$\sqrt{m}$) data to determine if mean stresses affect FCP in NaCl and perhaps vacuum. It may be difficult to separate differences in crack propagation rates due to crack closure or true intrinsic damage processes.

Environmental fatigue crack propagation modeling will be approached based on the physical details of cracking. The issues of importance are:

What Determines the Crack Advance Distance? The possible answers are: (a) plastic strain range above a critical level, because process zone damage requires a critical level of dislocation activity, (b) normal stress above a critical level, as necessary for local brittle fracture, or (c) microstructure and slip distance, as critical to fatigue damage.

What Determines the Number of Load Reversals for Crack Advance? A possible answer unique to environmental cracking is the number of cycles to develop a critical level of hydrogen in the process zone through either: (a) development of a critical dislocation substructure with microvoids to trap H, or (b) dislocation transport of a critical amount of hydrogen to existing microstructural H trap sites. A key issue in this regard is the determination of the failure criterion that relates the number of cycles for crack advance to local plastic strain, hydrogen concentration (and/or electrochemical activity), and normal stress. Ideally, such a failure criteria should be independently defined and the associated parameters established.

It is not known if a predictive crack growth rate model can be fully developed before the influences of microstructure and environment on FCP are broadly understood, and before the causes of each parallel cracking mechanism are physically understood.

References

1. R.S. Piascik and R.P. Gangloff, Metall. Trans. A, Vol. 22A, pp. 2415-2428 (1991).

2. K.T. Venkateswara Rao, W. Yu, and R.O. Ritchie, Metall. Trans. A, Vol. 19A, pp. 549-569 (1988).

3. K.T. Venkateswara Rao, R.J. Bucci, K.V. Jata, and R.0. Ritchie, "A Comparison of Fatigue-Crack Propagation Behavior in Sheet and Plate Aluminum-Lithium Alloys", Materials Science and Engineering A, in press (1991).

4. K. Donald, "Comments on Crack Closure Measurement and Analysis", Fracture Technology Associates, Springtown, Pa., unpublished research (1989).

5. R.E. Garz and M.N. James, Int. J. of Fatigue, pp. 437-440 (1989).

6. W.A. Herman, R.W. Hertzberg, and R. Jaccard, Fatigue and Fracture of Engineering Materials and Structures, Vol. 11 No. 4, pp. 303-320 (1988).

7. R.C. Dorward, Corrosion, Vol. 46 No. 4, pp. 348-325 (1990).

8. J.M. Newman, P.J. Gregson, P.D. Pitcher, and P.J.E. Forsyth, in Aluminum-Lithium Alloys V, T.H. Sanders Jr. and E.A. Starke Jr., eds., Vol. 2, pp. 1042-1052 (1989).

9. C.P. Blankenship Jr. and E.A. Starke Jr., Fatigue Fracture of Engineering Materials and Structures, Vol. 14 No. 1, pp. 103-114 (1991).

10. A.K. Vasudevan, P.E. Bretz, and A.C. Miller, Materials Science and Engineering, Vol. 64, pp. 113-133 (1984).

11. K.V. Jata and E.A. Starke Jr., Metall. Trans. A, Vol. 17A, pp. 1011-1026 (1986).

12. R. Balasubramaniam, D.J. Duquette, and K. Rajan, Acta Metallurgica et Materialia, Vol. 39 No. 11, pp. 2597-2605 (1991).

13. R.G. Buchheit, J.P. Moran, and G.E. Stoner, Corrosion, Vol. 46, pp. 610-617 (1990).

14. R.P. Gangloff, in Environment Induced Cracking of Metals, R.P. Gangloff and M.B. Ives, eds., NACE, Houston, TX, pp. 55-109 (1990).

15. S.B. Chakrabortty, Fatigue of Engineering Materials and Structures, Vol. 2, pp. 331-344 (1979).

16. S.D. Antolovich, A. Saxena, and G.R. Chanani, Engineering Fracture Mechanics, Vol. 7, pp. 649-652 (1975).

17. R.S. Piascik and R.P. Gangloff, "Environmental Fatigue Crack Propagation in Al-Li-Cu: Part II-Modeling of Crack Tip Hydrogen Damage", Submitted to Metall. Trans. A (1992).

18. G.R. Yoder, P.S. Pao, M.A. Imam, and L.A. Cooley, Scripta Metallurgica, Vol. 22, pp. 1241-1244 (1988).

19. M.O. Spiedel, in Stress Corrosion Cracking and Hydrogen Embrittlement of Iron Based Alloys, J. Hochmann, J. Slater, R.D. McCright, and R.W. Staehle, eds., Houston Texas NACE, pp. 1071-1094 (1977).

20. R. Balasubramaniam, D.J. Duquette, and K. Rajan, Acta Metallurgica et Materialia, Vol. 39 No. 11, pp. 2607-2613 (1991).

21. P.S. Pao, Ming Gao, and R.P. Wei, Scripta Metallurgica, Vol. 43 No. 4, pp. 204-207 (1987).

22. R.P. Gangloff, "NASA-UVa Light Aerospace Alloy and Structures Technology Program", Proposal No. MS-NASA/LaRC-5219-92, University of Virginia, Charlottesville (1991).

23. C.C. Bampton, J.A. Wert, and M.W. Mahoney, Metall. Trans. A, Vol. 13A, pp. 193-198 (1982).

24. D.L. Davidson, Int. Metals Reviews, Vol. 29 No.2, pp. 75-95 (1984).

25. E.I. Meletis, in Fracture, Measurement of Localized Deformation by Novel Techniques, W.W. Gerberich and D.L. Davidson, eds., AIME Fall Meeting, pp. 87-101 (1984).

26. N.J.H. Holroyd, "Microstructural Aspects Controlling the Environment-Sensitive Fracture of High Strength Aluminum Alloys", TMS Fall Meeting, Cincinnati, OH, (October, 1991).

27. G.G. Garrett and J.F. Knott, Acta Metall. Mater., Vol. 23, pp. 841-848 (1975).

28. J.A. Wert and W.M. Robertson, Metallography, Vol. 15, pp. 367-381 (1982).

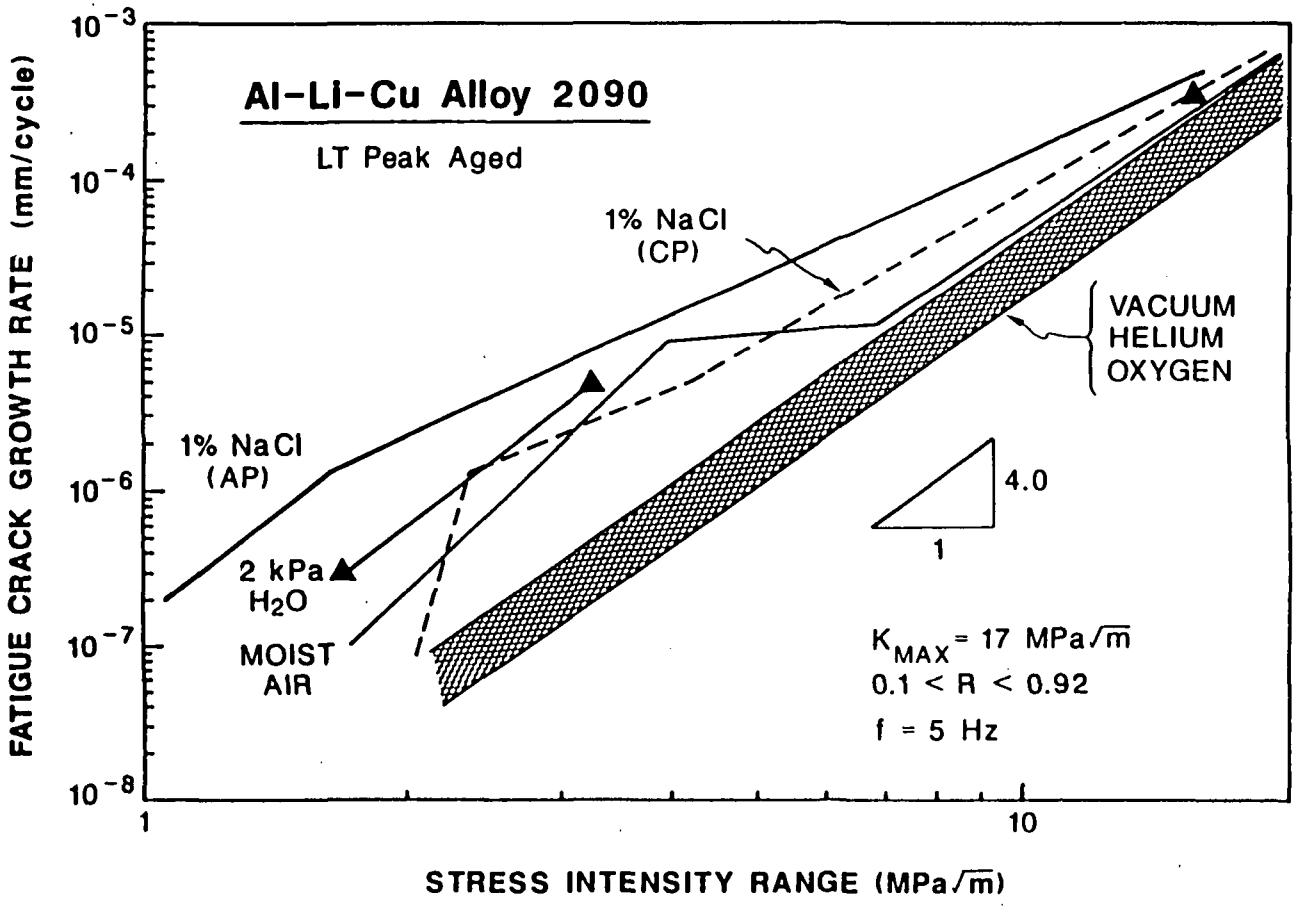

Figure 1 Fatigue crack growth rates of unrecrystallized 2090 plate, 190°C-4 hour age

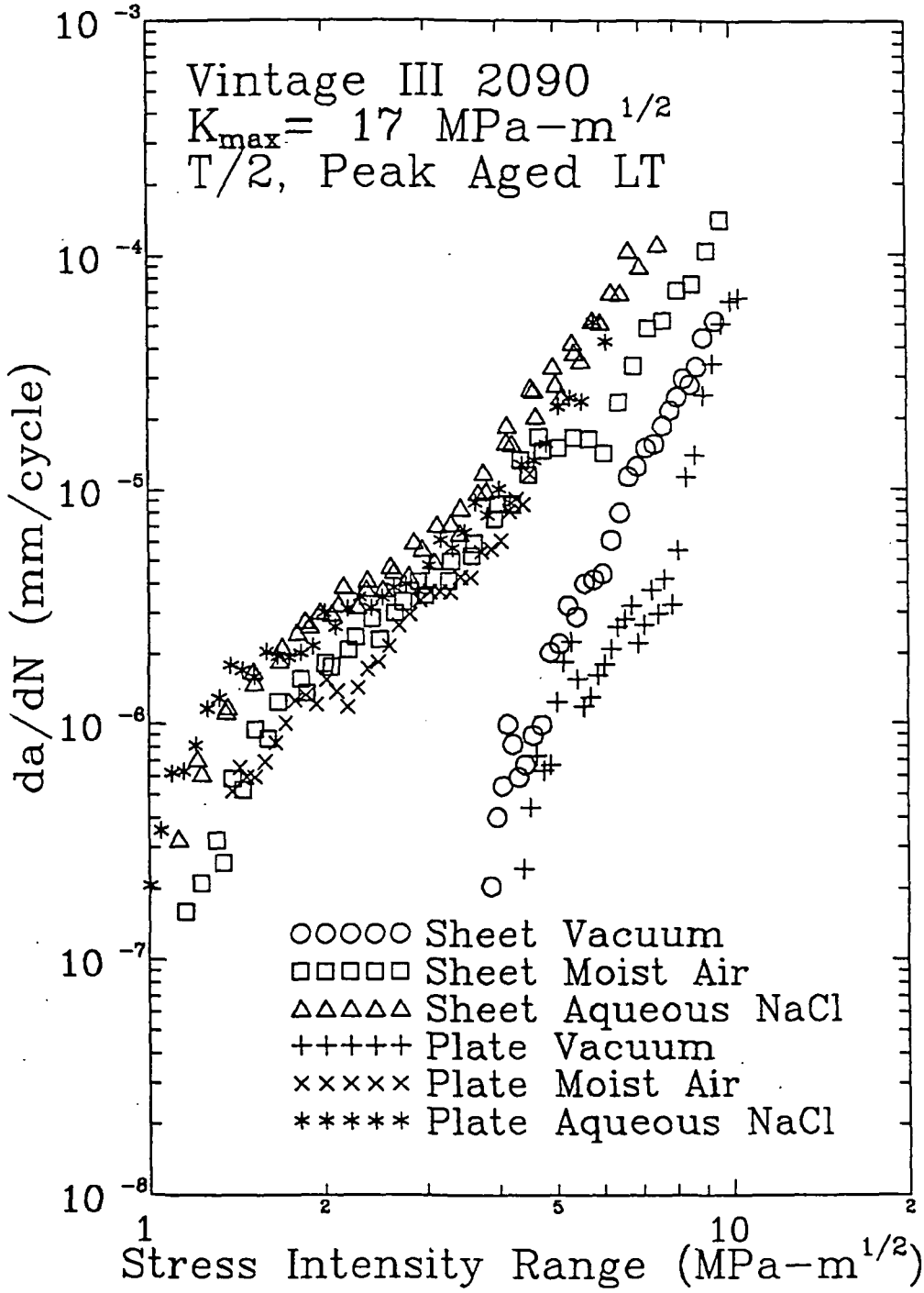

Figure 2 Fatigue crack growth rates of unrecrystallized 2090 sheet and plate, 155°C-18 hour age (Vintage III)

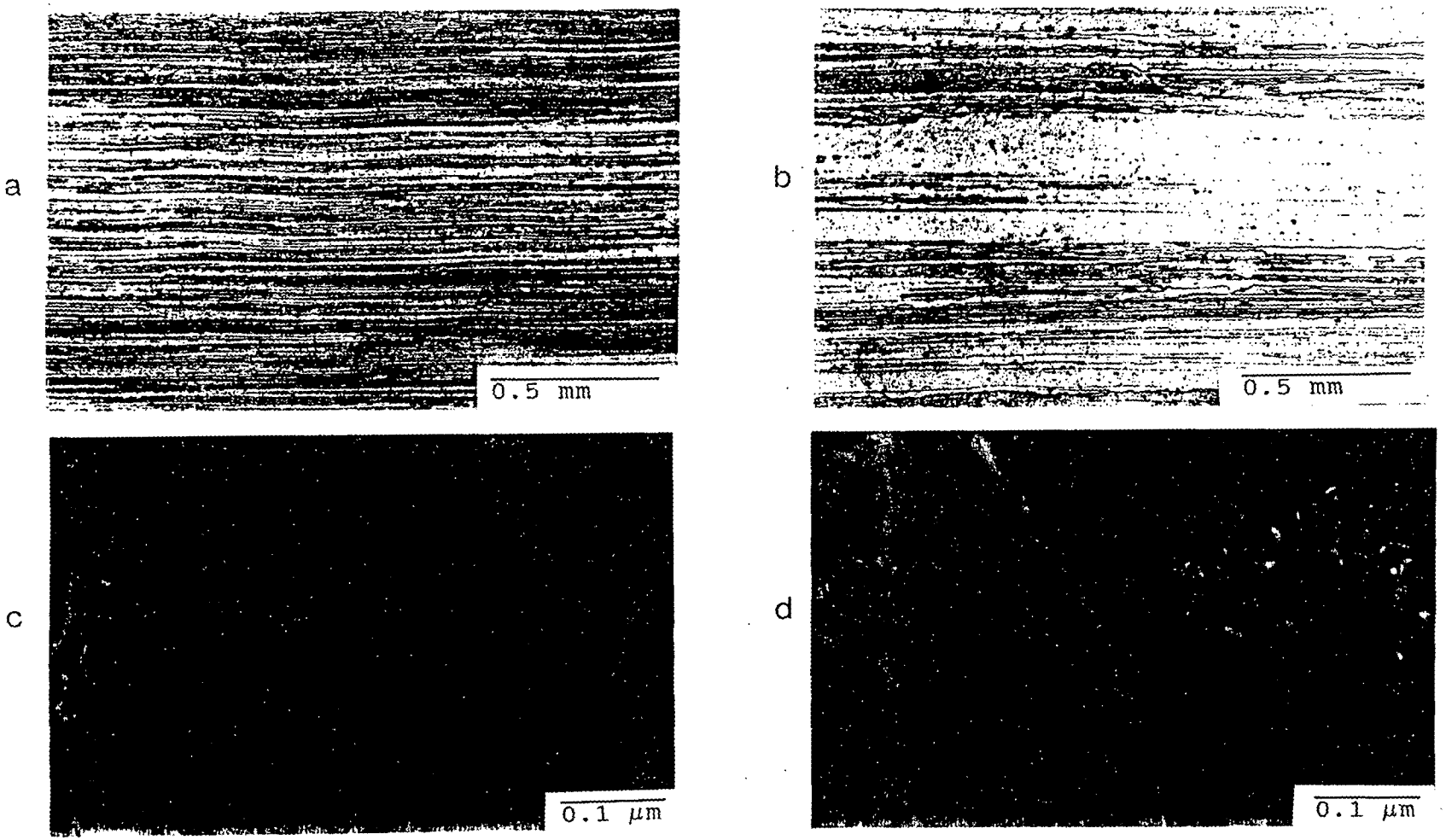

Figure 3 Unrecrystallized 2090 L-plane sections; (a) sheet grain structure, (b) plate grain structure, (c) sheet subgrain T_1, (d) plate subgrain T_1

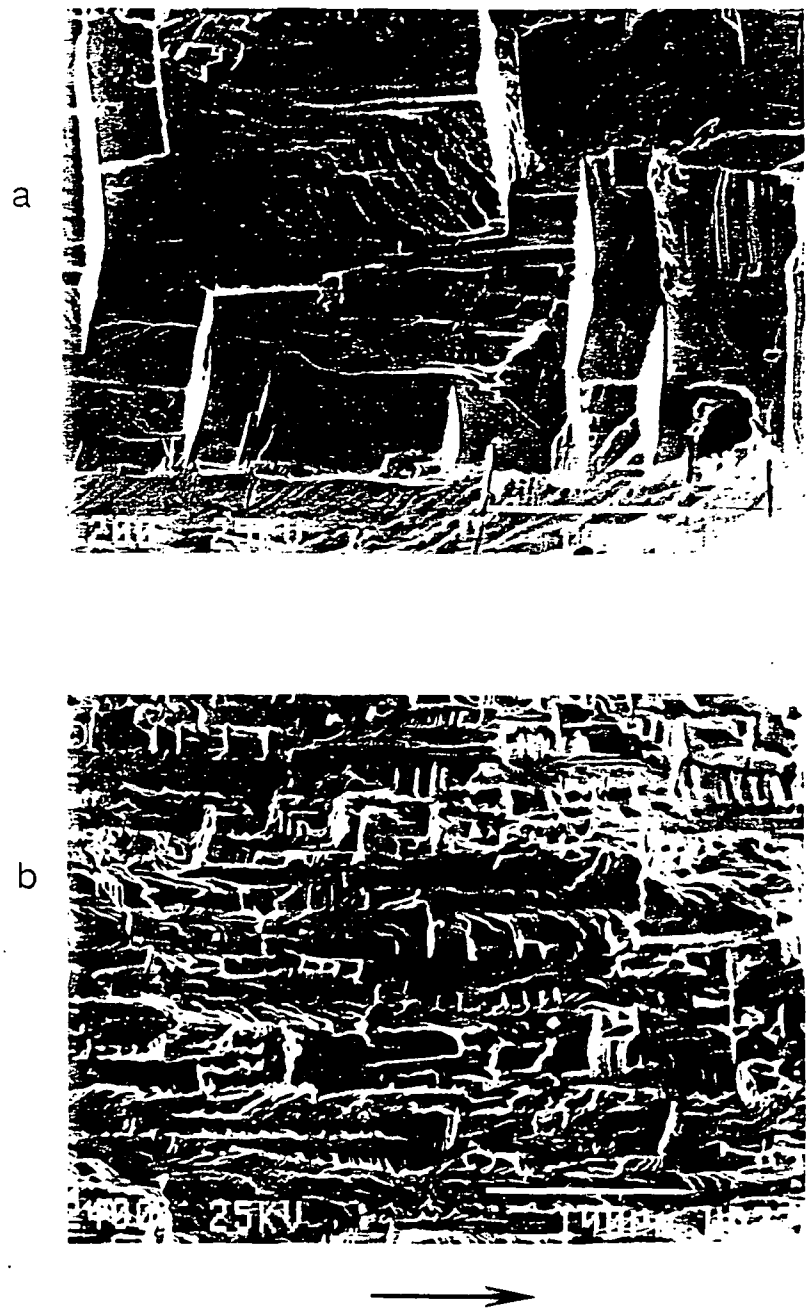

Figure 4 Unrecrystallized 2090 fractography, vacuum (arrow indicates the crack direction); (a) plate, (b) sheet

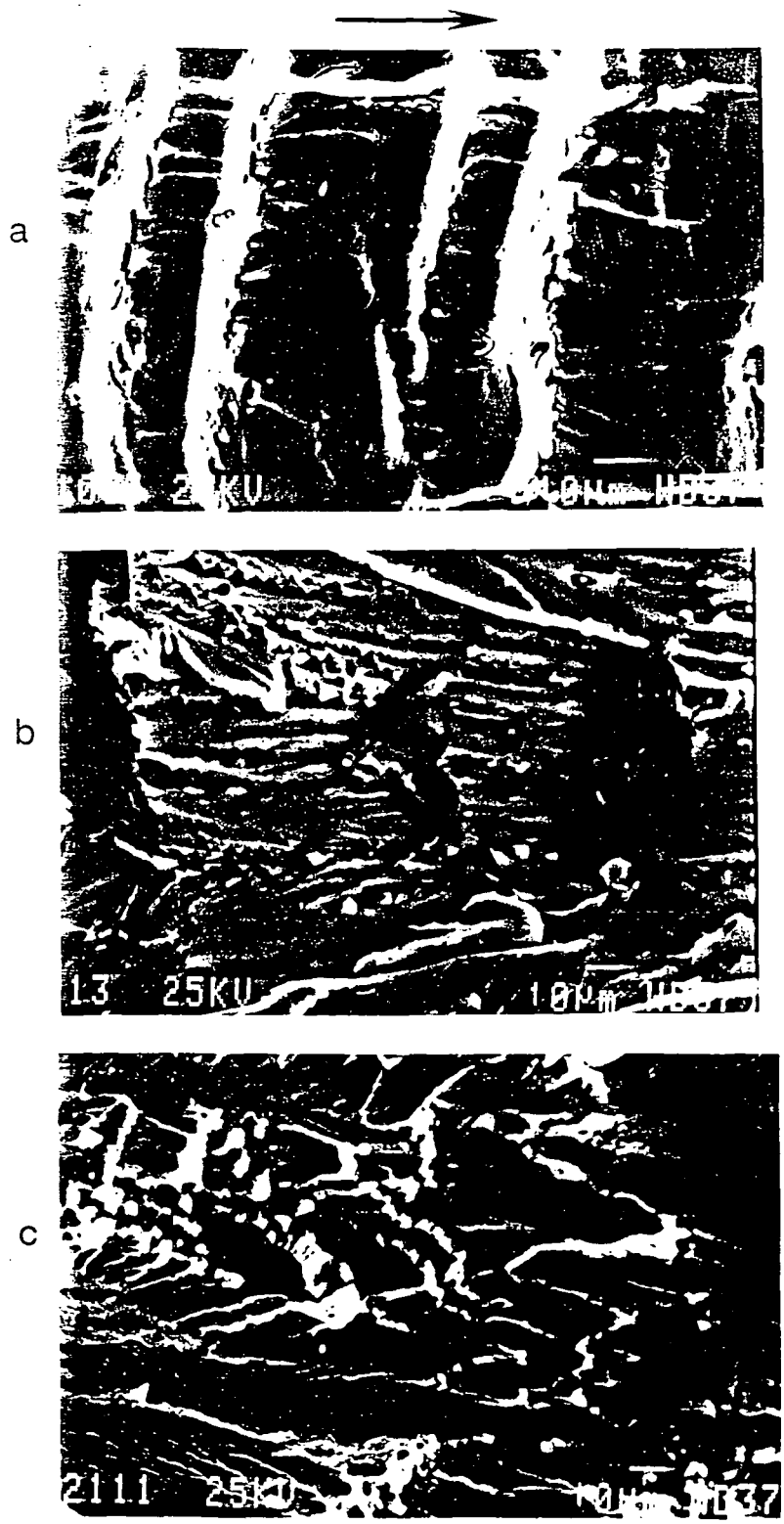

Figure 5 Unrecrystallized 2090 plate fractography, 1 wt% NaCl at -840 mV SCE (arrow indicates the crack direction); (a) ΔK=1.3 MPa$\sqrt{m}$, (b) ΔK=2.2 MPa$\sqrt{m}$, (c) ΔK=8.5 MPa$\sqrt{m}$

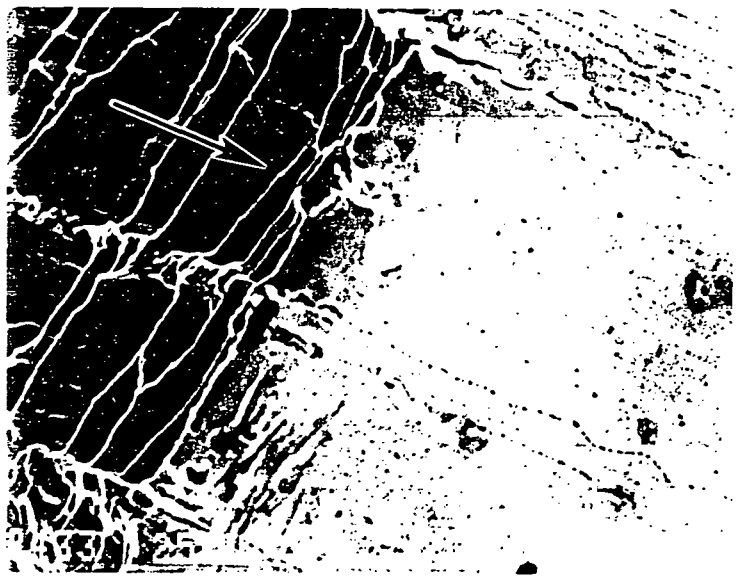

Figure 6 Etched T-plane section for 2090 unrecrystallized plate with a 30° tilt toward the fracture surface (ΔK=1.3 MPa$\sqrt{m}$, 1 wt % NaCl at -840 mV SCE, arrow indicates the crack direction)

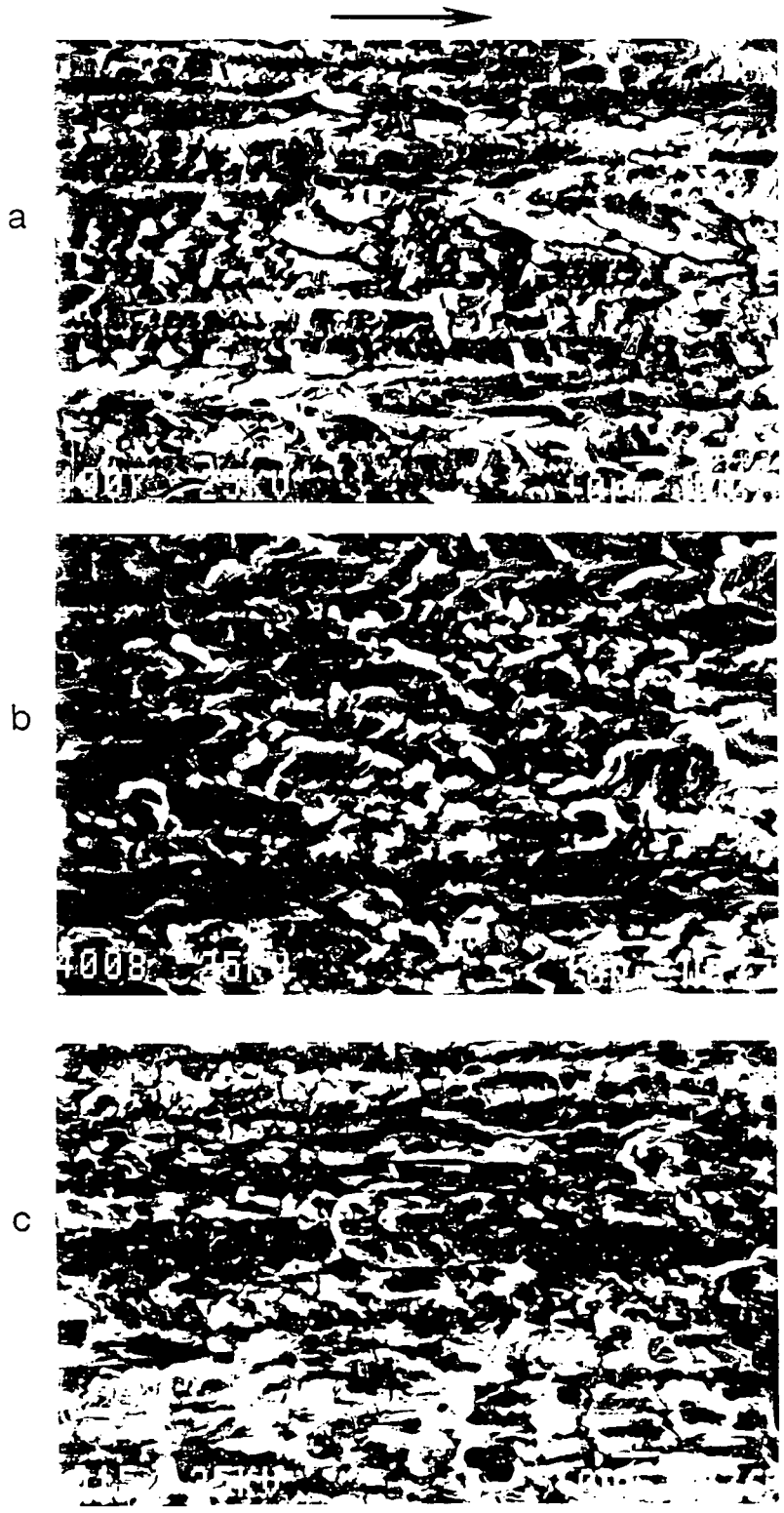

Figure 7 Unrecrystallized 2090 sheet fractography, 1 wt% NaCl at -840 mV SCE (arrow indicates the crack direction); (a) $\Delta K=1.3$ MPa$\sqrt{m}$, (b) $\Delta K=2.3$ MPa$\sqrt{m}$, (c) $\Delta K=8.6$ MPa$\sqrt{m}$

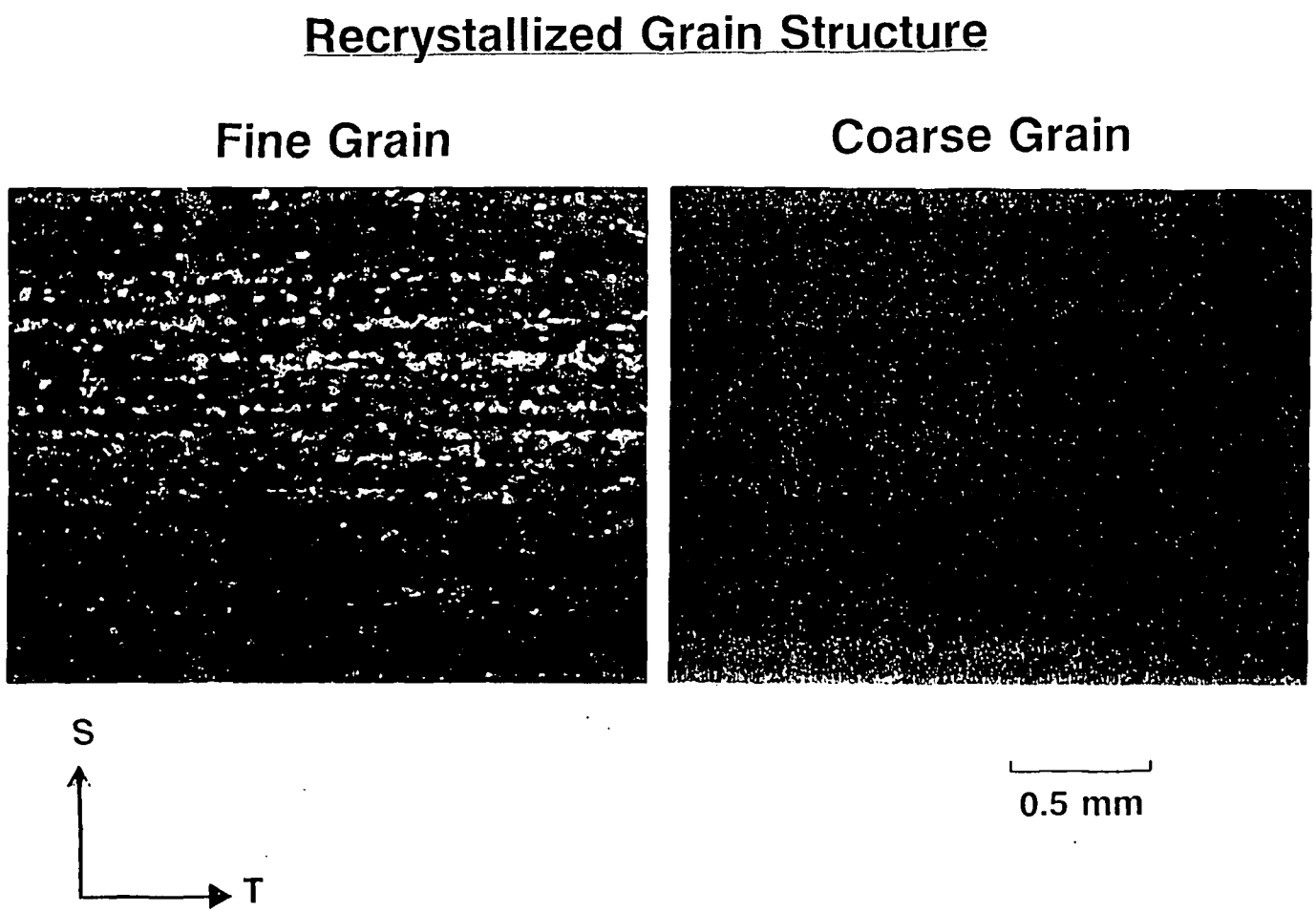

Figure 8 Fine and coarse grain recrystallized microstructures, T-plane section (Barker's etch and polarized light)

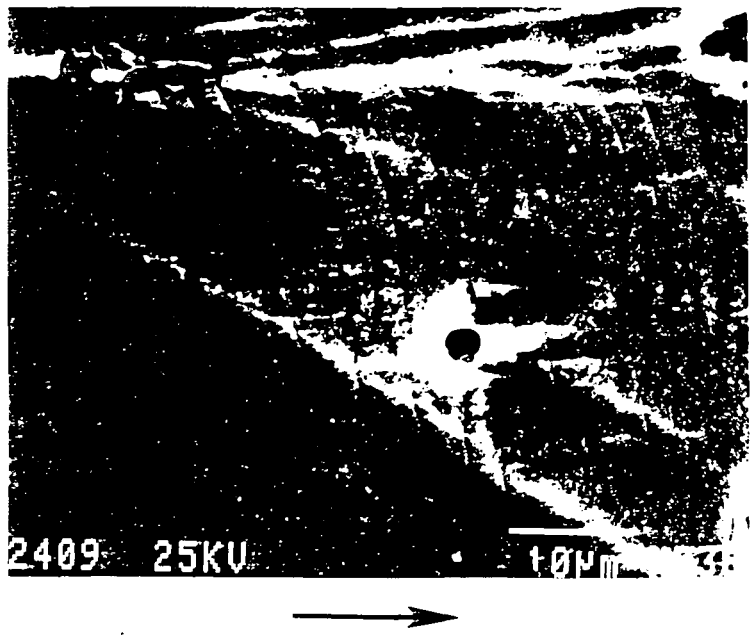

Figure 9 Fatigue crack striations in 2090 unrecrystallized plate, ΔK = 1.3 MPa$\sqrt{m}$, 1 wt % NaCl at -840 mV SCE (arrow indicates the crack direction)

Project 2 **Environmental Effects in Fatigue Life Prediction: Modeling Crack Propagation in Titanium Alloys**

Richard P. Gangloff and Sang-Shik Kim

Objective

The broad objective of the proposed research is to develop the data and mechanistic understanding necessary to quantitatively predict and incorporate environmental effects on FCP in titanium alloys into damage tolerant life prediction codes, particularly NASA FLAGRO.

Specific goals for the proposed three year project are to develop:

- oo FCP data that define the complex ΔK and time dependencies of crack growth rate;
- oo Empirical and linear superposition models for incorporation in NASA FLAGRO;
- oo Data on the importance of environment-sensitive small crack size and crack closure effects on the similitude principle embodied in NASA FLAGRO;
- oo Mechanistic understanding of the roles of surface film stability and microscopic crack tip damage processes in determining the environmental FCP response;
- oo A reaction rate/damage mechanism based model of da/dN-ΔK for incorporation in NASA FLAGRO.

Progress

This is a new program that will begin in the Summer of 1992.

During this reporting period, Professor Gangloff has continued to work with Dr. Robert S. Piascik of the Mechanics of Materials Branch to model environmental fatigue crack propagation in Al-Li-Cu alloys. Two papers are being prepared for publication; the Abstract and Conclusions for this work follow.

ENVIRONMENTAL FATIGUE CRACK PROPAGATION IN Al-Li-Cu: Part II--MICROSCOPIC FRACTURE PROCESSES PART III--MODELING OF CRACK TIP HYDROGEN DAMAGE

ABSTRACT

Based on a fractographic analysis of intrinsic environmental fatigue crack propagation (FCP) in Al-Li-Cu alloy 2090, a hydrogen-based model is developed to predict da/dN-ΔK kinetics. FCP rates are accelerated by hydrogen producing environments (pure water vapor, moist air and aqueous NaCl), as defined in Part I, with subgrain boundary cracking (SGC) for ΔK values where the crack tip plastic process zone envelops 5 μm subgrains in the unrecrystallized microstructure. SGC is related to strong hydrogen trapping at T_1 decorated subboundaries. At low ΔK, the process zone diameter is smaller than the subgrain size and FCP progresses along {100} planes due to either local decohesion or hydride cracking. For inert environments (vacuum, helium and oxygen), or at high ΔK where the hydrogen effect on da/dN is small, FCP is along {111} slip planes; the mode does not transition with increasing plastic zone size. The SGC and {100} crystallographic cracking modes, and the governing influence of the crack tip volume (ΔK), support hydrogen embrittlement rather than a surface film rupture and anodic dissolution mechanism. The process zone model equates da/dN to discontinuous crack advance over a distance equalling the extent of mobile dislocation transport of hydrogen above a critical plastic strain, and to the number of load cycles required to hydrogenate trap sites that fracture due to a local hydrogen concentration-tensile stress criterion. Multi-sloped log da/dN-log ΔK behavior is produced by process zone hydrogen-microstructure interactions; and is determined by the growth rates, ΔK dependencies, and proportions of each parallel cracking mode. Crack surface films hinder hydrogen uptake, reduce da/dN and alter the proportions of each FCP mode. Da/dN mildly increases with increasing loading frequency for 2090 in NaCl because the surface film is destabilized by increasing crack tip strain rate; hydrogenation of the process zone is enhanced.

CONCLUSIONS

1. Intrinsic rates of fatigue crack propagation (FCP) in peak aged Al-Li-Cu alloy 2090 are accelerated by aqueous NaCl and gaseous water-bearing environments due to hydrogen embrittlement.

2. ΔK uniquely governs the degree of the environmental effect on da/dN and the microscopic crack path for constant high K_{max}, establishing the central importance of

the crack tip cyclic process zone volume, consistent with hydrogen embrittlement but not surface film rupture and dissolution.

3. Low angle (unrecrystallized) grain boundaries with T_1 precipitates and {100} planes are preferred paths for environmental FCP alloy 2090. High angle grain boundaries do not affect L-S and L-T cracking.

4. The fatigue crack path depends on stress intensity range and environment. For hydrogen producing environments, the path transitions from along subgrain boundaries to {100} planes as ΔK decreases from moderate Paris regime to near threshold levels. For inert helium or vacuum environments at all ΔK, or when hydrogen environmental effects are minimal at high ΔK, FCP is along {111} slip planes due to precipitate induced slip localization. Slip plane cracking is dominant for pure oxygen, analogous to the inert environments; surface oxide has no effect on either da/dN or the microscopic FCP mode.

5. Complex, multi-sloped log da/dN-log ΔK behavior is solely due to the hydrogen environment; the change in intrinsic da/dN-ΔK slope results from the interaction of the embrittled crack tip process zone with microstructure. The ratio of cyclic plastic zone size to microstructural distance has no effect on the da/dN-ΔK relationship for inert environments.

6. Environmental FCP rates are described by a process zone model which equates da/dN to discontinuous crack advance over a distance, Δa, determined by the extent of mobile dislocation transport of hydrogen at crack tip plastic strains above a critical value; and to the number of load cycles, ΔN, required to sufficiently hydrogenate process zone trap sites that fracture due to a local hydrogen concentration-tensile normal stress criterion.

7. The process zone model explains the shape of the da/dN-ΔK relationship and crack path transitions. FCP in NaCl or moist gases at low ΔK is along {100} planes due to hydrogen-enhanced decohesion or hydride formation and because the embrittlement

process zone is smaller than the subgrain size; a single power-law da/dN versus ΔK relationship results. When ΔK increases to the level where the process zone just includes subgrains and dislocations reach such boundaries, environmental FCP transitions to the intersubgranular mode because of strong hydrogen trapping at subgrain boundary sites, resulting in a transition in the slope of da/dN-ΔK. A second transition occurs at higher ΔK when substantial slip plane cracking occurs due to mechanical damage. The shape of the growth rate law is determined by the absolute rates, ΔK dependencies and proportions of each parallel microscopic cracking mode; a wide variety of dependencies are possible including "plateau" behavior.

8. Crack growth rates decrease and the stress intensity required for the microscopic mode transition increases as the environmentally produced crack surface hydrogen concentration decreases. Crack surface films, produced by cathodic polarization in NaCl or by O_2 addition to water vapor, reduce hydrogen uptake and da/dN.

9. For 2090 and other 2000 series alloys in NaCl, da/dN increases with increased loading frequency because increased crack tip strain rate destabilizes otherwise protective surface films, and enhances hydrogen production and uptake in the process zone. Fast crack surface chemical reactions, short process zone diffusion distances and rapid dislocation transport of hydrogen preclude rate limited cracking, at least for frequencies less than about 150 Hz.

10. The process zone model does not quantitatively predict da/dN values because the local failure criterion for hydrogen cracking is not independently determined and the very near tip plastic strain distribution is not quantitatively defined. The mechanisms by which hydrogen promotes {100} and intersubgranular cracking are speculative.

Project 3 **Elevated Temperature Fracture of an Advanced Rapidly Solidified Powder Metallurgy Aluminum Alloy**

William C. Porr, Jr. and Richard P. Gangloff

Objective

The goal of this study is to characterize the fracture toughness of advanced powder metallurgy Al-Fe-V-Si alloy 8009 as a function of temperature, loading rate, environment and product form. The underlying mechanism for the temperature dependence of fracture toughness of 8009 will be understood from considerations of deformation mechanisms specific to the novel fine grained dispersion strengthened microstructure, greater than equilibrium substitutional solute content from rapid solidification, and the moist air environment.

Approach

The program approach and experimental procedures were detailed previously [1-8]. Fracture behavior was characterized quantitatively by J-Integral fracture mechanics techniques to determine both the plane strain fracture initiation toughness, K_{IC}, and crack growth toughness as measured by the tearing modulus, T_R.

Previous reports demonstrated a decrease in both initiation (K_{IC}) and growth (T_R) fracture toughnesses of AA 8009 with increasing temperature and decreasing loading rate, in both extruded bar and cross-rolled plate product forms [1-6,9]. For the extrusion, there is a significant difference in fracture properties with specimen orientation; the TL properties are 30% lower, however, the deleterious effect of increasing temperature is apparent. This anisotropy is a result of the orientation of prior ribbon particle boundaries heavily decorated with oxides from processing. The anisotropy in fracture behavior does not exist in the plate product, as additional deformation during processing more uniformly disperses the oxides.

Four possible micromechanisms for the deleterious effects of increasing temperature and decreasing loading rate on the fracture behavior of 8009 have been proposed [10]: (1) changes in extrinsic delamination toughening, (2) embrittlement from reactions with the moist air environment or retained dissolved hydrogen from processing, (3) dynamic strain aging,

or (4) a deformation and void nucleation mechanism unique to the ultrafine microstructure of elevated temperature powder metallurgy aluminum alloys. During the current reporting period, fracture experiments and matching fracture surface stereoimaging fractography were conducted to develop and examine these four mechanisms.

Research Progress and Results

Experimental results since the last reporting period include:

(1) Bridgman-type notched tensile bar experiments indicate that effective strain to fracture, as a function of the ratio of mean stress to effective stress at the center of the tensile bar, decreases with increasing temperature from 25 to 175°C. Figure 1 illustrates these results. Delamination occurred in specimens with smaller notch root radii (higher constraint) at both temperatures.

(2) Elastic stress intensity-Δa behavior was unaffected by testing in ultra-high vacuum as opposed to moist laboratory air at 175°C (Fig. 2) [7,8,10].

(3) Prolonged elevated temperature exposure, in air and vacuum, prior to testing caused no change in the resulting K-Δa behavior for 8009 at 25 and 175°C, as indicated in Fig. 2 [7,8,10]. Based on estimates of hydrogen diffusivity, temperatures and times were sufficient to ensure offgassing of mobile hydrogen from the material. Post heat treatment and testing analyses showed that hydrogen content was unchanged from the as-received material (4 ppm); such hydrogen was strongly trapped, probably at interfaces and associated with hydrated oxides on prior particle interfaces.

(4) Stereoimaging fractography of matching 8009 plate fracture surfaces indicated that the mode of fracture is microscopically ductile at all temperatures (Fig. 3). At 25°C, there is a dual distribution of equiaxed dimples, 1 μm and 5 μm in diameter. At 175°C, there is a single distribution of shallow dimples, 3 μm in diameter. The fracture appearance is the same for specimens tested in air and in vacuum [7,8,10].

(5) Preliminary microscopy of Bridgman tensile specimens, strained to various levels before fracture, at 25 and 175°C, only shows voids associated mainly with oxides at strains as high as 95% of the failure strain.

Four possible mechanisms for the temperature and deformation rate effects on the ductility and fracture behavior of 8009 have been proposed in the course of this study and by others:

(1) Temperature dependent changes in extrinsic delamination toughening [9,11].

(2) Oxidation or hydrogen embrittlement from moist laboratory air or retained hydrogen from processing [7-10,12].

(3) Dynamic strain aging associated with solid solution Fe [9,13,14].

(4) An elevated temperature deformation mechanism unique to ultrafine microstructure powder processed materials [7-10].

Work during the current reporting period has considered these mechanisms; experimental results to date are discussed with respect to each.

Delamination Toughening Details of this mechanism were discussed in previous reports [4-9]. Briefly, failure of prior particle boundaries perpendicular to primary fatigue and fracture toughness crack in LT oriented CT specimens, results in a loss of through-thickness specimen constraint and higher critical stress intensities for fracture initiation and propagation. Low magnification fractography indicates that delamination occurred in specimens of the extruded product loaded at 25°C, and after a small amount of stable crack growth in specimens tested at 316°C. This behavior correlates well to the T_R of the extruded material, which decreases with increasing temperature before increasing again at 316°, and is consistent with the K_{IC} results. (At 316°, the initial portion of stable cracking without delamination indicates that initiation occurred prior to any delamination.)

K_{IC} and T_R both decreased with increasing temperature from 25 to 175°C in the plate material, as in the extrusion, despite the fact that fractography on plate CT specimens indicated no change in delamination behavior with increasing temperature. No significant delamination occurred in the plate at 25°, however fracture toughness was high. Delamination did occur after a small amount of stable crack growth in specimens at 316°C, as with the extrusion, matching the rise in T_R at 316°. It is concluded that the elevated temperature decrease in fracture toughness is intrinsic to 8009; the delamination toughening mechanism only significantly affects crack growth resistance, T_R. The mechanism for the temperature dependence of delamination, proposed previously in the course of this study, depends on an intrinsic decrease in fracture toughness with increasing temperature in 8009 [9].

To confirm the intrinsic nature of decreased toughness and ductility with increasing temperature, Bridgman-type notched bar experiments were performed at 25 and 175°C. Independent of specimen constraint, or the occurrence of delamination, effective strain to

failure decreased from 25 to 175°C. This proves conclusively that decreased toughness and ductility with increasing temperature are intrinsic phenomena in AA 8009. Since K_{IC}, T_R, notched specimen reduction in area for a wide range of constraint, and uniaxial tensile specimen reduction in area all decrease with increasing temperature for 8009; it is concluded that "embrittlement" is not simply caused by local plastic instability typical of low work hardening materials.

Oxidation or Hydrogen Embrittlement Aluminum alloys were shown to embrittle in moist air environments at elevated temperatures [15]. To examine whether this was a factor in the elevated temperature cracking of 8009, a series of K-Δa (R-curve) experiments were conducted in ultrahigh dynamic vacuum (better than 30 μPa total pressure) at elevated temperatures. Results are shown in Fig. 2. R-curves for 8009 were identical at 175°C whether determined in moist laboratory air or in vacuum. Fractography showed no change in the ductile fracture mode or distribution of features with environment, further indicating the lack of a moist air environmental embrittlement. Thermodynamic considerations, however, predict that oxygen and water vapor pressures in the vacuum are sufficient to oxidize aluminum and produce atomic hydrogen. This may be inconsequential as the walls of the vacuum chamber were much colder (25°C) than the specimen and may effectively trap any oxygen and water vapor. Kinetic arguments of impeded gas molecule transport to crack tips due to crack wall interactions (Knudsen flow) can also discount possible effects of very low pressures of oxygen and water vapor on fracture toughness.

Embrittlement of 8009 from internal hydrogen, retained from powder processing in moist air and released during loading to fracture, represents a possible elevated temperature degradation mechanism. As received, both extruded and plate 8009 contain approximately 4 ppm total hydrogen content, assumed to be in the form of hydrides and water adsorbed on or chemically bound to oxide particles. It can be postulated that at elevated temperatures, hydrides decompose and water vapor releases from the oxide and reacts with the matrix aluminum to form embrittling atomic hydrogen. This reaction is highly favored by thermodynamics and previous researchers [16] reported that water vapor readily desorbes and hydrides decompose in this class of materials at the temperatures considered in this study. To address the possible role of hydrogen, R-curve experiments were conducted in air and vacuum on specimens that were heat treated to either improve or worsen this effect.

Two extrusion specimens were baked at 330°C in dynamic vacuum (<30 μPa) for

75 hours, sufficient to evolve all dissolved mobile hydrogen assuming $D_H > 5x10^{-6}$ cm^2/s [17]. These were then fractured in air and vacuum at 175°C; the resulting R-curves were equivalent to those determined in air with no prior heat treatment. Two plate specimens, one in air and one in dynamic vacuum, were held at 175°C under a 130 to 330 N load for 75 hours prior to testing at 175°C with no subsequent effect on R-curve behavior. A plate specimen was heated in air at 175°C for 100 hours under no load, and an extrusion specimen was held at 175°C for over 400 hours loaded to 1.8 kN (with some subcritical crack growth, K_{app} =12 to 15 MPa$\sqrt{m}$; see [18]), prior to testing at 25°C. The R-curves for these two specimens were equivalent to data from specimens that received no prior heat treatment prior to fracture at 25°C. All of these results appear in Fig. 2. Post-experiment hydrogen determinations, utilizing a vacuum fusion technique, indicated no change in total specimen hydrogen content resulting from the various heat treatments or fracture test conditions.

It can be interpreted from these results that process-originated hydrogen is strongly trapped in AA 8009 at temperatures as high as 330°C. Since this hydrogen would be similarly trapped at 25 and 175°C, there is no obvious mechanism by which the retained hydrogen would embrittle the 8009. This point is amplified by considering the reversible nature of embrittlement; subcritical crack growth occurred in one specimen at 175°C at load levels less than K_{IC}; however, when cooled to 25°C, the specimen showed no sign of embrittlement in subsequent monotonically increasing load testing. Additionally, time at temperature and prior thermal exposure appear to be insignificant to the tensile [19] and fracture behavior, in contrast to the deleterious effect of decreasing loading rate established previously. This indicates that the embrittlement of 8009 is loading rate, but not exposure time, dependent. This is not typical of an environmental embrittlement phenomenon. A complex hydrogen embrittlement mechanism that requires temperature dependent trapping at different sites in the microstructure, when under load, is possible but not likely.

Fractography of failed CT specimens tested at 175°C in either air or vacuum shows a void distribution similar to the oxide distribution in the starting material, implying a significant role of the oxides. A speculative mechanism can be proposed for decreased toughness in 8009, based upon low strain void nucleation at elevated temperatures and low loading rates, and in which desorbed water vapor is a factor. Water desorption at elevated temperatures may weaken or pressurize the oxide-matrix interface sufficiently to allow void nucleation at lower strain. Higher temperatures and lower loading rates could cause more

water release and greater dislocation activity, thereby lowering the macroscopic strain to nucleate voids. The desorption process could, in principle, be reversible if the water does not chemically react with the metal. This mechanism should, however, cause irreversible creep damage during long term sustained loading, counter to the observed behavior in Figure 2. Microscopy of sectioned Bridgman specimens from interrupted tensile experiments indicates that the growth and link-up of voids in 8009 is a rapid process; fracture is void nucleation controlled. This is consistent with the described mechanism. Microscopy is planned to examine the correlation of oxide and void distributions. Additional fracture experiments on lower hydrogen (< 1 ppm) 8009 will also address this mechanism.

Dynamic Strain Aging Dynamic strain aging (DSA) from dislocation interactions with metastable dissolved solute Fe has been proposed by several researchers [13,14] as the phenomena responsible for the elevated temperature degradation of fracture toughness and ductility in 8009. Researchers at Allied-Signal base this speculation on a measured solid solution Fe concentration of 0.5 atom % (100 times the equilibrium concentration) and correlation of the tensile elongation to failure and strain rate sensitivity minima with temperature for 8009 and a similarly produced Al-10Fe-5Si alloy. (The strain rate sensitivity, m, is the exponent in the powerlaw relationship between stress and strain rate.)

Bouchard and co-workers use semiquantitative arguments that consider solute-dislocation theoretical interaction energy, the temperature for the minimum value of m, and a "deduced" relaxation time to estimate a diffusion coefficient associated with solute atoms interacting with dislocations [14]. This diffusion coefficient is compared with a "generally accepted" value of 10^{-14} cm^2/s for serrated flow in materials subject to DSA. By this argument, Fe is identified as the DSA solute with a determined solute interaction diffusivity of 1.7×10^{-14} cm^2/s at a strain rate of 10^{-5} s^{-1} and temperature of 75°C. Qualitative arguments are presented that eliminate all but Fe as possible DSA solute based on this estimated diffusion coefficient and the relative interaction energies of the various solute species. It is interesting to note that the minimum values of tensile fracture strain and m do not occur at the same temperature in this study, inconsistent with the original argument that DSA due to solid solution Fe is the sole embrittlement mechanism in 8009.

To resolve the issue of DSA at 175°C resulting from a low diffusivity solute, both studies proposed explanations for DSA involving forest dislocation networks. This mechanism theorizes that solute diffuses along networked dislocations (pipeline diffusion) and

forms atmospheres along edges of dislocation entanglements. The strain fields of these atmospheres of solute and the dislocation network then inhibit the motion of passing mobile dislocations. This constraint on dislocation motion causes an increase in flow stress and work hardening. A decrease in m results in local plastic instability and decreased macroscopic ductility when measured in terms of elongation. The supposition of dislocation enhanced diffusion addresses the low temperature diffusion of the relatively immobile solute Fe necessary for a classical DSA mechanism.

This mechanism of DSA for 8009 is not be substantiated by microscopic observations; TEM of strained tensile specimens yields no evidence of forest dislocation networks to serve as solute diffusion paths. The lack of significant work hardening exhibited by 8009 at any temperature is consistent with this observation [20]. Additionally, decreased tensile elongation to failure in the temperature regime of dynamic strain aging is ascribed to rapid localized necking from plastic instability and the low strain rate sensitivity [21]. This decrease in elongation should not be accompanied with a decrease in tensile specimen neck reduction in area, contrary to the results of this study where reduction in area decreases in coincidence with elongation to failure, with increasing temperature. This result, and the various notched specimen and fracture mechanics parameters, are more indicative of a true material embrittlement.

Internal friction studies of aluminum with trace amounts of Fe indicate that solute Fe-dislocation interactions are maximized at higher temperatures (> 300-400°C) [22,23]. Internal friction peaks appear with the addition of Fe to pure aluminum, and increase in magnitude and are shifted to lower temperatures with increasing Fe concentration. The activation energy corresponding to the Fe peak (170-200 kJ/mol) is similar to the activation energy for diffusion of Fe in Al (190 kJ/mol). Assuming a conservatively high strain rate of 10^{-2} s^{-1} for the internal friction experiments, strain rate effects can not account for this temperature difference.

These same internal friction studies can be used to justify a lower temperature DSA-type mechanism. A low temperature internal friction peak typically exists for polycrystalline "pure" materials at 0.3 to 0.6 T_m, and was evident in these studies of aluminum at approximately 300°C. This peak was associated with grain boundary sliding, but could also be due to dislocation interactions with impurity solute along grain and subgrain boundaries. Although the temperature at which the low temperature internal friction peak is reported is

too high for direct comparison to the ductility and strain rate sensitivity minima in 8009, results indicate that it may be expected to occur at lower temperatures for very small grain sizes given a high boundary solute concentration.

Consider that dislocation emission and trapping occur only at subgrain and grain boundaries in 8009. This is consistent with the lack of residual dislocation structures observed in the material after significant plastic strain. With increasing temperature, the thickness of the solute rich boundary region increases by solute diffusion into the grain. The energy required for a dislocation to be emitted from the boundary is increased, inhibiting this dislocation source and raising the local flow stress of the material. As some sources become active, heterogeneous dislocation activity (localized plasticity) will occur, resulting in rapid void nucleation at boundaries or boundary particles. With further temperature increases, the solute strain field is reduced, the resistance to dislocation emission decreases, dislocation activity is more homogeneous, and void nucleation rate decreases with a resulting return of ductility and toughness. Voiding along high angle boundaries is consistent with fractography which indicated shallow dimples spaced on the order of the grain size. The previously mentioned correlation of voids with the oxide distribution may be coincidental: oxides are located along the high angle boundaries. Oxides may also represent sites of localized damage.

Dynamic strain aging from substitutional solute iron in 8009 has yet to be proven as a phenomenon: Mechanisms based on forest dislocation networks are not substantiated by microscopic observations; semi-quantitative arguments presented in the literature are inconclusive. The speculative DSA-type mechanism of dislocation-solute interaction in grain and subgrain boundary regions is an alternative, however, until the nature of dislocation-Fe solute interaction in aluminum is understood, DSA mechanisms must be considered with wariness. Internal friction studies with the fine grained 8009 would allow study of possible solute-dislocation interactions separate from any deformation mechanism, as strains are elastic and plastic damage is not occurring.

Elevated Temperature Deformation Mechanism Because of the ultrafine microstructure and the high volume fraction of strengthening dispersoids in rapidly solidified 8009, a unique elevated temperature deformation mechanism, not exhibited in standard wrought alloys, must be considered.

Grain rotation, the phenomenon associated with the development of texture, occurs

in aluminum alloys during thermo-mechanical processing. Voiding does not occur during elevated temperature deformation processing since strain compatibility is usually maintained across grain boundaries by slip in the adjacent grain. With working temperatures typically higher than 0.7 T_{melt}, diffusional processes and grain boundary sliding may also contribute to maintain boundary integrity. For AA 8009 at elevated temperatures, as crystal rotation occurs in response to deformation, voids may nucleate at grain junctions where strain compatibility is difficult to maintain.

To maintain grain to grain compatibility, dislocation activity on five independent slip systems is necessary to enable an arbitrary shape change in a grain in response to external stresses from neighboring grains. If, however, compatibility is not maintained across a grain boundary, voids form from high shear stresses in the boundary regions. Speculatively, the high volume fraction of boundary particles in 8009 (silicide dispersoids on low and high angle boundaries and oxides on high angle boundaries), and the clustering of particles on boundaries, may disrupt grain boundary compatibility. At lower temperatures and higher strain rates, solid solution strengthening from dispersed solute Fe causes homogeneous dislocation activity in grains, analogous to dispersoids homogenizing slip in larger grained materials, and void nucleation occurs at higher strains at multiple particle sites.

At intermediate elevated temperatures, solid solution strengthening is decreased, dislocation activity is increased (thermal enhancement of emission) and localized deformation occurs in response to strain incompatibility and high shear stresses at particle clusters. Voids nucleate along boundaries at lower strains, with the macroscopic result of reduced ductility and fracture toughness. Slower loading rates have a similar effect as increased temperature with respect to dislocation emission activity and solute strengthening. This mechanism can be applied generally to any elevated temperature PM aluminum alloy (MA Al-Ti, Al-Fe-Ce) in which some solid solution strengthening and a high volume fraction of heterogeneously distributed boundary particles are present. The elevated flow stress at intermediate temperatures may result from back stresses that develop from dislocation pileups at particle clusters prior to void nucleation.

At higher temperatures, creep mechanisms may begin to play a roll in the deformation and fracture behavior of the material. Diffusional creep could maintain grain to grain compatibility with the presence of particle clusters on boundaries or diffusional void healing may occur, such that void nucleation occurs at higher strains.

There are precedents for an elevated temperature ductility minimum resulting from temperature enhanced grain boundary void nucleation. Monel exhibits this behavior in the temperature range of 525 to 725°C [24]. Additional TEM and SEM microscopy on sectioned tensile bars, strained to near failure, is currently underway to look for evidence to support or invalidate this mechanism. It is not obvious, however, that accumulated damage resulting from this mechanism would be microscopically different from accumulated damage resulting from one of the DSA mechanisms. Hot straining stage TEM observations of dislocation activity in 8009, a capability that does not exist at UVa, may be the only way to prove conclusively the deformation mechanism proposed here.

Conclusions

1. The intrinsic nature of the elevated temperature "embrittlement" (or a degradation of fracture toughness and ductility) for alloy 8009 has been confirmed with notched tensile bar experiments. For a fixed level of specimen constraint, effective true strain to failure decreases with increasing temperature from 25 to 175°C.
2. K-Δa R-curve experiments in air and ultrahigh dynamic vacuum at 175°C indicate no embrittlement of 8009 from the moist air environment. A series of heat treatments in air and dynamic vacuum, followed by R-curve fracture testing, indicate that embrittlement from retained internal hydrogen from processing is unlikely.
3. Fractographic studies of failed CT fracture specimens of plate 8009 indicate that fracture is microscopically ductile at 25 and 175°C, however, there is a change in the nature of the voids with increasing temperature, but not environment. At 25°C, there is a dual size distribution (1 and 5 μm) of equiaxed voids, whereas at 175°C there is a uniform size distribution (3 μm) of shallow voids. The latter coincide with the distribution of oxide in the material.
4. Elevated temperature embrittlement of 8009 is most likely due to dynamic strain aging or an elevated temperature intergranular deformation and fracture mechanism. Hydrogen embrittlement from moist air reactions or process-retained hydrogen appears unlikely. Inconsistencies in reported results reduce the credibility of the dynamic strain aging mechanism.

Plans for Future Work

This project on the elevated temperature damage tolerance of aluminum alloy 8009 will be concluded during the coming reporting period. TEM and SEM of specimens will be concluded, with results to date analyzed and presented in a dissertation, fulfilling the requirements for Mr. Porr's Ph.D. degree.

References

1. R. P. Gangloff, G. E. Stoner, and R. E. Swanson, "Environment Assisted Degradation Mechanisms in Advanced Light Metals", University of Virginia, Report No. UVA/528266/MS89/103, January, 1989.

2. R. P. Gangloff, "UVA Light Aerospace Alloy and Structures Technology Program (Progress Report)", University of Virginia, Report No. UVA/528266/MS90/104, August, 1989.

3. R. P. Gangloff, "UVA Light Aerospace Alloy and Structures Technology Program (Progress Report)", University of Virginia, Report No. UVA/528266/MS90/105, December, 1989.

4. W. C. Porr, Jr., presentation at "UVA Light Aerospace Alloy and Structures Technology Program Grant Review Meeting", NASA/Langley Research Center, Hampton, VA, June, 1990.

5. R. P. Gangloff, "UVA Light Aerospace Alloy and Structures Technology Program (Renewal Proposal)", University of Virginia, Proposal No. MS-NASA/LaRC-4881-91, October, 1990.

6. R. P. Gangloff, "UVA Light Aerospace Alloy and Structures Technology Program (Progress Report)", University of Virginia, Report No. UVA/528266/MS91/107, January, 1991.

7. W. C. Porr, Jr., "Elevated Temperature Fracture of RS/PM Aluminum Alloy 8009", presented at the UVa-NASA LA^{2}ST Grant Review Meeting, Hampton, VA., July 10, 1991.

8. R. P. Gangloff, "UVA Light Aerospace Alloy and Structures Technology Program (Renewal Proposal)", University of Virginia, Proposal No. MS-NASA/LaRC-5219-92, October, 1991.

9. W. C. Porr, Jr., Y. Leng, and R. P. Gangloff, "Elevated Temperature Fracture Toughness of P/M Al-Fe-V-Si", Low Density, High Temperature P/M Alloys, W. E. Frazier, M. J. Koczak, and P. W. Lee, Eds., TMS-AIME, Warrendale, PA, pp. 129-155, 1991.

10. W. C. Porr, Jr, A. P. Reynolds, Y. Leng, and R. P. Gangloff, "Elevated Temperature Cracking of RSP Aluminum Alloy 8009: Characterization of the Environmental Influence", Scripta Metallurgica et Materialia, 25, pp. 2627-2632, 1991.

11. K.S. Chan, "Evidence of a Thin Sheet Toughening Mechanism in Al-Fe-X Alloys", Metallurgical Transactions A, 20A, pp. 155-164, 1989.

12. Y.-W. Kim and F.H. Froes, "Effect of Hydrogen in Rapidly Solidified Powder Aluminum Alloys", Aluminum, 64, pp. 1035-1038, 1989.

13. D. J. Skinner, M. S. Zedalis, and P. Gilman, "Effect of Strain Rate on Tensile Ductility for a Series of Dispersion-strengthened Aluminum-based Alloys", Materials Science and Engineering, A119, pp. 81-86, 1989.

14. E. Bouchard, L. Kubin, and H. Octor, "Ductility and Dynamic Strain Aging in Rapidly Solidified Aluminum Alloys", Metallurgical Transactions A, 22A, pp. 1021-1028, 1991.

15. C.D.S. Tuck, "The Embrittlement of Al-Zn-Mg and Al-Mg Alloys by Water Vapor", Metallurgical Transactions A, 16A, pp. 1503-1514, 1985.

16. Y.-W. Kim, W. M. Griffith and F. H. Froes, "Surface Oxides in P/M Aluminum Alloys", Journal of Metals, ASM, Metals Park, OH, pp. 27-33, August, 1985.

17. R. E. Ricker and D. J. Duquette, Office of Naval Research report No. N00014-67-A-0117-0012, Washington, D. C., 1986.

18. Y. Leng, W. C. Porr, Jr., and R. P. Gangloff, "Time Dependent Crack Growth at Elevated Temperatures in Al-Fe-V-Si Alloy", Scripta Metallurgica et Materialia, 25, pp. 895-900, 1991.

19. J.C. Lee, S. Lee, D.Y. Lee, and N.J. Kim, "On the Embrittlement of a Rapidly Solidified Al-Fe-V-Si Alloy after High Temperature Exposure", Metallurgical Transactions A, 22A, pp. 853-858, 1991.

20. Y. Leng, W. C. Porr, Jr., and R. P. Gangloff, "Tensile Deformation of 2618 and Al-Fe-V-Si Aluminum Alloys at Elevated Temperature", Scripta Metallurgica et Materialia, 24, pp. 2163-2168, 1990.

21. A. T. Santhanam and R. E. Reed-Hill, "The Influence of Strain Rate Dependent Work Hardening on the Necking Strain in α-Titanium at Elevated Temperatures", Metallurgical Transactions, 2, pp.2619-2622, 1971.

22. B. Ya. Pines and A. A. Karmazin, "Temperature Dependence of the Internal Friction of Aluminum Containing Iron Impurity", Fiz. Metal. Metalloved., 29, No. 1, pp. 197-199, 1970.

23. E. A. Attia, "Internal Friction in Aluminum Containing 0.25 wt.% Iron", British Journal of Applied Physics, 18, pp. 1343-1344, 1967.

24. F. N. Rhines and P. J. Wray, Transactions of the American Society for Metals, 54, pp.117, 1961.

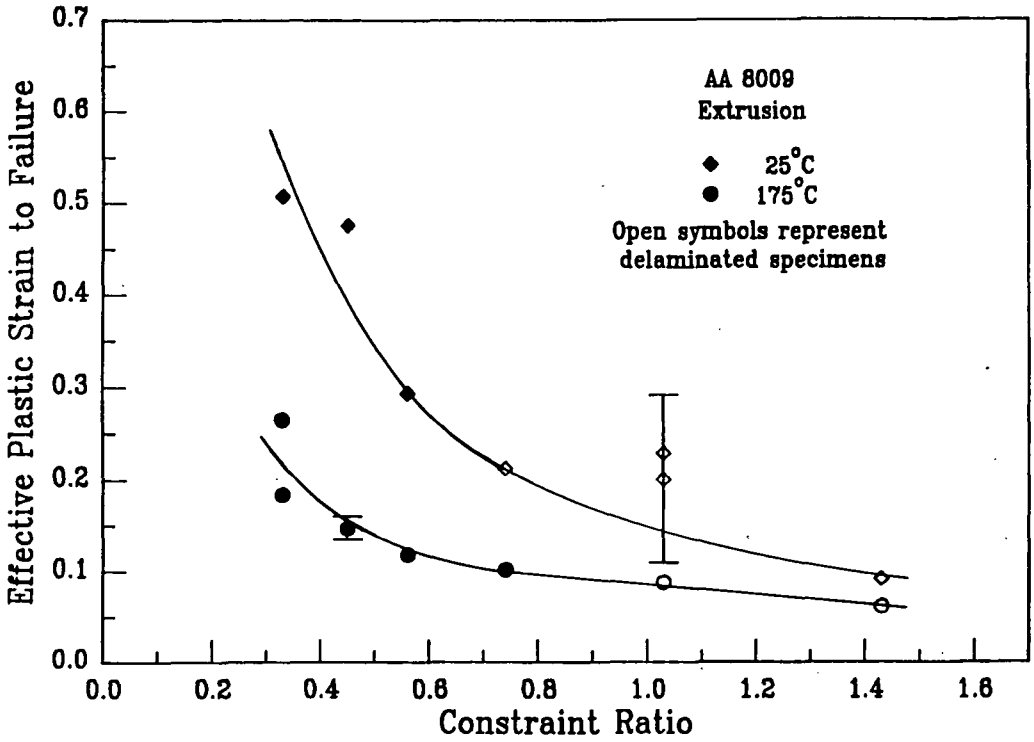

Figure 1. Effective plastic strain to failure, $\epsilon_f = 2 \ln(d_o/d)$, as a function of constraint parameter, $\sigma_m/\bar{\sigma}$, and temperature for alloy 8009. d_o is original notch root diameter; d is instantaneous diameter; σ_m is mean stress; and $\bar{\sigma}$ is effective stress.

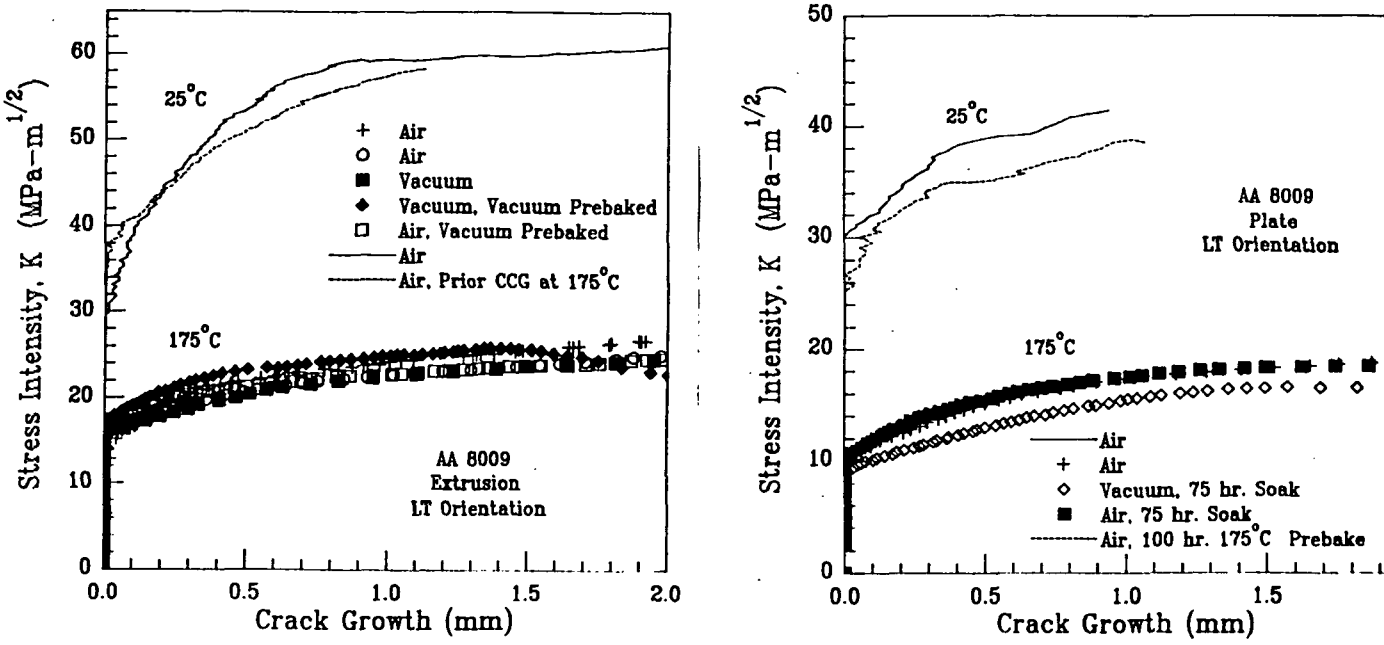

Figure 2. R-curves for aluminum alloy 8009 as a function of temperature, test environment, and prior heat treatment for (a) extrusion and (b) plate product forms. Constant actuator displacement rate = 2.54×10^{-3} mm/sec; LT orientation.

BACK

Project 3 **Elevated Temperature Crack Growth in Advanced Aluminum Alloys**

Yang Leng and Richard P. Gangloff

Objective

The objective of this study is to characterize time-dependent crack growth in advanced aluminum alloys at elevated temperatures with the fracture mechanics approach and to examine cracking mechanisms with a metallurgical approach.

Results During the Reporting Period

The following conclusions were established based on research conducted in 1991.

1. Conventional aluminum alloy 2618 and ultra-fine grain size P/M alloy 8009 are susceptible to elevated temperature, time-dependent (subcritical) crack growth under static load at stress intensity levels below K_{IC}. Fracture toughness and fatigue crack growth will be time dependent.

2. Time-dependent crack growth rates in 8009 do not correlate with the steady state creep crack growth parameter, C^*, nor with the transient CCG parameter, C_t. 8009 is not creep ductile.

3. 8009 is a creep brittle material; growth rates are described by K and more properly by J. The effect of limited ligament creep on J is unknown.

4. Similar creep crack growth kinetics are observed for 8009 in moist air and ultra-high vacuum at 175°C. Dissolved hydrogen or oxygen from crack surface reactions with the external environment do not contribute to the cracking mechanism.

5. The mechanism for CCG in 8009 may involve supersaturated solute embrittlement: for a given applied J, crack growth rate is high at 175°C and decreases with increasing temperature to 316°C.

6. Localized creep deformation may contribute to CCG at higher temperatures: the fracture mode changes from dimpled rupture at 175°C to mixed matrix superplastic rupture and matrix-dispersoid debonding at 316°C.

7. Creep deformation induced damage development is responsible for the observed crack growth in 2618 and 8009. A model based on cavity growth in an elastic stress/strain field semiquantitatively explains the measured correlation between crack growth rate and applied J.

8. None of the existing micromechanical mechanisms can explain the observed apparent threshold for creep crack growth.

Future Research

Dr. Leng has left UVa to assume a position on the faculty in the Department of Mechanical Engineering at the Hong Kong University of Science and Technology. A paper is being prepared to report the results of his research on elevated temperature creep crack growth. A new project (#4, below) will begin in the Summer of 1992, based on the results for 8009.

Project 4 **Elevated Temperature Damage Tolerance of Advanced Powder Metallurgy Aluminum Alloys**

Sang-Shik Kim and Richard P. Gangloff

Objective

The goal of this research is to characterize and model time-dependent and time-cycle-dependent fatigue crack propagation in advanced powder metallurgy aluminum alloys at elevated temperatures. Underlying mechanisms for temperature dependent cracking will be understood from considerations of deformation mechanisms and the influences of microstructure, alloy chemistry and environment.

Progress

This is a new program that will begin in the Summer of 1992.

Project 5 **Cryogenic Temperature Effects on the Deformation and Fracture of Al-Li-Cu-In Alloys**

John A. Wagner and R.P. Gangloff

Objective

The objective of this PhD research is to characterize and optimize the crack initiation and growth fracture resistance of Al-Cu-Li and Al-Cu-Li-In alloys for cryogenic tank applications. The program aims to understand microscopic fracture mechanisms; as influenced by ambient to cryogenic temperature, stress state and microstructure.

Approach

The approach to this goal was outlined in the proposal for the 1992 LA^{2}ST Program.[1] In summary our approach focuses on several areas including: (1) produce and characterize Al-Li-Cu-Zr alloys with and without indium additions, (2) implement an experimental fracture mechanics method to measure initiation and crack propagation resistance for both plane stress and plane strain conditions at ambient and cryogenic temperatures, (3) characterize the effect of temperature, stress state and microstructure on fracture toughness, (4) analyze fracture surfaces, and (5) develop and apply methods to investigate the deformation and fracture processes that are relevant to crack initiation and growth toughnesses.

The progress recorded over the past year is established in the last grant progress report,[2] and by a publication that is being submitted to Scripta Metallurgica et Materialia. The body of this paper is presented here.

---

[1] R.P. Gangloff, "NASA-UVa Light Aerospace Alloy and Structures Technology Program", University of Virginia, Proposal No. MS NASA/LaRC-5219-92, October, 1991.

[2] R.P. Gangloff, "NASA-UVa Light Aerospace Alloy and Structures Technology Program", UVa Report No. UVA/528266/MS91/108, July, 1991.

Introduction

Al-Li alloys are candidate materials for the fabrication of cryogenic propellant tanks for future launch vehicles because they exhibit high strength, low density and increased elastic modulus compared to the current cryogenic tank material, aluminum alloy 2219-T87. In addition significant overall launch system cost and weight savings can be realized through the combined utilization of Al-Li alloys and innovative tank fabrication methods such as superplastic forming (SPF) [1]. One alloy currently being investigated for this application is of the 2090-type composition with a minor alloy addition of indium. Indium additions have been shown to increase the strength of 2090-type alloys in the T6 condition, based on material produced from 14 kg permanent mold ingots; the mechanism appears to be an increase in the number density and homogeneity of the T_1 strengthening precipitate [2,3]. Accordingly, 2090 + In is particularly attractive for SPF, where post-SPF components cannot be stretched to increase strength to the T8 temper levels.

The initial part of this investigation focused on the age hardening characteristics and mechanical properties of 2090 + In-T6 sheet, thermomechanically processed for SPF application from 160 kg direct chill (DC) cast ingots. Results were published previously [4] and a summary of the salient findings is given below:

- A 10 to 15% increase in the hardness of 2090 with a minor alloy addition of In in the T6 condition was demonstrated for 14 kg permanent mold and 160 kg DC cast ingots. For the 160 kg ingot material, however, σ_{ys} did not increase consistent with the results of other investigations on 2090 + In-T6 produced from 160 DC ingots [5-7].
- In the T6 condition, 2090 + In tested at -185°C exhibited increased yield strength, ultimate tensile strength, elongation to failure and modulus compared to tensile deformation at 25°C. Notably, 2090 + In-T6 exhibited a decrease in toughness at -185°C, as indicated by a decrease in the tear strength to yield strength ratio from Kahn Tear toughness testing [8].

Because the 2090+In sheet was thermomechanically processed for enhanced SPF response, the microstructure of the alloy after solution heat treatment and T6 aging appeared to be partially recrystallized. This complicated the comparison of the fracture behavior of 2090 + In-T6 to commercial unrecrystallized 2090.

Fracture of commercial 2090-T81 plate usually occurs by transgranular shear (TGS)

fracture with a significant amount of delamination along high angle grain boundaries for specimens in the LT and TL orientations. Shear fracture is attributed to highly localized planar slip promoted by ordered and coherent δ' precipitates [16]. The increase in toughness with decreasing temperature is attributed to the contributions of increasing work hardening, due to increased slip homogenization [5,10], and to an increase in the amount of delamination and plane stress toughening [9]. In contrast fracture of 2090 + In-T6 has not been adequately addressed. Most ambient and cryogenic fracture toughness experiments have been conducted using the Kahn Tear method; there are no quantitative data on crack initiation and growth fracture toughnesses. Furthermore, understanding of microscopic fracture processes in the In bearing alloys is hindered by limited characterizations of microstructure, crystallographic texture and fracture surface morphologies.

The objective of the current study is to characterize, understand and optimize the crack initiation and growth fracture resistance of Al-Li-Cu and Al-Li-Cu-In alloys for cryogenic tank applications. Conventionally processed plate product forms were employed in fracture toughness testing to eliminate the variation in microstructure associated with SPF processed material. The fracture resistance of these materials was characterized using J-integral fracture toughness experiments to establish crack initiation and growth behavior at 25 and -185°C. Results show that commercially available 2090-T81 has superior toughness compared to 2090 + In-T6 at both test temperatures; the low toughness of 2090 + In-T6 is associated with intersubgranular (ISG) fracture attributed to extraordinary subboundary precipitates.

Experimental Procedure

The Al-Li alloys used in this investigation were 19.1 mm thick Vintage III 2090-T81 (Al-2.30Li-2.85Cu-0.10Zr-0.07Fe wt.%) aged at 163°C for 24 hours, commercially produced by Alcoa, and experimental 12.7 mm thick 2090 + In (Al-2.17Li-2.65Cu-0.13Zr-0.06Fe wt.%) produced by Reynolds Metals from 160 kg DC cast ingots. The T6 condition of 2090 + In was obtained by aging the material at 160°C for 75 hours which corresponds to the near peak strength condition [2,4]. Elastic-plastic fracture toughness testing was conducted using the unloading compliance technique, conforming to ASTM standard E 813. Compact tension specimens, 12.0 mm thick and 50.8 mm wide with 1.2 mm deep sidegrooves, were machined from the plate midplane thickness in the LT orientation. A

minimum of two specimens were tested for each condition from which crack initiation toughness (J_{Ic}), crack growth resistance toughness (J-Δa) and tearing modulus (T_R) were determined. Specimens were tested in a servohydraulic test frame. Fatigue precracking was conducted at 25°C with a stress ratio of 0.1. J-integral fracture toughness tests were conducted at 25 and -185°C at a constant actuator displacement rate of 4.2×10^{-3} mm/s. At the conclusion of each test, specimens were fatigued at a high R value to mark the final crack length.

Results and Discussion

Microstructure Metallographic observations in Fig. 1 and full {100} and {111} pole figure texture analyses of 2090-T81 and 2090 + In-T6 revealed that both microstructures were primarily unrecrystallized, as suggested by a strong brass rolling texture at a plate thickness of T/2 (Fig. 2). Also in Fig. 2 is a photomicrograph of 2090 + In-T6 showing copious subgrain boundary precipitates. This extreme precipitation on subgrain boundaries gives the false impression that the In alloy is substantially recrystallized, however, the pole figure clearly shows deformation texture components and the absence of cube texture analogous to 2090.

Extensive subgrain boundary precipitation in 2090 + In-T6 is unique to this alloy chemistry. Such precipitates were not observed in the solution treated condition, but were apparent after only 3 hours of aging at 160°C and increased in amount with increasing aging time. Optically visible large subgrain boundary precipitates are not observed for commercial 2090 after prolonged aging at 160°C. TEM analysis revealed that the subboundary precipitates in 2090 + In were primarily T_1; no In-bearing precipitates were observed on the subboundaries or within grain interiors. Much smaller T_1 are observed on subgrain boundaries and within grain interiors of commercial 2090 in the T6 and T81 conditions. The differences in subgrain boundary precipitation in 2090 + In-T6 compared to 2090-T81 dramatically affect the fracture toughness of these alloys, in terms of both the quantitative J-Δa behavior and microscopic fracture mechanisms.

Fracture Toughness Yield strength, fracture toughness data and fracture mode for 2090-T81 and 2090 + In-T6 are presented in Table I. The longitudinal yield strengths of both alloys increased with decreasing temperature, typical of 2090 [10]. In addition 2090-T81 had a higher yield strength at both ambient and cryogenic temperatures compared to

2090 + In-T6. This suggests that although In additions to 2090 based alloys qualitatively increase the number density of T_1, the additions are not effective in increasing yield strength compared to matrix dislocations produced by stretch deformation (T8 temper). The low yield strength of plate 2090 + In-T6 (441 MPa at 25°C) is consistent with earlier work on sheet 2090 + In-T6 in which In additions increased the ultimate tensile strength, but did not increase σ_{ys} [4-7].

Compared to the In bearing alloy, commercial 2090-T81 exhibits higher initiation fracture toughness as indicated by J_{Ic} values at both 25 and -185°C. K_{Ic} values are calculated from the relationship:

$$K_{Ic}=(J_{Ic}E/(1-v^2)) \qquad (1)$$

where E is Young's modulus and v is Poisson's ratio. 2090-T81 also has higher crack propagation fracture toughness at 25°C, compared to 2090 + In-T6, as illustrated by the elevated R-curve in Fig. 3. The values of K_{Ic} and T_R for 2090-T81 reported in Table I are consistent with the work of Suresh et al. on Al-Li-Cu alloys [11], however, yield strength of stretched and peak aged 2090 in that study is lower than σ_{ys} for Vintage III alloy.[3] The trend of higher initiation and growth toughness for 2090-T81 at ambient temperature is enhanced at -185°C. Referring to Table I, the average J_{Ic} of 2090-T81 increases by 65%, but essentially remains the same for 2090 + In-T6 over the temperature range from 25°C to -185°C, resulting an increase in the difference in toughness between the two materials - 185°C.

The trend of increasing toughness with decreasing temperature for 2090-T81 is reflected in an increase in the tearing modulus. The tearing modulus, T_R, represents the resistance of a material to stable crack propagation and is defined by Paris [12] as:

$$T_R=(E/\sigma_o)(dJ/da) \qquad (2)$$

where dJ/da is the slope of the J-Δa curve in the region of stable crack growth and σ_o is the flow stress equal to $1/2(\sigma_{ult} + \sigma_{ys})$ at any temperature. The values of dJ/da used for calculating T_R in Table I were determined from least squares linear regression of J-Δa data in the stable crack growth regime as outlined in ASTM standard E 813. The crack did not bifurcate during stable propagation. Given the thickness of the compact tension specimen,

[3]Suresh et al. reported the following properties for alloy 2090 that was stretched 2% and peak aged at 190°C: σ_{ys} = 490 MPa, J_{IC} = 8 kJ/m², K_{IC} = 30 MPa√m and T_R = 1.5.

the sidegrooves and the relatively low values of J/σ_o, it is likely that both the initiation toughness and the tearing modulus values in Table 1 are typical of dominant plane strain constraint.

For 2090-T81, the tearing modulus increases by 115% at -185°C, paralleling the temperature dependence of the initiation toughness. Surprising, however, is the increase in T_R for 2090 + In-T6 and from 0.7 at 25°C to 2.1 at -185°C; the initiation toughness exhibited a slight decrease over the same temperature range. For all tests except those conducted on 2090 + In-T6 at 25°C, the R-curves had two distinct slopes in the region of stable crack growth. This trend is illustrated graphically by the dashed lines for 2090-T81 in Fig. 3. (The values of T_R reported in Table I are generally close to the average of the two slopes.) The two slopes appear to be related to the occurrence of delamination fracture.

Fractography The primary reason for the high fracture toughness of 2090-T81 is a significant amount of out-of-plane delamination and TGS fracture, at both 25 and -185°C and typical of 2090 in the T8 condition [9,10,13]. Fig. 4 shows metallographic sections taken perpendicular to the crack growth direction and within 0.5 mm of the fatigue precrack for 2090-T81 and 2090 + In-T6. The sharply faceted crack surface of 2090-T81 is typical of cracking along {111} slip planes in textured peak aged 2090 [14]. Subgrain boundaries played no role in the fracture process, presumably because of the relatively small size of T_1 precipitates and associated δ' precipitate free zones. Delaminations along high angle grain boundaries are perpendicular to the primary crack plane and are parallel to the crack growth direction. In general short transverse delaminations increase toughness by reducing through-thickness constraint at the crack tip, as indicated by the necked ligaments between delaminations. For K_{IC} to be affected by delaminations, they must occur prior to crack advance as observed by Rao and coworkers [15].

Fig. 5 compares the macroscopic fracture surfaces of 2090 compact tension specimens tested at 25 and -185°C. Consistent with other investigations, increases in the fracture initiation and growth toughnesses of 2090-T81 with decreasing temperature are associated with an increasing amount and depth of delamination. Increase delamination is due to increased yield strength, and hence an increase in transverse stress, and to weakened boundaries at the cryogenic temperature [3]. Figure 6 shows that the microscopic fracture mode for alloy 2090 is transgranular shear at both 25 and -185°C. The cryogenic fracture toughness behavior of Vintage III 2090-T81 is entirely consistent with the known roles of δ'

localized slip [16] and high angle boundary delamination [9].

As shown by the cross section in Fig. 4, the fracture of 2090 + In-T6 at 25°C is relatively flat with no major delaminations or {111} slip plane fracture facets; consistent with the low fracture initiation and growth toughnesses. The microscopic fracture mode is characterized by intersubgranular fracture with no transgranular shear apparent. ISG cracking is a low energy event which presumably occurs prior the onset of slip band cracking in the indium bearing alloy. Either the boundary precipitates or the adjacent δ'/T_1 precipitate free zone (PFZ) may be the cause of the ISG crack path; and through boundary precipitate cracking, interface decohesion or strain localization in the PFZ.

At -185°C, 2090 + In-T6 exhibits an increase in the crack growth toughness as measured by an increase in T_R, but essentially the same crack initiation toughness. In contrast to ambient temperature, fracture at -185°C is associated with significant delamination, Fig. 5. A distinct distribution of small and large delaminations exist within the region of stable crack extension. Adjacent to delaminations are areas of transgranular shear fracture, approximately 20 μm wide, however, the microscopic fracture mode in the In alloy remained primarily ISG, Fig. 6. The insensitivity of J_{Ic} to the occurrence of delamination suggests that the crack initially advances prior to delamination. The primary influence of the delaminations in this work is to significantly increase the resistance to stable crack growth.

ISG fracture in 2090 +⁻ In-T6 is traceable to a high density of subboundary precipitates in the In bearing alloy, but is atypical of commercial 2090 in the T81 condition. The propensity for subboundary precipitation, and hence low fracture toughness, and the lack of enhanced yield strength associated with the In addition could prevent the commercial application of this alloy. The propensity for subboundary precipitation in In bearing 2090, and the location of indium within the microstructure, are not understood and are the subject of continued investigation. Recrystallization of the 2090 + In alloy is not a viable explanation for the extraordinary precipitation.

Summary

1. The superior fracture toughness of 2090-T81 is associated with transgranular shear fracture coupled with a significant amount of delamination.

2. The lower toughness of 2090 + In-T6 at 25°C is associated with intersubgranular cracking and minimal levels of delamination. This fracture mode is attributed to heavy precipitation of T_1 at unrecrystallized subgrain boundaries. Low toughness coupled with low yield strength may restrict the commercial use of this alloy.

3. Both 2090-T81 and 2090 + In-T6 exhibit an increase in the amount and depth of delamination fracture at -185°C compared to ambient temperature. Microscopic fracture modes are unchanged with decreasing temperature.

4. Increased delamination at -185°C results in an increase in crack initiation and growth toughnesses for 2090-T81, but only increased tearing modulus for 2090 + In-T6.

5. Delamination fracture results in R-curve behavior which is characterized by a stable crack growth region which exhibits dual dJ/da slopes.

Continued studies will focus on mechanistic explanations for the propensity for subboundary precipitation in 2090 + In-T6, the insensitivity of J_{Ic} in 2090 + In-T6 to delamination fracture, and the origin of the dual dJ/da slopes in the stable crack region of the R-curve for alloys that delaminate.

References

1. S.J. Hales and J.A. Wagner, in NASA CP-3109, Technology 2000, p. 200 (1990).

2. L.B. Blackburn and E.A Starke, Jr., in Light-Weight Alloys for Aerospace Application, E.W. Lee, E.H. Chia and N.J. Kim, eds., TMS-AIME, Warrendale, PA, p. 209 (1989).

3. L.B. Blackburn and E.A. Starke, Jr., in Al-Li Alloys V, T.H. Sanders, Jr. and E.A. Starke, Jr., eds., Birmingham, UK, p. 751 (1989).

4. J.A. Wagner, in Light-Weight Alloys for Aerospace Application, E.W. Lee, E.H. Chia and N.J. Kim, eds., TMS-AIME, Warrendale, PA, p. 221 (1989).

5. S.L Verzasconi and J.W. Morris, Jr., in Al-Li V, T.H. Sanders, Jr. and E.A. Starke, Jr., eds., Birmingham, UK, p. 1523 (1989).

6. S.P. Agarwal, M.L. Rommel and M.T. Hahn, in Design, Development and Characterization of Advanced Aluminum Structural Alloys for Enhanced Superplasticity, NAS1-17623, Northrop Corporation (1991).

7. E.L. Bradley, III, D. Chu and J.W. Morris, Jr., to be published in the Proceedings of the International Cryogenic Materials Conference, Huntsville, AL (1991).

8. J.G. Kaufman and H.Y. Hunsicker, in Fracture Toughness Testing, ASTM STP 381, ASTM, Philadelphia, PA, p. 290 (1965).

9. K.T. Venkateswara Rao, Y. Weikang and R.O. Ritchie, in Metallurgical Transactions A, 20A, p. 485 (1989).

10. J. Glazer, S.L. Verzasconi, R.R. Sawtell and J.W. Morris, Jr., Metallurgical Transactions A, 18A, p. 1695 (1987).

11. S. Suresh, A.K. Vasudevan, M. Tosten and P.R. Howell, Acta Metallurgica et Materialia, 35, p. 26 (1987).

12. P.C. Paris, H. Tada, A. Zahoor and H. Ernst, in Elastic-Plastic Fracture, ASTM STP 668, ASTM, Philadelphia, PA, p. 5 (1979).

13. R.C. Dorward, Scripta Metallurgica et Materialia, 20, p. 1379 (1986).

14. G.R. Yoder, P.S. Pao, M.A. Imam and L.A. Cooley, Scripta Metallurgica et Materialia , 22, p. 1241 (1988).

15. K.T. Venkateswara Rao and R.O. Ritchie, Acta Metallurgica et Materialia, 38, p. 2309 (1990).

16. K.V. Jata and E.A. Starke, Jr., in Metallurgical Transactions A, 17A, p. 1011 (1986).

Table 1: Summary of the fracture toughness of 2090-T8 and 2090+In-T6.

2090-T81	Yield strength (MPa)	J_{Ic} (kJ/m^2)	K_{Ic} (MPa$\sqrt{m}$)	T_R	Amount of delamination	Primary fracture mode
25°C	579	10.0 11.3 9.9	29.8 31.7 29.7	1.9 1.3 0.8	Medium Medium Medium	TGS TGS TGS
-185°C	648	18.1 14.1	40.8 36.0	3.0 2.5	High High	TGS TGS
2090+In-T6						
25°C	441	5.7 5.9	22.6 23.0	0.6 0.7	Very low Very low	ISG ISG
-185°C	483*	5.6 6.5	22.4 24.2	2.2 2.0	Medium Medium	ISG ISG

* estimated from cryogenic tensile data of sheet 2090+In-T6
TGS = Transgranular shear fracture
ISG = Intersubgranular fracture

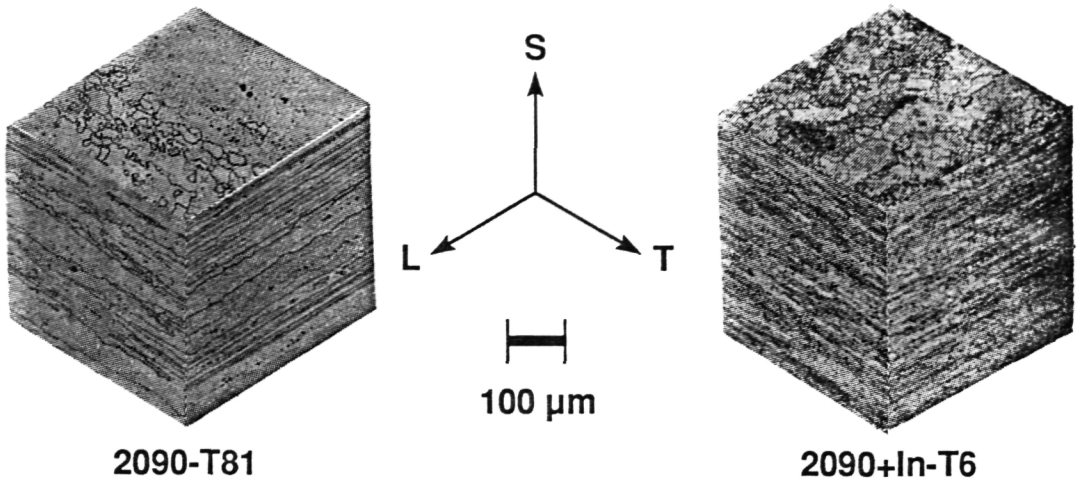

Figure 1. Microstructures of 19.1 mm 2090-T81 and 12.7 mm 2090+In-T6 plates.

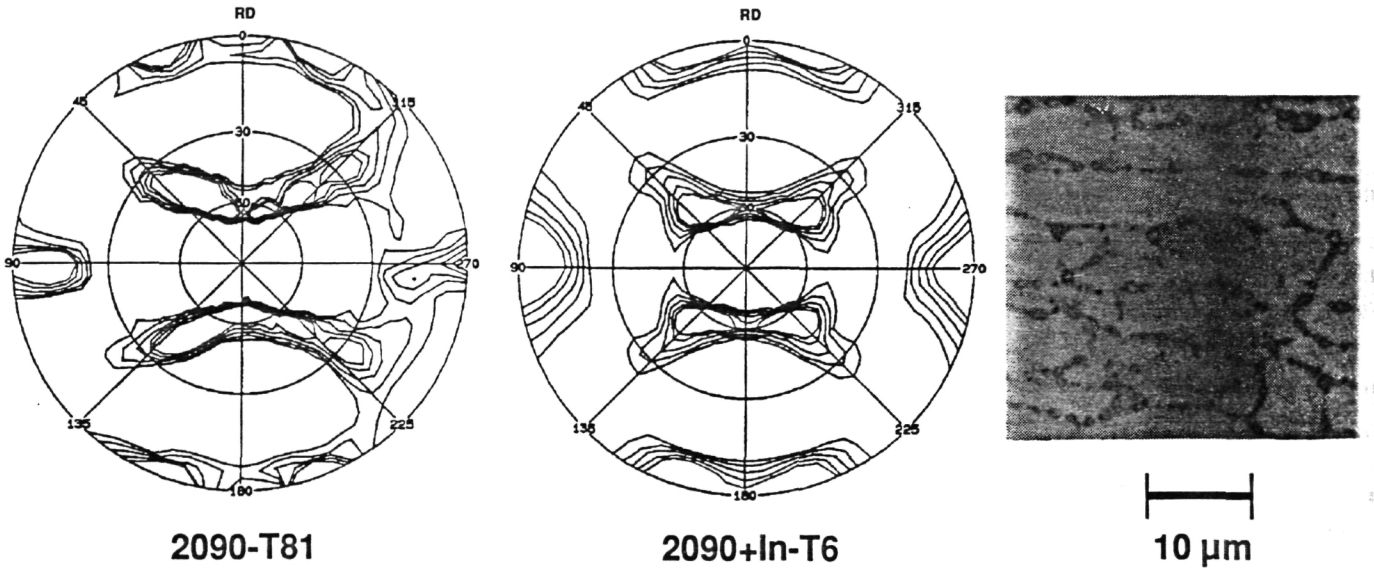

Figure 2. Full {111} pole figures at T/2 for 2090-T8 and 2090+In-T6 and photomicrograph showing subboundary precipitates in 2090+In-T6.

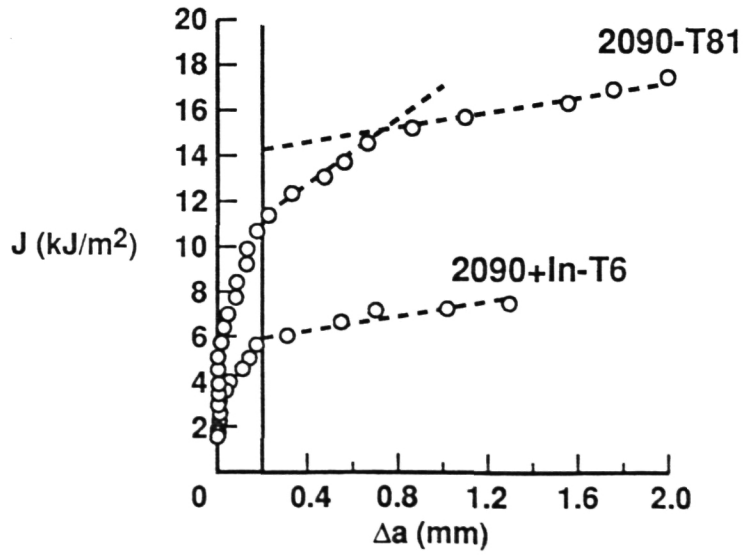

Figure 3. Fracture toughness R-curves for 12.0 mm specimen with side groove at 25°C.

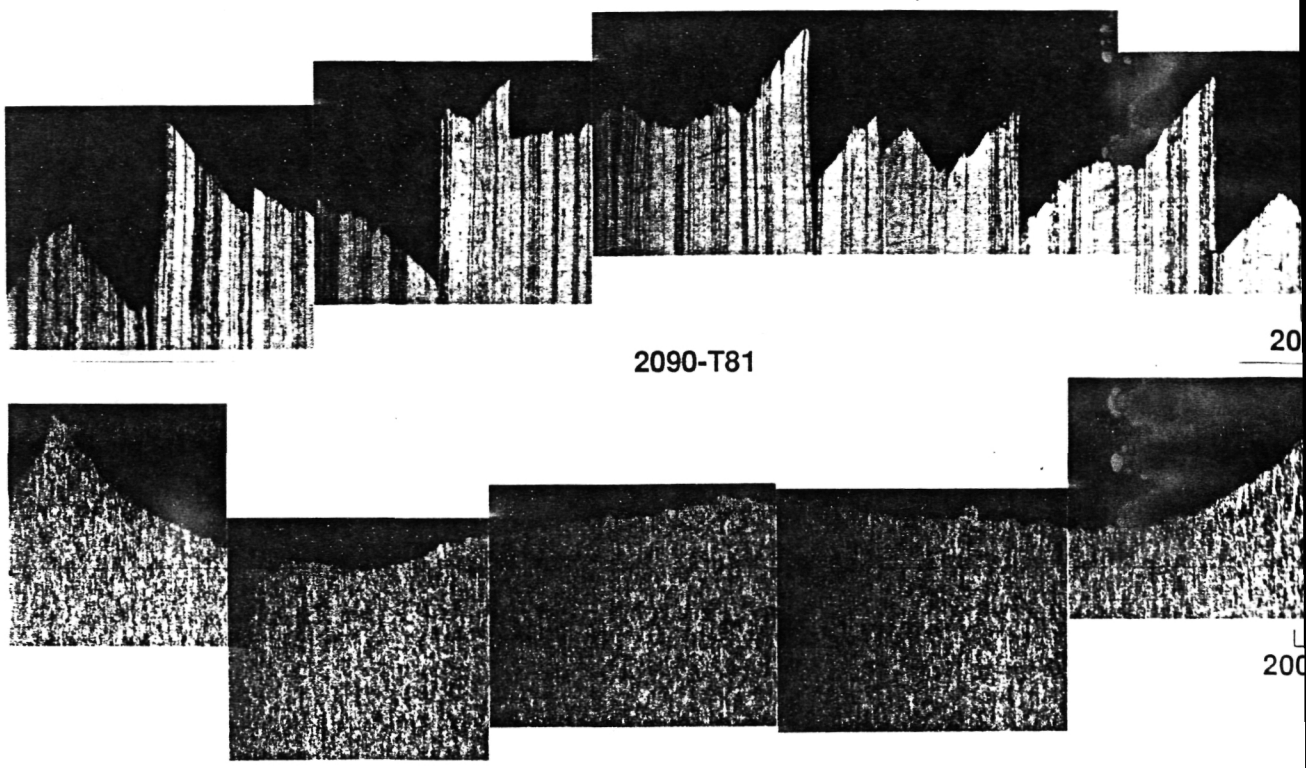

Figure 4. Cross-sections of specimens tested at 25°C.

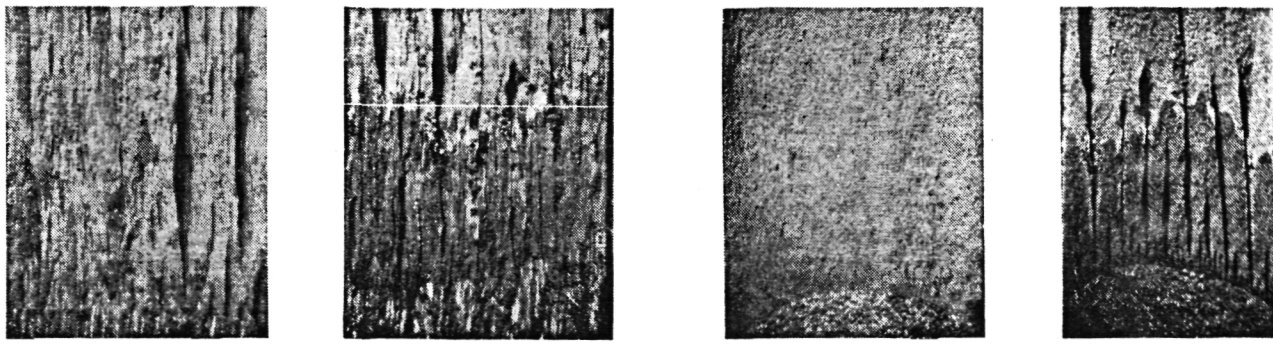

Figure 5. Microscopic fracture appearance for specimens tested at 25°C and -185°C.

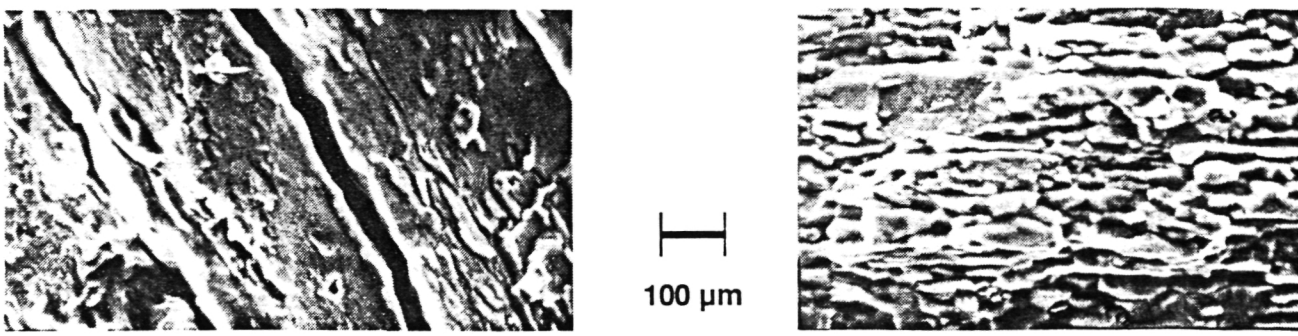

Figure 6. Fractographs showing transgranular shear fracture in 2090-T81 and intersubgranular fracture in 2090+I

Project 6 **The Effect of Cryogenic Temperature on the Fracture Toughness of Weldalite™ 049**

Cynthia L. Lach and Richard P. Gangloff

Objective

The objective of this research is to characterize the uncertain effect of temperature on the deformation and fracture behavior of Weldalite™ from cryogenic to elevated temperatures. We will measure fracture resistance and emphasize the determination of fracture mechanisms, including slip plane cracking, high angle boundary delamination, subgrain boundary cracking, and microvoid coalescence.

Background

Aluminum-lithium-copper alloys are being developed to replace conventional 2XXX and 7XXX aluminum alloys for aerospace structural applications. Al-Li-Cu alloys such as 2090 offer increased stiffness and decreased density due to lithium, and exhibit increased strength and increased fracture toughness with decreasing temperature from room to cryogenic levels. Increasing toughness at cryogenic temperatures greatly facilitates fracture mechanics damage tolerant designs because cold proof-testing is not required; a room temperature evaluation suffices.

Weldalite™ X2095 is a weldable Al-Li-Cu alloy developed by Martin Marietta Corporation. The nominal composition of Weldalite™ X2095 is 3.9-4.6Cu, 1.0-1.6Li, 0.25-0.6Ag, 0.25-0.6Mg, 0.04-0.18Zr, and 0.1Ti (weight percent); with the balance being aluminum. The alloy is notable for the high strength levels that are achieved by either natural or artificial aging.

The temperature dependent fracture of Weldalite™ may be significantly different from that of the Al-Li-Cu compositions examined to date. One or more of the following factors are likely to critically affect the toughness of the Weldalite™-type alloys:

- A high volume fraction of large (15 to 50 μm) primary copper rich phases.
- Subgrain boundary T_1 precipitates in the unrecrystallized microstructure.
- High yield strength and low work hardening.
- Slip localization and slip plane cracking (this is only likely to be important for

lower Cu and higher Li concentrations that promote ordered δ' precipitation).

oo High angle grain boundary delamination (this has not been reported for Weldalite™).

The importance of each metallurgical factor may depend on temperature, stress state, and either the crack initiation or propagation stage of toughness. In particular, the effects of test temperature and aging condition on the fracture toughness of Weldalite™ X2095 are uncertain.

Technical approach

The basic approach to this problem was presented in the renewal proposal for 1992.[1] Modifications to this direction are outlined below.

Material Two Weldalite™ X2095 compositions are selected for study to examine the limits of the Li and Cu levels for the alloy designated X2095. The high Li-Cu alloy (Al-4.64Cu-1.53Li-0.34Ag-0.37Mg-0.17Zr; wt%) was obtained from Reynolds Metals in the form of rolled plate. A large ingot of this alloy was cast and hot rolled to a thickness of 38.1 mm at the McCook production facility. Subsequently, the alloy was rolled to a final thickness of 12.7 mm, solution heat treated, quenched and stretched (6%) by laboratory-scale processing at Reynolds Metals. The low copper alloy (Al-4.04Cu-1.00Li-0.37Ag-0.36Mg-0.15Zr; wt%) was similarly fabricated on a production scale by Reynolds Metals and delivered in December of 1991.

The expectation is that the selected alloys will contain substantially different amounts of primary phase to enable examination of the effect of this feature on fracture toughness. Several aging conditions, conducted at NASA-LaRC, will be employed to vary yield strength, work hardening rate, and the volume fraction and distribution of the δ' and T_1 strengthening precipitates. Metallurgical effects on toughness will be assessed for similar alloy flow properties.

Deformation and Fracture The only change in this portion of the work, compared to the renewal proposal, is the compact tension specimen thickness. The thickness will be 3.9 mm (0.15 inches) to produce both plane strain crack initiation toughness (K_{IC}), and plane stress crack growth resistance (R-curve) data based on the J-integral methods outlined in ASTM Standards E813-89 and E1152-87.[2,3] Crack extension will be measured by unloading compliance. Limited experiments will be conducted with thicker compact tension

specimens to define K_{IC} by a more conventional method and to qualitatively indicate the extent to which the R-curve is influenced by thickness and the degree of plane strain constraint.

Proposed Research

With these Weldalite™ compositions and the compact tension J-Δa method, three areas will be sequentially examined. The first two areas, fracture toughness measurement at 25°C and at cryogenic temperatures, will be emphasized; work on fracture mechanics will be initiated but completed in 1993.

Fracture Toughness at 25°C The goal of these experiments is to characterize the crack initiation and growth resistance, and associated microscopic fracture modes, for Weldalite™ X2095 at ambient temperature. Both K_{IC}, from J at the onset of crack growth, and the tearing modulus from $dJ/d\Delta a$ will be measured with the 3.9 mm thick C(T) specimen. The R-curve will be determined for each of the two Weldalite™ X2095 compositional variants; aged at 143°C for 10, 20 or 24, 30, and 72 hours; to determine the interactive effects of yield strength, work hardening, subgrain boundary T_1 and δ' precipitation (for the high Li alloy).

Effect of Cryogenic Temperature The objective of these experiments is to determine the effect of cryogenic temperature on the fracture toughness and microscopic fracture processes for Weldalite™ X2095. The low Li-Cu alloy will be tested at the aging condition that provides the best toughness (according to Reynolds Metals, 143°C for 20 hours). The full J-Δa curve will be measured, with 3.9 mm thick C(T) specimens, at several temperatures ranging from -196°C to 125°C. Uniaxial tensile yield strength, work hardening and fracture strain will be characterized at -196°C and 23°C. Crack surfaces will be examined by SEM and quantitative image analysis.

Fracture Mechanics of Thin Sheet Crack Propagation The aims of this portion of the study are: (a) to address the effect of compact tension specimen thickness on the R-curve characterization, and (b) to compare K_{IC} and tearing modulus data with literature findings for similar Weldalite™ compositions, but alternate specimen thicknesses and geometries, including thin center-cracked tension and surface cracked plate configurations. The low Li-Cu alloy, most probably aged at 143°C for 20 hours, will be tested at a single temperature. J-Δa relationships will be characterized as a function of the following C(T)

specimen thicknesses: 2.5, 7.6, and 12.0 mm; and 12.0 mm with sidegrooves. The interest here is to determine if a "valid" K_{IC} value is determinable from a J-Δa measurement, and to define the effect of stress state and far-field stresses on crack growth resistance.

Progress During the Reporting Period

Preliminary to the work with the two main Weldalite™ compositions, a 5.1 cm wide and 1.8 cm thick extrusion (Al-4.28Cu-0.84Li-0.36Ag-0.41Mg-0.14Zr; wt%) was characterized in terms of fracture toughness at 25°C. The R-curves are presented in Figure 1 for two aging heat treatments and C(T) specimen thicknesses. (The thick C(T) specimens, M1K and M2K, are sidegrooved from 12.0 mm to a net thickness of 9.3 mm. The thin C(T) specimens, M1J and M2J, are 3.9 mm thick. The alloy was aged at 143°C for 14 and 75 hours which resulted in tensile yield strengths of 606 MPa and 717 MPa respectively.) Plane strain fracture toughnesses (K_{IC}) and tearing modulus ($[dJ/d\Delta a]\cdot[E/\sigma_{ys}]$) were determined for each heat treatment and specimen thickness; Table I. σ_{ys} values were reported by Pickens for each aging condition[4]. J_i and the associated K_i were determined as the initiation toughnesses at the onset of crack growth, as detected by direct current electrical potential monitoring. J_{IC} and the associated K_{IC} were determined by the intersection of the J-Δa curve with the offset (0.2 mm) blunting line. Each thin specimen bifurcated after crack initiation, therefore the validity of the M1J and M2J test data is questionable.

Several points are relevant to the data in Figure 1 and Table I.

- oo Considering the thick sidegrooved specimen (gross thickness of 11.7 mm and net thickness of 9.3 mm), K_{IC} and K_{JIC} values, the later calculated according to ASTM E813-89, bracket K_{IC} values calculated per ASTM E399-83 by Pickens (see Table 1.)[4]. The difference in crack initiation toughness values is due to the fact that each ASTM Standard has a different definition of the critical load at which the crack starts to grow. Electrical potential (or compliance) indications of crack growth initiation precede offset blunting line toughness; with the magnitude of the difference increasing with increasing $dJ/d\Delta a$.
- oo Considering the thin C(T) specimens, K_{IC} from electrical potential was higher than the corresponding value for the side grooved specimen for each aging condition. This result is unexpected because empirical results for steels suggest that a plane strain crack initiation toughness, K_{IC}, is definable from an elastic-plastic J-integral

experiment provided that specimen thickness exceeds 25 times the ratio of J at initiation to σ_o. (σ_o is approximated by σ_{ys} for low work hardening aluminum alloys such as Weldalite™). From this equation, the C(T) thickness (3.9 mm) easily exceeds the values indicated in Table I; plane strain initiation toughnesses are expected. Since the crack bifurcated for each thin C(T) specimen, presumably associated with the microstructure or texture of extruded Weldalite™, it is not possible to unambiguously compare the thick and thin specimen toughness results.

oo For the Weldalite™ extrusion, fracture toughness decreases with increasing aging time at 143°C, and with increasing yield strength. Both plane strain initiation toughness and plane strain tearing modulus decrease with increasing aging time.

Figure 2 presents the 25°C J-Δa curves for the high 4.6%Cu-1.5%Li Weldalite™ plate and three aging heat treatments. The alloy is textured, unrecrystallized and hardenable by either T_1, S' and Θ' (aged at 165°C for 24 hours; σ_{ys} = 610 MPa), or by T_1, δ' and Θ' (145°C for 24 and 72 hours; σ_{ys} = 572 and 620 MPa, respectively). The alloy contains a potentially significant amount of primary Al-Cu-Li phase sized on the order of 30 μm. The following points are relevant to the fracture behavior of plate material.

oo Similar plane strain fracture toughnesses (K_{IC}) were determined by the thin specimen (3.9 mm thickness) J-integral R-curve (14.7, 18.8 and 23.7 MPa√m) method and by the thick sidegrooved C(T) (12.1, 15.3 and 20.3 MPa√m; gross thickness equalling 12.0 mm and net thickness equalling 9.6 mm). While a systematic difference exists, the values from each method do not differ to the extent indicated by the data for the extrusion, Figure 1 and Table I. Crack bifurcation was not observed for the thin C(T) specimens from the Weldalite™ plate. These data suggest that the proposed method, with the 3.9 mm thick C(T) specimen, will effectively characterize the fracture toughness of Weldalite™.

oo Crack growth resistance, approximated by the applied K level at the validity limit for J-controlled crack growth (2 mm of crack extension), is relatively high and similar to the results for other Weldalite™ compositions[1].

oo For the high Li-Cu plate, fracture toughness decreases with increasing aging time at 143°C and decreases with increasing aging temperature at constant σ_{ys}.

oo Delamination and slip band cracking are not observed for either heat treatment of the

Weldalite™. Presumably, the volume fraction of ordered δ' is insufficient to produce the latter fracture mode.

Table II compares the plane strain fracture toughness values of the extrusion to those of the high Li-Cu alloy plate. Generally, K_{IC} values for the 4.6%Cu-1.5%Li alloy are lower (12 to 18 MPa$\sqrt{m}$) than the results for the 4.3%Cu-0.8%Li alloy (45 to 50 MPa$\sqrt{m}$) at similar high yield strengths (610 MPa). Crack initiation toughnesses for the high Li-Cu plate are generally low compared to literature data for Weldalite™ [1]. Plate fracture surfaces exhibited cracked primary phases and some intersubgranular separation for each aging condition. Metallographic analyses revealed a substantial volume fraction of primary phases in the microstructure of solution treated high Li-Cu Weldalite™. While the low toughnesses are possibly ascribable to the high copper level and primary phases in the X2095 composition, literature data indicate higher toughnesses for higher Cu alloys[1]. The high Li-Cu plate Weldalite exhibited similar high tearing resistance compared to lower Cu Weldalite™, suggesting that primary phases may not dominantly degrade fracture toughness[1]. This conclusion is speculative because of the uncertain effect of specimen geometry and constraint on K_c.

The low Li-Cu alloy was obtained from Marshall Space Flight Center and a preliminary aging study was conducted. Figures 3 and 4 compare the aging behavior of the high Li-Cu alloy to the low Li-Cu alloy. Figure 5 displays the aging behavior of the Weldalite (4.3Cu-0.8Li) extrusion. A comparison of the aging curves for the three Weldalite™-type alloys at 145°C is shown in Figure 6. The aging temperature for the high Li-Cu and the low Li-Cu alloys was selected to be 14°C. An in-depth aging study will be conducted on these two alloys at 145°C for 1 to 100 hours. In an effort to investigate the effect of various strength levels on the fracture toughness of the material; four different aging times will be selected along the hardness curve.

Returning to the issue of the effect of the Li to Cu ratio on the amount of primary phases present in the microstructure during solution treatment, Figures 7 and 8 show typical microstructures for the high and low Li-Cu Weldalites™. Each alloy is presumably unrecrystallized. Qualitatively, and consistent with the phase diagram by Silcock, the high Li-Cu alloy contains large primary phases (probably T_1 and/or T_B), while the low Li-Cu composition should be nearly single phase at the solution temperature[1]. Of course, such phases are unaffected by aging time and temperature. The size and volume fraction of

primary phases will be quantitatively determined for each alloy composition. Preliminary results indicate that the 4.6%Cu-1.5%Li alloy contains 5.7 volume per cent of primary phases (the values for two replicate specimens are 4.7% and 6.7%).

Future plans

The fracture toughness experiments will measure the J-crack growth response, based on the automated unloading compliance method, for cryogenic to ambient temperatures and above (125°C). Fracture surfaces will be examined by scanning electron microscopy and metallographic cross sections.

The uniaxial tensile deformation behavior of Weldalite™ X2095 will be characterized at selected temperatures spanning the range from -196 to 25°C. The stress-strain relationship based on the Ramberg-Osgood power-law relation will be used to identify work hardening characteristics for uniform deformation prior to necking.

References

1. R.P. Gangloff, "NASA-UVa Light Aerospace Alloy and Structures Technology Program", Proposal No. MS-NASA/LaRC-4881-92, University of Virginia.

2. "Standard Test Method for J_{IC}: A Measure of Fracture Toughness", Annual Book of ASTM Standards, Vol. 03.01, ASTM, Philadelphia, PA, pp. 577-588 (1991).

3. "Standard Test Method for Determining J-R Curves", Annual Book of ASTM Standards, Vol. 03.01, ASTM, Philadelphia, PA, pp. 825-835 (1991).

4. "Standard Test Method for Plane-Strain Fracture Toughness of Metallic Materials", Annual Book of ASTM Standards, Vol. 03.01, ASTM, Philadelphia, PA, pp. 480-504 (1988).

Table I. Fracture Toughness of a Weldalite^{TM}-type Extruded Alloy at 25°C

Spec. I.D.	T(°C)/hrs	Y.S., MPa Pickens'	J_i, KJ/m^2	B/B_{NET}, mm	B, bo> 25(J_i/YS)	$K_i^2=J_i \times [E/(1-\upsilon^2)]$ $K_i = K_{IC}$ MPa$\sqrt{m}$	Valid per E813	K_{IC}, MPa$\sqrt{m}$ Picken's	dJ/da (MPa)	T_R
M1K	143°C/14	605.5	23.3	11.7/9.3	B > 0.97 mm	44.6	YES	49.0	21.5	4.2
M2K	143°C/75	717.2	9.2	11.7/9.3	B > 0.32 mm	28.0	YES	36.5*	4.3	0.75
M1J+	143°C/14	605.5	45	3.9	B > 1.86 mm	61.9	YES+	-	-	-
M2J+	143°C/75	717.2	14.7	3.9	B > 0.51 mm	35.4	YES+	-	-	-

Spec. I.D.	T(°C)/hrs	Y.S., MPa Picken's	J_{IC} KJ/m^2	B/B_{NET}, mm	B, bo> 25(J_{IC}/YS)	$K_{JIC}^2=J_{IC}x [E/(1-\upsilon^2)]$ K_{JIC}, MPa$\sqrt{m}$	Valid per E813	K_{IC}, MPa$\sqrt{m}$ Pickens'	dJ/da (MPa)	T_R
M1K	143°C/14	605.5	38	11.7/9.3	B > 1.57 mm	56.9	YES	49.0	21.5	4.2
M2K	143°C/75	717.2	15.7	11.7/9.3	B > 0.55 mm	36.6	YES	36.5*	4.3	0.75
M1J+	143°C/14	605.5	-	-	-	-	-	-	-	-
M2J+	143°C/75	717.2	-	-	-	-	-	-	-	-

+: out-of-plane cracking
*: conditional test

Table II. Fracture Toughness of Weldalite^{TM}-type Alloys at 25°C

Specimen I.D.	T(°C)/hrs	Weight % Cu/Li	Material Format	Y.S., MPa	B/B_{NET}, mm	$K_i = K_{IC}$ MPa$\sqrt{m}$
M1K	143°C/14	4.28/0.84	extrusion	605.5	11.7/9.3	44.6
M2K	143°C/75	4.28/0.84	extrusion	717.2	11.7/9.3	28.0
M1J+	143°C/14	4.28/0.84	extrusion	605.5	3.9	61.9+
M2J+	143°C/75	4.28/0.84	extrusion	717.2	3.9	35.4+
MM	143°C/14	4.28/0.84	extrusion	605.5	-	49.0
MM	143°C/75	4.28/0.84	extrusion	717.2	-	36.5*
N3D	143°C/24	4.64/1.53	plate	572.4	11.7/9.3	20.3
N9B	143°C/72	4.64/1.53	plate	620.7	11.7/9.3	15.3
N2B	165°C/24	4.64/1.53	plate	610.3	11.7/9.3	12.1
N5C	143°C/24	4.64/1.53	plate	572.4	3.9	23.7
N7C	143°C/72	4.64/1.53	plate	620.7	3.9	18.8
N6C	165°C/24	4.64/1.53	plate	610.3	3.9	14.7

+: out-of-plane cracking *: conditional test MM=Martin Marietta Data

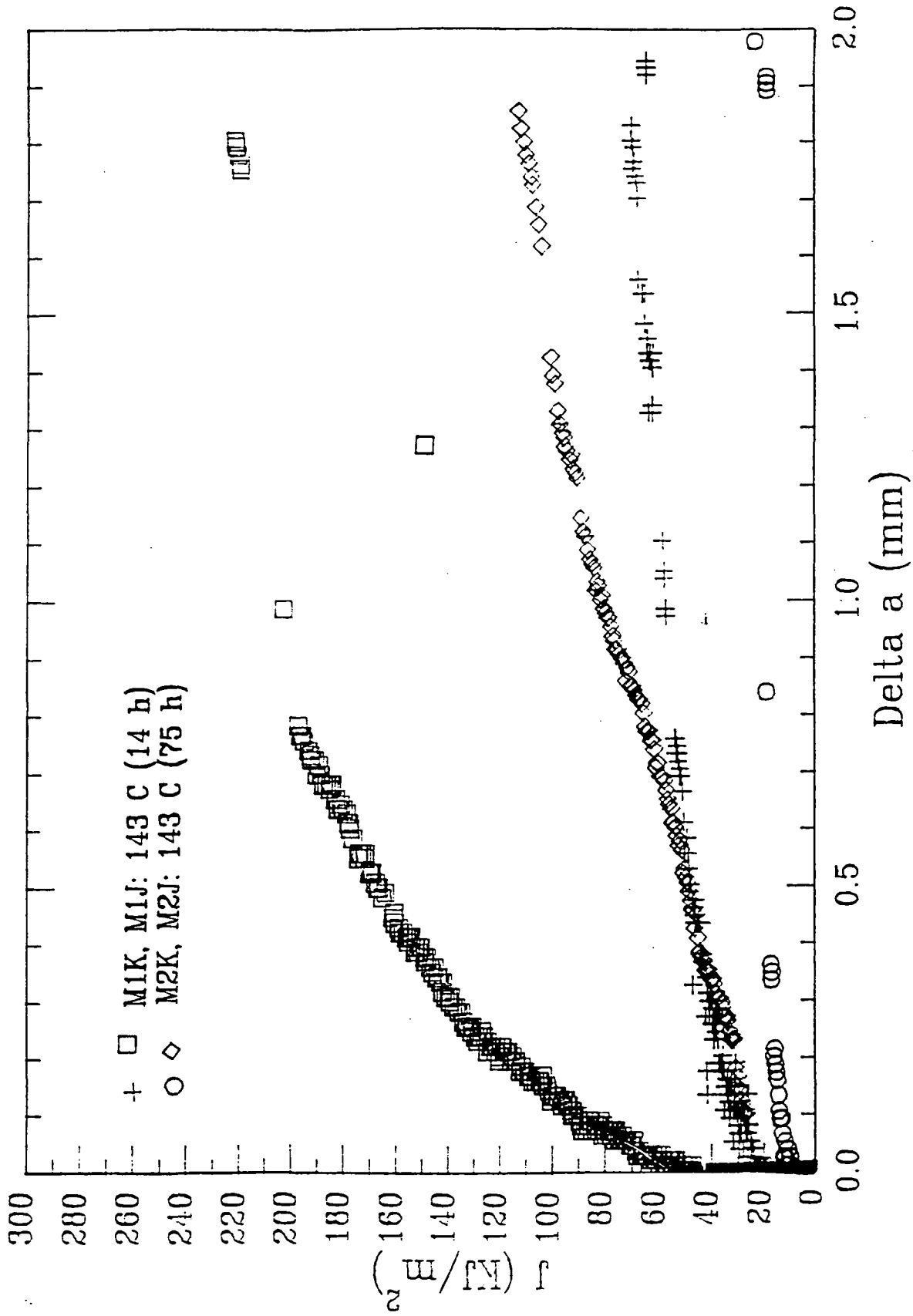

Figure 1: Fracture toughness J-Δa R-curves for 4.3%Cu-0.8%Li Weldalite™ extrusion loaded at 25°C, including results for the 3.9 mm thick and 11.7 mm thick sidegrooved compact tension specimens.

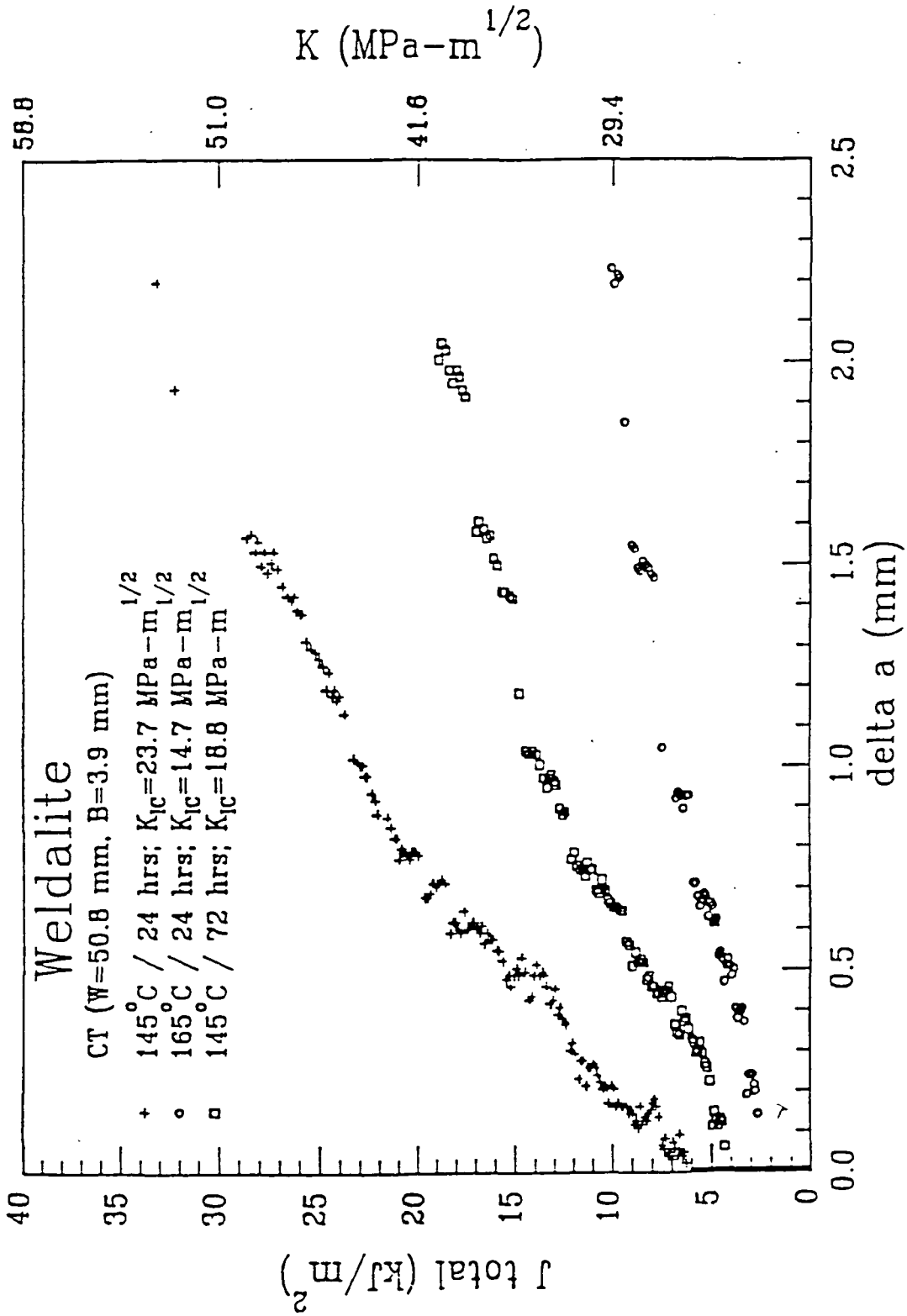

Figure 2: Fracture toughness J-Δa R-curves for 4.6%Cu-1.5%Li Weldalite™ plate loaded at 25°C, including results for the 3.9 mm thick and 12.0 mm thick sidegrooved compact tension specimens.

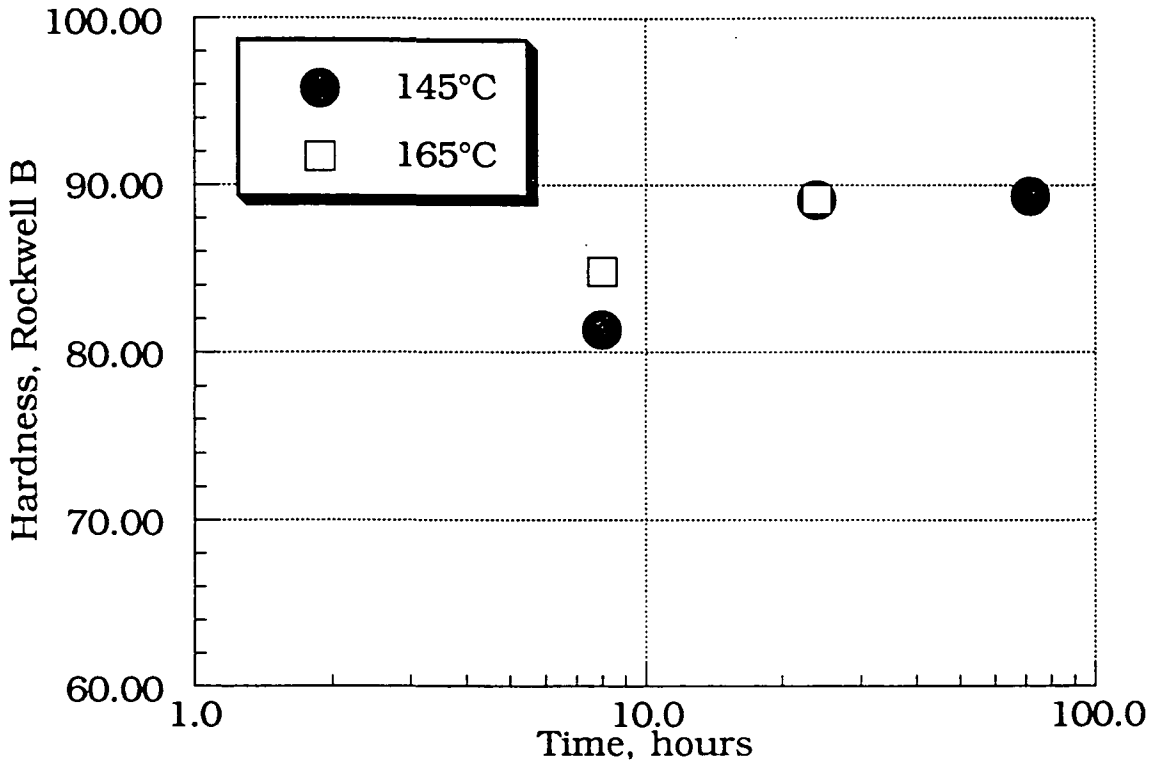

Figure 3 Aging curves of high Li-Cu alloy (4.6Cu1.5Li).

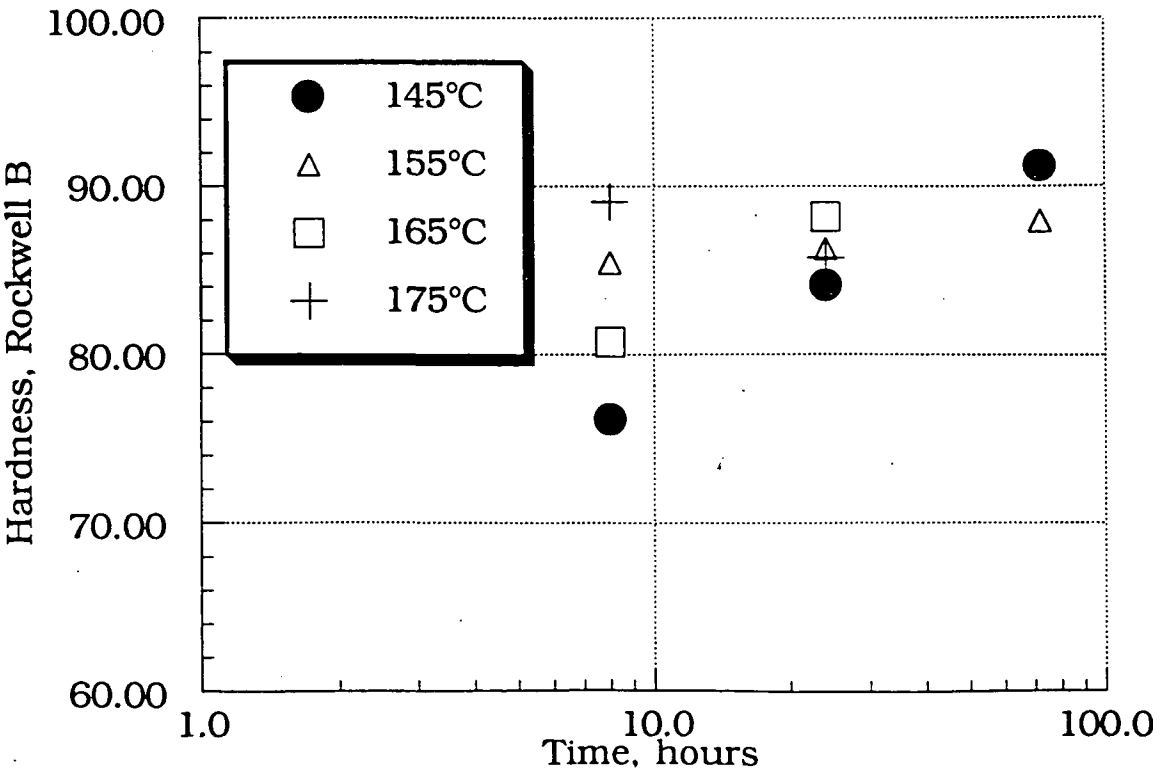

Figure 4 Aging curves of low Li-Cu alloy (4.0Cu1.0Li).

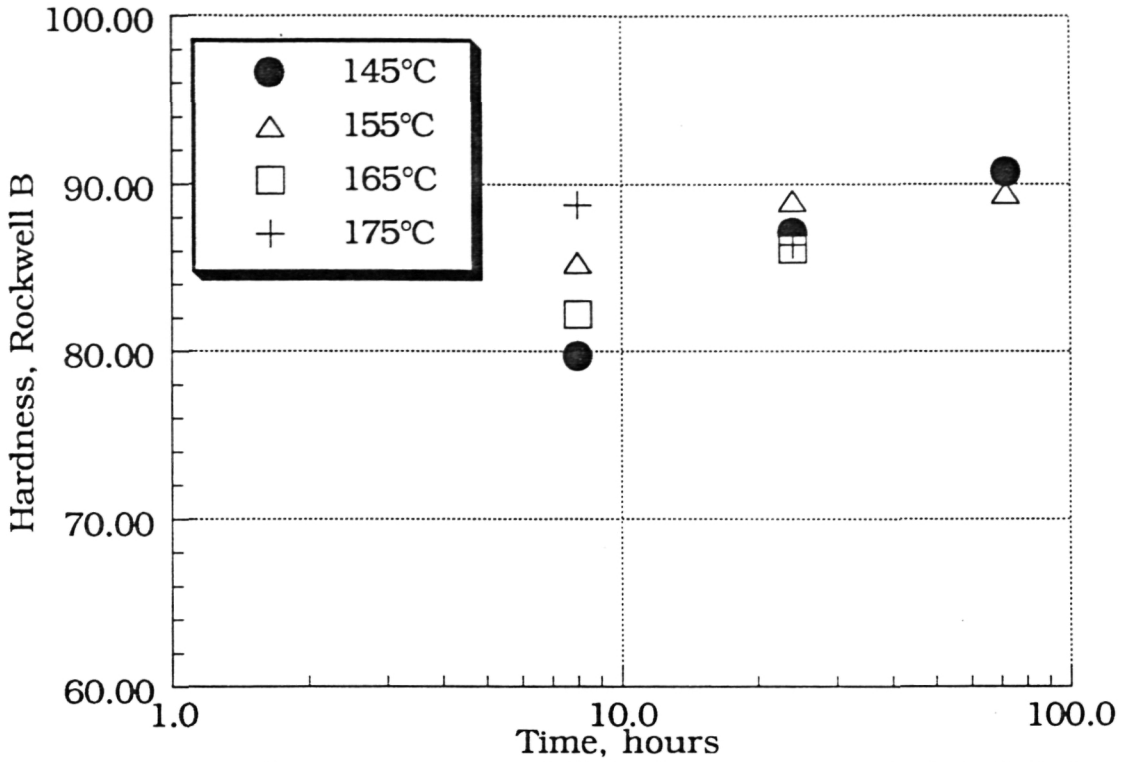

Figure 5 Aging curves of Weldalite extrusion (4.3Cu0.8Li).

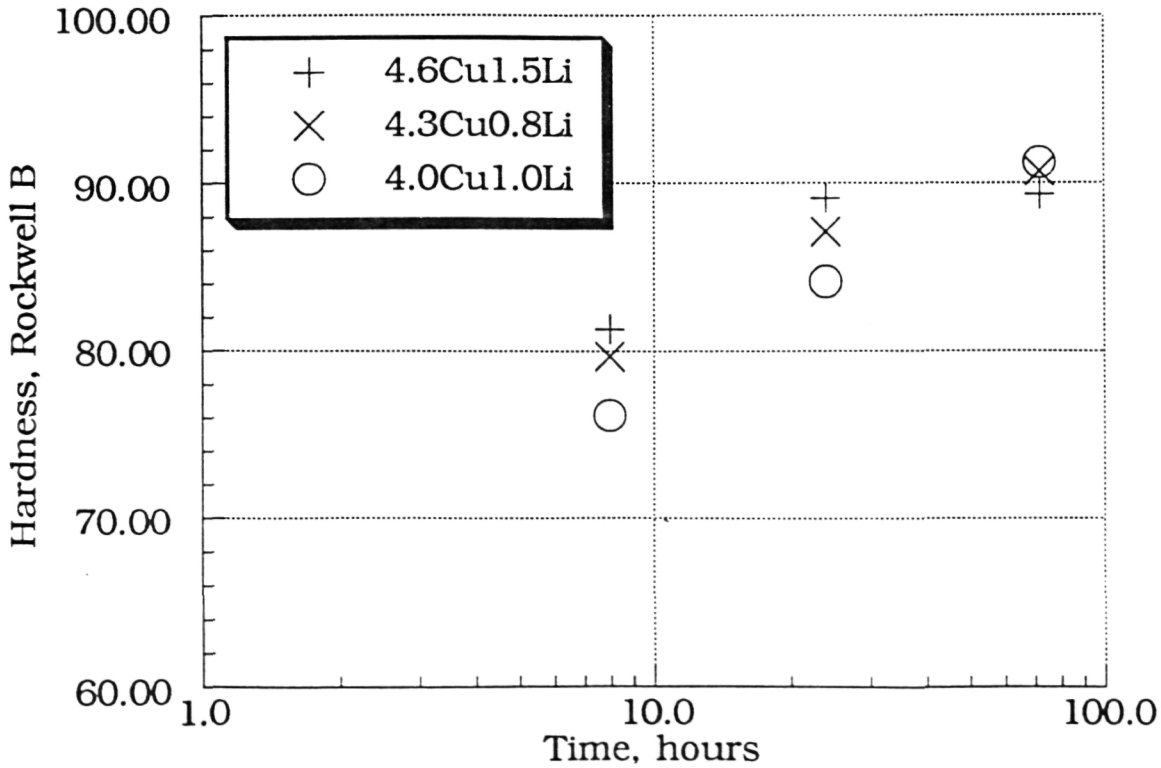

Figure 6 Aging curve of all three alloys at 145°C.

WELDALITE™ X2095

Al 4.64Cu 1.53Li 0.34Ag 0.37Mg 0.17Zr: wt%

145°C for 24 hours

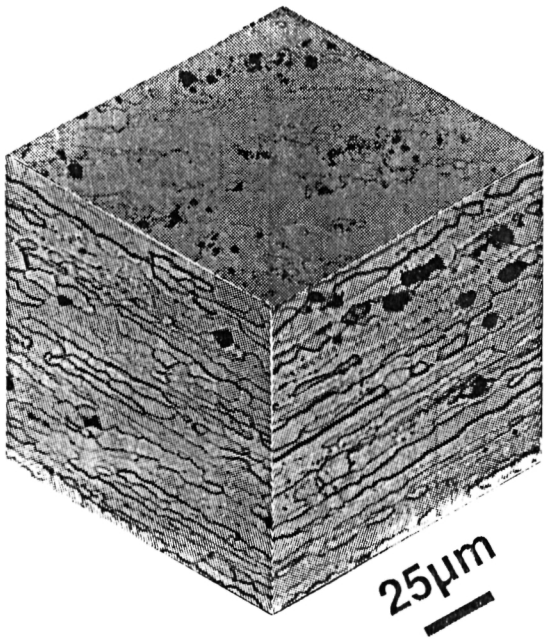

145°C for 72 hours

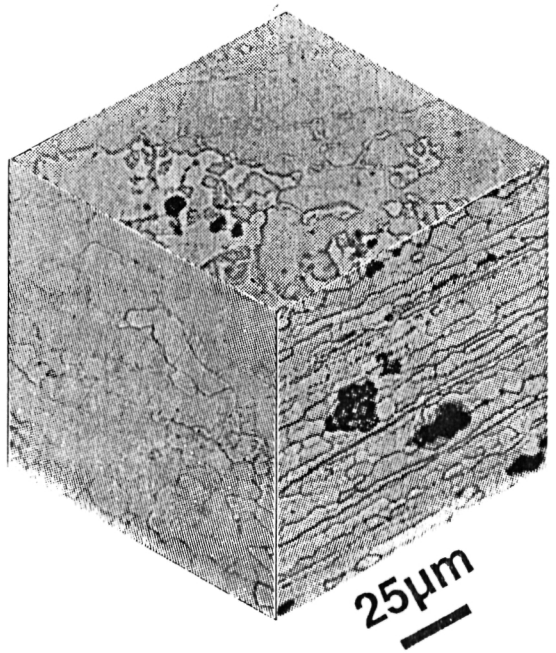

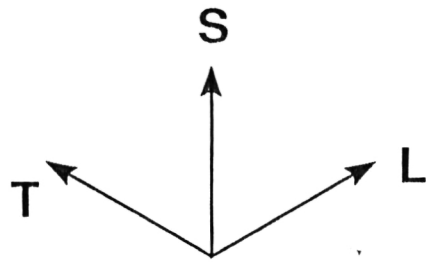

Figure 7 Microstructure of high Li-Cu alloy at 145°C Age.

WELDALITE™ X2095

Al 4.04Cu 1.00Li 0.37Ag 0.36Mg 0.15Zr: wt%

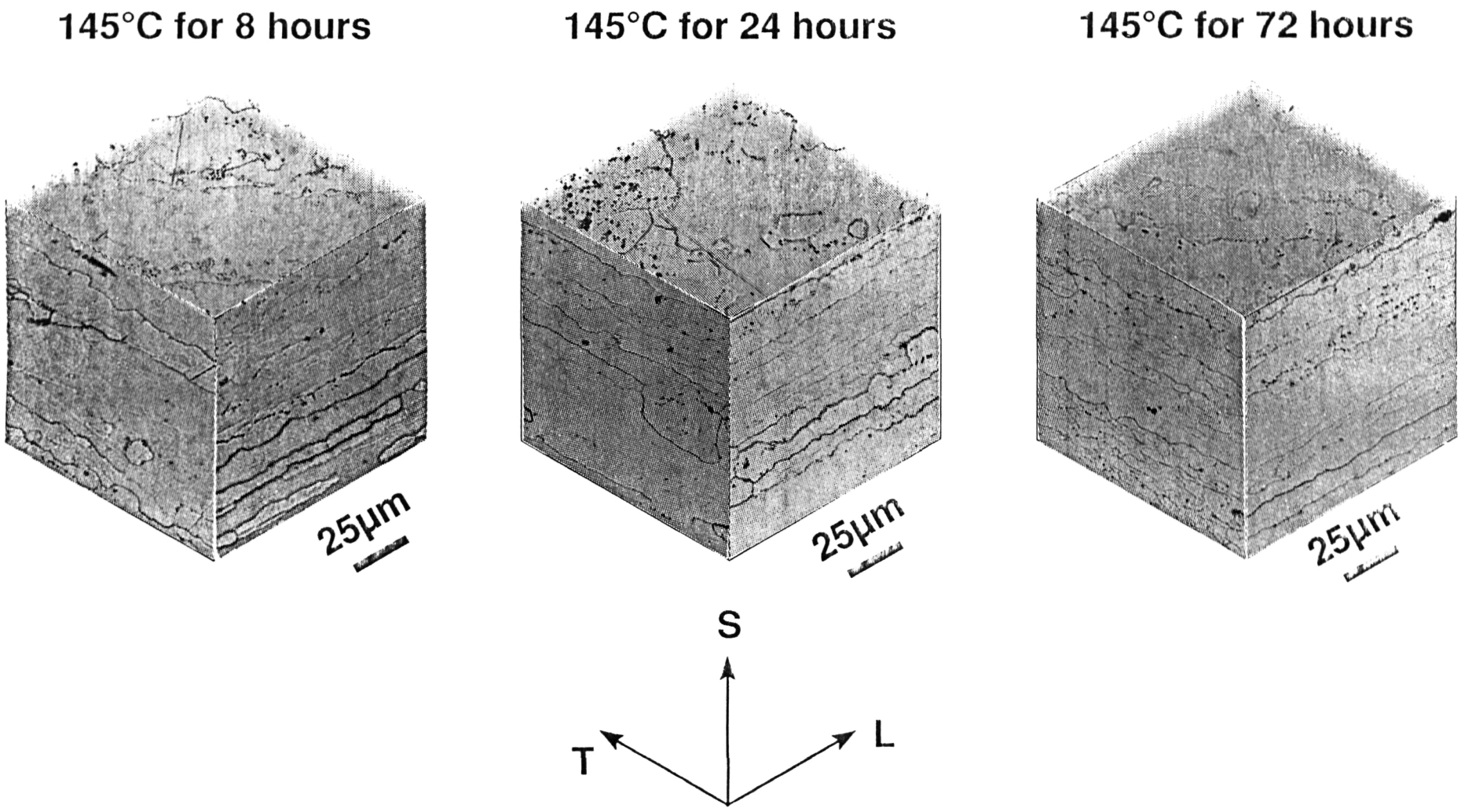

Figure 8 Microstructure of low Li-Cu alloy at 145°C Age.

Project 7 **Mechanisms of Localized Corrosion in Al-Li-Cu-Mg-Ag Alloy X2095 and Compositional Variations**

F. Douglas Wall and Glenn E. Stoner

Objectives

The objectives for this research project are to determine the contributions of environment and microstructure to the localized corrosion of aluminum alloy X2095 and an Al-4.0 Cu-1.0 Li alloy.

Approach and Results

Experimentation during the first six months of this project was focused on characterizing the electrochemical behavior of three tempers of the X2095 alloy in chloride and chloride/chromate environments and documenting the SCC behavior as a function of applied potential in a chloride/chromate environment. All experimental work was performed on three tempers of the X2095 alloy which were received from Reynolds Metals Corporation in September of 1991. These tempers will be referred to as X2095-A, B, C and the corresponding aging processes are as follows: (A) 290°F/20 hrs, (B) 290°F/30 hrs, (C) 290°F/20 hrs + ramp to 400°F at 50°F/hr + 400°F/5 min.

Electrochemical parameters were assessed through potentiodynamic polarization experiments performed on 1 cm^2 samples at a scan rate of 0.2 mV/sec in aerated 0.1M NaCl + 0.1M Na_2CrO_4. Results of these experiments are given in Table 1.

The presence of chromate ions tends to raise the breakaway potential (E_{br}) of the three tempers to potentials ranging from -0.060 to -0.210 V_{SCE}. In the same environment bulk T_1 (Al_2LiCu) has been shown to have an E_{br} value of approximately -0.5 V_{SCE} [1]. Thus, in the chromate environment a potential window can be established in which the matrix material is passivated while the precipitate phase is rapidly dissolving. A study of aluminum alloy 2090 in the same environment has shown that stressed samples polarized within the potential window defined by the E_{br} values will fail rapidly, and samples polarized below E_{br} of T_1 yield no failures [1]. To determine if alloy X2095 obeys this criteria for rapid failure,

Table 1

Electrochemical Parameters of X2095 Determined by Potentiodynamic Polarization

0.6M NaCl, deaerated

Material	EOC (mV_{SCE})	E_{BR} (mV_{SCE})	I_{pass} (μA)
X2095-A	-970	-690	0.2
X2095-B	-950	-670	0.1
X2095-C	-950	-710	0.1

0.1M NaCl + 0.1M Na_2CrO_4, aerated

Material	EOC (mV_{SCE})	E_{BR} (mV_{SCE})	I_{pass} (μA)
X2095-A	-690	-60	2.0
X2095-B	-720	-230	3.0
X2095-C	-780	-210	3.0

constant load SCC experiments were performed in the inhibiting chloride/chromate environment at three applied potentials (-550, −475 and -450 mV_{SCE}), thus bracketing the E_{br} value of T_1. Samples of all three tempers polarized within the potential window of susceptibility failed within ten hours. Samples polarized below E_{br} of T_1 produced no failures after five days of testing.

To this point the criteria for rapid SCC failure of 2090 and X2095 has not been differentiated. Both materials are strengthened by T_1, but the distribution is much more homogeneous in the case of the X2095. Initial results indicate that the rapid SCC criterion is not sensitive to this difference in distribution.

Current and Future Work

Recent efforts have focused on performing variations of the TTF experiments described above. Although insufficient data have been collected to establish definite trends in material behavior, two exceptions to the criteria for rapid failure have been observed.

In one scenario the sample was polarized approximately 50 mV below E_{br} of T_1. After five days of stability (indicated by a low corrosion current), a mechanical flaw was

induced by scratching the sample with a glass rod. Subsequent sample failure occurred within five hours. This was the first sample observed to fail at a potential below E_{br} of T_1. One anodic dissolution based mechanism for Al-Li-Cu alloys relies on a rapidly corroding crack tip flanked by a passive matrix or crack wall [2]. Until now conditions for this mechanism were only achieved for samples polarized above E_{br} of T_1 in an inhibiting environment. However, experiments which have yielded failures outside of this condition suggest that cracks may propagate at potentials below the E_{br} of bulk T_1 or that the breakaway potential of T_1 is suppressed in the occluded crack environment. Further investigation of this phenomenon will require studies of T_1 and matrix dissolution in the solution chemistries of propagating SCC cracks. It may be possible to determine the crack chemistries through the use of ion chromatography (IC). If this can be accomplished, electrochemical studies of the phases in bulk form can be performed in the crevice environment, helping to refine the understanding of the SCC process.

In another TTF experimental variation, a sample was exposed to chloride/chromate solution under free corrosion conditions for 20 hours prior to being polarized within the window of susceptibility (-0.450 V_{SCE}). During the open circuit exposure, the open circuit potential of the sample dropped about 200 mV from approximately -0.800 to -0.600 V_{SCE}. This sample did not fail after five days of polarization. An identical sample that was at free corrosion conditions for less than five minutes failed within ten hours of being polarized to −0.450 V_{SCE}. In the case of the first sample, it is possible that depletion of surface T_1 occurred during the free corrosion period yielding a sample devoid of initiation sites for SCC. To determine if T_1 depletion occurs, samples at open circuit will be monitored for changes in polarization resistance using electrochemical impedance spectroscopy (EIS). Since T_1 is much more active than the surrounding matrix phase, a surface containing large amounts of T_1 will have a lower polarization resistance than a clean, passive matrix surface. Also it may be possible to monitor the test solution with IC to determine the stoichiometry of ions dissolving from the sample surface. If T_1 is the primary corroding phase, results would indicate an increase in Al, Li and perhaps Cu ions in the test solution until the majority of the T_1 has dissolved.

Other studies to be initiated include potentiostatic testing of unstressed materials to look at IGC and make comparisons with crack propagation in stressed materials. Evaluation of material microstructure will be performed using scanning electron microscopy. Crack

morphologies and fracture surfaces will be examined and documented. Real time observations of crack propagation will be attempted using an optical microscope in conjunction with video recording equipment. Material for future experimentation will include two compositional variations of X2095 (designated RX820, RX821) to be provided by Reynolds Metals Corporation, and an Al-4.0 Cu-1.0 Li alloy to be provided by NASA.

All of the mentioned experiments are designed to contribute towards the ultimate goal of this research: elucidating the correlations between microstructure, environment and localized corrosion in Al-Li-Cu alloys. The experiments to date and those proposed thus far are concentrated on the study of anodic dissolution mechanisms for SCC. Future goals of this work will also include studying the contribution of hydrogen to the localized corrosion of these alloys in conjunction with Task 9 by Scully and Smith.

References

1. R.G. Buchheit, F.D. Wall, G.E. Stoner, J.P. Moran, "The Effect of Applied Potential in Constant Load SCC Testing of 2090 in Cl^- and Cl^-/CrO_4^- Environments", ECS Fall meeting, Seattle, WA, Oct., 1990.

2. R.G. Buchheit, "Mechanisms of Localized Corrosion in Al-Li-Cu Alloy 2090", Ph.D. Dissertation, Univ. of Virginia, 1991.

Project 8 **The Effects of Zinc Additions on the Precipitation and Stress Corrosion Cracking Behavior of Alloy 8090**

Raymond J. Kilmer and G.E. Stoner

Objectives

The objectives of this PhD research are to document and characterize the effects that Zn additions have on the microstructure of alloy 8090 under different aging conditions and to correlate SCC behavioral changes with changes in alloy composition and microstructure. Emphasis will be placed on optimizing SCC behavior and alloy density.

Introduction

The four principle design criteria typically considered when developing or evaluating an aluminum alloy for aerospace application are strength, density, toughness and resistance to environmental fracture. As with most conventional aluminum aerospace alloys, Al-Li alloys may become susceptible to stress corrosion cracking (SCC). SCC is the phenomenon whereby an environmentally induced crack grows under the application of a static tensile stress. This stress may be residual or externally applied. There is general agreement that SCC occurs in aluminum alloys via a discontinuous process following two principle stages: initiation and propagation.

In the initiation stage, localized corrosion occurs either intergranularly or at a constituent particle forming a pit or notch in the material. An example of SCC initiation in alloy 2090 (Al-Li-Cu-Zr) was given in a recent paper by Buchheit, Moran and Stoner [1]. A stress concentration then develops at the base of the notch. Propagation involves two substages. Initially, local deformation occurs at the notch or crack tip which violates the integrity of the oxide film and the crack propagates along a grain or subgrain boundary. Propagation may be significantly aided by hydrogen embrittlement within or ahead of the crack tip in many alloys. Once the crack propagates a finite distance, Δa, newly exposed anodic material rapidly corrodes until reformation of a passive oxide or film occurs. These events are cyclic and increase in frequency as the stress intensity increases with increasing effective crack length. These processes occur until the critical crack length is achieved and

the component fails by tensile overload. Pure metals are generally considered immune to SCC, and in general, the SCC process is governed by alloy chemistry and alloy microstructure.

In commercial Al-Li-Cu-Mg-Zr alloys, SCC is generally associated with an anodic dissolution based process along or adjacent to grain and subgrain boundaries {2,3,4]. Zn additions to these alloys have been shown to result in materials of greatly improved SCC resistance most notably in 8090 and 8090-type alloys [5]. It also has been demonstrated that Zn additions can have a marked effect upon the systems' precipitation events [6,7]. The emphasis of this paper is focussed on the correlation of Zn content with the resultant microstructure, specifically precipitation during aging. Furthermore, the interrelation between specific microstructural changes and their possible effects on SCC, most notably SCC propagation, will be discussed.

Experimental

Four sheet alloys and four plate alloys were fabricated by Alcoa, having thicknesses of 2.5 mm and 43 mm respectively. The alloys were stretched to obtain a T3 condition and the alloys chemical compositions are listed in table 1.

Alloy	Product Form	Chemical Composition (wt-%)				
		Li	Cu	Mg	Zn	Zr
S1	Sheet	2.44	1.06	0.63	: : :	0.10
S2	Sheet	2.27	1.07	0.60	0.21	0.10
S3	Sheet	1.91	1.07	0.62	0.58	0.10
S4	Sheet	2.09	1.00	0.59	1.07	0.10
P1	Plate	2.53	1.22	0.67	1.36	0.12
P2	Plate	2.47	1.23	0.74	0.99	0.12
P3	Plate	2.54	1.23	0.49	1.00	0.12
P4	Plate	2.55	1.16	0.69	0.02	0.12

Table 1: Chemical compositions of the experimental alloys.

The alloys microstructures were studied employing TEM to assess the effect of alloy chemistry on precipitation during artificial aging. S-T tensile bars were machined from the plate alloys for time-to-failure (TTF) experiments (ASTM G49) in a 3.5 w/o NaCl alternate immersion environment (ASTM G44). Phase identification included Guinier phase analysis at Alcoa, TEM employing CBED and SAD analysis along with EDS capabilities.

Mechanical properties were evaluated at UVa and Alcoa, and included uniaxial tensile tests of S-T round tensile specimens and fracture toughness measurements were obtained on fatigue pre-cracked S-L compact tension specimens.

To determine the magnitude and character of misorientations of grain and subgrain boundaries, Kikuchi patterns on each side of the boundary were taken and analyzed.

Results and Discussion

In alloys P1-P4, coarse Cu, Mg and Zn rich precipitates were evident in the T3 condition along many grain and subgrain boundaries. Precipitation of this type was not seen to occur at the grain interiors in any of these alloys. With additional aging at 160°C, further precipitation was seen to occur along these boundaries resulting in a bimodal size distribution of boundary precipitates. δ' (Al_3Li) free zones occurred initially along boundaries occupied by the larger precipitates. The timing of the formation of this PFZ was not as critically dependent on boundary misorientation as on the size and distribution of the precipitates residing on the boundary. Although vacancy gradients can also lead to PFZ's this evidence would seem to indicate that the formation of the δ'-FZ's along these boundaries occurs primarily as a result of Li incorporation into the boundary precipitates. This change in the precipitate's chemical makeup may influence it's structure with aging. δ'-FZ's began to be evident around 10 hrs at 160°C and a typical PFZ in alloy P1 is shown in the micrograph included as Figure 1. The finer sized and later nucleated precipitates reside on boundaries not displaying a PFZ by 20 hrs at 160°C and are shown in Figures 2a. and 2b.

Guinier phase analysis was performed on all four sheet alloys and on plate alloys P1 and P4, the baseline 8090 employed as a control. To promote boundary precipitation, the alloys were solution heat treated at 540°C, air quenched and aged at 175°C for 36 hrs. The results indicate that the equilibrium phase, δ, is present in all the alloys but that the Zn additions appear to promote an increased volume fraction of the precipitate. Also of primary interest to this investigation was the presence of reflections characteristic of T_2 (Al_6Li_3Cu)

or T' (a phase, $Mg_{32}(Al,Cu,Zn)_{49}$ seen in low Zn/Mg content 7000 series alloys).

In alloy S1, CBED indicated the predominant presence of the icosahedral T_2 (5-fold symmetry) phase. However, in the alloys with Zn additions S2-S4 and P1-P3, EDS revealed the boundary precipitates to be rich in Mg, Cu and Zn while CBED revealed particles with a 4-fold symmetry suggesting that these particles were T' or some isomorphous variant to T'. Sodergren et. al. [8] also witnessed the formation of T' in their evaluation of the effect of Li in 7000 series alloys. The Zn and Mg contents of these alloys were much higher and the Cu contents somewhat less indicating that the phase field for T' is likely to be quite extensive. Gregson et. al. [7], in their evaluation of two Al-Li-Zn-Mg-Cu-Zr alloys reported the observance of η ($MgZn_2$) on grain and subgrain boundaries. None of the alloys studied in this investigation contained either η or η' in the aging periods and temperatures studied.

S-L fracture toughness (K_{IC}) values were obtained from all the plate alloys with the degree of degradation dependent on the Mg content. In the S-L orientation fracture occurs intergranularly and intersubgranularly in all the alloys and the occurrence of the coarse intermetallic phases on the boundary likely governs the K_{IC} values. As Mg content and solute supersaturation increase, the volume fraction of $Mg_{32}(Al,Cu,Zn)_{49}$ should also increase and the K_{IC} values decrease (all other factors being equal). This is the trend observed.

Alloy	Temper	Composition (wt-%)				K_{IC} (S-L) (MPa$\sqrt{m}$)	TYS (MPa)
		Li	Cu	Mg	Zn		
P1	UA*	2.53	1.22	0.67	1.36	14.1	287
P2	UA*	2.47	1.23	0.74	0.99	8.8	287
P3	UA*	2.54	1.23	0.49	1.00	20.1	278
P4	UA*	2.55	1.16	0.69	0.02	30.7	276

Table 2: K_{IC} values for plate alloys in underage temper.

(* indicates an SCC susceptible temper)

The results of the TTF tests are presented in Table 3. It is evident that Zn additions result in alloys with markedly improved lifetimes after heat treatments of 20 to 100 hrs at 160°C when compared with alloy P4, the baseline 8090 alloy. It should be noted, however, that these three plate alloys P1 to P3, are susceptible to SCC in markedly underaged tempers (1 to 5 hrs at 160°C). As such, some microstructural change or changes occur between the 5 and 20 hr tempers which results in improved SCC resistance. The microstructural state

was determined at 5 hrs, 10 hrs, 15 hrs and 20 hrs at 160°C for alloy P1, as it displayed the most promising combination of strength, toughness and SCC performance. From these

Alloy	Temper (hrs at 160°C)	Exposure Stress					
		138 MPa		207 MPa		276 MPa	
		F/N	Days	F/N	Days	F/N	Days
P1	1	3/3	2,2,3	3/3	2,2,2	N/A	
	5	2/3	2,3	3/3	1,1,2	N/A	
	20	0/3	- - -	0/3	- - -	N/A	
	40	0/3	- - -	0/3	- - -	N/A	
	60	0/3	- - -	N/A		0/3	- - -
	80	0/3	- - -	N/A		0/3	- - -
	100	0/3	- - -	N/A		1/3*	- - -
P2	1	2/3	3,10	3/3	2,2,2	N/A	
	5	3/3	1,1,2	3/3	1,1,2	N/A	
	20	0/3	- - -	2/3	2,3,9	N/A	
	40	0/3	- - -	0/3	- - -	N/A	
	60	0/3	- - -	N/A		0/3	- - -
	80	0/3	- - -	N/A		0/3	- - -
	100	0/3	- - -	N/A		0/3	- - -
P3	1	3/3	2,3,3	3/3	3,4,17	N/A	
	5	3/3	2,2,3	3/3	1,2,2	N/A	
	20	1/3	17	2/3	9,17	N/A	
	40	0/3	- - -	0/3	- - -	N/A	
	60	0/3	- - -	N/A		0/3	- - -
	80	0/3	- - -	N/A		0/3	- - -
	100	0/3	- - -	N/A		0/3	- - -
P4	1	3/3	4,5,17	3/3	4,6,7	N/A	
	5	3/3	3,3,5	3/3	1,2,3	N/A	
	20	2/3	3,4	3/3	2,2,2	N/A	
	40	2/3	3,5	3/3	3,3,4	N/A	
	60	1/3	4	N/A		3/3	- - -
	80	2/3	3,6	N/A		3/3	- - -
	100	3/3	2,2,3	N/A		3/3	- - -

Table 3. Time to failure results of alloys P1 to P4. (* Indicates sample fractured at threads.)

observations possible models will be examined to account for the improvement in SCC resistance and for the applicability of these models to these alloys.

One possible mechanism by which Zn additions may result in improved SCC resistance centers on their alteration of the electrochemical activity of the boundary phases. Zn additions clearly alter precipitation on the boundaries and the end result may be a decreased electrochemical difference between the boundaries and the grain interiors reducing the galvanic driving force for SCC. This identical concept of the lessening of the electrochemical differences was proposed by Gray et. al. [5] as a mechanism for improved SC resistance in their Al-Li-Cu-Mg-Zn-Zr alloys. However, their argument was that Zn additions promote increased S' (Al_2CuMg) precipitation in the grain interiors depleting them of copper and reducing the electrochemical driving force in this manner. S' was seen via HREM at approximately 13 hrs at 160°C and could be detected in SAD patterns by 15 hrs at 160°C in both Zn and non-Zn containing alloys. By the 20 hr temper, S' had precipitated copiously on dislocations introduced during the stretch in all alloys. The magnitude of the apparent differences in S' volume fraction at this aging condition between the two alloys did not seem to be so great as to be solely responsible for a profound difference in TTF lifetimes. Narrowing the aging time window between susceptible and unsusceptible tempers may provide more insight into the role S' and only a quantitative evaluation between alloys of like composition with and without Zn, will demonstrate Zn's influence on S'.

If boundary precipitation controls the magnitude and extent of SCC then the evidence that the Zn containing alloys are still highly susceptible to SCC in the 5 hr temper is significant. It would suggest that the electrochemical activity of the boundary phases change between the 5 and 20 hr aging treatments. This change could be accomplished in at least two distinct manners: the Cu, Mg and Zn solute ratios of the boundary phases could change possibly to include Li as evidenced by the δ'-FZ's, or the relative proportions of the different boundary phases (T_2, T', δ) could change imparting a new electrochemical character to the boundaries.

The increase in the volume fraction of δ with increasing Zn content may also contribute to improving the SCC resistance if Zn promotes δ precipitation between the 5 and 20 hr tempers. Previous research [10] on Al-Li binaries has demonstrated that the dissolution of δ may lead to crack tip blunting slowing crack growth. Further investigation is required and is underway.

Acknowledgements

This work was supported by a grant from NASA Langley Research Center under grant NAG-745-1-4, W.B. Lisagor and D.L. Dicus project monitors. It was cosponsored by Alcoa, Pittsburgh, PA. It was originally presented at the Al-Li VI conference and J.J. Witters of Alcoa was a co-author. Much thanks is extended to the significant contributions made by J. Casato, J. Liput, A. Smith, J. Newman, J. Moran and R. Rioja at Alcoa.

Recent Results

The above paper was presented at the Sixth Al-Li Conference in Garmish-Partenkirchen, West Germany, in October of 1991. Research continued on the four 8090 + Zn alloys and the focus of the research centered on better defining the aging condition where the transition from SCC susceptible to SCC resistance occurs. The aging "window" previously narrowed down this transition to occur between 5 and 20 hrs at 160°C. Alternate immersion TTF tests were performed on the alloys after aging 10 and 15 hrs at 160°C and the results are amended to include this data and are included as Table 4. From these results, it is apparent that alloy P1 had the earliest transition time with no failures at 138 MPa and 207 MPa (20 and 30 ksi) after 30 days. This is especially significant because S' (a possible contributor in defining SCC resistance) cannot be detected in SAD patterns until 15 hrs at 160°C or as an occasional tiny nuclei at 13 hrs at 160°C via HREM. S' is therefor not integrally responsible or necessary for improvement of SCC in these alloys. Current focus on the mechanism responsible is centered on boundary precipitation and its effect on SCC at 5 and 10 hrs at 160°C in alloy C200. This alloy will be focussed on because of its dramatic and clear cut change in SCC behavior with a short aging difference and because these two aging conditions are somewhat simplified, given the fact that S' hasn't precipitated.

Future Work

The bulk of the microstructural characterization of the 8090 + Zn alloys is now essentially complete and the transition "windows" (for aging at 160°C) defined. The next, and final phase of research will focus on the electrochemical differences between the SCC susceptible and SCC resistant tempers, specifically on alloy P1. A number of initial experiments will focus on the boundary precipitates' electrochemical activity (and the possible contribution of hydrogen) via:

* immersion of TEM foils in 3.5 w/o NaCl solution and examination of resultant attack
* hydrogen charging experiments looking at the relative susceptibility of hydrogen absorption at the SCC susceptible and SCC resistant tempers, and the effect on fracture energy.
* evaluation of the SCC behavior as a function of applied potential.

References

[1] R.G. Buchheit, Jr., G.E. Stoner: Corrosion, 46, (1990) 610.

[2] T.D. Burleigh: Corrosion, 47, 2 (1987) 89.

[3] A. Gray, N.J.H. Holroyd, W.S. Miller: "1st Int. SAMPE Conf.", SAMPE (1987) 339.

[4] R. Ricker, J. Finke, A. Vasudevan: Met Trans A, 22A (1991) 264.

[5] A. Gray, N.J.H. Holroyd, J. White: "Proc. of Fifth Int. Al-Li Conf.", (1989) 1175.

[6] R.J. Kilmer, G.E. Stoner: Scripta Met., 25 (1991) 243.

[7] P.J. Gregson, K. Dinsdale, S.J. Harris, B. Noble: Mat Sci and Tech., 3 (1987) 7.

[8] A. Sodergren, D.J. Lloyd: Acta Met., 36, 8 (1988) 2107.

[9] W.A. Cassada, G.J. Shiflet, S.J. Poon: Journal of Microscopy, 146, 3, (1987) 323.

[10] L. Christodoulou, L. Struble, J.R. Pickens: "Al-Li Alloys III", (1983) TMS 561.

Alloy	Temper (hrs at 160°C)	Exposure Stress					
		138 MPa		207 MPa		276 MPa	
		F/N	Days	F/N	Days	F/N	Days
P1	1	3/3	2,2,3	3/3	2,2,2	N/A	
	5	2/3	2,3	3/3	1,1,2	N/A	
	10	0/3	- - -	0/3	- - -	N/A	
	15	0/3	- - -	1/3*	- - -	N/A	
	20	0/3	- - -	0/3	- - -	N/A	
	40	0/3	- - -	0/3	- - -	N/A	
	60	0/3	- - -	N/A		0/3	- - -
	80	0/3	- - -	N/A		0/3	- - -
	100	0/3	- - -	N/A		1/3*	- - -
P2	1	2/3	3,10	3/3	2,2,2	N/A	
	5	3/3	1,1,2	3/3	1,1,2	N/A	
	10	3/3	1,1,5	3/3	1,2,5	N/A	
	15	1/3	2	1/3	1,1	N/A	
	20	0/3	- - -	2/3	2,3,9	N/A	
	40	0/3	- - -	0/3	- - -	N/A	
	60	0/3	- - -	N/A		0/3	- - -
	80	0/3	- - -	N/A		0/3	- - -
	100	0/3	- - -	N/A		0/3	- - -
P3	1	3/3	2,3,3	3/3	3,4,17	N/A	
	5	3/3	2,2,3	3/3	1,2,2	N/A	
	10	2/3	5,5	3/3	1,2,3	N/A	
	15	1/3	16	1/3	3	N/A	
	20	1/3	17	2/3	9,17	N/A	
	40	0/3	- - -	0/3	- - -	N/A	
	60	0/3	- - -	N/A		0/3	- - -
	80	0/3	- - -	N/A		0/3	- - -
	100	0/3	- - -	N/A		0/3	- - -
P4	1	3/3	4,5,17	3/3	4,6,7	N/A	
	5	3/3	3,3,5	3/3	1,2,3	N/A	
	10	2/3	4,11	2/3	1,5	N/A	
	15	1/3	5	3/3	1,2,3	N/A	
	20	2/3	3,4	3/3	2,2,2	N/A	
	40	2/3	3,5	3/3	3,3,4	N/A	
	60	1/3	4	N/A		3/3	- - -
	80	2/3	3,6	N/A		3/3	- - -
	100	3/3	2,2,3	N/A		3/3	- - -

Table 4. Appended time to failure results of alloys P1-P4.
(* Indicates sample fractured at threads.)

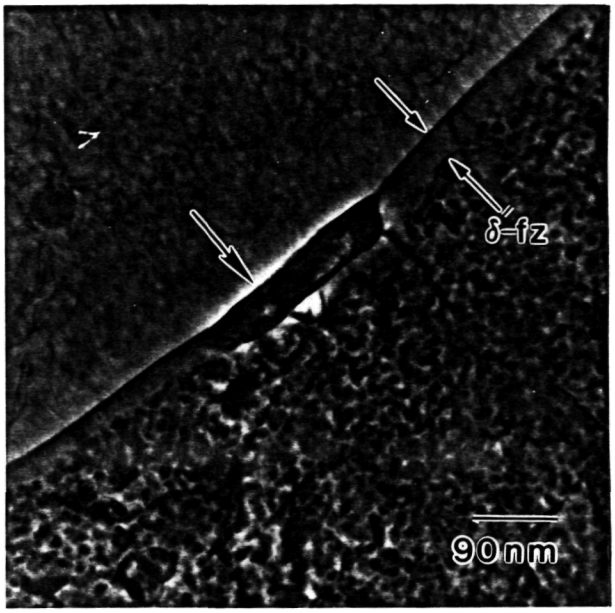

Fig. 1: TEM micrograph of coarse Cu, Mg and Zn containing boundary phase. The half width of the δ'-FZ is arrowed with the precipitate.

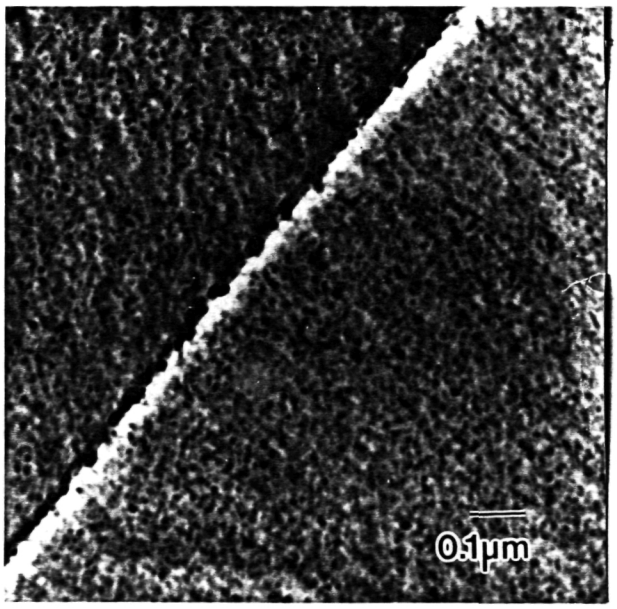

Fig. 2a: TEM micrograph of T' phase on boundary in P1. Off [001].

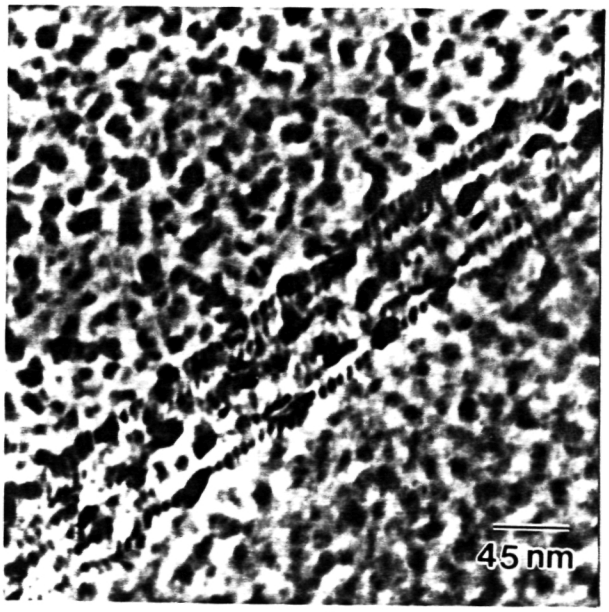

Fig 2b: T' phase of 2a inclined to another [001]

Project 9 **Hydrogen Interactions in Aluminum-Lithium Alloy 2090 and Selected Complimentary Model Alloys**

S.W. Smith and J.R. Scully

Objective

The objective of this work is to develop a fundamental understanding of the effects of dissolved and trapped hydrogen on the mechanical properties of selected Al-Li-Cu-X alloys. We propose to: (a) distinguish hydrogen induced EAC from aqueous dissolution controlled processes, (b) correlate hydrogen induced EAC with mobile and trapped hydrogen concentrations and (c) identify significant trap sites and hydrides (if any) through the utilization of model alloys and phases.

Background and Problem Statement

Al-Li-Cu-X alloys are being studied for use in aerospace applications, due to the improved stiffness and strength to weight ratio in comparison to conventional aluminum alloys. Several research projects have been conducted to prove these alloys do suffer from environmentally assisted cracking (EAC).[1] Although it is easy to demonstrate thermodynamically that hydrogen is produced at the crack tip in aluminum lithium alloys, when exposed to moist air and many aqueous solutions, the role hydrogen plays in the embrittlement of aluminum lithium alloys has not been clearly distinguished from aqueous dissolution effects. This study will consist of three major elements. These are: (1) distinguish hydrogen induced EAC from aqueous dissolution controlled EAC, (2) correlate hydrogen induced EAC with mobile and trapped hydrogen concentrations, and (3) identify significant trap sites and hydride phases (if any) through utilization of model alloys and phases. The intended approach and current program status is reviewed.

Technical Approach

Throughout the past quarter, research has been centered around: (i) cathodic charging of alloys in order to produce hydrogen levels which cause mechanical damage, and (ii) evaluating hydrogen production rates on a bare metal surface of these alloys during the film

rupture process in aqueous environments. Ultimately we seek to cathodically charge alloys with atomic hydrogen to levels representative of those achieved at the crack tip in aqueous solutions without the competing effects of dissolution.

The experimental work performed over the past few months has involved two major sub-tasks: (i) study of mechanical properties with the addition of absorbed hydrogen introduced by cathodic charging, and (ii) examination of hydrogen production at a crack tip for Al-Li-Cu-X alloys after mechanical destabilization of the passive film. This is simulated by performing scratch tests on model alloys.

Mechanical Properties Mechanical testing of Al alloys in aqueous solutions can actually result in creating more questions than producing answers, if it is not conducted properly. The first obstacle encountered is the native oxide on these alloys which acts as a barrier to hydrogen diffusion. The oxide makes it difficult to uniformly charge these materials. The second issue is to separate the effects of aqueous dissolution from those of hydrogen assisted cracking, in order to truly delineate the role absorbed hydrogen plays in environmentally assisted cracking. We have tried to resolve both of these issues by charging specimens in two different ways. The first method is to galvanostatically apply a cathodic current to these specimens in 0.1 M Na_2CrO_4. Since the chromate minimizes anodic dissolution, there has been some success using this method in the past.[2] However, charging in chromate may result in the caustic attack of the specimen surface. For this reason it is necessary to remove these specimens from the environment and repolish the surfaces before evaluating the mechanical properties. The repolish eliminates any stress concentrations due to aqueous dissolution.

The second charging method accomplishes both removal of the oxide and avoidance of corrosion. These goals are achieved by deposition of palladium onto the specimen. Oxide removal is accomplished by sputter etching the surface of the specimen to remove all of the oxide. Corrosion resistance is achieved by sputtering a thin film of palladium onto the "clean" surface of the specimen. This method was also found to have limitations. The total amount of hydrogen that could be introduced into these alloys was limited by the adhesion of the palladium coating. During extended charging of the coated samples absorbed hydrogen in the palladium results in a volume expansion of the film, leading to spalling of the film. For this reason the specimens that have been coated with palladium were removed from the charging environment before spalling of the film occurred.

In addition to surface preparation methods which facilitate hydrogen uptake, two other experimental variables have been examined for these tests. The first one being storage time of the specimen before conducting mechanical tests. Increasing storage time will allow for volume diffusion of hydrogen to the interior of the tensile specimens. A theoretical concentration profile is depicted in Figure 1. These calculations were performed using the method outlined by Meron and coworkers.[3] A diffusion coefficient of 1 x 10^{-9} cm^2 sec^{-1}, which is approximately the value that is expected for the volume diffusion of hydrogen in Al-Li-Cu-X alloys, was assumed. This figure shows the limitation of the charging procedure used to date. The profiles for storage times of 24 hours and 2 weeks shows that it is possible to obtain higher levels of hydrogen in the interior portion of the specimens, however, the total amount of hydrogen remains the same, assuming that outgassing during storage is minimized. The curve showing the highest level of hydrogen in the sample is for a total charging time of two weeks, which is a condition we have not attempted to date. Since nickel does not experience as large a volume expansion with hydrogen additions as that seen in palladium, it is possible to obtain such a profile by sputter deposition of nickel onto the

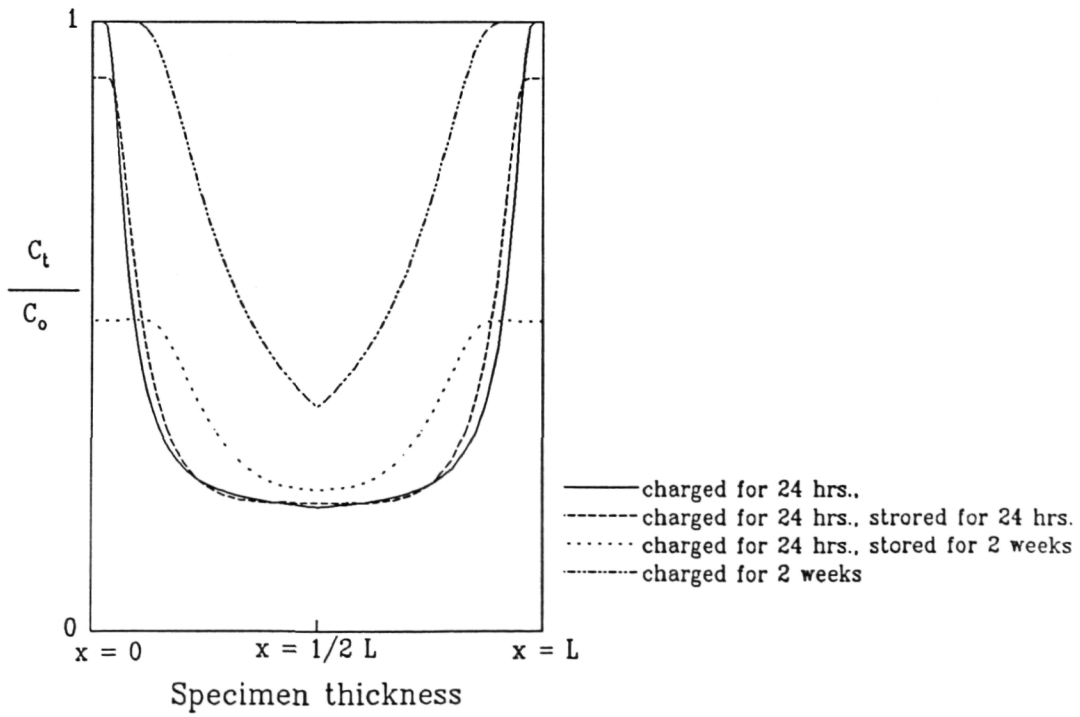

Figure 1. Theoretical hydrogen concentration profile for various charging conditions. Diffusion coefficient of 1 x 10^{-9} cm^2 sec^{-1} and a specimen thickness of 0.228 cm was used.

specimens. The use of nickel coatings on aluminum foils has been shown to be useful by Latanision and co-workers.[4] In addition to varying storage time we are looking at the effect of applied load during charging. This is accomplished by placing a tensile bar in an ASTM G49 constant extension test jig, and then charging. The specimen remains in the load jig during storage.

Hydrogen Production Scratching electrode tests were conducted to try to gain some insight into the hydrogen reaction rates and fugacities present at a crack tip during film rupture. Several model alloys were prepared by metallographic mounting. Polished metal surfaces are then coated with an insulating nonreactive material (high vacuum grease or sputter deposited SiO_2). The specimen is then placed into the test solution and a diamond scribe is used to scratch the surface. The scratch exposes bare metal to the solution, which is equivalent to the conditions experienced when an oxide film is ruptured at a crack tip. Upon scratching the surface, the potential transient was measured using a high speed data logger. The potential monitored is only for the electrochemical reactions occurring on the exposed metal. The minimum potential reached can be directly related to the maximum hydrogen fugacity that can be obtained for a material within the environment being used.[5] The fugacity for the hydrogen evolution reaction in aqueous solutions can be determined by solving for the Nernst equation:[6]

$$\frac{\Delta E}{30mV} = -\log(f_{H_2}) \qquad (1)$$

Where ΔE is the measured potential minus the reversible potential, and the fugacity is given in units of atmospheres. These tests have been done in several environments, varying the pH and ionic species. Several tests are being done in $AlCl_3$ to simulate the chemistry present at a crack tip. The hydrogen fugacity present during film rupture is often assumed to be the same as that present for a passive metal with an oxide in a simulated crack solution, However, we have shown that the potential of the bare material, prior to repassivation, is significantly lower than that with an intact oxide. This information justifies the high hydrogen concentrations which may be achieved with palladium or nickel coated Al alloy samples. Ideally we seek to select a hydrogen concentration which is representative of that present at the crack tip.

Summary of Important Conclusions

Mechanical Testing Since the hydrogen embrittlement of 7075-T6 is well documented,[1,7] initial mechanical testing has been performed on specimens of this alloy in the LT orientation. 7075-T6 can then be directly compared to 2090, under conditions known to cause hydrogen interactions. The mechanical testing of these specimens for various charging condition is shown in Figure 2. This work clearly shows there is an adverse affect on the mechanical properties of 7075-T6 from cathodic charging. These results indicate significant hydrogen ingress has been achieved by utilizing the charging procedures described above. Since these test were conducted in air, they are totally independent of anodic dissolution. The results summarized in Table 1 express the degree of embrittlement by the loss seen in two different mechanical properties, fracture energy and strain to failure. The fracture energy is calculated as the area under the stress stain curve, and the strain to failure is the engineering strain present at final fracture. In addition to the results for 7075-T6, Table 1 shows results to date for 2090-T3. The reduction in mechanical properties for 2090-

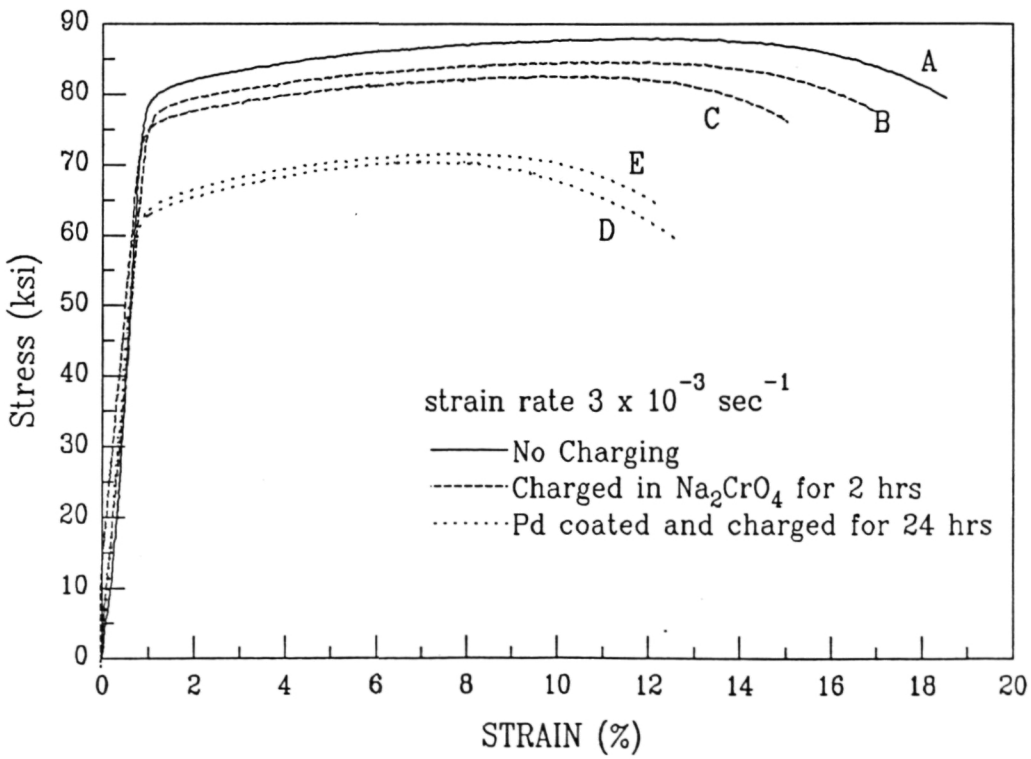

Figure 2. Stress strain curves for 7075-T6 LT specimens tested in lab air. A represents an uncharged specimen, C is stored for 24 hrs., E is stored for 48 hrs. and B&D are stored for 2 weeks.

T3 are not statistically significant and one can not conclude that any hydrogen damage has occurred for this alloy under this condition. However, the equivalent test for 7075-T6 also resulted in only slight damage. More significant damage was observed for palladium coated samples charged for longer time periods. This suggests that mechanical damage might be observed for 2090 after longer time periods. In order to determine if hydrogen does play a role, additional specimens under various charging conditions will be tested.

Table 1: Results from mechanical testing in lab air

Specimen History	FE (MJ/m^3)	FE loss (%)	ϵ_f (%)	ϵ_f loss (%)
7075-T6,LT in air	113.8	-0-	18.43	-0-
7075-T6,LT Pd coated charged 24 hrs stored 2 days	56.67	50.19	12.31	33.21
7075-T6,LT Pd coated charged 24 hrs stored 2 weeks	61.64	45.9	12.67	31.25
7075-T6,LT charged 2hrs in Na_2CrO_4 stored 1 day	94.94	16.60	16.89	8.36
7075-T6,LT charged 2 hrs in Na_2CrO_4 stored 2 weeks	85.56	24.85	15.19	17.58
7075-T6,LT charged 2hrs in Na_2CrO_4 loaded to 70% σ_y stored 2 weeks	94.73	16.82	17.22	6.57
2090-T3,LT in air	44.68	-0-	13.02	-0-
2090-T3,LT charged 2hrs in Na_2CrO_4 stored 1 day	42.82	4.18	12.80	1.69

At first glance some of the information presented in Table 1 appears to be contradictory. The data for 7075-T6 charged in 0.1 N NaOH with a palladium coating show that a 2 week storage time results in no additional degradation, if not actual improvement in the mechanical properties. However, when charging is performed in 0.1 M Na_2CrO_4 the mechanical properties become worse when stored for two weeks, although the chromate never produces results as severe as those observed for palladium coated samples. There are two possible explanations for this behavior. The first reason may be related to the fact that

specimens charged in Na_2CrO_4 must be repolished before testing. An average of 0.01 inch is removed from each side. As shown in Figure 1 the metal layer removed from a specimen stored for 1 day will contain a greater percentage of the absorbed hydrogen than the same metal layer removed from a specimen stored for 2 weeks. The second possible explanation for these results is that some hydrogen outgassing may occur upon storage. In the case of the samples charged in Na_2CrO_4 the oxide minimizes the amount of hydrogen that can escape from the material. For palladium coated specimens charged in NaOH, the palladium coating may act as a high mobility path for hydrogen to diffuse from the specimen during storage, which may result in the reversibility observed after storage. The effect of possible outgassing is not shown in the concentration profiles of Figure 1. The degree of outgassing will be evaluated in the next quarter by doing hydrogen analysis using thermal desorption spectroscopy (TDS) and a modified Devanathan-Stachurski permeation measurement, as outlined in the previous progress report. These issues may also be surmounted by continuously charging for two weeks with nickel coated samples to obtain more uniform hydrogen profiles.

Hydrogen Production The results of scratch tests performed in 0.5 M Na_2SO_4 buffered to different pH's are shown in Figure 3. This information clearly shows that the partial pressures of hydrogen obtained within the crack tip during film rupture can be several orders of magnitude higher than if the oxide remains undamaged. Additional scratch tests were conducted in a simulated crack chemistry of 0.25 M $AlCl_3$, these results are summarized in Table 2. Once again it is seen that the increase in hydrogen partial pressure is several orders of magnitude.

Table 2: Results from scratch test in 0.25 M $AlCl_3$, E_r = -0.359 V vs. SCE

Material	E_{oc} (V vs. SCE)	P_{H2} (atm)	E_{min} (V vs. SCE)	P_{H2} (atm)
Al - 99.999%	-1.129	1.7×10^{12}	-1.567	3.4×10^{19}
2090 SHT	-0.670	3.8×10^{4}	-1.728	1.6×10^{22}
Al - 3 Li SHT	-0.848	3.5×10^{7}	-1.413	9.3×10^{16}
Al - 3 Cu SHT	-0.992 *	8.9×10^{9}	-1.738 *	2.4×10^{22}

* These values are for a single data point, all other values are the average of three data points.

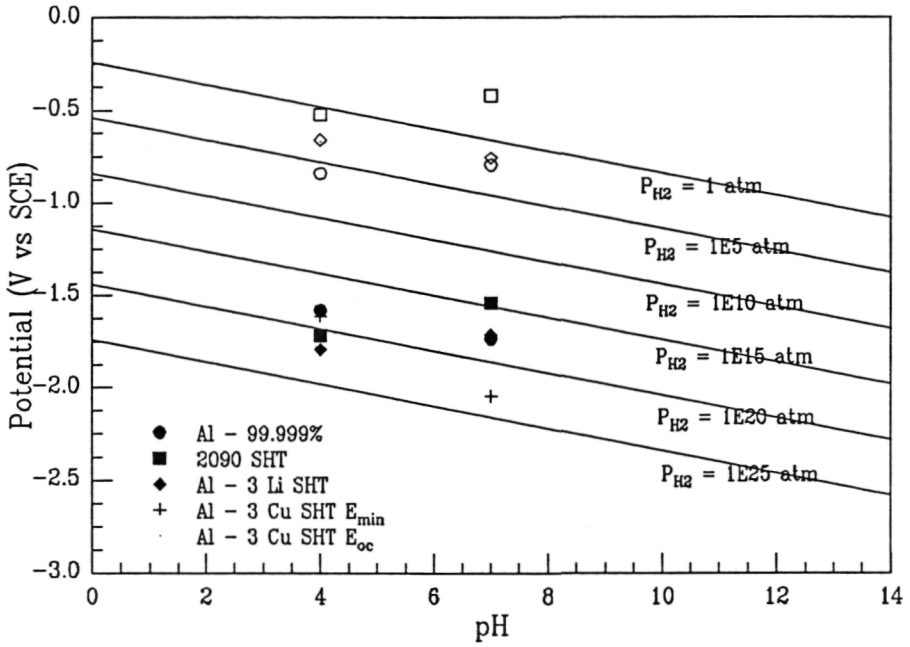

Figure 3. Hydrogen partial pressures for scratched electrode test in 0.5 M Na_2SO_4. ●, ■, ♦, and + are E_{min} after scratching. ○, □, ◇, and · are E_{oc} measurements.

Future Work

The anticipated work for the next reporting period is to continue along the methods outlined in this report and to integrate the analytical methods detailed in the previous report. The outline for this work is as follows:

- oo Additional mechanical testing of 2090-T3 and 2090-T6 using a nickel coating to aid in cathodic charging.
- oo Fractographic analysis to aid in the determination of fracture mode present in charged specimens.
- oo Assemble TDS system and optimize analysis procedure for Al-Li-Cu-X alloys and model alloys.
- oo Use TDS to determine how atomic hydrogen is incorporated in Al-Li-Cu-X alloys and significant constituent phases.

- oo Perform permeation measurements to determine hydrogen diffusion rates in aluminum and selected alloys.
- oo Perform additional scratch tests varying the simulated crack chemistry. Tests using T_2 (Al_6Li_3Cu) will also be run.
- oo Perform potentiostatic scratch tests, cathodic and anodic to the E_{min} values already determined. This information can be used to determine Evans diagrams for dissolution and the production of hydrogen on bare alloys, thereby, making it possible to calculate dissolution rates and hydrogen evolution reaction kinetics.

References

1. T.D. Burleigh, Corrosion **[47]**, 2 (1991): pp. 89-98.

2. T.F. Klimowicz and R.M. Latanision, Met. Trans. A, Vol.9A, (1978): pp. 597-599.

3. M. Meron, et al., Metal Progress, (1981): pp. 52-54.

4. C. Younchang, Y. Heyun, and R.M. Latanision, in Hydrogen and Materials, eds. P. Azou and C. Nanping, (1988): pp. 114-115.

5. R.C. Newman, in Corrosion Chemistry within Pits, Crevices and Cracks, ed. A. Turnbull, (1987): pp. 317-356.

6. E. Gileadi, E. Kirowa-Eisner and J.Penciner, Interfacial Electrochemistry - An Experimental Approach, Addison Wesley (1975).

7. N.J.H. Holroyd, in EICM Proceedings, pp. 311-343.

BACK

Project 10 **Investigation of the Effect of Thermal Treatment on the Mechanical Properties of Ti-1100/SCS-6 Composites**

Douglas B. Gundel and F.E. Wawner

Objective

The objective of this study is to investigate the influence of thermal exposure, both isothermal and cyclic, on the microstructure, mechanical properties, and fracture characteristics of Ti-1100/SCS-6 fiber composites.

Approach

The Ti-1100/SCS-6 composites evaluated in this study will be fabricated at NASA Langley Research Center. These materials will be subjected to thermal exposure at UVa and evaluated for microstructural changes, tensile properties in longitudinal and transverse directions, and fracture characteristics. Thermal cycling experiments will include both low to high temperature and ambient to cryogenic temperatures. Scanning and transmission electron microscopy will be utilized to delineate microstructure and any associated changes with environmental exposure. It is anticipated that an upper practical temperature limit will be defined for utilization of this composite system. The influence of selected diffusion barrier-compliant layer coatings on the reinforcing fibers and on localized matrix regions will be correlated with composite properties. Fracture analysis will be conducted by SEM to relate interface and microstructure contribution to the failure process.

The specific research plan has been outlined previously [1].

Research Progress

Thermal Cycling: The apparatus used to thermally cycle the samples has been described previously [2]. Tensile samples of Ti-1100/SCS-6 composite (4-ply fiber), both longitudinal and transverse, and Ti-1100 matrix (4-ply) were cut prior to the exposure (0.25 by 3.5 inches). Thus far all cycling has been done in argon or air from 150°C to 700 or 800°C for 500 cycles. The general shape of the thermal cycle has been reported [2], but the times required for a full cycle varied depending on the thermal mass in the specimen container of the cycler. For example, bare samples cycled in air required 3.2 minutes for

a full cycle, while the same number of samples encapsulated in argon-filled quartz tubes required 5.5 minutes.

The results of the cycling on the matrix samples are presented in Table 1, and it is apparent that there was no appreciable degradation of tensile properties as a result of the exposures.

The effect of thermal cycling on the tensile properties of longitudinal composite samples is given in Table 2. Cycling in air up to 700°C and argon cycling up to 800°C did not significantly degrade the properties, but cycling in air up to 800°C was detrimental.

One of the salient features of the fracture surfaces of all of the samples (even as-fabricated) was a region of flat fracture around the edge (see Fig. 1). This region is thought to be more brittle than the bulk matrix because of its flat, featureless, cleavage-like appearance and the fact that it was often observed to contain cracks. The thickness of the layer grew as a result of cycling in air up to 800°C and stayed approximately the same size for the other exposures. As described previously [2], when any of the samples were bent over a mandrel to a tensile strain of 0.8% cracks were found perpendicular to the direction of strain. The initially present, as-fabricated layer (about 20 μm thick) has been attributed to the release agent (boron nitride) used to keep the sample from bonding to the platens of the vacuum hot-press during fabrication. It should be noted that the all of the samples used to this point had this subsurface layer, but the most recently received (untested) material has been processed to remove this layer.

A study was undertaken to determine the effect of this layer on the tensile properties of cycled longitudinal composites. Some samples were mechanically polished to remove about 50 μm of matrix from the faces of the composite (the composite was then about 100 μm thinner). Three of these samples were encapsulated in argon-filled quartz tubes and three others were placed in open-ended quartz tubes for air exposure. Three unpolished samples were similarly placed in open-ended quartz tubes. The samples were then cycled from 150 to 800°C 500 times using 8.7 minute cycles, and then tensile tested. The results are given in Table 3. The argon exposed samples showed no loss in tensile properties and no brittle subsurface region was found on these samples (see Figure 2). The air-exposed samples all exhibited a strength loss following cycling. The average strength of the polished samples was slightly higher than the unpolished ones but this may simply be due to the limited number of samples studied. It should be noted that these strengths are slightly less than those

reported in Table 2 presumably because of the longer cycle time (longer exposure to high temperatures). From this data it has been concluded that the initial brittle subsurface layer may have a small effect on the post-cycling tensile properties in longitudinal samples, but the damage accumulated during thermal cycling in air is due primarily to sample-environment interactions.

The fracture surfaces of the longitudinal samples cycled to 800°C in air that were referred to in Table 2 were studied to help determine the cause of the lower strength and modulus. The areas most damaged by the cycling appeared to be near the cut edges of the sample (see Figure 3). There are at least four features on this micrograph that are the result of specimen-environment interaction and may explain its lower strength. The most prominent features are regions where the matrix is flat (A) and presumably more brittle than the normal regions of ductile rupture closer to the middle of the sample (B). Also, the matrix tends to debond from the fiber in regions where there is a great deal of matrix embrittlement (C). In some cases (only to a limited extent in this micrograph) a delineation of the diffusion-bond line appears (D) and the original matrix plies sometimes separate. This indicates that this area (not visible on fracture surfaces of as-fabricated or argon-cycled samples) may be a weak spot in these materials after cyclic thermal exposure in air.

Another important result of thermal cycling can be seen in Figure 3. At (E) there is an area of flat fracture that in some places is covered by a rough scale. With the use of a stereomicroscope this scale can be seen clearly and is primarily located in spots around the perimeter of the sample. It appears dull gray as opposed to the shiny flat fracture region that covers the rest of the perimeter. This indicates that cracks enter the sample from the surface during cycling and their surfaces become coated with the scale (most likely titanium oxide). In order to view one of these cracks a cycled composite was mounted as shown in Figure 4. There is a crack present that enters the composite from the cut edge and extends to the first fiber inside the composite (the front face was polished down to the first fiber layer).

Embrittlement of the matrix, fiber-matrix debonding, matrix ply separation, and cracking of the matrix all seem to be the result of matrix-environment interactions and may be solely responsible for the strength loss of the composite. The effect of the exposure on the fibers of the composite has not yet been assessed, but isothermal exposure of SCS-6 fibers in air at 800°C up to 300 hours did not cause a significant strength loss [3]. The matrix alone is not affected by the thermal cycling (Table 1), and neither are the argon-

encapsulated samples, thereby leading to the conclusion that the environment interacts with the composite in a unique and detrimental manner during the exposure. Two explanations for this behavior are suggested: 1) The coefficient of thermal expansion (CTE) mismatch between the fiber and the matrix gives rise to stresses in the matrix that, combined with the embrittling nature of air at high temperatures [4], lead to enhanced matrix damage (as suggested by Smith et al. [5] in the Ti-14Al-21Nb/SCS-6 system); and 2) The fiber-matrix interface provides a fast path for diffusion of matrix-embrittling species from the air. For (1) crack growth is envisioned occurring by embrittlement of the matrix ahead of the crack during the high temperature portion of the exposure, and the subsequent extension of the crack through the embrittled region during cooling when the tensile stresses in the matrix are expected to be increasing. The evidence for the occurrence of (2) is the flat fracture of the matrix surrounding fibers that have direct contact with the environment (see [2]). The most direct solutions to these problems are to lower the temperature of the exposure, or coat the sample with an oxidation-resistant layer.

Tensile samples in the transverse orientation were also cycled and tested and the results are given in Table 4. The composite is more sensitive to thermal cycling in the transverse direction than the longitudinal samples with a 70% reduction in strength for cycling to 800°C in air. This is not surprising since the transverse tensile properties are dominated by the matrix and the interface, and cycling in air was found to be detrimental to the matrix of the longitudinal samples. As explained previously [2], the fracture surfaces of the samples cycled in air to 800°C revealed that the matrix between the fibers fractured to yield a flat surface, while the matrix in the as-fabricated sampled failed solely by dimpled rupture. This result is most probably due to the many fibers intersecting the surface acting as conduits for embrittling species from the air to enter the sample (mechanism (2) above). The extent of damage to the fiber-matrix interface in this case is not known, but it may play a role in the overall property degradation.

Isothermal Exposure: From the recorded temperature versus time of the thermal cycles of the specimens exposed in air to 800°C, an equivalent isothermal exposure was calculated. The calculation was based on finding the temperature necessary to expose the sample for the same length of time and yield the same diffusion distance. This was done by using diffusivity data of oxygen and nitrogen in titanium [6] to convert the temperature versus time data to diffusivity versus time. The area under this curve was then used to

calculate the equivalent diffusivity, hence the equivalent temperature necessary. To simulate the thermal exposure of the 500 thermal cycles (3.2 minute duration) a temperature of 735°C for 26.5 hours was used.

The results of the exposures are given in Tables 1, 2, and 4 for the matrix, longitudinal composite, and the transverse composite, respectively. The exposure did not significantly effect the matrix or the longitudinal composite, but the transverse properties were slightly degraded. The only noticeable difference between as-fabricated and isothermally exposed longitudinal fracture surfaces was a narrow region of flat matrix fracture surrounding the fibers that were in direct contact with the surface (see Figure 5). The lower strength of the transverse samples is most probably due to embrittlement of the matrix and degradation of the fiber-matrix interface. Further investigations of isothermal exposure are necessary, however, to supplement this work.

Conclusions

1. Thermal cycling in argon had no significant effect on the tensile properties of the composite or matrix.

2. Thermal cycling in air up to 700°C had little effect on composite tensile strength, but cycling in air to 800°C caused appreciable degradation in both the longitudinal and transverse orientations.

3. The effect of the initial, brittle subsurface layer on the tensile properties of the composite is not known, but it does not contribute greatly to strength loss incurred during cycling.

4. Cycling in air to 800°C caused considerable damage to the composite including matrix embrittlement, environmental-assisted matrix cracking, fiber-matrix debonding, and matrix ply separation.

5. The isothermal exposure used to simulate the thermal exposure of the cycling did not degrade the properties as severely as thermal cycling.

Future Work

1. Further investigation of the nature of the composite-air interaction and determination of the temperature range where it becomes important.

2. Use the recently received samples that do not have the brittle surface layer to study the effect of thermal cycling.

3. Study the effects of long-term, moderate-temperature, isothermal and cyclic exposures in air on the properties and microstructure of the composites.

References

1. F.E. Wawner, D.B. Gundel, in **NASA-UVa Light Aerospace Alloy and Structures Technology Program**, Proposal No. MS-NASA/LaRC-5219-92, pp. 92-100, October, 1991.

2. D.B. Gundel, F.E. Wawner, in **NASA-UVa Light Aerospace Alloy and Structures Technology Program**, UVa Report No. UVA/528266/MS91/108, July, 1991.

3. D.B. Gundel, M.L. Gambone, F.E. Wawner, unpublished research.

4. C.E. Shamblen, T.K. Redden, "Air Contamination and Embrittlement of Titanium Alloys," in **The Science, Technology and Application of Titanium**, Eds. R.I. Jaffee and N.E. Promisel, Pergamon Press, New York (1970).

5. W.C. Revelos, P.R. Smith, "Effect of Environment on the Thermal Fatigue Response of a Ti-24Al-11Nb/SCS-6 Composite," in **Titanium Aluminide Composite Workshop Proceedings**, WL-TR-91-4020 (1991).

6. H. Conrad, "Effect of Interstitial Solutes on the Strength and Ductility of Titanium," in **Prog. in Materials Science**, Vol. 26, pp. 123-403, Pergamon Press, New York (1981).

Table 1. Matrix Tensile Tests

	As Fab	Isothermal Exposure	150-700C 500X Air	150-800C 500X Air	150-800C 500X Argon
Modulus (GPa)	112	109	107	103	113
UTS (MPa)	1023	1000	1038	910	982

Table 2. Longitudinal Tensile Tests

	As Fab	Isothermal Exposure	150-700C 500X Air	150-800C 500X Air	150-800C 500X Argon
Modulus (GPa)	186	189	183	163	189
UTS (MPa)	1496	1417	1420	1083	1682

Table 3. Longitudinal Tensile Tests
Polished versus Unpolished
Cycled 150 to 800°C 500X

	Argon (Polished)	Air (Polished)	Air (Unpolished)
Modulus (GPa)	192	162	158
UTS (MPa)	1390	902	772

Table 4. Matrix Tensile Tests

	As Fab	Isothermal Exposure	150-700C 500X Air	150-800C 500X Air	150-800C 500X Argon
Modulus (GPa)	121	73	92	68	103
UTS (MPa)	467	262	383	142	459

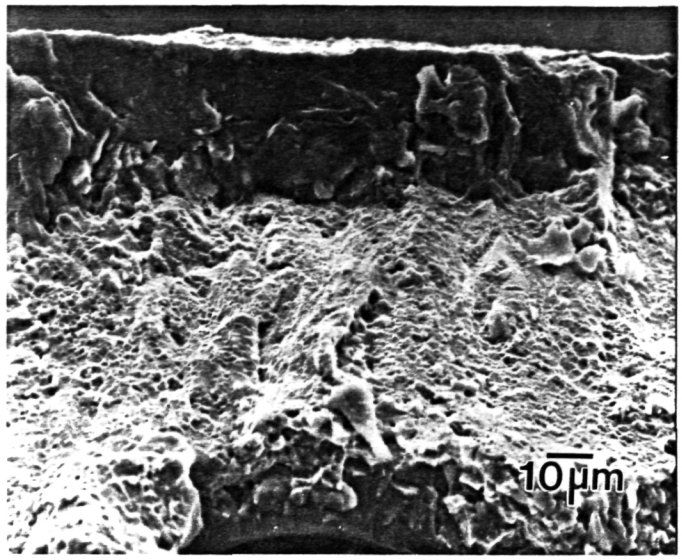

Figure 1. Flat fracture area of matrix under the surface of as-fabricated composite fracture surface.

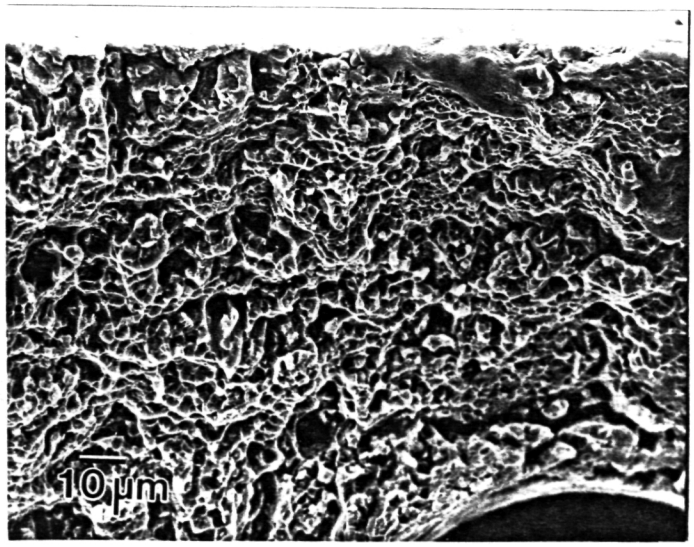

Figure 2. Embrittled subsurface layer not present on fracture surface of polished sample cycled in argon to 800°C.

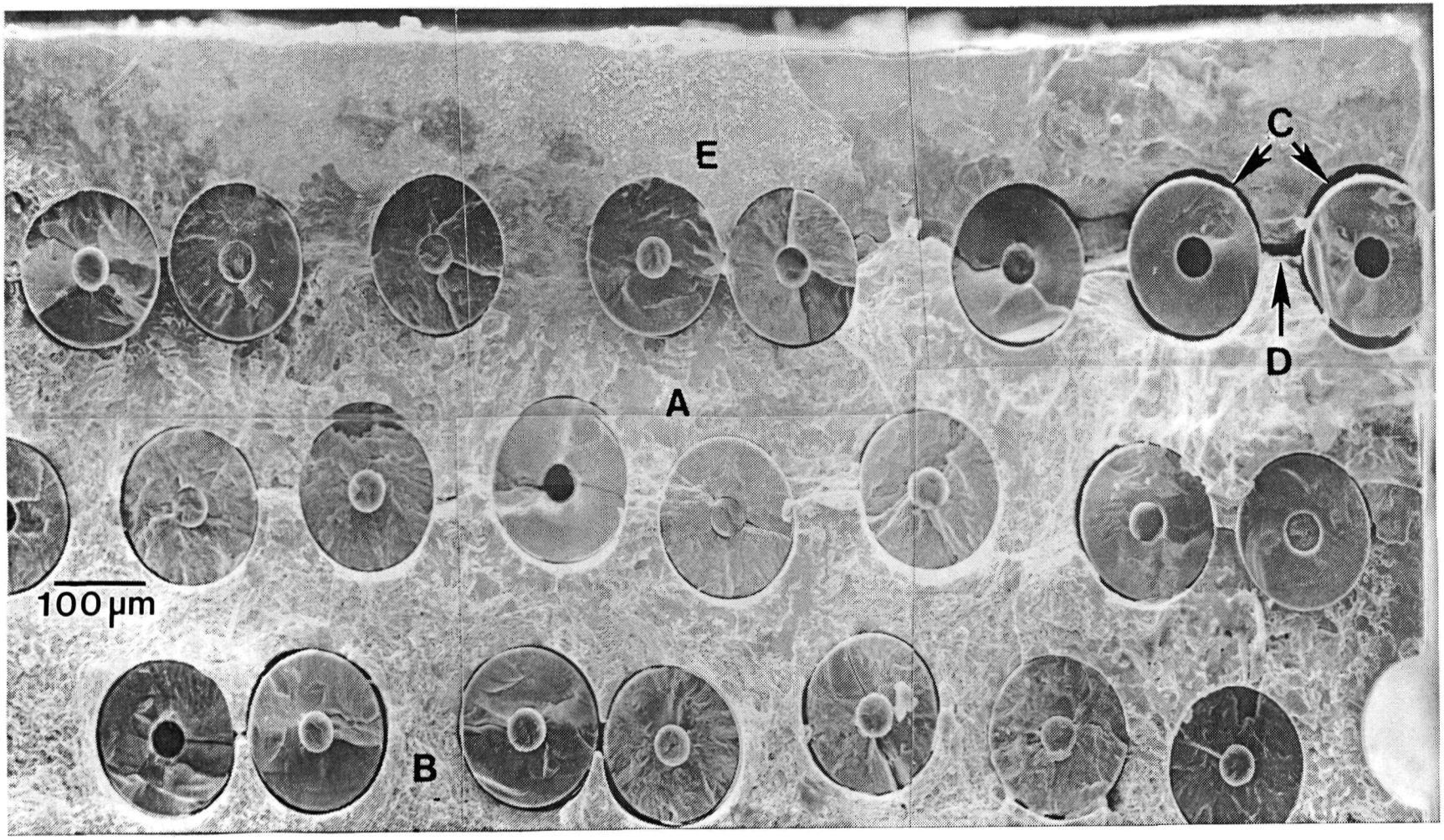

Figure 3. Corner of fracture surface of sample cycled in air to 800°C showing: A) Flat fracture regions, B) Dimpled rupture, C) Fiber-matrix debonding, D) Matrix ply delamination, and E) Scale on surface.

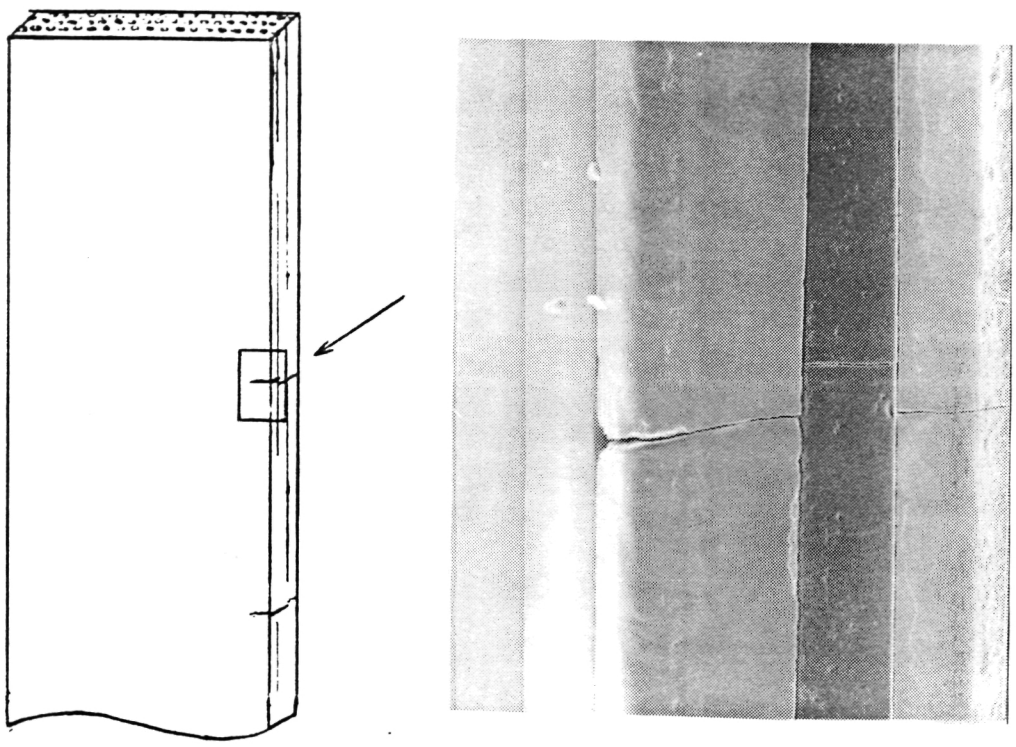

Figure 4. Crack entering the edge of a sample cycled in air to 800°C.

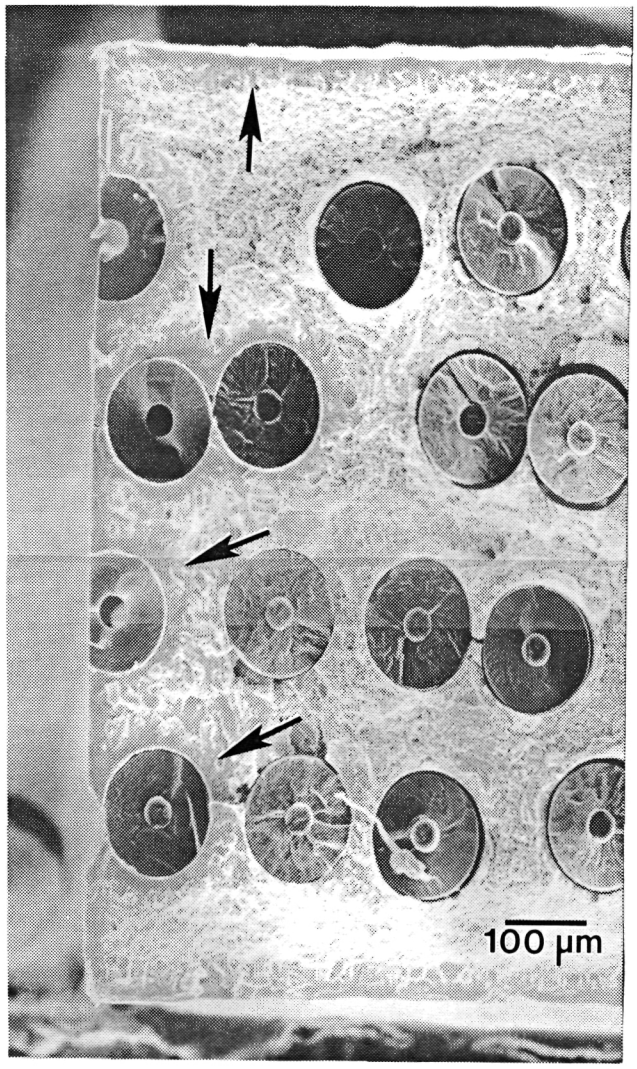

Figure 5. Edge of isothermally exposed sample. Arrows denote regions around fibers where the matrix has been embrittled by the environment.

Project 11 **Quantitative Characterization of the Spatial Distribution of Particles in Materials: Application to Materials Processing**

J.B. Parse and J.A. Wert

Objective

The objective of the present investigation is development of a broadly-applicable method for the quantitative analysis and description of the spatial distribution of second phase particles. This method should characterize the spatial distribution and its inhomogeneities in a manner which is of use to the materials scientist. As the method is intended to be available to a wide range of researchers in materials science, it has been designed to operate on a desktop computer. A second objective is application of the method for characterizing second phase particle distributions in a materials processing problem. The problem we have selected in consultation with the NASA technical monitor is understanding the effect of consolidation processing parameters on oxide particle distributions in a PM aluminum alloy.

Progress During the Reporting Period

During 1991, research work on this project was completed. Over its three-year life, the project encompassed two major activities. The first activity was creation of a set of computer programs enabling quantitative description of the spatial distribution of particles in materials. This effort involved implementation of established mathematical procedures for geometrical analysis of particle distributions, as well as extension of these procedures to perform completely new types of analyses.

Once these computational procedures were established, they were used to determine the effect of deformation processing on the oxide particle distribution in powder metallurgy (PM) aluminum alloys. The oxide particles originate from the alloy powder produced by rapid solidification. If the oxide layer on the surface of the powder particles is not broken-up and dispersed during deformation processing, poor transverse properties often result. Owing to the lack of appropriate analysis methods, all previous analyses of the effect of various consolidation and deformation processing methods on the oxide particle distribution were qualitative. Investigation of a PM aluminum alloy using the new analysis methods has

provided a quantitative basis for selecting deformation processing parameters to optimize the dispersal of oxide particles. In particular, we established that direct rolling of compacted billets is a less effective method for break-up and dispersal of the oxide particles than processes involving forging prior to rolling.

Two research papers describing the work performed under this task are in preparation. The first paper, which is being submitted to Metallurgical Transactions, describes the computational procedures and illustrates their application to computer-generated particle distributions. The second paper, which will discuss oxide particle dispersal during processing of a PM aluminum alloy, will be presented at the TMS meeting in San Diego in March 1992, and will be published in the conference proceedings volume. The remainder of the present report presents the Abstract, Introduction, Conclusions and Figures sections from the Metallurgical Transactions paper. A full copy of this manuscript is available upon request.

A GEOMETRICAL DESCRIPTION OF PARTICLE DISTRIBUTIONS IN MATERIALS

J.B. Parse and J.A. Wert

Department of Materials Science and Engineering

University of Virginia

Charlottesville, VA 22903-2442

This paper describes a geometrical technique, based on the Dirichlet tessellation, for quantitative characterization of inhomogeneities in the spatial distribution of second-phase particles. The Dirichlet tessellation representation allows a detailed, statistical description of particle distribution properties, including local particle density and vector nearest-neighbor distances. Incorporation of an assumed particle interaction distance allows quantitative description of clustering in the particle distribution in terms of the fraction of particles clustered; and the number, size, and spatial distribution of clusters. The tessellation and clustering characteristics of several types of computer-generated particle arrays (random, clustered, and hexagonal) are presented. Observed mean values of tessellation properties for random particle arrays are in good agreement with analytical predictions. The effects of deformation on the tessellation and clustering characteristics of the particle arrays have been examined for plane-strain deformation. Tessellation and clustering characteristics of the random particle arrays are insensitive to plane-strain deformation. Several tessellation and clustering properties of the hexagonal and clustered particle arrays are found to vary with increasing plane-strain deformation. The observed changes can be interpreted based on deformation effects on the inhomogeneous particle distributions.

1) Introduction

The spatial distribution of second-phase particles is of broad interest in materials science. Since the distribution of second-phase particles is a characteristic of the microstructure, quantitative description of the distribution is important for understanding the link between microstructure and bulk properties. Likewise, if it is necessary to produce a material a with desired distribution of second-phase particles, a method for quantitative characterization of changes in microstructure resulting from variations in processing conditions is needed. Progress in these areas has been limited by the lack of established methods for characterizing spatial distributions of second-phase particles.

Several techniques might be considered as a basis for analysis of the spatial distribution of particles:

i) Fractal dimension analysis [1], describing self-similarity in the scaling behavior of objects, has been developed in recent years. The approach is to evaluate some measure, M(s), of the object (such as perimeter length) over several orders of magnitude of scale, s. If D (= $d\log M(s)/d\log s$) is constant over a wide range of scale, it is known as the fractal dimension describing the feature.

ii) Percolation analyses [2] consider the connectivity of a system composed of a large number of discrete interconnected elements or nodes. Since percolation analyses require a description of the interconnections between nodes, they assume previous knowledge of the spatial distribution of the elements.

iii) Cluster analysis encompasses several methods [3] which attempt to distinguish natural groupings of objects in a multi-dimensional space whose dimension corresponds to the number of variables. Operational details vary with the approach [3], but many cluster analysis methods attempt to locate some number of cluster centroids

by minimizing the total squared distance between objects and their cluster centers.
iv) The Dirichlet tessellation technique in *n* dimensions [4,5] is a geometrical technique for partitioning a point array into a unique set of convex polyhedra (frequently referred to as *Voronoi polyhedra*), each of which is associated with and contains one of the points. Analysis of characteristics of these polyhedra provides information about the local environment of the particles. In materials science, characterization of particle distributions in three dimensions is desirable. However, determining the locations of particles in three dimensions, in a metallic matrix, is a tedious exercise. Moreover, the symmetries inherent in many processing methods (rolling of sheet, extrusion of flat bars, etc.) allow two-dimensional analysis of particle arrays to reflect the salient inhomogeneities of the three-dimensional arrays. The Dirichlet tessellation technique in two dimensions has been selected as the basis of the analysis presented here, and will be discussed later in more detail.

Embury and Burger et al. [6,7] used the Dirichlet tessellation technique and nearest-neighbor distance clustering criteria to characterize the spatial distributions of second-phase particles in steels and Al alloys, and examined the effects of clustering on recrystallization and fracture processes. Tessellation characteristics of computer-generated particle distributions which are sensitive to the nature of the distribution were identified. The variance of Voronoi polygon area, and the mean and variance of the polygon aspect ratio were found to be relatively strong indicators of clustering in the computer-generated particle distributions. The mean and variance of nearest-neighbor distance were found to be weak indicators of clustering. The nearest-neighbor distance distribution was found to be useful for distinguishing different particle dispersions, as the basis for a distance-based clustering analysis. It was noted, however, that particle dispersions containing different sizes and distributions of clusters might produce similar clustering results by this technique [7]. Tessellation analysis of the recrystallization

behavior of deformed Al-Si-Cu single crystals indicated that particle-stimulated nucleation of recrystallization depended on clustering of second-phase particles, rather than on particle size or overall average strain [7]. Modeling of creep fracture by void nucleation on grain boundaries for different void distributions predicted a decrease in global void growth rate with increased clustering of void sites [7].

Spitzig et al. [8,9] used the Dirichlet tessellation technique to examine the spatial distribution of carbide and sulfide inclusions in steels, and of graphite fibers in Al. Observed mean values and standard deviations of nearest-neighbor distances were compared to expected values of these parameters for random distributions of the same number density. Results of these analyses indicated that the distribution of carbides in steels and graphite fibers in Al were approximately random, while the sulfide inclusion distribution was a superposition of clustered and random distributions. The mean local area fraction (intercepted particle area / polygon area) of non-equiaxed inclusions in rolled steels was found to be orientation-dependent and significantly larger than the overall area fraction. Near- and nearest-neighbor distances were found to be orientation-dependent and were incorporated into a void coalescence model of ductile fracture which exhibited good agreement with experiment.

Wray et al. [10] used the Dirichlet tessellation technique to characterize random and non-random point arrays, with emphasis on nearest-neighbor distance distributions. The average intercept length on the Dirichlet tessellation technique was used to investigate the effects of deformation on point arrays. A random array of points was found to remain random during deformation.

Shehata and Boyd [11] evaluated the spatial distribution of oxide and oxy-sulfide inclusions in a microalloyed Ti-V steel in the as-cast and rolled conditions using the

Dirichlet tessellation technique. Voronoi polygon area associated with the inclusions was calculated, and combined with measured particle sizes to generate local area-fraction distributions. The mean values and variances of local area fraction for equivalent random particle arrays were generated and compared to results found for inclusions in steel. Results of the analysis indicated that inclusions in all steel samples were clustered relative to the random distributions, with the rolled samples exhibiting higher number densities of inclusions and increased clustering relative to the as-cast material. The latter was attributed to break-up of the inclusions during the rolling process.

Lewandowski et al. [12] used a modified Dirichlet tessellation technique to study the effects of clustering of SiC particles on fracture in discontinuously reinforced AA7000-series metal-matrix composites. The size, size distribution and clustering of SiC particulates were characterized. Regions on the surface of controlled-propagation fracture specimens were analyzed before and after the passage of the crack, revealing that clustered regions were preferred sites for damage initiation and appeared to serve as preferred sites for damage accumulation ahead of the crack tip.

The investigations described above demonstrate the utility of the Dirichlet tessellation approach for characterization of the spatial distribution of second-phase particles in materials. The means and variances of properties such as nearest-neighbor distance and local particle density reflect ordering, randomness, or clustering of the particle distribution. Distance-based investigations of clustering can be used to distinguish materials with different degrees of particle clustering [5]. In many applications where the sizes and spatial distributions of particle clusters are of particular interest, an extension of previously developed methods, providing a more complete description of the microstructure, is desirable.

The objective of the present research is to further explore Dirichlet tessellation methods for quantitative characterization of the spatial distribution of second-phase particles. The methods described in the present paper provide a useful description of the characteristics and spatial distribution of clusters present, as well as statistical information relative to the local environments of individual particles. A subsequent paper will be devoted to application of these methods to analysis of oxide particle distributions in a consolidated powder-metallurgy aluminum alloy.

[For the sake of brevity, detailed descriptions of the analysis method, results, and discussion are omitted here, but are available from the authors.]

5) Conclusions:

The results of this investigation of tessellation methods, applied to characterization of the spatial distribution of second-phase particles, lead to the following conclusions.

1. Average polygon and tessellation properties determined for randomly distributed particles are in good agreement with analytically-derived expected values. Average tessellation properties and clustering characteristics of random particle distribution were found to be unaffected by plane-strain deformation, as expected.

2. Some average polygon and tessellation properties of nonrandom particle distributions reflect spatial inhomogeneity. The mean values of the contact number and the nearest-neighbor distance for hexagonal and clustered particle arrays were significantly lower than analytical predictions for a random particle array of the same areal density. The mean polygon area for the clustered particle arrays was significantly lower than that of an equivalent, random particle array, while that of the hexagonal particle arrays was only slightly lower than the expected value for a random particle array.

3. The principal effect of plane-strain deformation on the tessellation properties of clustered particle arrays was a significant increase in the vertical-neighbor distance, consistent with break-up of the clusters. The hexagonal particle arrays exhibited a large increase in mean nearest-neighbor distance (50%) with plane-strain deformation to a strain of 1, and a decrease in vertical-neighbor distance.

4. The use of a parameter representing a particle interaction distance extends the tessellation analysis and allows a quantitative description of particle clustering, including such characteristics as number, size and spatial distribution of clusters identified. Such information may be of interest when considering damage initiation, accumulation, and crack propagation in materials.

5. The effects of plane-strain deformation on the clustering characteristics of hexagonal and clustered particle arrays were consistent with effects of deformation on particle spacing and the effects of interaction distance on clustering characteristics.

6) Acknowledgements

The authors wish to acknowledge helpful discussions with Dr. J.M. Duva and Mr. O.R. (Duke) Singleton. This work was sponsored by NASA Langley Research Center, whose support is gratefully acknowledged, under grant NAG-1-745; the contract monitor was Dr. D. Tenney.

7) References

1. R. F. Voss: in *The Science of Fractal Images*, H. Peitgen and D. Saupe, eds., Springer-Verlag, New York, NY, 1988, pp. 58-62.

2. A.L. Efros: *Physics and Geometry of Disorder*, Mir, Moscow, USSR, 1986.

3. R. Dubes and A.K. Jain: *Pattern Recognition*, 1976, vol. 8, pp. 247-260.

4. G.L. Dirichlet: *Journal fur die reine und angewandte Mathematik*, 1850, vol. 40, pp. 209-227.

5. W. Brostow, J. Dussault, and B.L. Fox: *Journal of Computational Physics*, 1978, vol. 29, pp. 81-92.

6. J. D. Embury and G. Burger: in *Seventh Annual Conference on the Strength of Metals and Alloys*, H.J. McQueen, J.P. Bailon, J.I. Dickson, J.J. Jones, and M.G. Akben, eds., Vol. 3, Pergamon Press, Oxford, 1986, pp. 1893-1915.

7. G. Burger, E. Koken, D. S. Wilkinson and J. D. Embury: in *Advances in Phase Transitions*, J.D. Embury and G.R. Purdy, eds., Pergamon Press, Oxford, 1988, pp. 247-262.

8. W. A. Spitzig: *Acta Metallurgica*, 1985, vol. 33, pp. 175-184.

9. W. A. Spitzig, J. F. Kelly, and O. Richmond: *Metallography*, 1985, vol. 18, pp. 235-261.

10. P. J. Wray, O. Richmond, and H. L. Morrison: *Metallography*, 1983, vol. 16, pp. 39-58.

11. M. T. Shehata and J. D. Boyd: in *Inclusions and Their Influence on Material Behavior*, ASM International, Metals Park, 1988, pp. 123-131.

12. J. J. Lewandowski, C. Liu, and W. H. Hunt, Jr.: *Materials Science and Engineering*, 1989, vol. A107, pp. 241-255.

13. A. Getis and B. Boots: *Models of Spatial Processes*, Cambridge University Press, Binghamton, N.Y., 1978, pp. 121-151.

14. A. Hald: *Statistical Theory with Engineering Applications*, John Wiley & Sons, New York, NY, 1952, pp. 1-187.

15. C. Nunez and S. Domingo, *Metall. Trans. A*, 1988, vol. 19A, pp. 2937-44.

16. H. Hermann, H. Wendrock, and D. Stoyan: *Metallography*, 1989, vol. 23, pp. 189-200.

17. J. R. Fisher and J. Gurland: *Metallurgical Transactions*, 1981, vol. 12A, pp. 167-171.

18. D. Weaire and N. Rivier: *Contemporary Physics*, 1984, no. 1, vol. 25, pp. 59-99.

19. W.M. Griffith, Y-W. Kim and F.H. Froes: in *Rapidly Solidified Powder Aluminum Alloys*, ASTM STP 890, M.E. Fine and E.A. Starke, Jr., eds., American Society for Testing and Materials, Philadelphia, 1986, pp. 283-303.

20. G. Staniek: *AFWAL-TR-83-4157*, Air Force Wright Aeronautical Laboratories, Air Force Systems Command, Wright-Patterson Air Force Base, Ohio, 45433. (DTIC AD-A145 919)

Table I

Expected and Observed Mean Values of Several Tessellation Properties

	contact number	polygon area	nearest-neighbor distance	horizontal-neighbor distance	vertical-neighbor distance
Expected value*	6.000	0.00200	0.02236		
Random					
Undeformed	5.941	0.00199	0.0221	0.0425	0.0423
$\epsilon = 0.5$	5.944	0.00196	0.0224	0.0423	0.0425
$\epsilon = 1.0$	5.929	0.00196	0.0226	0.0414	0.0425
Clustered					
Undeformed	5.870	0.00163	0.0107	0.0279	0.0267
$\epsilon = 0.5$	5.880	0.00163	0.0108	0.0222	0.0369
$\epsilon = 1.0$	5.872	0.00175	0.0118	0.0228	0.0478
Hexagonal+					
Undeformed	5.795	0.00479	0.0200	0.0445	0.1160
$\epsilon = 0.5$	5.844	0.00461	0.0242	0.0481	0.0910
$\epsilon = 1.00$	5.893	0.00502	0.0306	0.0377	0.0773

* Getis and Boots [13] Expected values for 500 randomly located particles per unit area.

+ Hexagonal particle arrays contain 200 particles per unit area.

Table II

Clustering Characteristics of Random and Clustered Particle arrays
(particle interaction distance = 0.028 units)

	number of particles in clusters	number of clusters	mean cluster occupancy	mean cluster length	total cluster length
Random					
Undeformed	334	110	3.1	0.027	3.0
$\epsilon = 0.5$	344	114	3.0	0.030	3.4
$\epsilon = 1.0$	340	108	3.2	0.030	3.2
Clustered					
Undeformed	489	52	9.4	0.055	2.9
$\epsilon = 0.5$	486	60	8.1	0.055	3.3
$\epsilon = 1.0$	470	73	6.4	0.050	3.7
Hexagonal*					
Undeformed	147	43	3.4	0.032	1.4
$\epsilon = 0.5$	122	45	2.7	0.021	0.9
$\epsilon = 1.0$	98	42	2.3	0.018	0.7

* The hexagonal particle arrays contain 200 particles each; the random and clustered particle arrays each contain 500 particles.

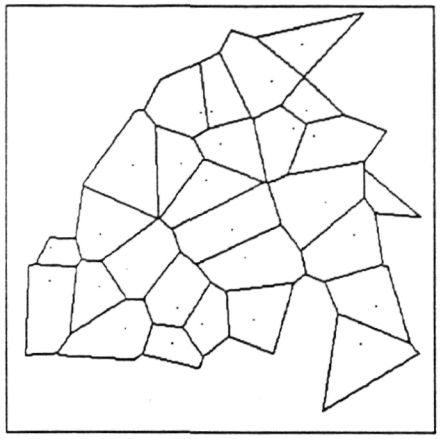

(a) Primary tessellation

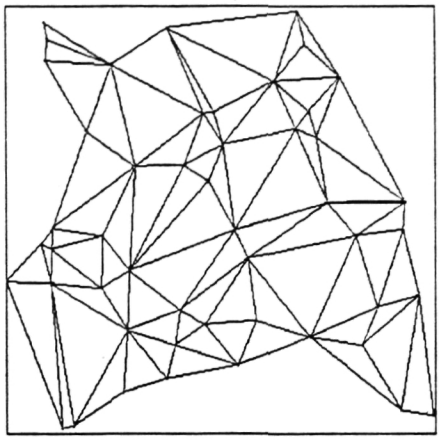

(b) Dual tessellation

Fig. 1. Primary and dual tessellations for a random array of 50 particles.

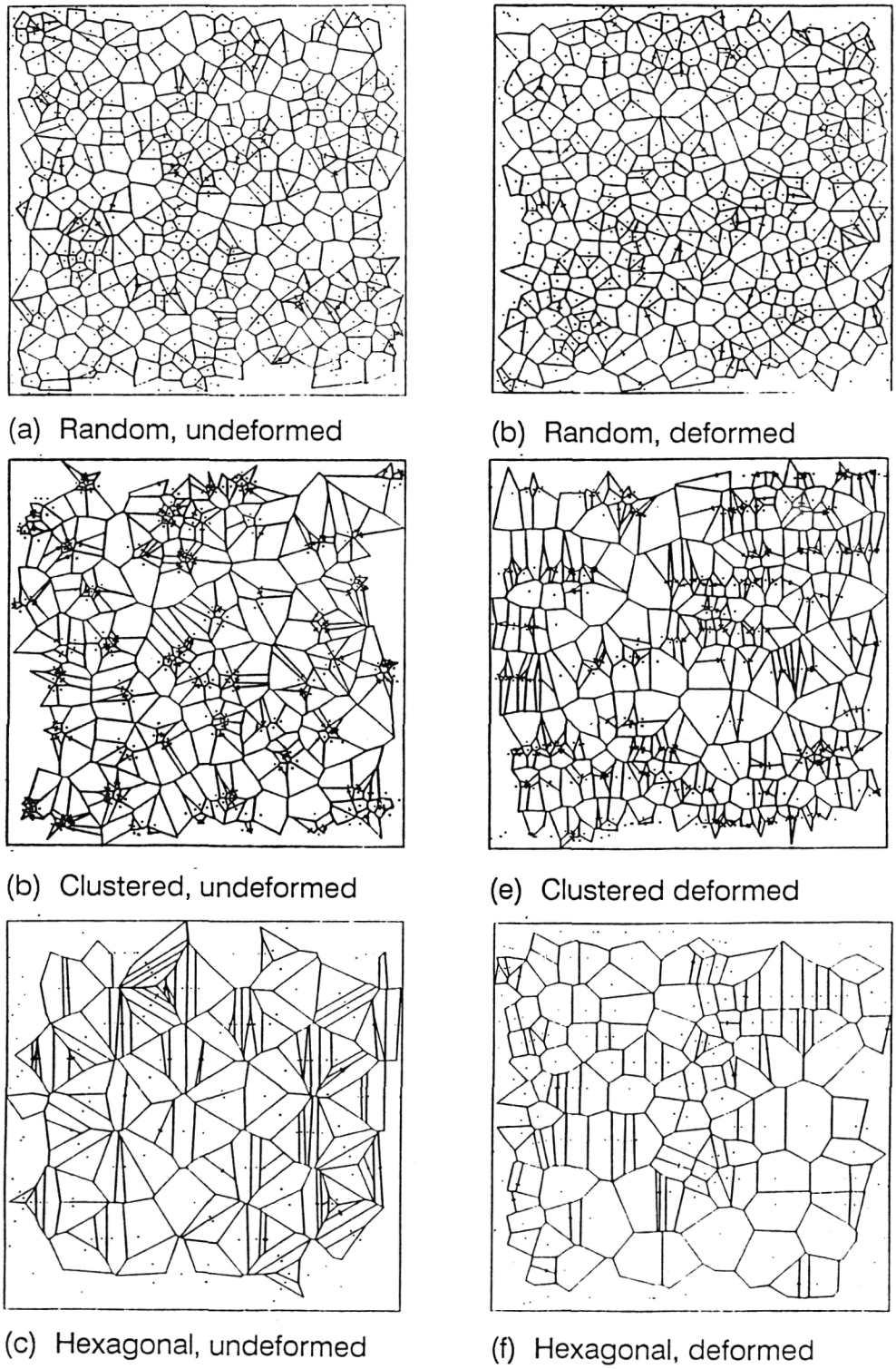

Fig. 2. Primary tessellations of computer-generated particle arrays (random, clustered, and hexagonal); undeformed and deformed (plane-strain = 1).

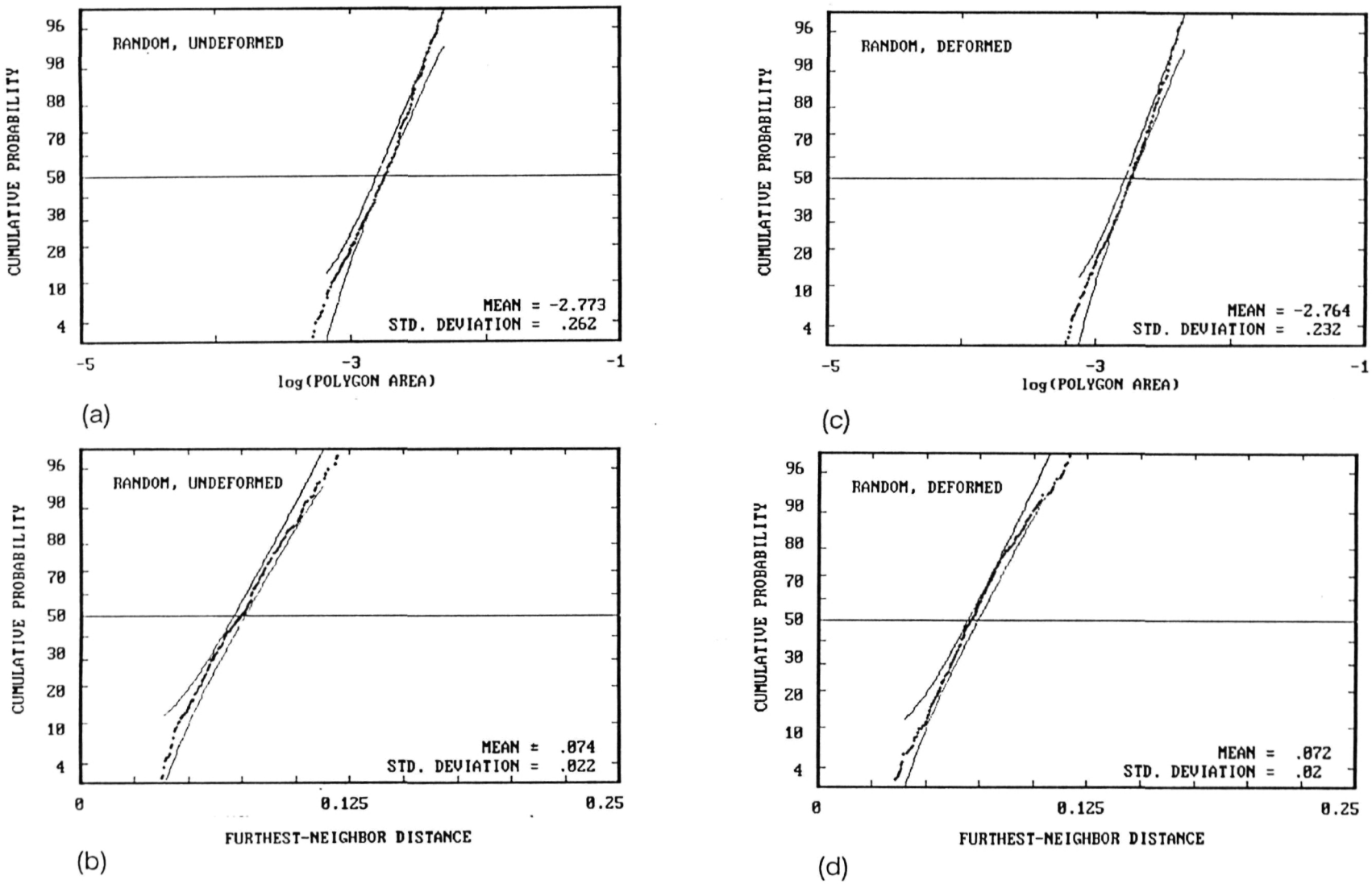

Fig. 3(a-d). Plots of cumulative probability versus log(polygon area) and furthest-neighbor distance for random particle arrays (undeformed and plane strain = 1).

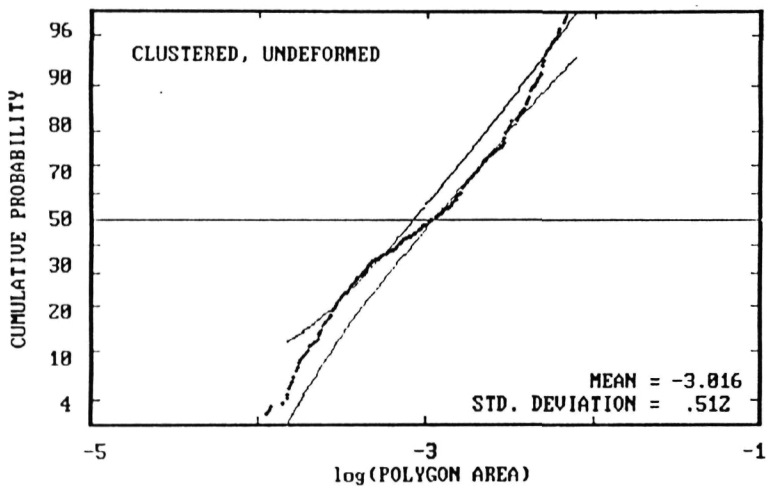

(e)

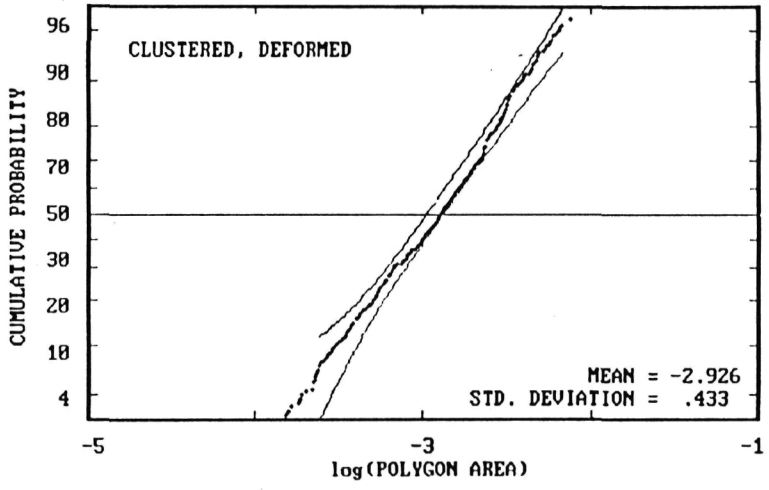

(g)

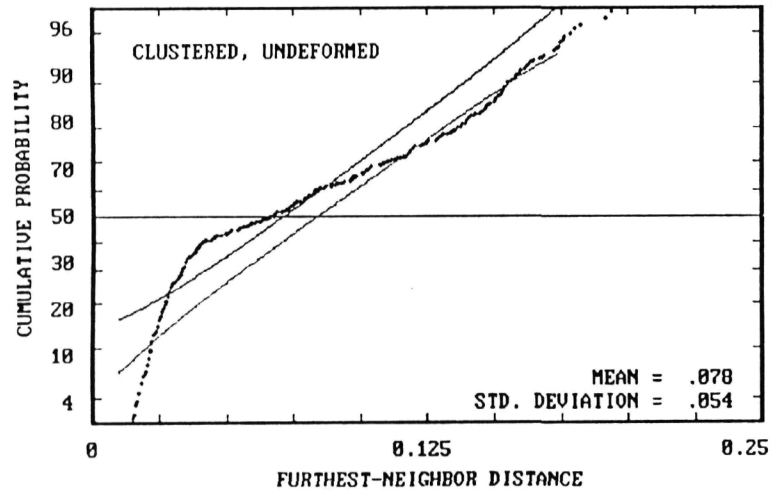

(f)

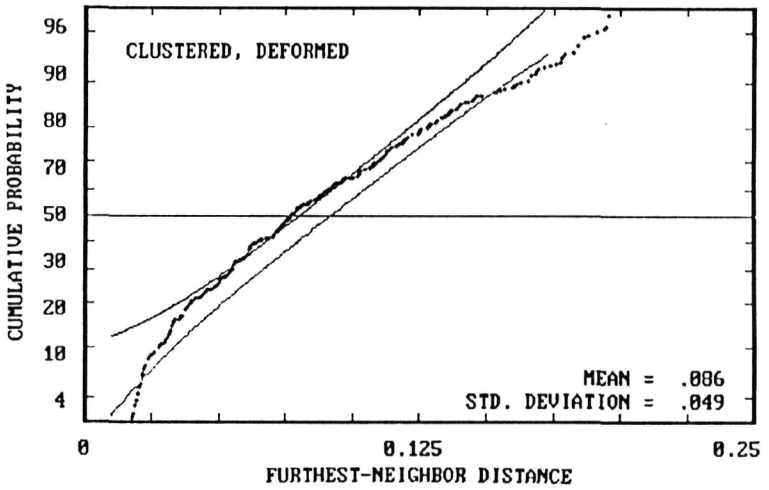

(h)

Fig. 3(e-g). Plots of cumulative probability versus log(polygon area) and furthest-neighbor distance for clustered particle arrays (undeformed and plane strain = 1).

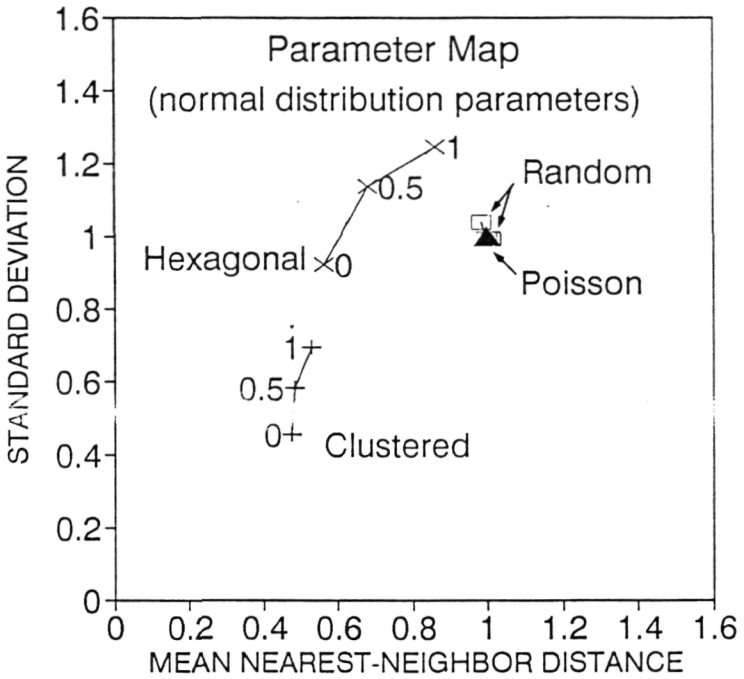

Fig. 5. Parameter map of normalized mean nearest-neighbor distance and standard deviation for random, clustered, and hexagonal particle arrays at plane-strains of 0, 0.5, and 1.0.

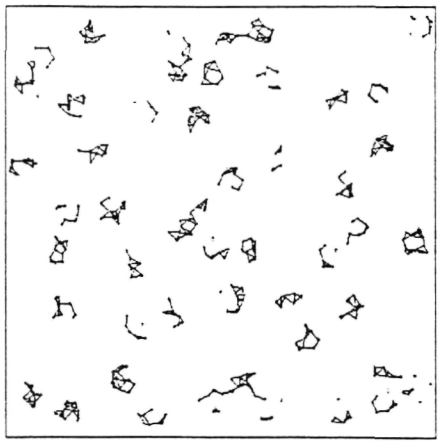

(a) Random, undeformed

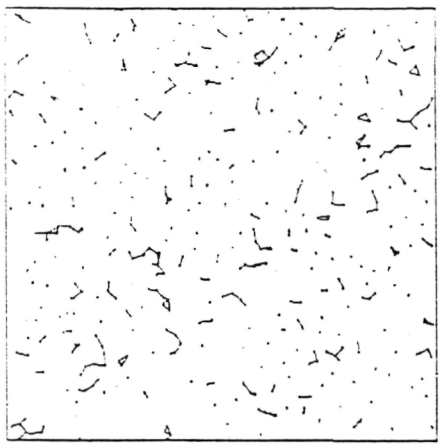

(b) Random, deformed

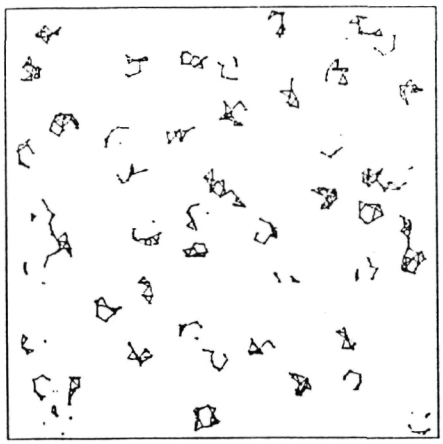

(b) Clustered, undeformed

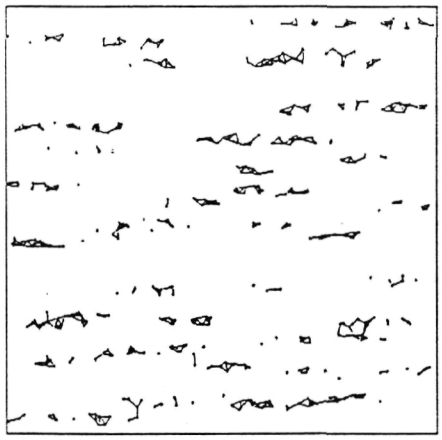

(e) Clustered deformed

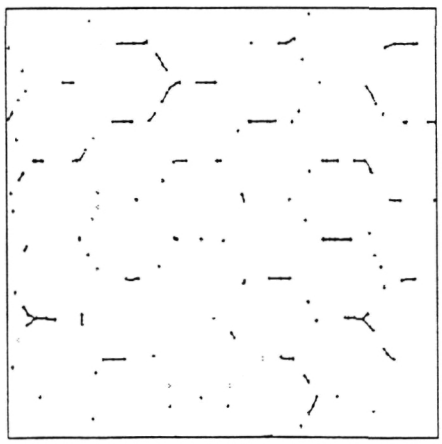

(c) Hexagonal, undeformed

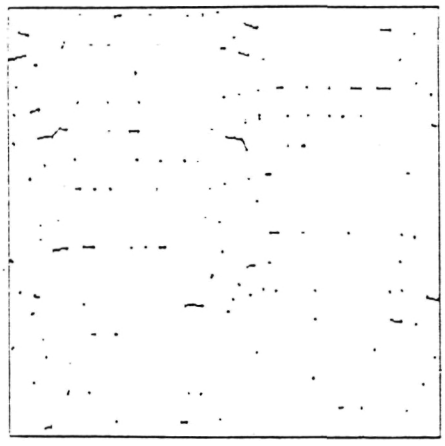

(f) Hexagonal, deformed

Fig. 6(a-f). Clusters identified for particle arrays of Fig. 2(a-f) respectively, (random, clustered, and hexagonal); undeformed and deformed (plane-strain = 1), using a particle interactiion distance of 0.028 units.

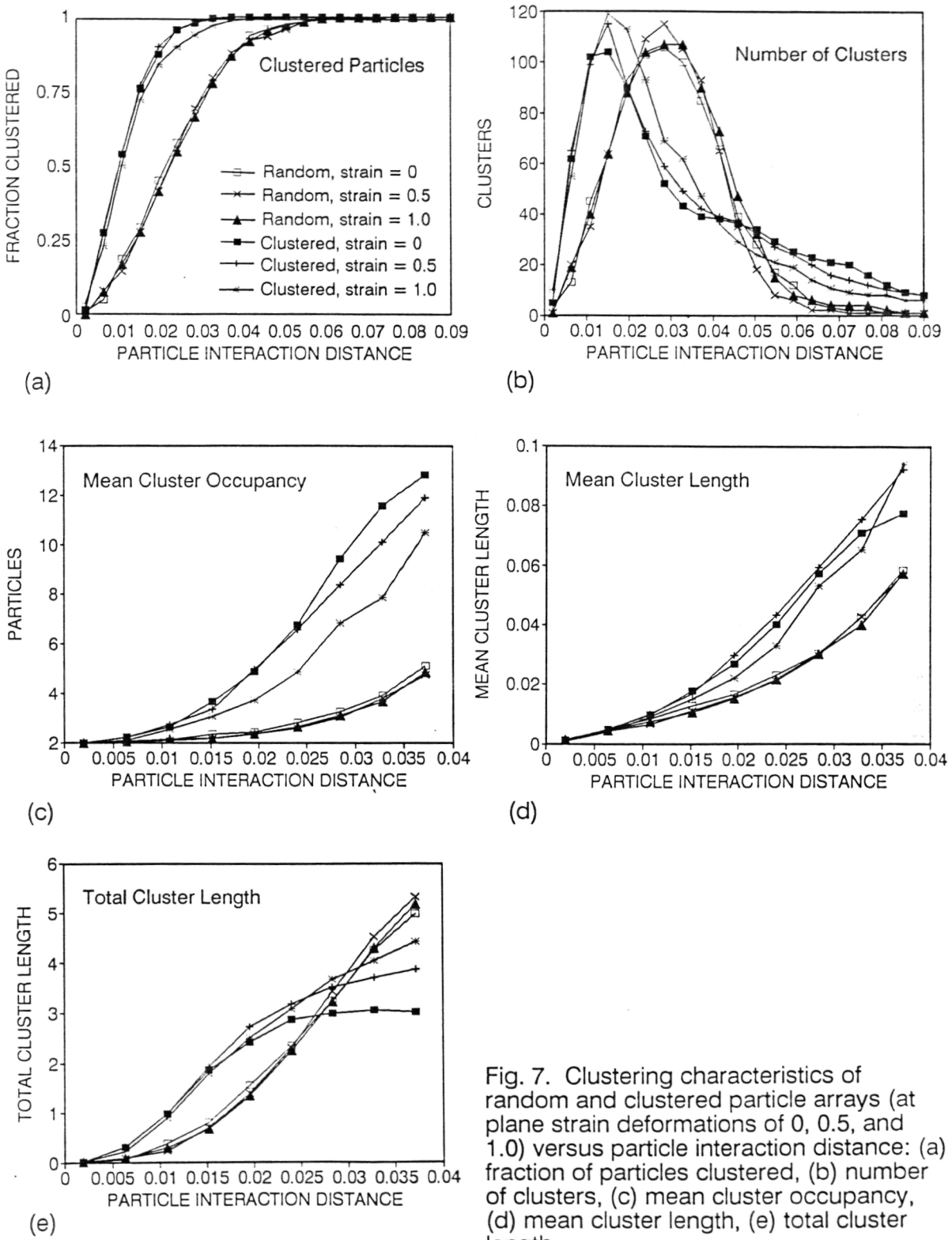

Fig. 7. Clustering characteristics of random and clustered particle arrays (at plane strain deformations of 0, 0.5, and 1.0) versus particle interaction distance: (a) fraction of particles clustered, (b) number of clusters, (c) mean cluster occupancy, (d) mean cluster length, (e) total cluster length.

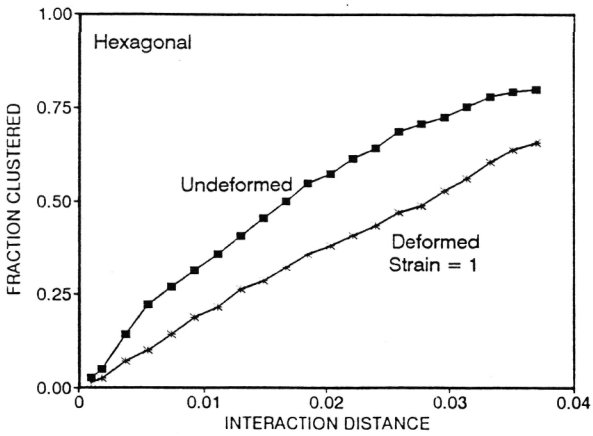

(a)

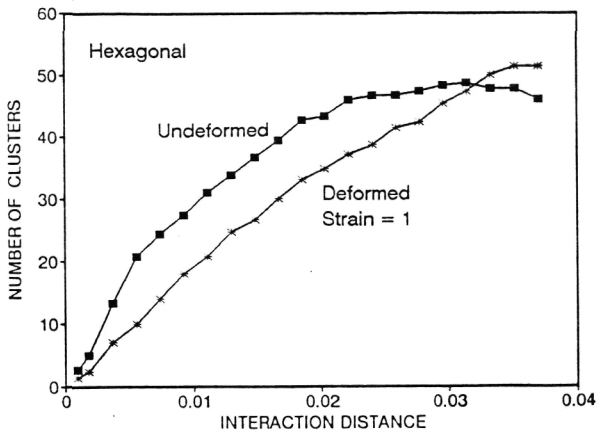

(b)

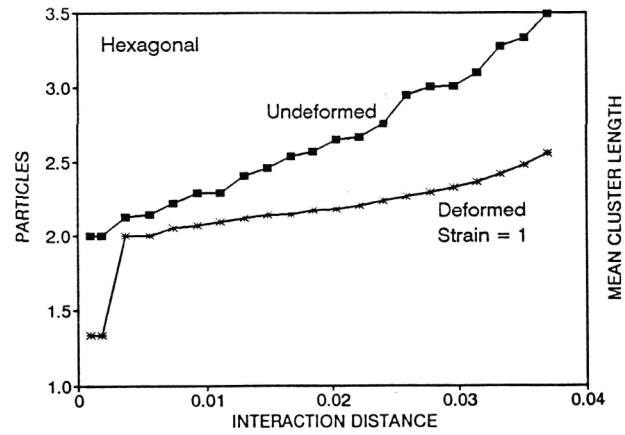

(c)

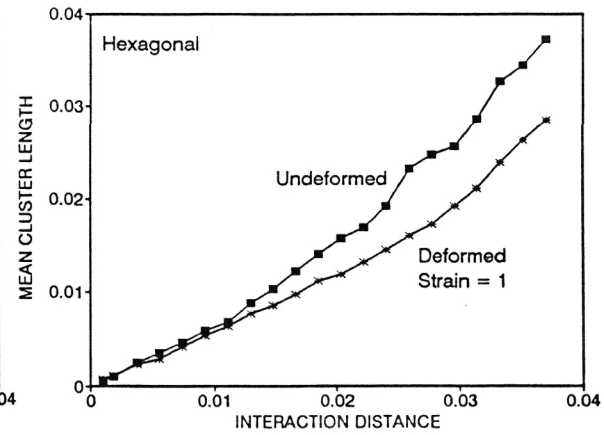

(d)

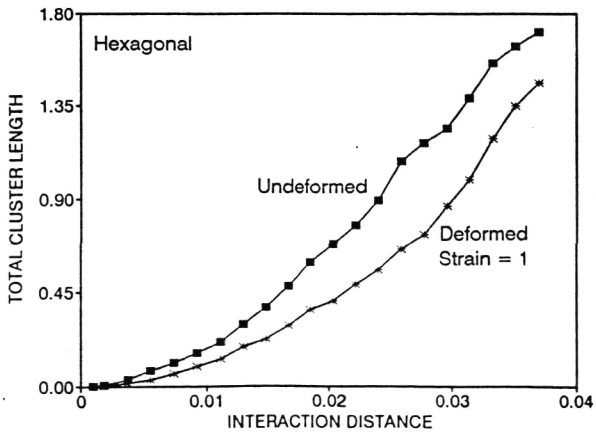

(e)

Fig. 8. Clustering characteristics of hexagonal particle arrays (at plane strain deformations of 0 and 1.0) versus particle interaction distance: (a) fraction of particles clustered, (b) number of clusters, (c) mean cluster occupancy, (d) mean cluster length, (e) total cluster length.

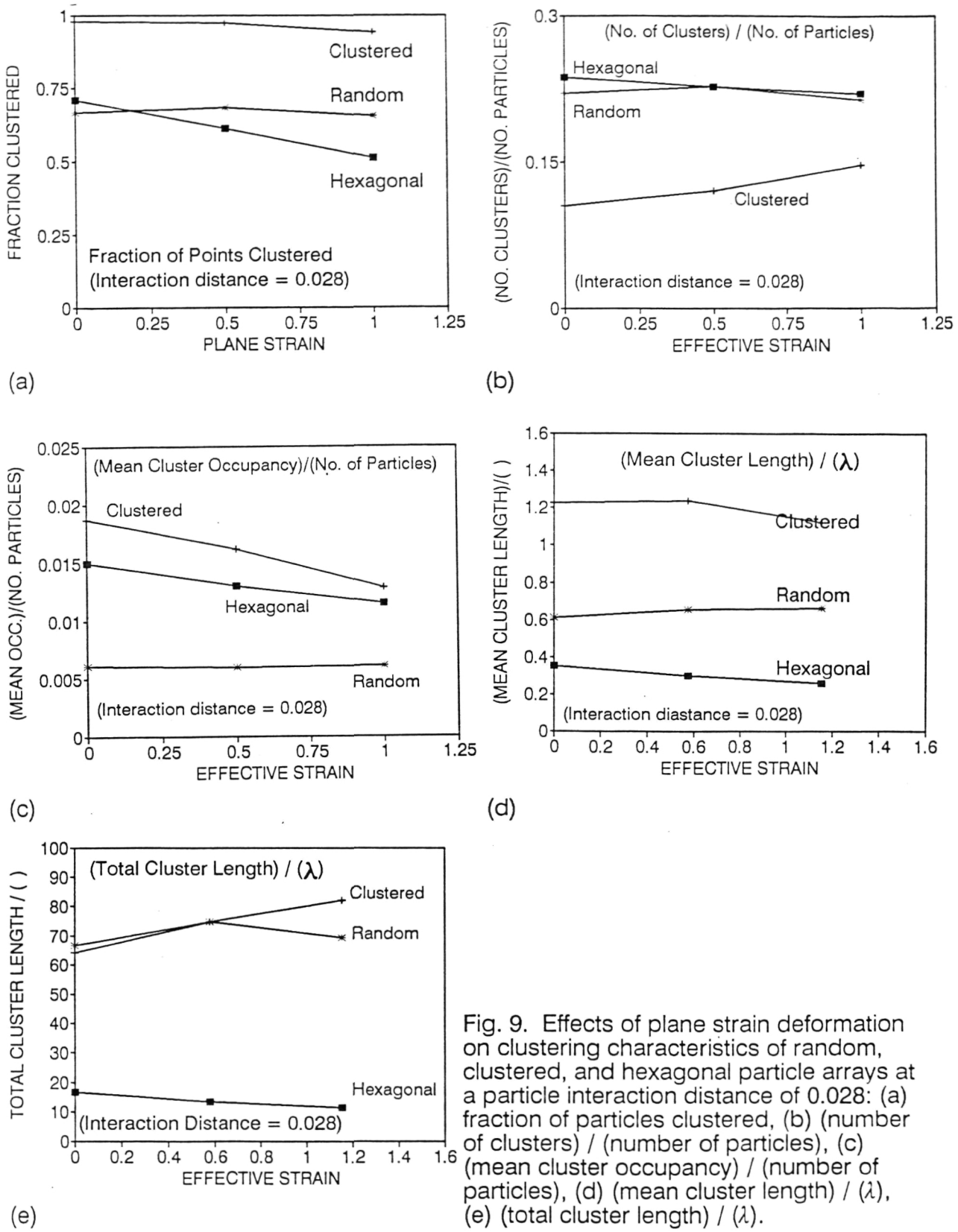

Fig. 9. Effects of plane strain deformation on clustering characteristics of random, clustered, and hexagonal particle arrays at a particle interaction distance of 0.028: (a) fraction of particles clustered, (b) (number of clusters) / (number of particles), (c) (mean cluster occupancy) / (number of particles), (d) (mean cluster length) / (λ), (e) (total cluster length) / (λ).

BACK

Project 12 **Processing and SPF Properties of Weldalite™ Sheet**

Mark Lyttle and John A. Wert

Objective

The objectives of this proposed research project are to establish the cause of variable superplastic properties of Weldalite sheet and to identify the thermomechanical processing steps that introduce the variability.

Technical Background and Statement of the Problem

The SPF properties of Weldalite sheet, like those of other SPF aluminum alloys, depend on creation of a fine-grain microstructure suitable for superplastic deformation [1]. To gain an understanding of how the microstructure needed for SPF is created, it is necessary to consider the thermomechanical processing methods used to impart superplastic characteristics to this alloy. While the companies that produce SPF aluminum alloys are reluctant to reveal the details of their processes, the general aspects are relatively well known.

Aluminum alloys suitable for superplastic forming contain a dispersoid-forming element, usually Zr, which prevents conventional recrystallization of cold- or warm-rolled material by impeding boundary migration. Experience with Al-Li-base alloys suggests that Li in solid solution also contributes to boundary drag, although direct evidence for this effect has not been reported.

The alloys containing dispersoid particles are warm or cold rolled to a total reduction of thickness of roughly 80%. This deformation introduces the microstructural features that ultimately evolve into the fine grain microstructure needed for superplastic deformation. Until recently, many characteristics of deformation microstructures were not known. Previous investigations at UVa [2,3] have shown that microstructures of SPF aluminum alloys after rolling contain mostly low-angle boundaries, but high-angle boundaries of two types are present. High-angle boundaries of one type divide the microstructure into layers parallel to the rolling plane. These are either prior grain boundaries or collapsed transition bands resulting from the rolling deformation. A second type of high-angle boundary is

associated with large precipitate particles [4] that may be present as a result of overaging treatments conducted before rolling.

The as-rolled microstructure is not suitable for superplastic deformation. Although the subgrain size is small, the subgrains are bounded by predominately low-angle boundaries. Several fundamental studies have shown that low-angle boundaries cannot undergo grain boundary sliding [5,6], the principal deformation mechanism contributing to superplastic deformation. It is during the initial phases of the superplastic deformation process that the subgrain microstructure present after thermomechanical processing evolves into the grain structure required for superplastic forming. Results for Al-Zr-Si and Al-Cu-Zr-Si alloys suggest that the evolution of boundary character mostly occurs between a strain of 0.2 and 0.5 at the SPF temperature [2,3]. If the material is simply heated to the SPF temperature and annealed, the proper microstructure does not develop, indicating that straining plays an essential role in the microstructural evolution. It is thought that straining drives the rotation of subgrains having a large misorientation with at least one neighboring grain (i.e., having at least 1 high-angle boundary). Finding direct evidence for this type of process has been difficult, but experimental methods recently developed at UVa support such subgrain rotation [2,3]. Continuation of this process provides for gradual conversion of the subgrain boundary structure present after rolling into a grain structure suitable for superplastic deformation. This process of microstructural evolution is known as continuous recrystallization because it relies on continuous, recovery-type mechanisms to produce a recrystallized microstructure, in contrast to the discontinuous nucleation and growth process associated with conventional recrystallization.

In prior discussions with NASA personnel concerning SPF Al-Li-base alloys for various applications, it was suggested that the SPF properties of Weldalite sheet are somewhat variable and the origin of the variability is presently unknown. From the above description of the general aspects of processing of this type of SPF material, it seems likely that conversion of the microstructure resulting from thermomechanical processing into the microstructure suitable for SPF forming is not taking place in a consistent fashion. Detailed characterization of the microstructure and crystallographic texture at various stages in the processing and SPF cycle are needed to establish the cause of inconsistent SPF properties and to identify a modification to the current processing method that can provide consistent SPF properties.

Experimental Results

NASA has provided 2 Weldalite sheets to be used for this task. The compositions have been previously analyzed; alloy designations and compositions are given in Table 1. The Weldalite 049 (complete designation: Weldalite049™-RT72 SPF) was produced by Reynolds Metals in their research laboratory, while the X2095 was produced in a full-scale commercial production facility. NASA's prior experience with the SPF properties of these two alloys suggests that Weldalite 049 exhibits more variability in SPF properties than X2095.

Table 1

Compositions of Weldalite Alloys

Alloy	Cu	Li	Mg	Ag	Z
Weldalite 049	4.76	1.27	0.36	0.38	4.
X2095	4.49	1.15	0.40	0.37	7.

Microstructure characterization at the optical microscopy level has been performed for the two SPF alloys. Fig. 1 shows optical micrographs of specimens prepared using Keller's etch. The alloys both contain coarse precipitate particles which formed at the rolling temperature of approximately 573 K. The precipitate particles have an average diameter of approximately 6 μm in the X2095, slightly larger than the 4 μm diameter estimated for the Weldalite 049. The difference in particle size is probably associated with different thermal exposure of the alloys during thermomechanical processing, since the difference in alloy composition is small.

Previous work at UVa with an Al-Cu-Zr alloy suggests that precipitate particles with smaller diameters (in the range 0.5 to 1 μm) do not have a significant effect on the continuous recrystallization process. To what extent the larger particles in the Weldalite 049 and X2095 affect continuous recrystallization is a question to be addressed in the present research. We also plan to use X-ray or electron diffraction to identify these particles.

In addition to characterizing the nature and distribution of precipitate phases, the grain and subgrain structure is also of interest. Barker's etch has been used to reveal the grain structure of both specimens at the optical microscopy scale. As usual in warm-rolled aluminum alloys, the grains are elongated parallel to the rolling direction (L). The average

thickness of a grain in the short transverse direction (S) is about 20 μm in the Weldalite 049 and about 30 μm in the X2095. The size difference may reflect a difference in the as-cast grain size or differences in the thermomechanical processing treatments for the two alloys. Prior work at UVa suggests that the high-angle boundaries present in the deformation microstructure play a key role in continuous recrystallization in superplastic alloys. The subgrain structure is not revealed by Barker's etch; future analyses using TEM will be necessary to characterize the deformation microstructure on a finer scale.

In addition to microstructural analyses, the texture of the alloys has also been analyzed. Fig. 2 shows {111} partial pole figures for both alloys. Both alloys possess deformation textures typical of rolled aluminum alloys, although small differences are observed. The Weldalite 049 exhibits a stronger Cu or S texture component (it is difficult to distinguish these in {111} pole figures) while the X2095 exhibits stronger brass components. The differences in texture reflect differences in the thermomechanical processing methods applied to the two alloys. Future research will reveal whether the texture differences have a significant effect on SPF properties.

Future Work

During the upcoming year, we expect to make significant progress in characterizing the continuous recrystallization process in the two Weldalite alloys. TEM and texture analyses will be the primary tools used for these investigations. We plan to use the SPF forming facilities at NASA LaRC to strain specimens of each alloy to moderate strain levels. Analysis of the microstructure, microtexture, and macrotexture of these samples will provide insight into the mechanisms by which continuous recrystallization converts the subgrain boundaries into grain boundaries. We will use these results to better understand how processing variations affect SPF characteristics, which will provide a basis for optimizing the processing method to reduce the variability of SPF properties.

References

1. J.A. Wert, in Mechanical Properties and Phase Transformations in Engineering Materials, S.D. Antolovich, R.O. Ritchie and W.W. Gerberich (eds), TMS, Warrendale, 1986, pp. 307-323.

2. H. Gudmundsson, D.D. Brooks and J.A. Wert, Acta Metallurgica et Materialia, Vol. 39, 1991, pp. 19-36.

3. D.D. Brooks, H. Gudmundsson, and J.A. Wert, in Hot Deformation of Aluminum Alloys, T.G. Langdon, H.D. Merchant, J.G. Morris and M.A. Zaidi (eds), TMS, Warrendale, 1991, pp. 55-88.

4. F.J. Humphreys, Acta Metallurgica, 25 (1977) 1323.

5. P. Lagarde and M. Biscondi, Canadian Metallurgical Quarterly, 13 (1974) 245.

6. T. Wananade, N. Kuriyama and S. Karashima, in Proc. Fourth International Conference on the Strength of Metals and Alloys, Nancy, France, 1976, 1, pp. 383-387.

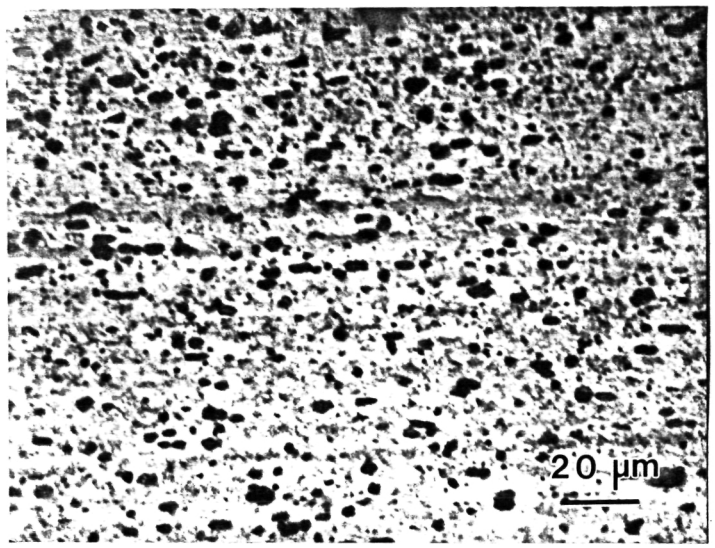

(a) Weldalite049

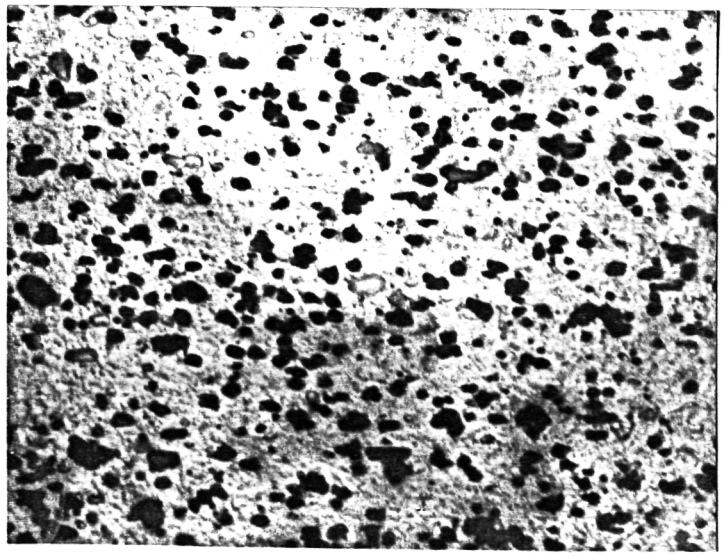

(b) X2095

Figure 1. Microstructure of SPF alloys showing precipitate particles present after thermomechanical processing.

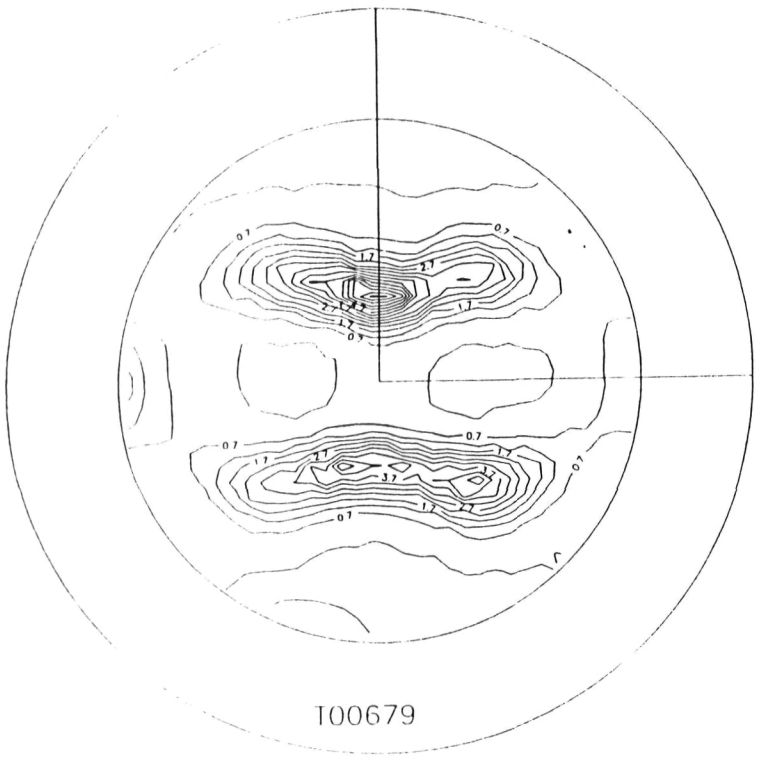

a) Weldalite049

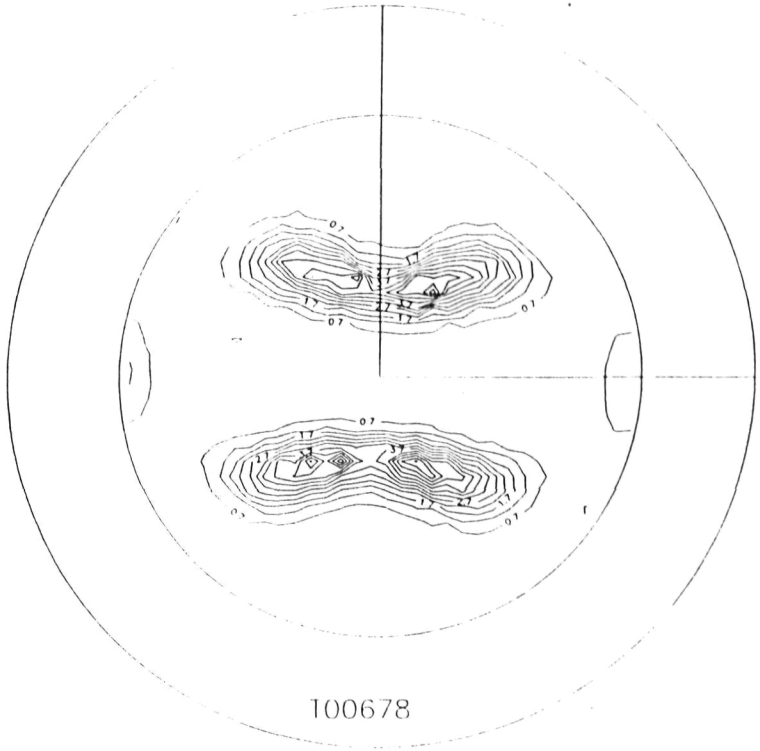

(b) X2095

Figure 2. 111 partial pole figures for SPF alloys.

BACK

Project 13 **The Development of Low Alloy High Strength Aluminum**

A.K. Mukhopadhyay and E.A. Starke, Jr.

General Considerations And Major Objective

Consideration of successful age hardenable aluminum based alloys produced via the commercial ingot metallurgical (I/M) route points out a common feature in that the mechanical properties of these materials deteriorate rapidly when exposed to aging temperatures between 100 and 200°C. The major reason for such a phenomenon is the coarsening of the fine strengthening precipitates in these alloys. The various transition phases and the equilibrium phases nucleate in order of increasing precipitate-matrix interfacial energy such that metastable phases having fully coherent and subsequently semi-coherent interfaces with the matrix are the ones which form at the initial stages of the aging cycle and constitute the basis for major strengthening in these alloys. However, continued aging leads to coarsening and gradual loss of coherency of these phases together with an increase in the interparticle spacing. The consequences are the changes in the hardening mechanism from shearing to looping accompanied simultaneously by a decrease in the alloy's strength properties.

There are a few practical solutions to the problems associated with the particle coarsening. Additions of suitable surface active elements may be made, which, in turn, can lower the surface energy (γ) at the interface between the matrix and the precipitate, thus decreasing the rate of particle coarsening. Alternatively, suitable trace alloy additions can be made to certain alloy systems to directly encourage formation of stable phases in high number density, as well as simultaneously bypassing one or more metastable phases in the precipitation hierarchy of the alloy system concerned. The utilization of these additions in the multicomponent commercial Al alloys is, however, greatly hindered by the presence of several strengthening phases in each such alloy system. The implication is that not all the phases in the same alloy system can be affected by such trace alloy additions. Furthermore, trace element effects on certain precipitate types, otherwise found in the constituent binary or ternary systems, are often lost in the presence of other elements or phases in the multicomponent alloys of commercial interest.

In view of these difficulties together with the increasing demand for cheaper I/M Al-based alloys for use as major structural components in the next generation high speed commercial transport systems, it is important that alloys capable of retaining a stable microstructure at temperatures in the range 150-200°C during service period be designed and developed.

Approach

These considerations led our research group to investigate and to explore the potential advantages associated with the Al-(Si,Ge) alloys of nucleating stable phases directly during aging heat treatment. An additional important feature of both Si and Ge particles is also their extremely small critical size for the transition from shearing to looping by dislocations at the yield stress. The essence is that these alloys containing a fine and uniform distribution of noncoherent hard particles within the microstructure should be capable of exhibiting a high degree of hardening even for a relatively small volume fraction of phase particles. Furthermore, of major practical importance, such materials properties should also persist even at elevated aging temperatures of interest.

Excerpts From Our Immediate Previous Work

Reported work in the literature on the Al-Si and Al-Ge alloys points out that elemental Si and elemental Ge having the diamond cubic structure are the only precipitate types which form in the respective binary systems during aging heat treatment. The precipitation hardening in both systems is poor as precipitation nucleation is strongly vacancy sensitive, i.e., their hardening ability depends on both the solutionizing and the quench bath temperatures as well as on the cooling rate. The resultant microstructure is, therefore, typically characterized by a gross heterogenous distribution of the Si and Ge precipitates on multiple habit planes in the matrix together with the presence of large precipitate free zones adjacent to the grain boundaries.

Our earlier work showed that the undesirable microstructural features in both binary alloys can be largely altered in ternary Al-Si-Ge alloys: the precipitate density is an order of magnitude higher and the small equiaxed GeSi precipitates are much more evenly distributed. Also, there is no disturbance of this distribution by dislocations, and the PFZs around the grain boundaries are much less pronounced. The effects are based on the explanations in

that, in metallic solid solution, Si is smaller and Ge is larger than Al. Therefore, the atomic size misfit is compensated by the formation of pairs of Si and Ge, and such effect is, in fact, accentuated because of the similarities in the electronic structure between Si and Ge. The result is the attainment of the critical size by a large number of clusters containing the two elements to act as the nucleation centers for the diamond structure, even if aided less by the vacancies. Figures 1 (a)-(c) depict the typical microstructural features of binary Al-1Si, binary Al-1Ge and ternary Al-0.5Si-0.5Ge alloys obtained under identical heat treatment conditions. The variation in the degree of hardening in these alloys, as shown in Figure 2, may also be compared with the corresponding changes in the degree of refinement and uniformity of the precipitates observed.

Our previous work also showed that the level of hardening in the ternary alloys increased consistently with increasing (Si + Ge) content (cf. Figure 2), and that the alloys containing Si and Ge in equal concentrations maximized such effects. Metallographic evidence revealed that the use of higher amounts of solutes is, however, restricted to Si and Ge contents of 1 at% each owing mainly to the relatively low solid solubility of Si in Al as well as to the problem of segregation encountered in ingot casting and subsequent difficulties associated with the incomplete homogenization of the cast ingots within the practical homogenizing time and temperature.

Attempts to refine the (GeSi) diamond precipitates by trace alloy additions to the ternary Al-1Si-1Ge baseline alloy, as was discussed in our earlier report, were unsuccessful. Mg additions, ranging from 1 to 0.2 wt%, to these alloys were also found to produce $Mg_2(Si,Ge)$ precipitates at the expense of finer (GeSi) diamond precipitates. These results, therefore, demonstrated that elements such as Mg and Zr, which would interact with both Ge and Si, and certain trace elements having high binding energies with the vacancies in aluminum to slow down the normal GeSi phase nucleation, cannot be added to the ternary baseline alloy for its further development.

These results, in accordance with theoretical considerations, further demonstrated that although the microstructural stability of the ternary baseline alloy is considerable at commercial aging temperatures and that the level of hardening is appreciable for the given minimum amounts of solute contents and, hence, for the given minimum volume fraction of precipitates, the strength level of the baseline alloy is inadequate for the targeted engineering applications.

Research Objective During The Reporting Period

The objective of the current research is to improve the strength of the baseline alloy.

Approach

(a) Alloying of the baseline alloy with "suitable alloying elements" so as to further refine the GeSi precipitates having the diamond structure as well as to incorporate, in this process additional strengthening phases, if any, into the microstructure.

(b) Suitable grain refining additions to the baseline alloy in order to gain additional strength via substructural strengthening in the final wrought microstructure.

Major Experiments, Results And Discussion

Effects of Alloying Element Additions Ag, Cu and Zn having adequate solid solubility in aluminum as well as having negligible affinity to interact with the vacancies in aluminum were chosen as the appropriate alloying additions for this purpose. Varying amounts of solute content for each element (i.e., 0.5 and 2 wt%) were added to the baseline alloy and in total, therefore, 6 ingots were initially made in order to examine the effects of both kinds of solute elements as well as the amounts of solute on the aging behavior of the baseline Al-1Si-1Ge alloy.

The alloys were prepared using the laboratory scale ingot casting facilities available in our department. The alloys were prepared from high purity components in the induction furnace under argon atmosphere and in a graphite crucible and cast into a copper mold. The compositions of the materials were checked through chemical analyses. The 25 gram cylindrical cast ingots with 12 mm diameter were then subjected to the homogenization treatments. Thermal analysis of the cast materials was undertaken in a Perkin Elmer DSC (Differential Scanning Calorimeter) at a heating rate of 10°C/minute in order to determine the optimum homogenization temperatures for the cast ingots. The results indicated that the temperature range for the endothermic reaction (indicative of the dissolution of the low melting eutectic phase mixtures) for the baseline alloys containing Ag and Zn were similar to that of the baseline alloy (Fig. 3(a)), while, increasing copper additions have had the effect of shifting the endothermic reaction to the left of the temperature axis (Fig. 3(b)). An optimum homogenization temperature of 490°C was, therefore, selected for all the ingots

prepared. The cast ingots were successfully homogenized within 30 hours at 490°C. The homogenized materials were later either cold rolled with intermediate annealing or hot rolled to 2.5 mm sheet. The materials were solution treated for 1 hour at 500°C followed by water quenching to room temperature. Materials were then artificially aged at 160°C up to 100 hours to examine the aging response.

The results indicated that Ag and Zn additions to the baseline alloy had no influence, while Cu additions increased both the magnitude of hardening as well as the rate of aging (see Fig. 4 and Fig. 5). Figure 5 shows the age hardening curves for the baseline alloys containing varying amounts of copper. It may be noted that 2 wt% Cu additions do not change the desired microstructural stability of the baseline alloy at least up to 100 hours of aging at 160°C that has been recorded so far.

The above success associated with the Cu additions to the baseline alloy led us to evaluate the optimum amount of copper which could be added to the baseline alloy without disturbing the characteristic microstructural stability of the baseline alloy. The results depicted in Fig. 5 indicate that increasing the Cu content to 2.5 wt% results in a peak hardness value of 108 VHN after 5 hours followed by a negligible overaging even after 100 hours of aging at 160°C. Figure 6 shows that similar microstructural stability even persists at an aging temperature of 200°C, although the overall hardness level is a little reduced owing to the concomitant reduction in the volume fraction of the precipitates with increasing aging temperatures. Figure 5 further indicates that Cu additions of $\geq$ 3wt% increase the hardness of the alloys further to about 132 VHN at 160°C; however, alloys containing this amount of copper do overage, i.e., lose hardness after 24 h aging.

TEM studies explained the varying nature of the aging curves (cf. Fig. 7). It was found out that in baseline alloys containing $\leq$ 2.5 wt% Cu, a fine distribution of diamond precipitates is the only precipitate type in the microstructure (Fig. 7a). On the other hand, at Cu contents $\geq$ 3 wt%, θ' precipitates in the Al-Cu system also form in addition to the GeSi precipitates having the diamond structure. θ' precipitates were found to nucleate heterogeneously upon matrix dislocations and at the GeSi precipitate/α-Al interfaces (Fig. 7b). TEM studies showed that the rapid coarsening of the θ' precipitates with aging is responsible for the rapid overaging observed in the θ' containing alloys. These results indicate that the copper content in these alloys is to be appropriately adjusted so as not to allow θ' nucleation to occur.

Compared to the baseline alloy, on the other hand, the large increment in the hardness level (by about 60%) in the Al-1Si-1Ge-0.9at% Cu alloy within a shorter aging period implies rapid work hardening in the quaternary alloy. These results typically represent the age hardening behavior of materials containing a fine and uniform distribution of noncoherent particles. Our TEM results point out that copper additions have the effect of producing more numbers of stable precursory clusters upon quenching which at the aging temperature act as the nucleation centers for the diamond precipitates. TEM results of the copper-bearing quaternary alloys also point out that the spherical shape of the noncoherent GeSi precipitates in the baseline alloy has now changed to the rod type aligned along the <100> Al directions. We point out that such a change in the shape of the particles is attributed to and is consistent with the reduction in the strain energy of the noncoherent diamond precipitates having larger volume than the α-Al matrix. The alignment of the precipitates along the <100> Al directions can be understood from the anisotropic elasticity, since the value of the Young's modulus for all FCC metals has a minimum along the <100> directions.

X-ray EDS analyses of the diamond precipitates in TEM thin foils in the heat treated Al-Si-Ge-Cu alloys indicate the presence of Si, Ge and Cu within the diamond precipitates. However, given the dissimilarity in the electronic and structural constituents between the copper atoms and the Si and Ge atoms, together with no solid solubility of Cu in either Si or Ge, it is logical to suggest that the smaller copper atoms segregate to the GeSi/α-Al interfaces, thus reducing both the growth of the precipitates during aging as well as the strain energy of the precipitates, and thereby determining also the shape change of the particles. These interpretations are also consistent with the similar role of copper in an Al-Si-Cu alloy suggested by Stewart and Martin in an earlier communication.

Figure 8 shows the TEM micrograph depicting the uniform deformation produced around a hardness indentation in the θ' containing (baseline + 3 wt% Cu) alloy aged for 10 hours at 160°C. The micrograph suggests that the diamond precipitates are very effective in homogenizing deformation within the microstructure.

Effect of grain refining additions 0.4wt% Mn was added to the baseline alloy containing varying amounts of copper. Figure 9 shows the age hardening curves for the Al-Si-Ge-Cu-Mn alloys at 160°C. The results indicate that Mn additions reduce the aging response of the alloys, although increasing Cu content has the effect of restoring the strength

to some extent. It may, however, be noted that Mn additions do not disturb the characteristic microstructural stability of these alloys. Figure 10 shows the TEM micrograph of an artificially aged baseline + 2.5wt% Cu + 0.4wt% Mn alloy. The micrograph shows that the presence of coarse Al_x(MnGeSiCu) based precipitates (arrowed in the micrograph) result in the (GeSi) precipitate free zones around them. In addition, the strong Mn-vacancy binding in aluminum should also be responsible for producing, in general, a coarser GeSi precipitate dispersion (compare Fig. 7a with Fig. 10), and hence reduced strength properties in these materials.

Major Conclusions

(1) An Al-1at%Si-1at%Ge alloy (i.e., the baseline alloy) can be strengthened by Cu additions. The hardness increment in the baseline alloy containing up to 1 at% (~2.5 wt%) Cu is about 60%. This amount of Cu in the baseline alloy does not alter the superior microstructural stability of the baseline alloy when aged at temperatures ≤ 200°C. The hardness increment associated with the Cu additions is understood primarily to be due to the refinement of the noncoherent (GeSi) precipitates within the microstructure.

(2) Cu contents exceeding 2.5 wt% in the baseline alloy cause θ' nucleation to occur. θ' nucleation occurs predominantly at the (GeSi)-α-Al interfaces and coarsens rapidly with aging, thus causing the onset of rapid overaging in these alloys.

(3) Mn additions (~0.4 wt%) to the Al-1Si-1Ge-1at%Cu alloy reduce the strength (in terms of the hardness values) of these alloys. Formation of coarse Al_x(GeMnSiCu) particles and the presence of (GeSi) precipitate free zones around those coarse particles are understood to be the major reason for such strength reduction.

Immediate Future Plans

1. Controlled thermomechanical treatments to make use of the (GeSi) precipitates themselves to control the grain structure in the wrought products.
2. Tensile tests on the bulk Al-1Si-1Ge-1at%Cu and the Mn-bearing Al-Si-Ge-Cu alloys to evaluate the tensile properties.

3. Evaluation of the tensile anisotropy and the fatigue behavior of the materials.
4. Search for suitable alloying elements, heat treatment schedules and optimization of the alloy compositions to refine the GeSi precipitates having the diamond cubic structure, thus improving the strength properties further (cf. Fig. 11).

Figure 1. TEM micrographs showing Si, Ge and GeSi precipitation in (a) Al-1Si (b) Al-1Ge (c) Al-0.5Si-0.5 at%Ge alloys.

Figure 2. Age hardening curves at 160°C showing the effects of combined additions of Si and Ge to aluminum.

Figure 3. DSC thermographs depicting the presence of low melting eutectics in the as cast (a) Baseline alloy and (b) Baseline + 3wt%Cu alloys.

Figure 4. Age hardening curves at 160°C showing the effects of Ag, In and Zn additions to the baseline alloy.

Figure 5. Age hardening curves at 160°C showing the effects of varying amounts of Cu additions to the baseline alloy.

Figure 6. Age hardening curves at 200°C showing the effects of Cu additions (up to 2.5wt%) to the baseline alloy.

Figure 7. TEM micrographs showing the (a) GeSi precipitates in baseline + 2wt%Cu alloy aged at 160°C for 5 hours and (b) GeSi and θ' nucleation in baseline + 4wt%Cu alloy aged at 160°C for 18 hours. Note the θ' nucleation (arrowed) at the GeSi/α-Al interfaces.

Figure 8. TEM micrograph showing a very uniform deformation in a baseline + 3wt%Cu alloy aged at 160°C for 10 hours.

Figure 9. Age hardening curves at 160°C showing the effect of Mn additions to the baseline + Cu alloys.

Figure 10. TEM micrograph showing coarser GeSi dispersion together with the PFZs around the coarse Al_x(GeMnSiCu) particles in a baseline + 2.5wt%Cu + 0.4wt%Mn alloy.

Figure 11. Calculated increase in yield stress of aluminum by Si, Ge particle sizes and volume fractions.

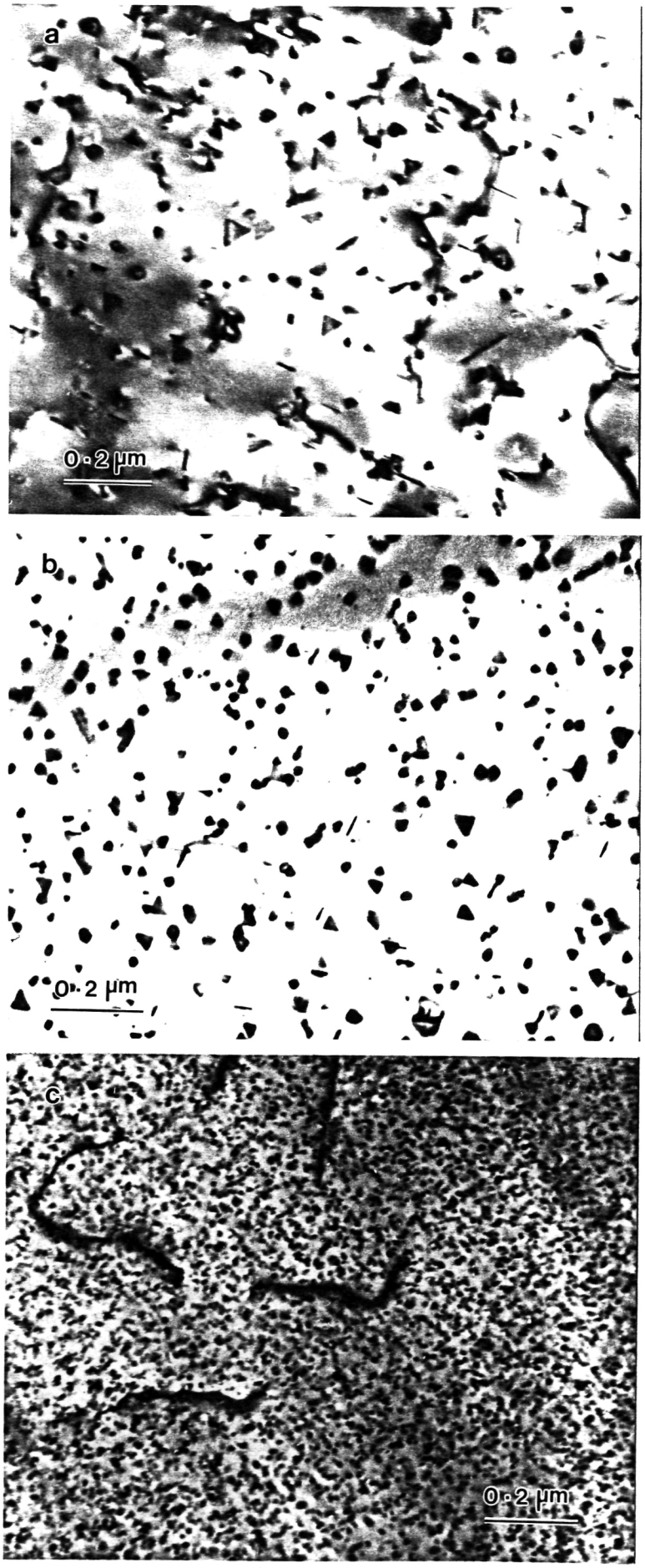

Figure 1.
TEM micrographs showing Si, Ge and GeSi precipitation in
(a) Al-1Si
(b) Al-1Ge
(c) Al-0.5Si-0.5 at%Ge alloys.

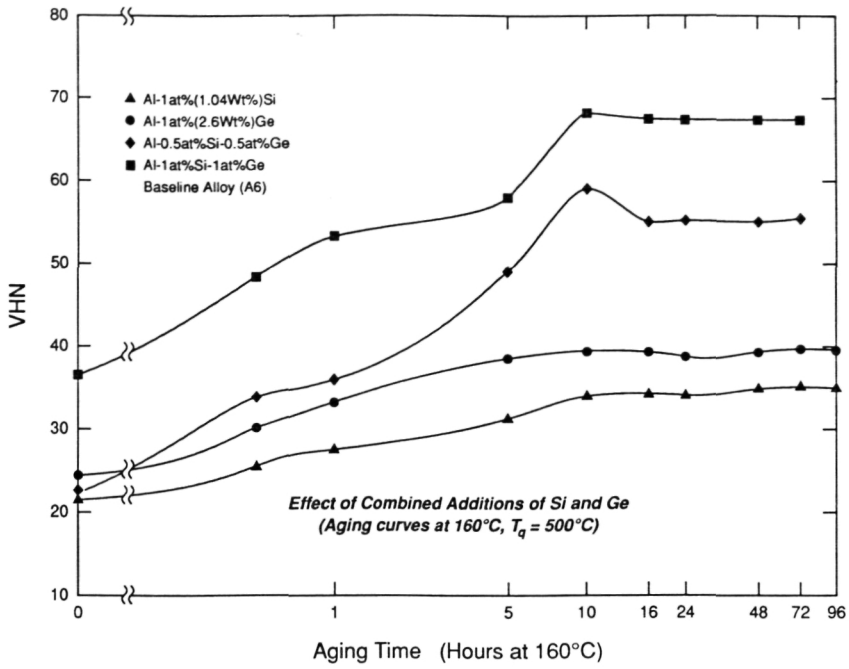

Figure 2. Age hardening curves at 160°C showing the effects of combined additions of Si and Ge to aluminum.

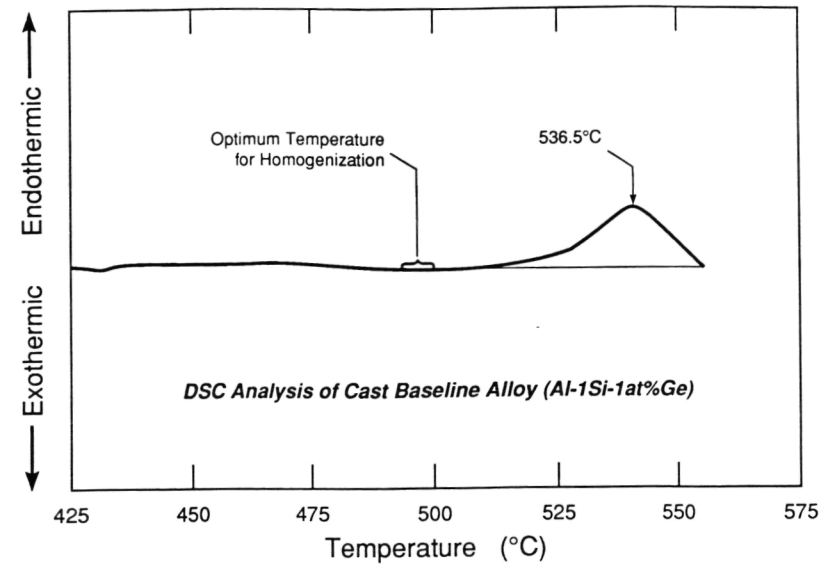

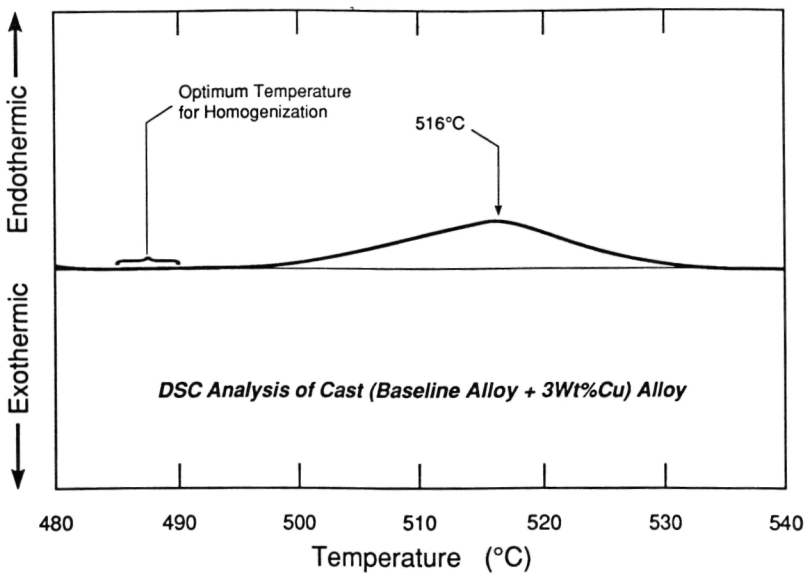

Figure 3. DSC thermographs depicting the presence of low melting eutectics in the as cast (a) Baseline alloy and (b) Baseline + 3wt%Cu alloys.

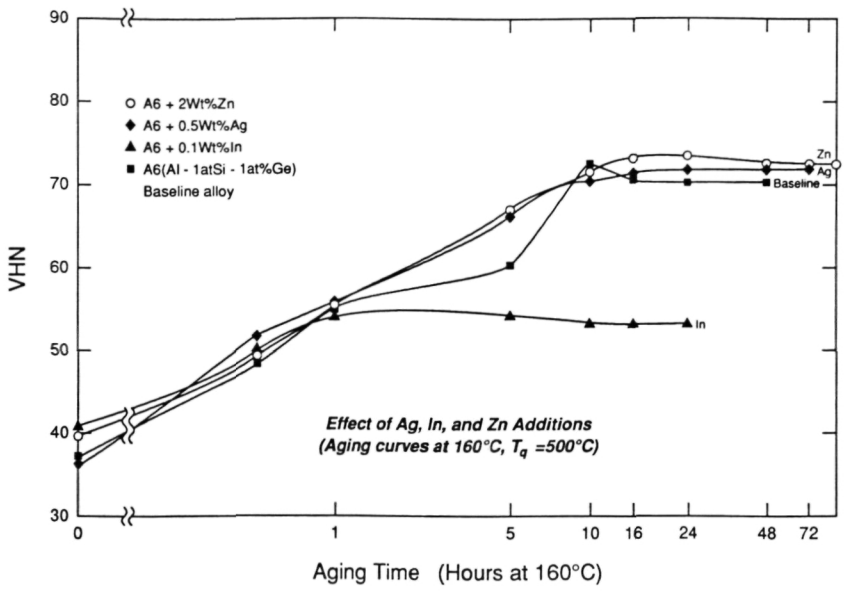

Figure 4. Age hardening curves at 160°C showing the effects of Ag, In and Zn additions to the baseline alloy.

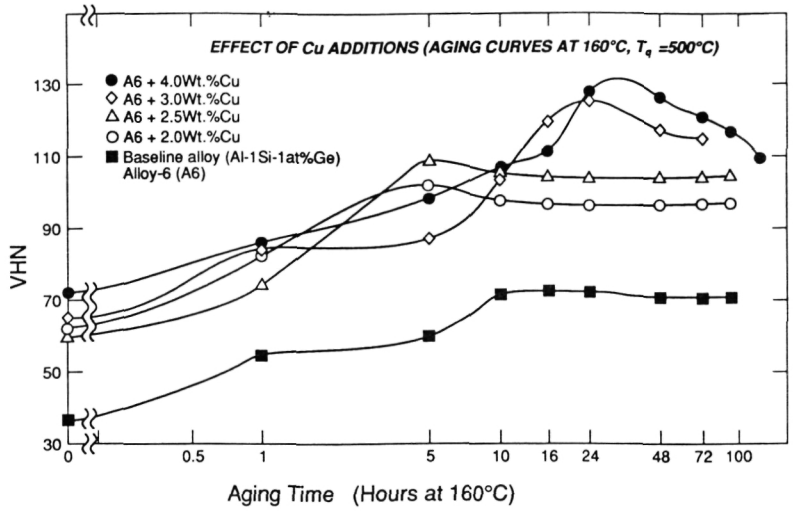

Figure 5. Age hardening curves at 160°C Showing the effects of varying amounts of Cu additions to the baseline alloy.

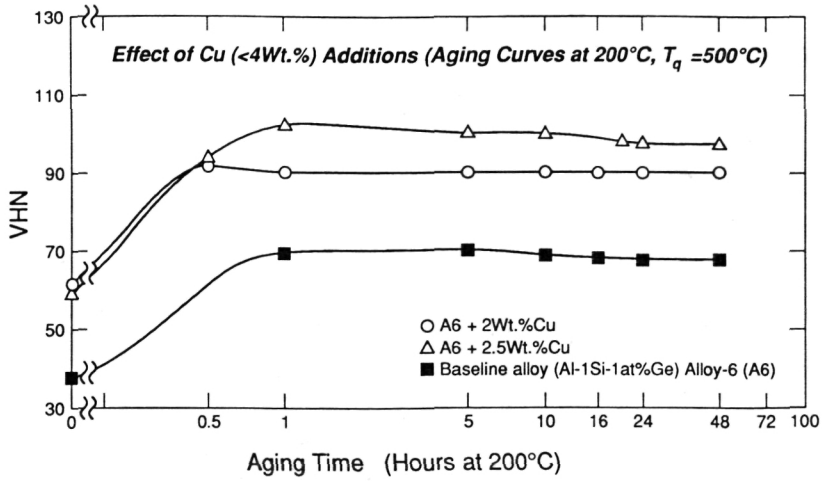

Figure 6. Age hardening curves at 200°C showing the effects of Cu additions (up to 2.5wt%) to the baseline alloy

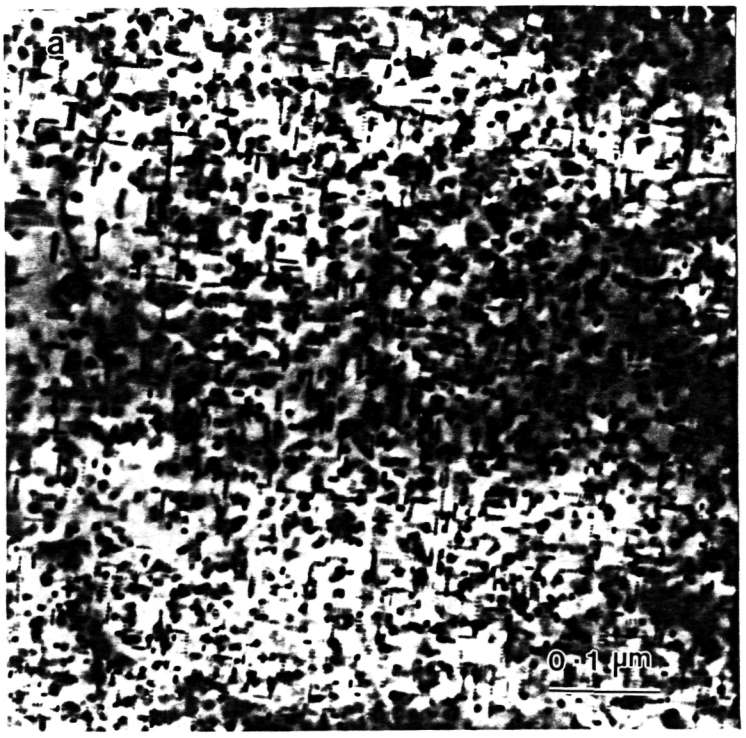

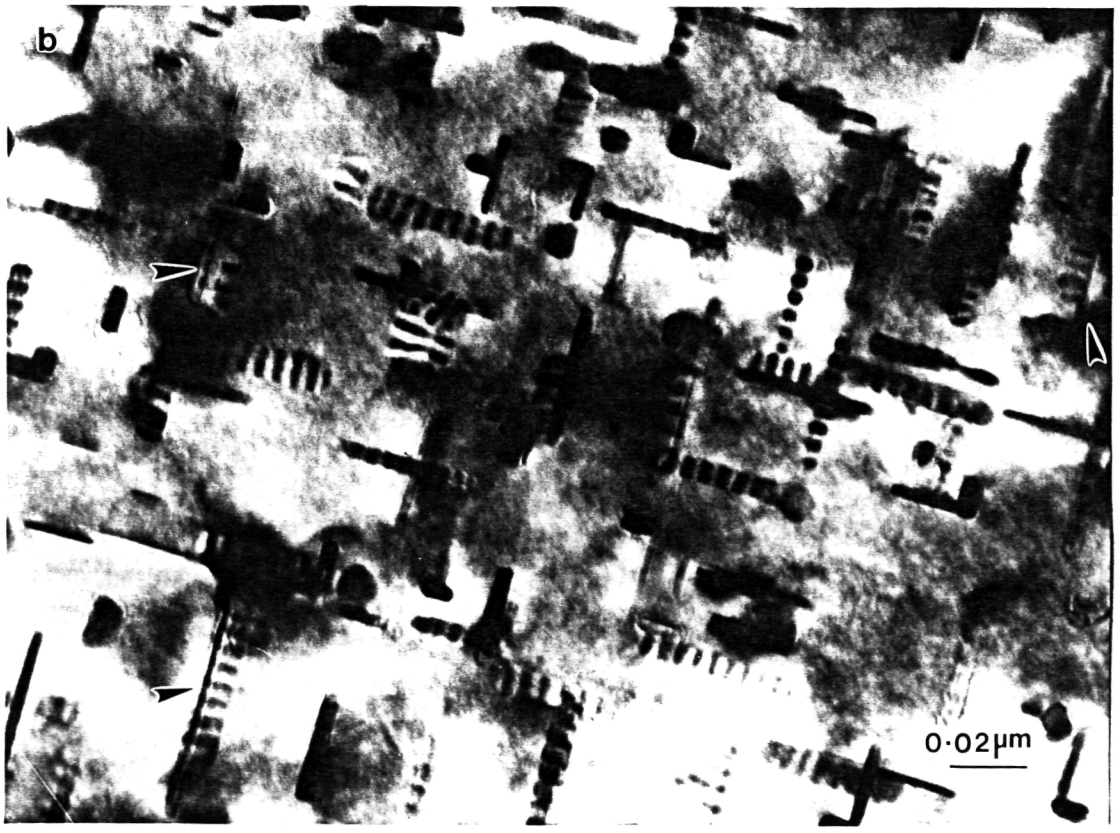

Figure 7. TEM micrographs showing the (a) GeSi precipitates in baseline + 2wt%Cu alloy aged at 160°C for 5 hours and (b) GeSi and θ' nucleation in baseline + 4wt%Cu alloy aged at 160°C for 18 hours. Note the θ' nucleation (arrowed) at the GeSi/α-Al interfaces.

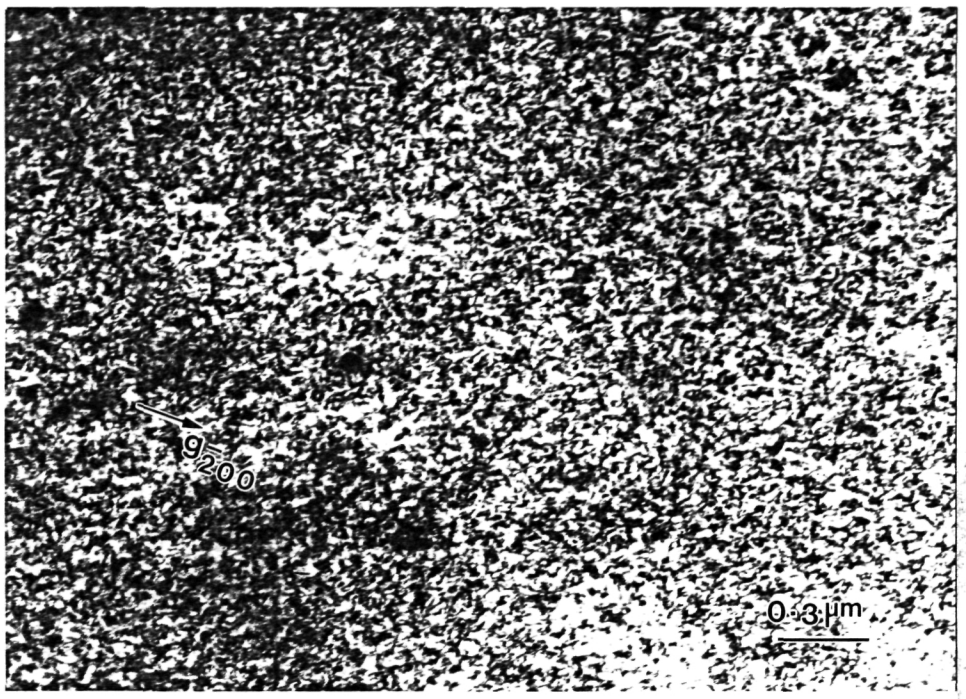

Figure 8. TEM micrograph showing a very uniform deformation in a baseline + 3wt%Cu alloy aged at 160°C for 10 hours.

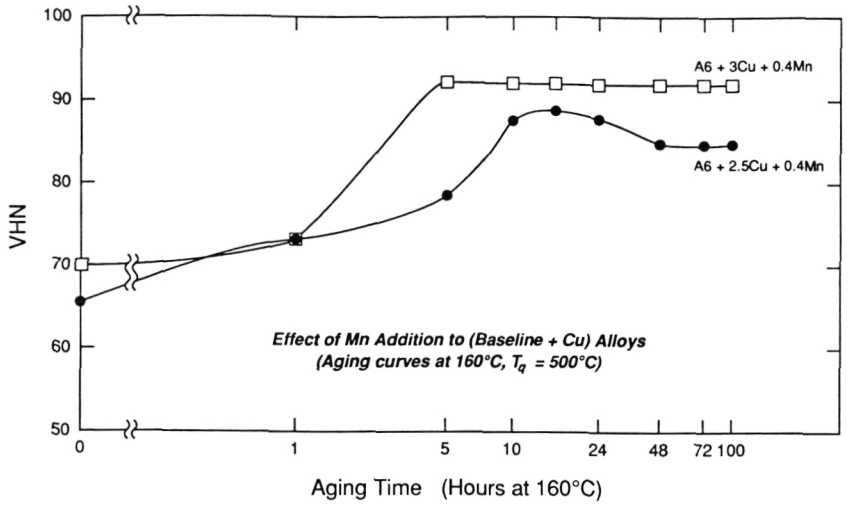

Figure 9. Age hardening curves at 160°C showing the effect of Mn additions to the baseline + Cu alloys.

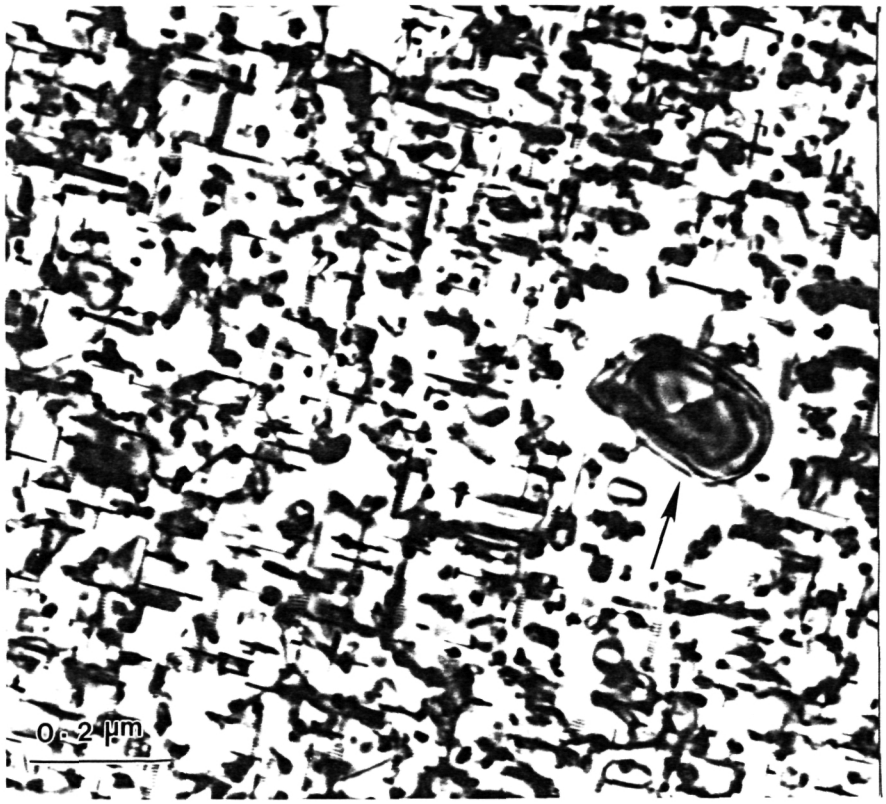

Figure 10. TEM micrograph showing coarser GeSi dispersion together with the PFZs around the coarse Al_x(GeMnSiCu) particles in a baseline + 2.5wt%Cu + 0.4wt%Mn alloy.

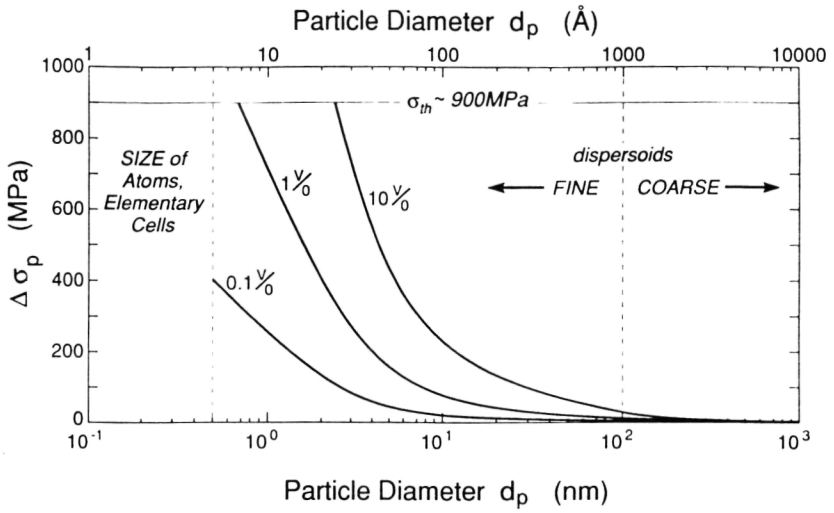

Figure 11. Calculated increase in yield stress of aluminum by Si, Ge particle sizes and volume fractions.

Project 14 **Inelastic Response of Metal Matrix Composites**

C.J. Lissenden, F. Mirzadeh, M.-J. Pindera and C.T. Herakovich

Objective

The long-term objective of this investigation is aimed at attaining a complete understanding of the inelastic response of metal matrix composites subjected to arbitrary, biaxial load histories. The core of the research program is a series of biaxial tests conducted on different types of advanced metal matrix composite systems using the combined axial/torsional load frame in the Composite Mechanics Laboratory at the University of Virginia. These tests involve primarily tubular specimens and include tension, compression, torsion and combinations of the above load histories in order to critically assess the inelastic response of advanced metal matrix composites in a wide temperature range.

Approach

The approach employed to characterize the inelastic response of advanced MMCs over a wide temperature range and arbitrary biaxial loading consists of a combined experimental and analytical program. The analytical program involves the development of models to predict initial yielding and subsequent inelastic response of MMCs using a combined micromechanics approach and laminated plate and tube analysis [1-9]. The micromechanics approach is based on the method of cells model that is capable of generating the effective response of MMCs in both the linear elastic and inelastic ranges in the presence of temperature-dependent constituent properties and imperfect bonding. Micromechanical predictions for the response of a unidirectional ply subsequently will be employed as input in macroscopic laminate analyses to predict the response of multidirectional composite tubes under combined loading. The analytical predictions will in turn be employed in identifying load histories aimed at critically testing the predictive capabilities of the developed models under the most general loading conditions.

The experimental program consists of two stages. The first stage entails development of a test method most appropriate for the given MMC system selected. SCS-6/Ti-15-3 tubes [Figure 1(a)] are currently available for testing purposes. The interfacial zone between the

silicon carbide fibers and the titanium matrix is known to be susceptible to damage. Therefore it is important to be able to distinguish between inelastic response due to the accumulation of damage and that due to actual matrix plasticity. The actual test program is carried out in the second stage.

Progress during Reporting Period

Micromechanical analyses were performed using previously written programs to determine how imperfect bonding affects the elastic properties of both unidirectional, [0] and angle ply, $[\pm 45]_s$ SCS-6/Ti-15-3 composite. In this approach the flexible interface model is used [10,11]. The nature of the imperfect bond is characterized by a normal bonding parameter R_n and a tangential bonding parameter R_t. A value of zero corresponds to a perfect bond, while a value of infinity corresponds to no bond. Figure 2 shows how elastic properties (normalized with respect to their perfect bond values) of a [0] composite degrade as the fiber/matrix bond is damaged. Clearly the axial modulus is unaffected by the bond between the constituents. All other properties shown are affected by at least one of the bonding parameters. The degradation of axial and shear moduli for a $[\pm 45]_s$ laminate is shown on a log plot in Figure 3(a). The axial modulus has a value of 22.0 msi for perfect bonding but is reduced to 6.3 msi if R_t is increased to 1.0. The degradation in axial modulus is also dependent on R_n, but to a much smaller degree. The model predicts a relatively small degradation of the shear modulus, 10.6 msi to 8.6 msi, which is also dependent upon both bonding parameters.

An initial attempt to predict the initiation of damage in a $[\pm 45]_s$ tube was made. The method was general enough to consider the residual stresses created in the manufacturing process as well as any internal pressure, axial load, or torsional load applied to the tube. A tube analysis program was used as well as a damage initiation criterion based upon Johnson, et al. [12] visually observing fiber/matrix separation in the same material system (but a different fiber volume fraction) at a transverse fiber stress level of about 20 ksi. The results were used to determine what type of experiments would be most beneficial and also to compare with the experimental results.

Test Method A series of axial or torsional tests to sequentially higher load levels was prescribed. At each load level, both axial and torsional stiffnesses were measured. Designate a series of axial tests as Type I Loading and a series of torsional tests as Type II

Loading. Figure 1(b) schematically shows one such test in the series, for each type of loading. This procedure provided an assessment of the inelastic response due to both matrix plasticity and damage to the fiber/matrix interface. It is anticipated that this procedure will also enable the authors to distinguish between matrix plasticity and damage.

$[0_4]$ Tests Two $[0_4]$ tubes were tested to failure, one using Type I loading and one using Type II loading. A total of 40 experiments were conducted on the two specimens. As expected, no inelastic response was observed for the Type I loading. However, an ultimate strength of 120 ksi was attained, which is far below the expected strength of 230 ksi. The failure occurred at the end of the gage length where the tube was bonded to the fixture that introduces the load from the test machine into the specimen. The fracture surface indicated that failure was due largely to bending stresses at the end of the fixture. A finite element analysis using the ABAQUS program revealed that, at the end of the fixture, large stress concentrations exist in all components of stress; axial, radial, hoop and shear. The radial stress concentrations were the highest, approximately 125% of the transverse strength of a [0] specimen. This high radial stress concentration was caused by the restraint the fixture provided to the transverse deformation of the tube during axial loading. Effectively, large bending stresses were present at the end of the fixture.

Inelastic response was observed for Type II loading. By comparison with the analytical model the inelastic response can be attributed to damage to the fiber/matrix interface. This damage caused the stress/strain response to have a distinct change in stiffness at a stress level of 40 ksi. The experimental stress/strain curve above the 40 ksi stress level was essentially flat. This behavior was not predicted by the current analytical model. Modifications to the analytical model currently being made under a different research program indicate, at least in a preliminary sense, that the behavior seen in the experiment can be approached analytically.

No degradation of the axial or shear moduli was observed experimentally. The analytical model predicted no change in the axial modulus with damage, but did predict a rather large change in the shear modulus for an imperfect R_t bonding parameter. Figure 5(a) shows both axial and shear moduli at one point on the tube determined from a strain gage rosette.

Preparations have also been made to allow for the introduction of an internal pressure into the [0] tubes. To accomplish this, hardware has been modified and equipment tested.

Analytical predictions have been made to determine the results of hypothetical experiments. These predictions indicate that certain tests will show a large degradation of the transverse modulus.

$[\pm 45]_s$ Tests A total of 32 experiments have been conducted on two $[\pm 45]_s$ specimens, one specimen was devoted to Type I loading and one to Type II loading. Type I loading was incremented until failure occurred at an axial stress of 68 ksi, but the torsional failure load was unattainable for Type II loading due to the large torsional rigidity of the tube.

Both $[0_4]$ and $[\pm 45]_s$ tubes were manufactured using the hot isostatic pressing technique. In the manufacturing process the silicon carbide fibers are woven together with molybdenum wires to form a cloth. Alternating layers of titanium foil and fiber cloth are wrapped around a mandrel to form the tube. A seam in the fiber cloth is present where the two ends come together. An imperfect seam has fiber rich zone and a fiber depleted zone. The $[\pm 45]_s$ tubes exhibit an imperfect seam. The variation in the fiber volume fraction introduces a non-uniformity in the measured stiffness of the tube as shown in Figure 3(b). Away from the seam the axial stiffness was 16.1 to 16.6 msi, while near the seam the stiffness varied from 14.6 to 20.6 msi. These stiffness values were derived from the stress/strain response after the initial knee. This knee will be discussed later in the report. Seven strain gages were used to measure strains around the circumference of the tube.

The analytical model predicted that the response of the $[\pm 45]_s$ tubes to axial, Type I loading would be largely nonlinear, while the response to torsional, Type II loading would exhibit only a small degree of nonlinearity. Experimentally, a highly nonlinear response consistent with the prediction was obtained for Type I loading. However, no nonlinear response was observed up to the torsional capacity of the test machine for Type II loading. Figure 4(a) shows the axial stress/strain response for the Type I loading experiments performed on a specimen. The data shown were collected by one strain gage rosette and are typical of the tube response. Data are shown from Test #10, where nonlinear response was first observed, to Test #20 when failure occurred. Close scrutiny of the figure reveals that a certain amount of hysteresis takes place during the loading and unloading cycles. This could be due to the opening and closing of cracks in the fiber/matrix interfacial zone. Coupling exists between the axial and torsional responses for Type I loading at high axial stress levels. These tests were conducted in load control, hence when the torsional loading

was applied the axial stress was held constant. The axial strain however did not remain constant, but increased as the torsional load increased. The analytical model qualitatively predicted that coupling does exist at high load levels, but at this time is unable to simulate the experiment precisely. The nonlinear response seen in the figure is caused first by damage to the fiber/matrix interface, then to plasticity effects of the titanium matrix, then to the coupling previously discussed. The initiation of damage was accompanied by sound emissions that grew in intensity as the damage state progressed until a peak or saturation level was achieved. These sound emissions followed the Kaiser effect in that the sound emissions were not heard in a subsequent experiment until after the maximum stress level of the previous experiment was reached.

During each increment of the Type I loading experiments where a nonlinear response was obtained the axial stiffness degraded. Figure 4(b) shows the degradation in the axial stiffness for a typical increment. The initial stiffness is high relative to the stiffness measured for the remainder of the experiment. This initial stiffness drops after the initial knee, which is thought to correspond to overcoming the residual stresses from the manufacturing process. Once further damage starts to occur, the stiffness degrades further. Plasticity effects reduce the stiffness even more. During the biaxial portion of the experiment, coupling can take place and cause the stiffness to be zero, because the axial stress is being held constant. Upon unloading, the stiffness is always less than the initial stiffness and stays relatively constant. The degradation of both the axial and shear moduli is shown in Figure 5(b) for Type I loading. This data is from a point on the tube and is determined from a strain gage rosette.

A comparison between the analytical model and experimental data is given for Type I loading in Figure 6. The predicted axial response for perfect bonding, $R_n = R_t = 0$ and total debonding, $R_n = R_t = 1$ bracket the experimental results nicely. However, the experimental shear modulus degraded much more than the model predicted it would.

Future Work

The analytical model predicts a large degradation in the transverse modulus as the normal bonding parameter increases [see Figure 2(a)]. To verify this phenomenon experimentally a $[0_4]$ tube will be subjected to internal pressure. A biaxial stress state generated by internal pressure and either axial load or torsional load applied to the $[0_4]$ tubes will help to ascertain whether the model can accurately predict the material response to this

type of biaxial loading.

The next anticipated experiments to be conducted on the $[\pm 45]_s$ tubes are biaxial tests comprised of different ratios of torsional to axial load. These experiments will be aimed at characterization of the initial damage envelope for a $[\pm 45]_s$ tube. They will provide guidance in the development of a model that can predict with sufficient accuracy, the initial damage envelope for a general multidirectional composite. The experiments will also provide a more general description of how damage affects the material properties.

Efforts will be continued to correlate theoretical predictions with the experimentally obtained data. Improvements to the predictions of initial damage to a multidirectional MMC will be made until a satisfactory agreement with the experimental data is achieved. Comparison of theory and experiment for the overall inelastic response of a MMC to a most general loading will be attempted.

References

1. Derstine, M.S. and Pindera, M-J., "Nonlinear Response of Composite Tubes Under Combined Thermomechanical Loading," in Composites and Other New Materials for PVP : Design and Analysis Considerations, ASME PVP-Vol 174, D. Hui, T.J. Kozik, G.E.O. Widera and M. Shiratori, Eds., pp. 19 - 28, 1989.

2. Derstine, M.S., Pindera, M-J. and Bowles, D.E. Combined Mechanical Loading of Composite Tubes," CCMS-88-11 (VPI-E-88-18) Report, VPI & SU, Blacksburg, VA., June 1988.

3. Pindera, M-J. and Herakovich, C.T., "Influence of Stress Interaction on the Behavior of Off-Axis Unidirectional Composites," in Fracture of Composite Materials, G.C. Sih and V.P. Tamuzs, Eds., Martinus Nijhoff, 1982.

4. Aboudi, J., "Elastoplasticity Theory for Composite Materials," Solid Mechanics Archives, Vol. 11, pp. 141-183, 1986.

5. Pindera, M-J and Aboudi, J., "Micromechanical Analysis of Yielding of Metal Matrix Composites," Int. Journal of Plasticity, Vol. 4, pp. 195-214, 1988.

6. Herakovich, C.T., Aboudi, J. and Beuth, J.L., Jr., "A Micromechanical Composite Yield Model Accounting for Residual Thermal Stresses", (to be submitted).

7. Pindera, M-J. and Lin, M.W., "Micromechanical Analysis of the Elastoplastic Response of Metal Matrix Composites," Journal of Pressure Vessel Technology, Vol. 111, June 1989, p. 183.

8. Pindera, M-J., Becker, W., Aboudi, J. and Herakovich, C.T., "Nonlinear Response of Unidirectional Boron/Aluminum," Journal of Composite Materials (1989, in press).

9. Pindera, M-J. and Aboudi, J., "Recent Developments in the Micromechanics of Advanced Composites," Proceedings of the Second International Conference on Development and Design with Advanced Materials - ATMAM '89, August 16 - 18, 1989, Montreal, Quebec, Canada.

10. Jones, J.P. and Whittier, J.S., "Waves at a Flexibly Bonded Interface," Journal of Applied Mechanics, pp 905-909, Dec. 1967.

11. Aboudi, J., Mechanics of Composite Materials A Unified Micromechanical Approach, Elsevier, Amsterdam, The Netherlands, pp 284-310, 1991.

12. Johnson, W.S., Lubowinski, S.J., Highsmith, A.L., "Mechanical Characterization of Unnotched SCS-6/Ti-15-3 Metal Matrix Composites at Room Temperature," ASTM Standard Technical Publication 1080-1990.

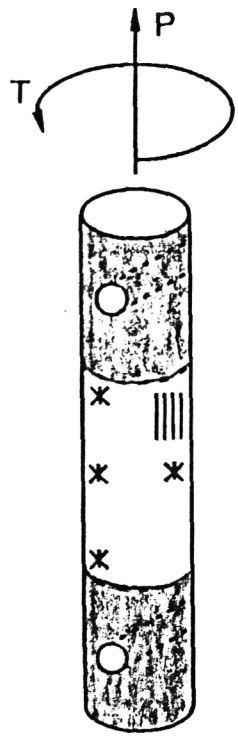

$[0_4]$

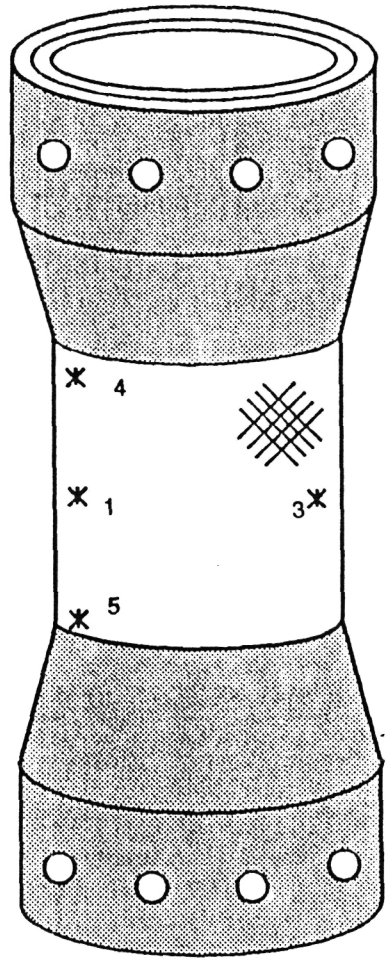

$[\pm 45]_s$

(a) Tube Geometry

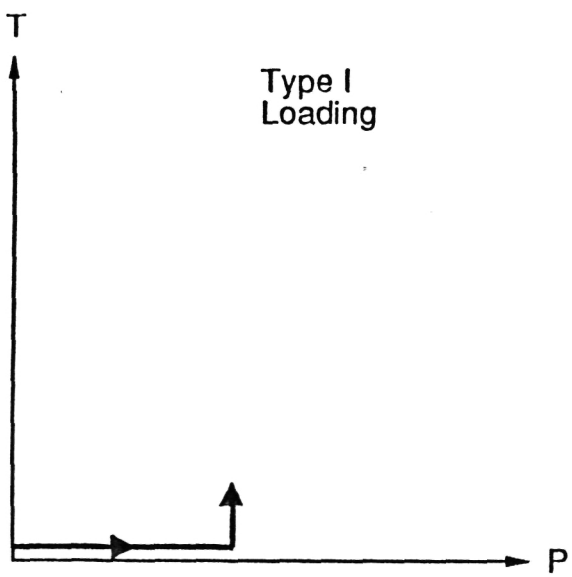

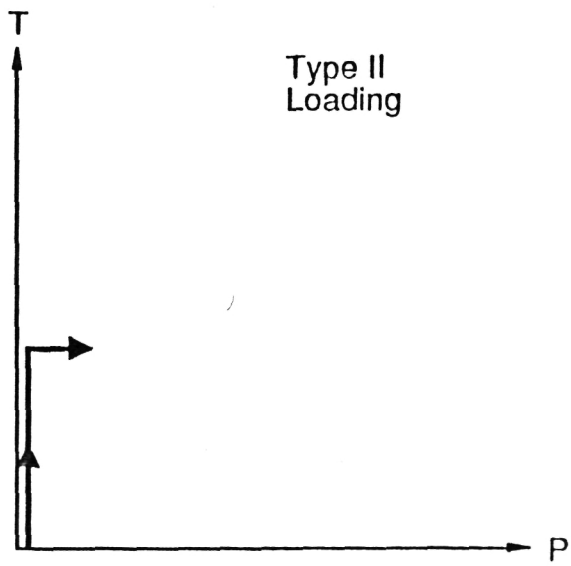

(b) Biaxial Loading Types

Figure 1: Tube Geometry and Loading

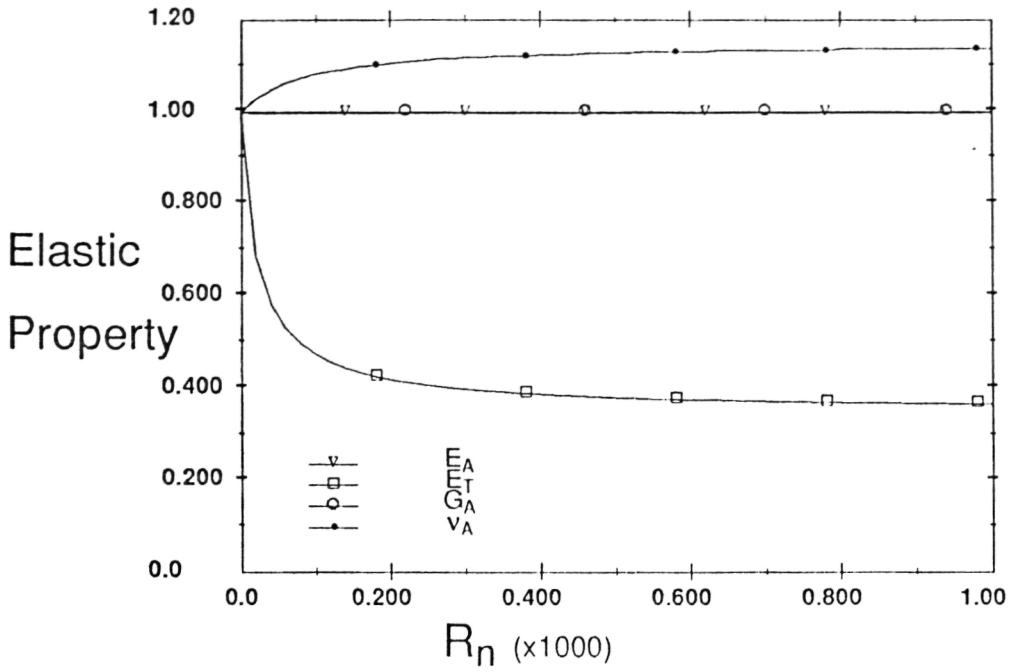

(a) R_n Variation

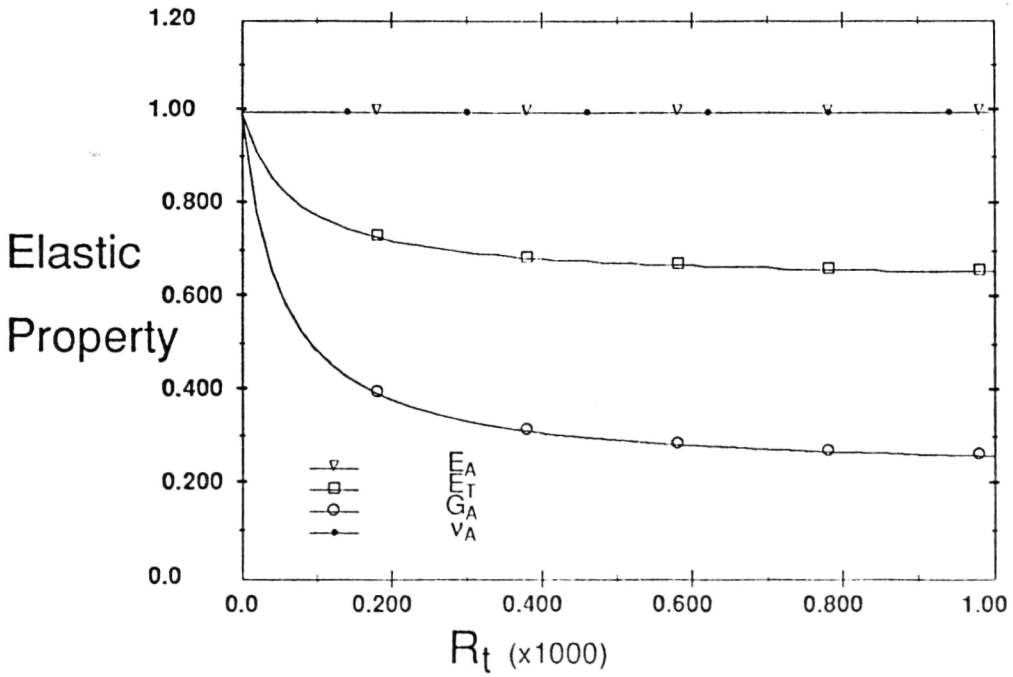

(b) R_t Variation

Figure 2: Variation in Properties for [0]

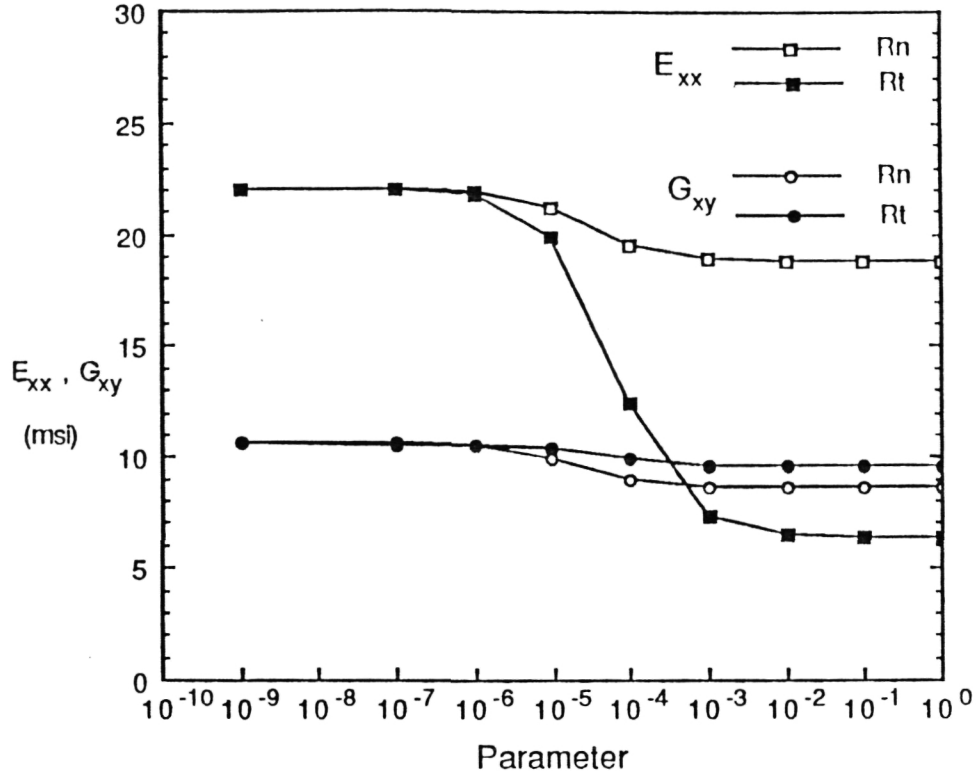

Figure 3(a): Variation in Properties for $[\pm 45]_s$

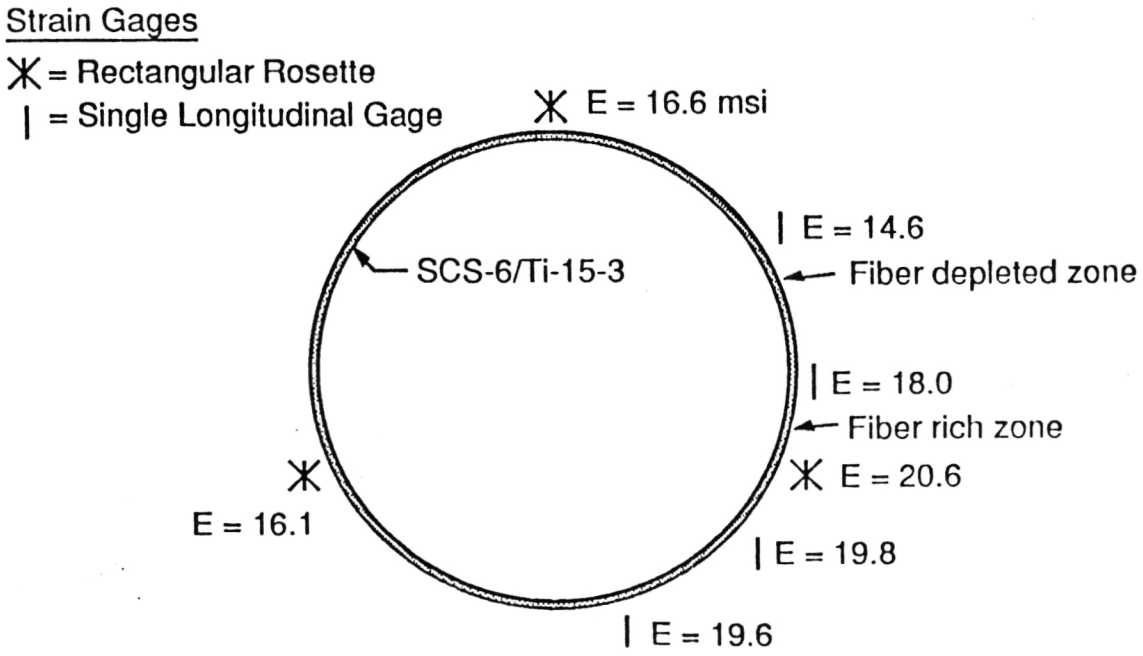

Figure 3(b): Non-Uniformity of $[\pm 45]_s$

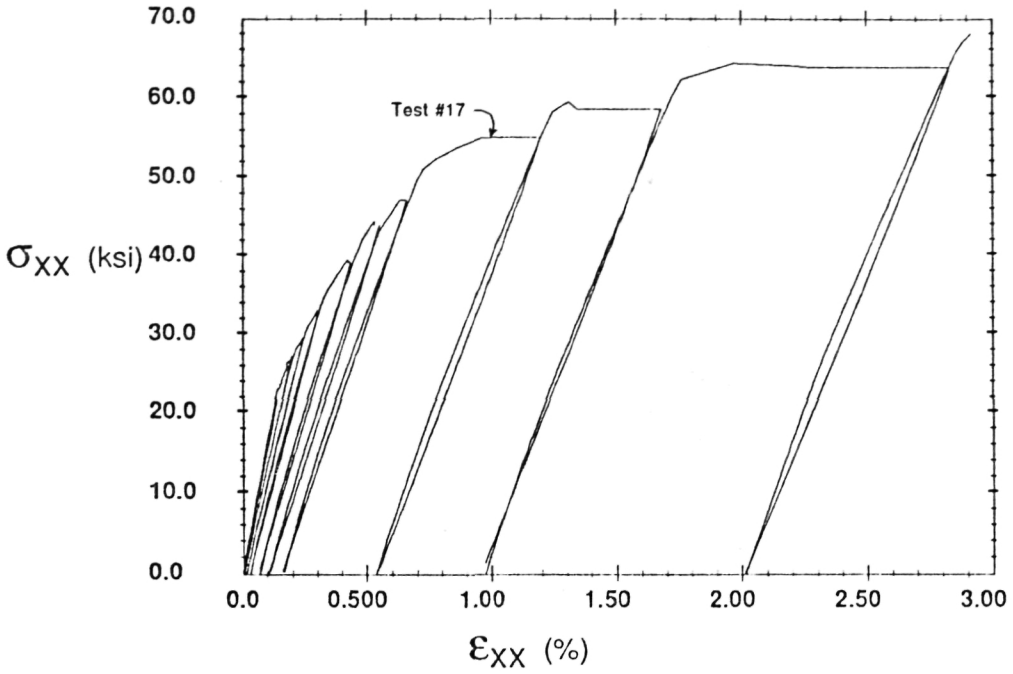

(a) Stress-Strain Response (Tests 10-20)

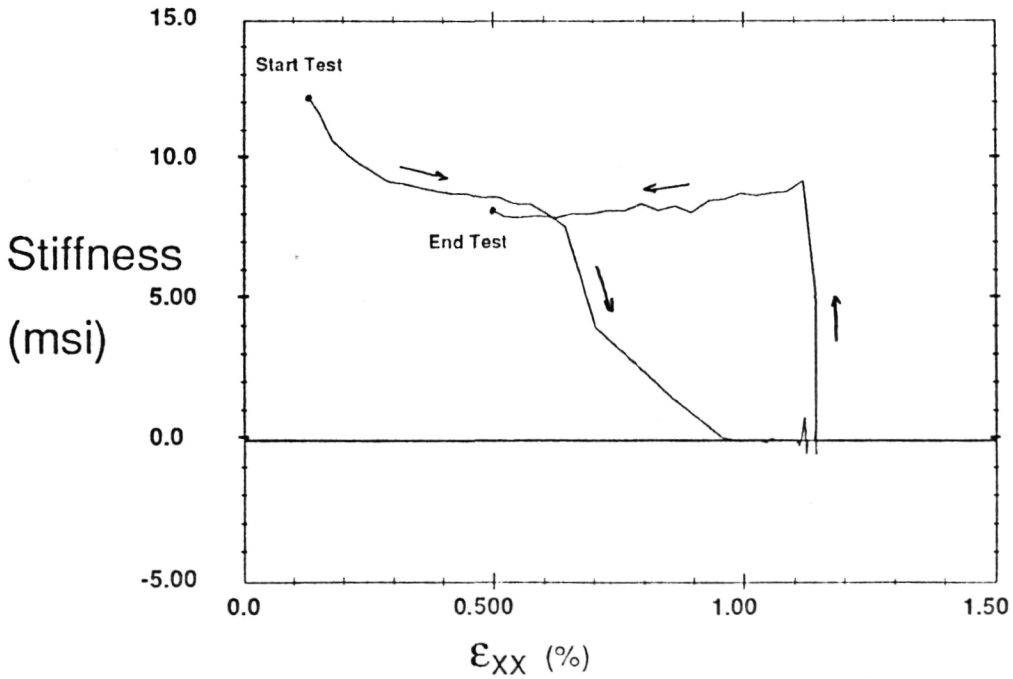

(b) Test#17 Stiffness Degradation

Figure 4: $[\pm 45]_s$ Experimental Results

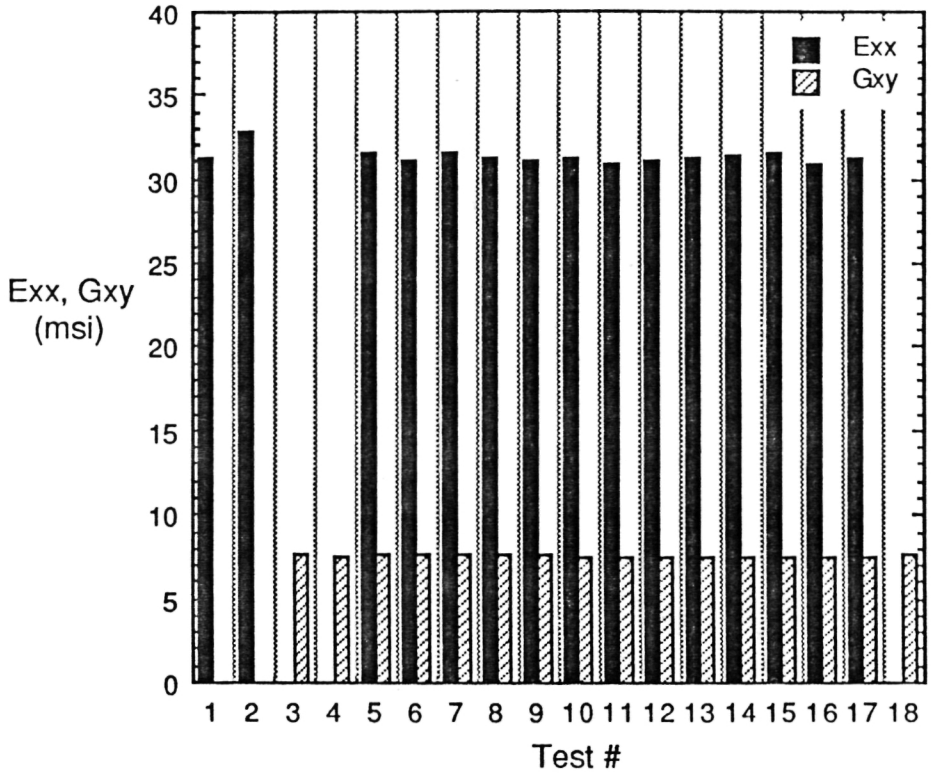

(a) $[0_4]$ Type II Loading

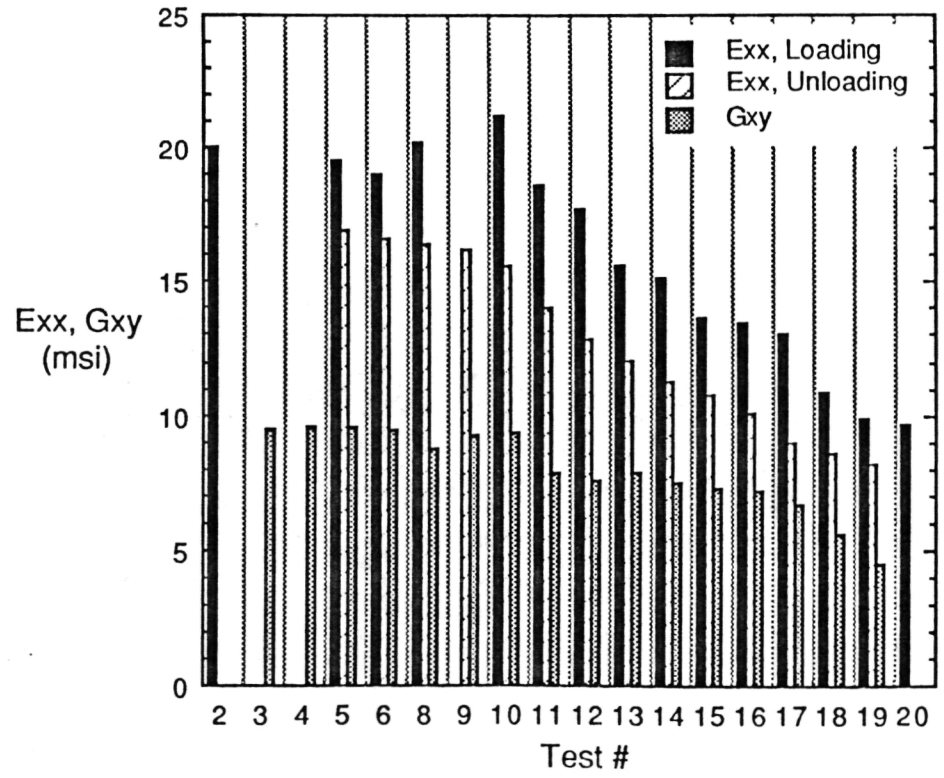

(b) $[\pm 45]_s$ Type I Loading

Figure 5: Experimental Moduli

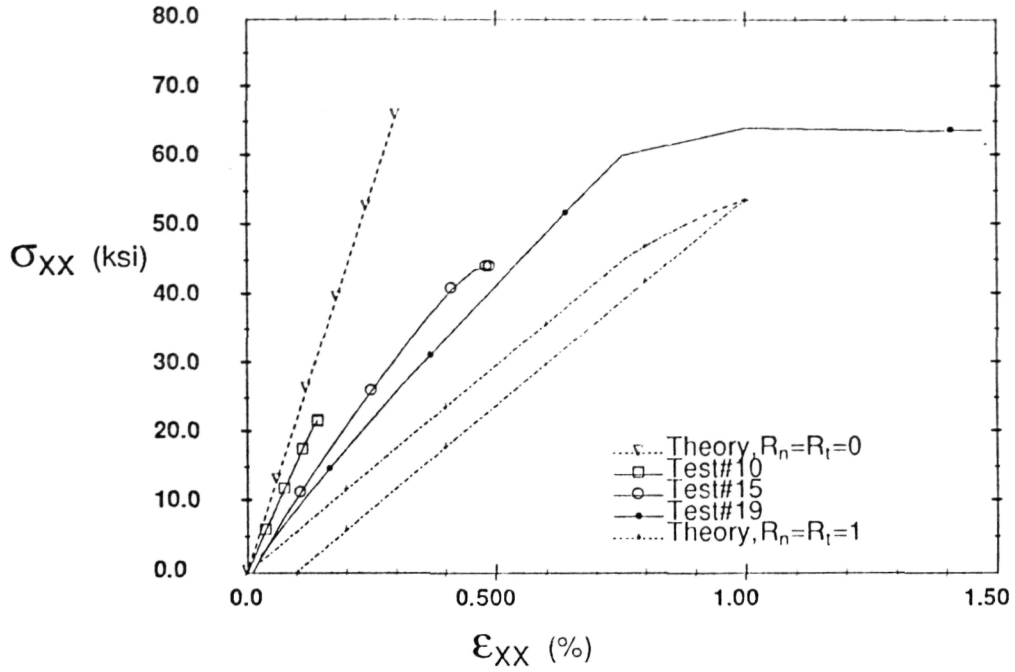

(a) Axial Response

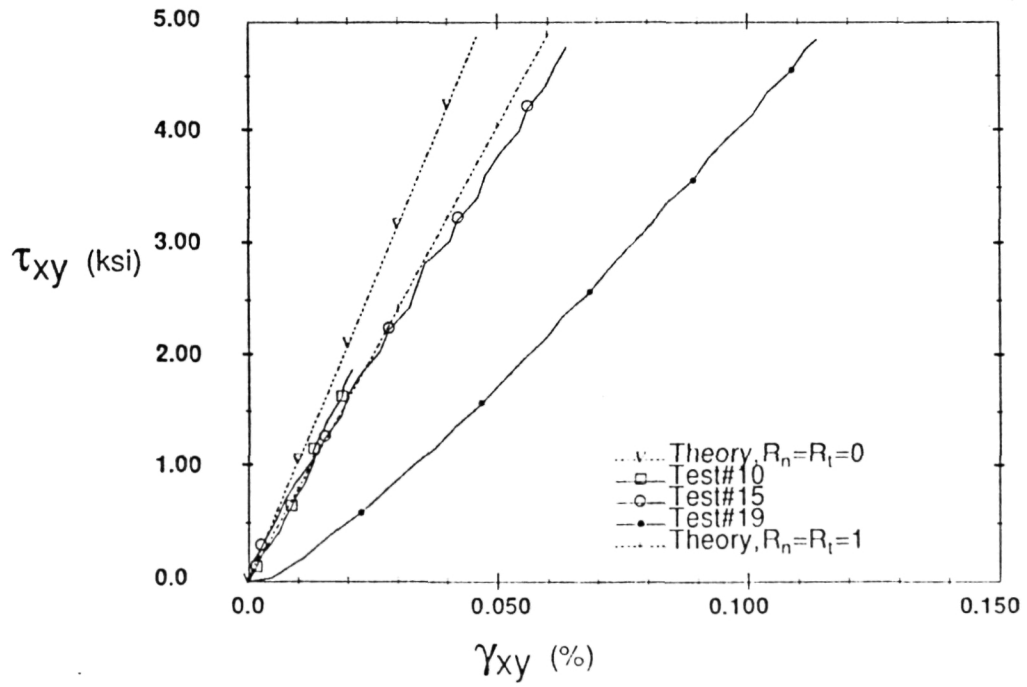

(b) Shear Response

Figure 6: $[\pm 45]_s$ Theory/Experiment Comparison

BACK

Project 15 **Effect of Temperature on the Response of Metallic Shell Structures**

C. Copper, K. McCarthy, T. Johnson, W.D. Pilkey and J.K. Haviland

Research Objectives

The research for 1990 and previous years had the title "Design of Cryogenic Tanks for Space Vehicles". This was carried over to the beginning of 1991. The objective was to investigate a new structural design for the tanks of large launch vehicles, using the proposed Advance Launch System (ALS) vehicle as an example. The proposed design consisted of superplastically formed corrugated hat-section stringers and frames in place of the integrally machined I-section stringers and skins supported by separate frames that had been originally planned. The stringers and frames would be manufactured in subassemblies which would be spot-welded into place on the skins.

The present objective is to investigate thermal problems in shell structures, such as the hydrogen tanks in the Aerospace Plane or the fuselage structures of high speed civil transports. Such thermal problems would arise when a shell is subjected to external heating while the internal walls are maintained at the temperatures of cryogenic fuels in the Aerospace Plane, or when there are severe temperature variations around or along the fuselage of a high speed civil transport. Depending on the particular design, the tank could be load carrying, subject to compression and bending loads. The presence of stiffeners and frames could complicate the problem considerably, especially because they could lead to thermal buckling.

An additional objective, of a program supported by a related NASA grant, is to define a set of test problems which can be used to evaluate the accuracy of structural finite elements with thermal loads. These tests could then be used to choose appropriate elements to be used to analyze a real problem, and to help code developers to identify weaknesses of existing elements.

Finally, we are developing improved formulas for cross-sectional thermal stresses in structural members. Such formulas are tractable now due to the availability of computers to practicing engineers.

Approach

The principal method of analysis has been computational finite element analysis. The stringer investigation mainly involved buckling analyses using the COMPUTATIONAL ANALYSIS TESTBED (COMET) program at NASA-LaRC. Unfortunately, this could not handle the thermal analysis problems started later in the year. Therefore, the EAL program was used for thermal analyses. All of the computational work was done remotely using TELNET, both to send inputs to the CONVEX computer at NASA-LaRC and to recover the results for plotting by PATRAN at the University.

Test problems for finite elements are defined using pre-existing solutions to known problems. A problem can be a candidate test problem if it has a fairly simple geometry, it's boundary conditions that can be easily reproduced on the majority of finite element codes, and it has a known solution that can be expanded to consider temperature dependant material properties. Many possibilities can come to mind, but different test problems should exhibit different problem geometry, element geometry, and loading.

For the effort to determine accurate cross-sectional thermal properties of beams, new formulations for the calculation of shear forces caused by linearly varying temperature changes are being developed.

Progress During the Reporting Period

The work done on the program "Design of Cryogenic Tanks for Space Vehicles" was discussed in the previous report for 1990. In brief models of integrally machined stringers and superplastically formed corrugated hat-section stringers were constructed, and buckling stresses were determined by analyzing single stringers attached to skin panels, much as is done analytically in classical panel buckling calculations. It was confirmed that the formed stringers performed as well as the integrally stiffened ones. Attention was next directed to the question of how they could be used in a pressurized tank design, which was to have been 30 feet in diameter, and 30 feet high, with the upper quarter (7.5 feet) made from 0.25 inches thick aluminum. Available computer memory ruled out the possibility of using the original stringer details for the preliminary analyses. Therefore a stringer model (see Fig. 1) was used to determine beam properties of the stringer. These properties were then used to model offset beams in a one sixteenth (7.5 feet long, 90 degree arc) tank model. The same stringer design was used to model circular frames.

The overall tank design was intended to carry an ultimate load of 5.3 kips/in (that is, overall buckling load per inch of circumference) with an internal pressure of 26 psi. It was found that the tank buckled at 10 kips/in, although, had local buckling in the stringers been considered, buckling would have occurred around 6 kips/in. Lacking design specifications, it was assumed that the tank should not buckle in the absence of internal pressure, since it would still be otherwise operational. A buckling analysis without internal pressure and without rotational stiffness in the stringers (an uncertain quantity) gave a buckling strength of 5.9 kips/in. The buckling mode (see Fig. 2) involved stringers and frames rather than local skin buckling.

For the thermal analyses, a tank with a diameter of 120 feet and a half length of 60 feet and aluminum skin, 0.75 inches thick, was modeled using shell elements. A plane of symmetry was assumed at the center of the tank. Two open-ended models were developed, one was quarter (90 degrees) round, the other was half (180 degrees) round. Two further quarter and half round tanks were modeled with spherical ends. A fifth quarter round open-ended tank was also modelled using solid elements, for comparison with the tanks modelled using shell elements. These five tank models are shown in Fig. 3. All of the tank models were subjected to temperature gradients of 1000 degrees per inch. Thus, the internal temperatures were -375°F, and external temperatures were 375°F. Because this was intended as a first look, the numbers of elements were kept low, ranging from 100 for the open-ended quarter round tank to 400 for the closed-ended half round tank. It was found that stresses were one dimensional, i.e., midplane stresses were zero and internal surface stresses were exactly equal to:

(Young's Modulus) x (Therm. Exp. Coeff.) x (Half Thick.) x (Temp. Grad.) / (1 - nu)

The only exceptions were seen within about 3/10 of the tank radius from an open end, when the stresses in the axial direction headed for zero. Displacements were also zero except near the open ends, where the skins bent inward.

The half round open-ended tank was also subjected to a sinusoidal temperature variation in the circumferential direction. Temperatures were two-dimensional except within about 3/10 of the tank radius from the open end.

A half round closed-ended tank was fitted with three internal fin bulkheads (0.75 inch

thick, 55 inch internal radius) which were held at the internal -375°F temperature. Considerable displacements and stress variations were noted which made it appear that the tank might be subjected to buckling. However, a buckling analysis revealed no positive eigenvalues. A similar tank with external bulkheads held at the external 375°F temperature was found to buckle, however, the first buckling mode mainly involved buckling of the fin itself. When the bulkheads were replaced by tubular ring frames with areas of 3.75 sq. in. (the same as the bulkheads), buckling was noted when the frames were held at the external temperature of 375°F at an eigenvalue of 2 (equivalent to surface temperatures of ± 750°F, but there is no absolute temperature here). Of course, when the frames were held at -375°F, buckling eigenvalues were negative. The first buckling mode indicated small deflections in the frames and large deflections in the skins (see Fig. 4). These results point to the conclusion that it is best that any stiffeners on the tanks should be submerged in the cryogenic fuel, and that they should not be subjected to external heating.

An extensive bibliography on thermal stresses was found. It was not used in this period.

Some consideration was given to the best finite element program for this study. It was concluded that, for the short term, EAL was best. However, for the long term, especially where nonlinearities are important, ABAQUS may be the most appropriate program.

Test problem development for finite elements has concentrated on a plane stress or plane strain problem of a flat disk or the cross section of a thick pipe. The finite element models a 10 degree arc of the total structure with the help of symmetry (see Fig. 5). ANSYS elements have been used as test elements. Results have shown that the accuracies of different elements are affected differently as material properties are varied.

For the cross-sectional properties problem, examples are being run comparing a more precise theory for normal stress to the classical strength of materials theory. An error of up to 15 percent is being realized for some temperature distributions. This error occurs in highly stressed sections of the beam.

Conclusions

1. The proposed design for large tanks, using superplastically formed stringers and frames, appears to be feasible. Such tanks could be fabricated by first making

superplastically formed grids consisting of stringer and frame sections, and then by spot-welding them to the inner surfaces of the tank. Further analyses to confirm this concept should look at the effects of manufacturing defects and should be performed on a much more detailed model in a supercomputer. There are no plans now for such work.

2. Thermal stresses in uniform unstiffened shells appear to be close to one-dimensional, although effects of circumferential and longitudinal temperature gradients remain to be studied.

3. Hot external stiffeners could cause buckling of a tank, and such designs should be checked carefully. Cold internal stiffeners, however, may result in stable tank structures.

4. The results of the thermal analyses of tanks carried out to date must be treated with caution because the models used consisted of very few elements.

5. It is apparent that different material property temperature dependencies have a important effect on finite element accuracy.

6. There is a significant difference between classical strength of materials and theory of elasticity in determining beam cross-sectional stresses.

Tasks for Next Reporting Period

1. Use the bibliography mentioned above for an extensive literature search; most especially, to locate models which can be used to verify finite element solutions.

2. Extend current work on unstiffened tanks to include non-cylindrical tanks, and tanks with various temperature gradients.

3. Study various designs for stiffened tanks and fuselage sections, especially to look for instances of thermal buckling. Stiffening could include stringer/frames, double walls,

and sandwich construction, with or without insulation.

4. Study use of the ABAQUS program (available at UVA).

5. Use ABAQUS to study nonlinear effects.

6. Start analyses of tanks with composite skins.

7. The next test problem of finite element codes to be considered will be the surface of a sphere with a temperature distribution varying from pole to pole.

8. The completion of a theory of elasticity based formulation for shear stresses in thermally loaded beams.

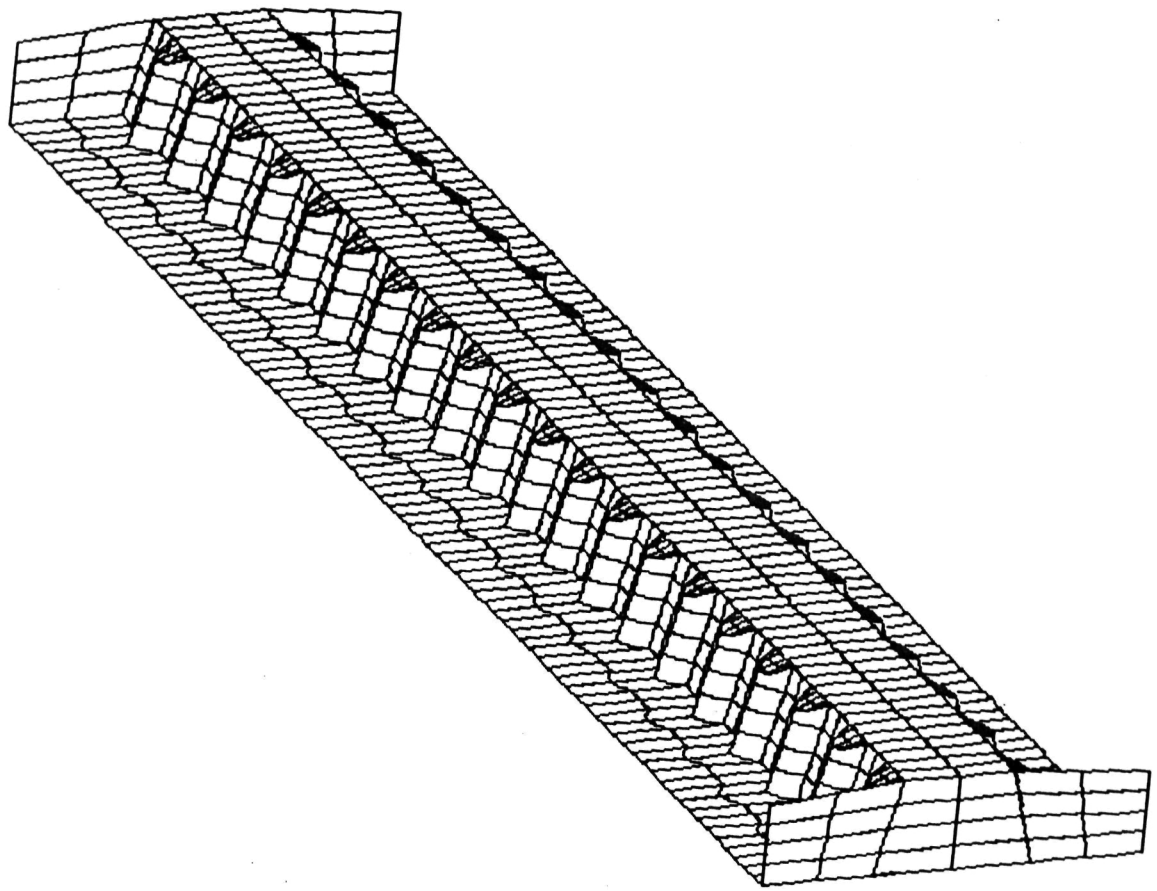

Figure 1: FEM Model of SPF Hat for the ALS Fuel Tank

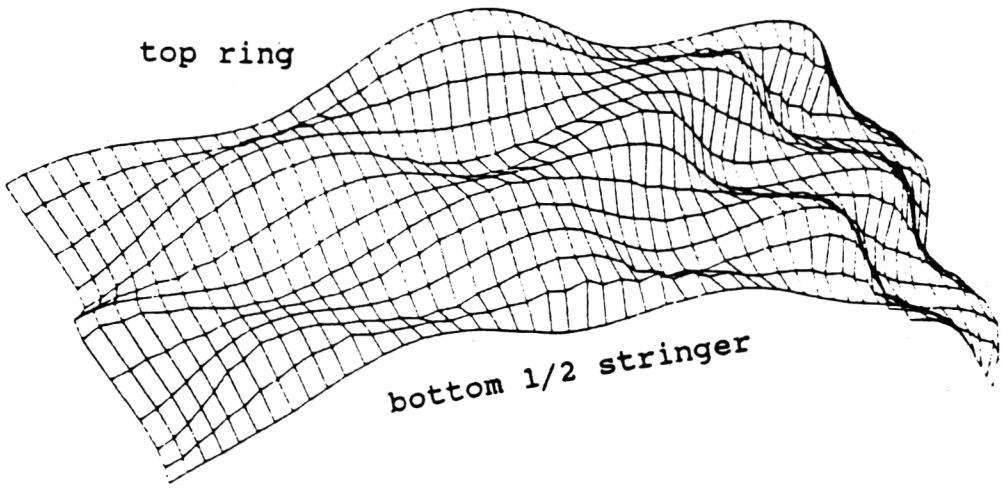

Figure 2: Buckling Mode of the Upper 1/4 of the ALS Fuel Tank

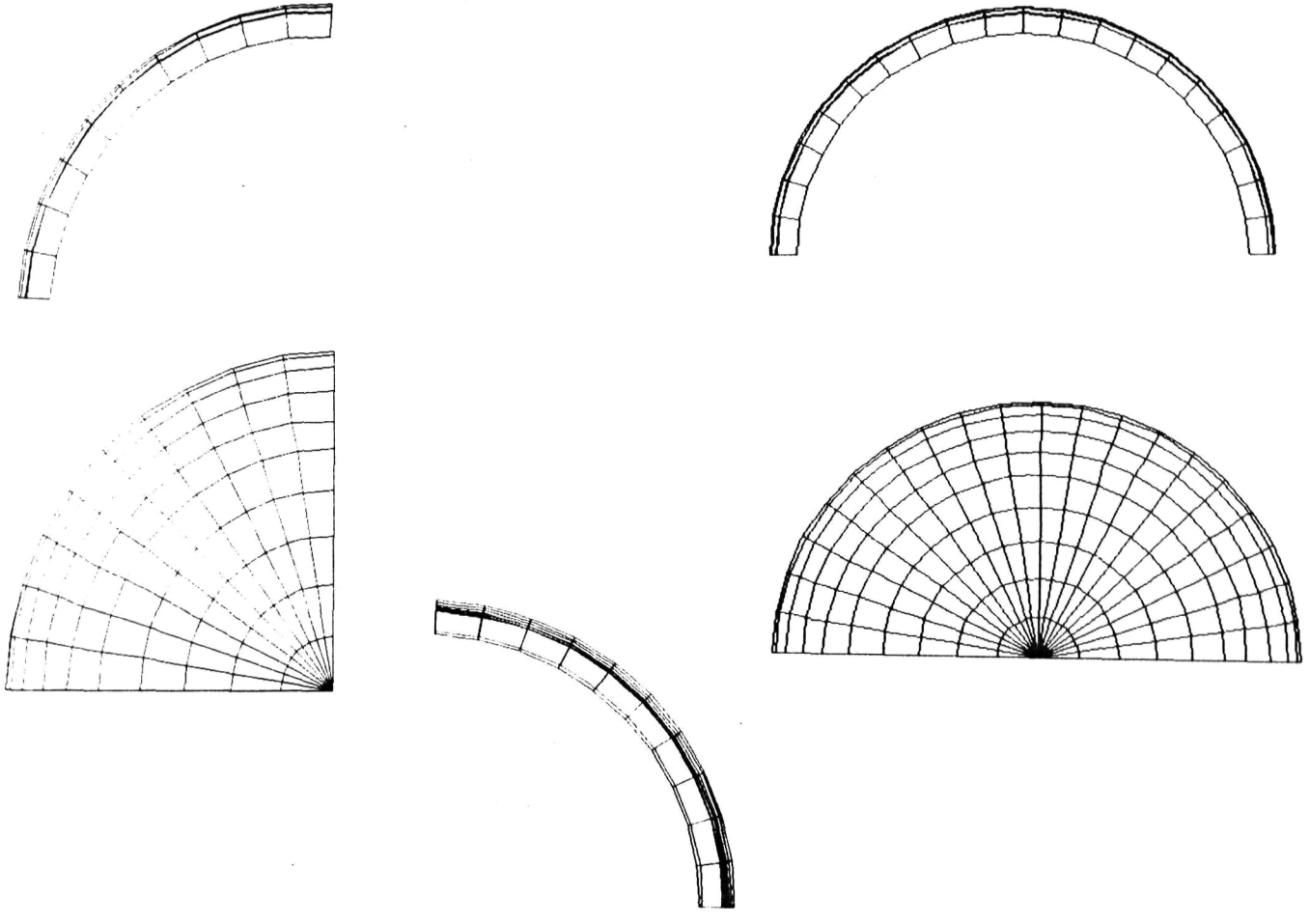

Figure 3: Thermal Displacements of Five Tank Models (end axial view)

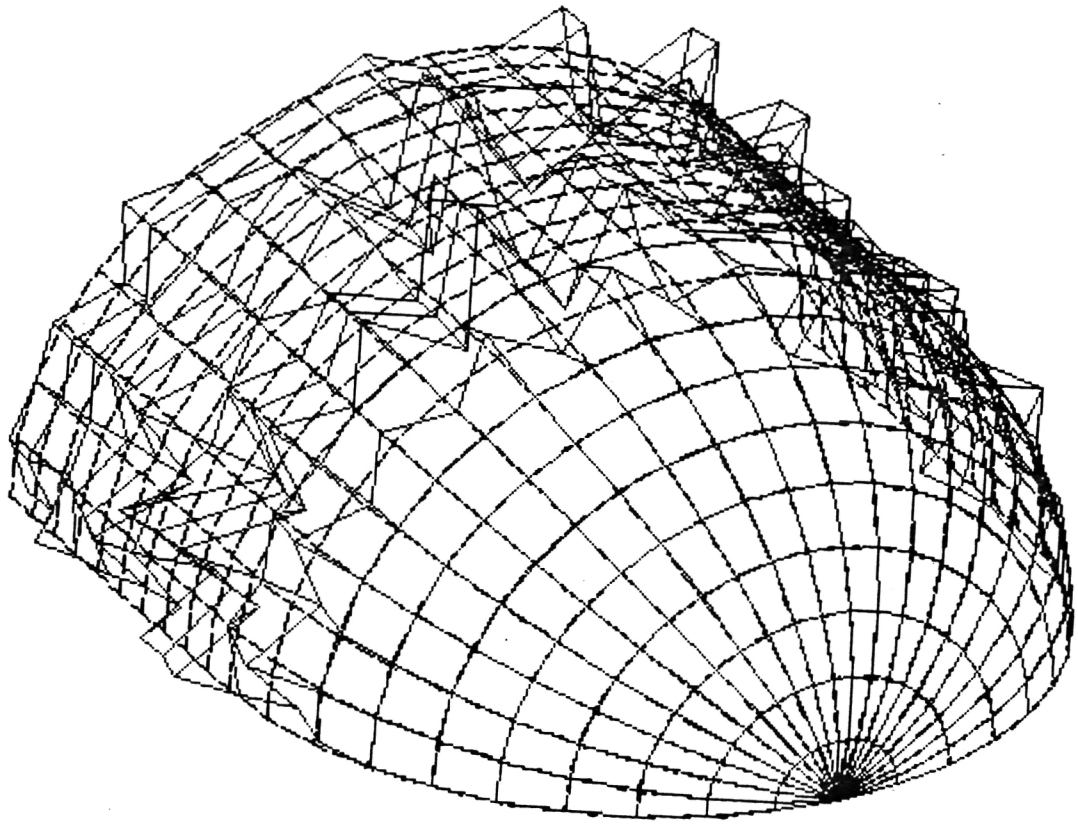

Figure 4: First Thermal Buckling Mode of a Tank with Rings

Figure 5: Plane Strain Test Problem

Example: Long Circular cylinder

(Plain Strain)

Inner Radius = 3
Outer Radius = 9

Thermal Distribution

$T(r) = -\ln(r/3)/\ln(3) + 100$

Material Properties (2 cases)

Case 1
E(T) = 20.0E6 - T(10E4)
v(T) = 0.4 - T(0.002)
alpha(T) = 10E-6 + T(10E-8)

Case 2
E(T) = 10E6 + T(10E4)
v(T) = 0.4 - T(0.002)
alpha(T) = 20E-6 - T(10E-8)

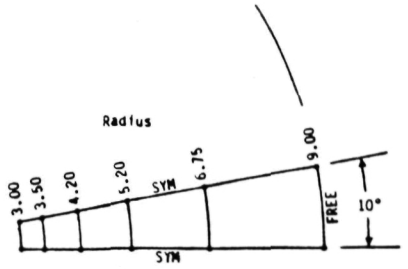

Boundary Conditions

Free at inner and outer radius
Symmetry elsewhere

Test Elements

ANSYS Stif42 and Stif82
(4 and 8 node plane strain elements)

Accuracy of Inner Radial Displacement

Mat. Prop. Case	Stif42 (% Error)	Stif82 (% Error)
1	9.9	1.0
2	4.0	28.5

BACK

Project 16 **Experimental Study of the Nonlinear Viscoplastic Response of High Temperature Structures**

Marshall F. Coyle and E.A. Thornton

Objectives

The basic objective of this research program is to investigate experimentally the viscoplastic response of thermal structures for high speed flight. An additional objective of the experimental program is to provide high quality data for validation of finite element analysis using unified viscoplastic constitutive models.

Approach

Simplified structures of representative high temperature superalloys and/or advanced aluminum alloys will be designed and tested. These alloys will display typical biaxial stress states with appropriate temperatures and stress gradients. The simplified structures will provide well-defined thermal and structural boundary conditions.

Research Progress

A series of experiments were conducted on a 1/8 in. thick 10 x 15 in. rectangular Hastelloy-X panel. Figure 1 is a schematic of the test setup. The test panel (denoted Panel No. 2) was supported at four points to provide well defined boundary conditions and to minimize heat losses. The supports were located 4 in. on either side of the transverse center line and 1/2 in. inside the transverse edge. A Research Inc. "High-Intensity Infrared Elliptical-Reflector" 16 in. long line heater (lamp) was used to heat the panel along the long transverse center line. The line heater produced a narrow (1/8 - 1/4 in. wide) heated strip. The edges of the panel were cooled by running chilled water through PVC pipes adhesively bonded to opposite edges of the panel. Each edge of the panel was inserted and bonded in a slot machined into a PVC pipe. A chilled water system provided coolant at a constant temperature. The panel was fully insulated except for a tapered slot along the heated strip to facilitate the heat flux from the line heater.

The panel was instrumented with 18 thermocouples to measure the temperature

distribution. The panel was also instrumented with 15 LVDTs to measure out-of-plane displacements. The LVDTs were fitted with a ceramic insulator to reduce heat loss and for protection from the heated panel.

A series of tests were conducted at different heat flux levels. The series of tests performed on this panel are summarized in Table 1. The heat flux intensity will be discussed in terms of percent of maximum heat flux. A lamp characterization study will be discussed later that correlates these output percentages to actual heat flux.

In the first group of tests, the lamp's controller was programmed to raise the panel's temperature to a specified temperature at a constant rate and then maintain that temperature for 60 min. The controller controlled the panel's temperature by varying the heat flux intensity. For example, in test No. 0815A, the controller was programmed to raise the panel's center temperature from 70°F to 300°F in 30 min. and maintained that temperature for 60 min. At the beginning of the test, the lamp's output was 3% and increased steadily to 6% at an elapsed time of 30 min. It then dropped back to 4.6% at elapsed time of 39 min. and was maintained at this intensity for the remainder of the test.

In the next series of tests, the heat flux was held constant through each test. Initially the flux levels were low to insure a elastic response of the test panel. The flux levels were increased in small increments from test to test until residual permanent deformations were detected in the panel. This occurred at a lamp output of 8%, which produced a temperature differential of 430°F. Further tests were conducted on this panel with increasing flux levels. This provided information on the panel's temperature response to different flux levels.

Results from test No. 1119B will be used to illustrate some of the data that was collected. In this test, the lamp's output was set at 25% and the cooled edges were maintained at 60°F. Figure 2 shows the temperature profile along the Y-axis at different time increments. The temperature profile is initially nonlinear and begins to approach a linear state as time increases. The through-the-thickness temperature gradient was found to be negligible. The displacements along the X-axis at different time increments are shown in Figure 3. Note that in this series of tests a positive displacement is away from the heat source. Figure 4 is a plot of temperature versus displacement at the center of the panel. The displacement offset is due to residual deformations from previous tests. This figure shows a initial nonlinear response which becomes near linear in the middle temperature range. The out-of-plane displacements are initiated by the panel's initial shape and bending-buckling

resulted from compressive thermal stresses.

A third Hastelloy-X panel has been instrumented with 29 thermocouples and 15 LVDTs. A type K thermocouple was used on this panel instead of type T previously used. The Type K thermocouple enable temperatures to be measured up to 2300°F. This panel has more thermocouples along the Y-axis to better measure the nonlinear temperature distribution in greater detail, and it has more thermocouples along the X-axis to measure the temperature variation along the heated centerline.

The behavior of the Research Inc. "High-Intensity Infrared Elliptical-Reflector" 16 in. long line heater is very important to the test program. To understand the spatial variation of the heat flux on a deformed test panel, a special lamp test fixture was designed and fabricated. Figure 5 is a schematic of the test fixture. The quartz lamp is suspended above a array of heat flux calorimeters. The calorimeters are mounted on a water cooled table. A chiller provides coolant to the table to maintain a constant temperature. The table is indexed under the lamp with a X-Y motor driven actuator. The lamp's elevation is controlled with a manual screw driven linear actuator. A data acquisition system is used to collect heat flux and temperature measurements from the calorimeters. A computer controls the X-Y position of the table along with data acquisition system, and it also stores the collected data. The system is programmed to perform a survey in the X-Y plane automatically. This system will also be used to correlate lamp output percentage to actual incident heat flux. Figure 6 presents some preliminary results from a lamp heat flux test.

A Measurement Group System 4000 data acquisition system has been purchased. This system is presently setup to handle 20 strain gages and 20 thermocouples.

Plans for the Future Research

In the next six months, tests will begin on the two instrumented panels. The first set of experiments will use panel No. 3 which is instrumented with 29 thermocouples. The panel will also be instrumented with 15 LVDTs to measure displacements. A series of tests will be conducted in the elastic range. Then a test will be run with a flux level that will cause plastic deformation. A second set of experiments will be conducted on panel No. 1, which was previously instrumented. It is instrumented with 14 strain gages and 20 thermocouples. This panel will also be instrumented with 15 LVDTs used to measure displacements. This set of experiments will provide strain data in addition to temperature and

displacement acquired in the first sets of experiments.

Efforts will continue on the line heater surveys. Tests will be conducted with different lamp output percentages. This information will be used to correlate the thermal behavior of the panel with given flux levels.

We are expecting to receive some 0.090 in. thick 8009 aluminum alloy material from NASA Langley. This material will be used for a new series of tests. These test panels will be measured and then instrumented with thermocouples and strain gages. Efforts will begin in correlating experimental results with analytical results.

Table 1

Test No.	Type of Control	Control Setting
0427A	TEMP	70-250 in 30 min. with 60 min. hold
0505A	TEMP	70-250 in 30 min. with 60 min. hold
0612A	TEMP	70-250 in 30 min. with 60 min. hold
0613A	TEMP	70-250 in 30 min. with 60 min. hold
0624A	TEMP	70-300 in 30 min. with 60 min. hold
0625A	TEMP	70-300 in 30 min. with 60 min. hold
0625B	TEMP	70-300 in 30 min. with 60 min. hold
0626A	TEMP	70-300 in 30 min. with 60 min. hold
0627A	TEMP	70-300 in 30 min. with 60 min. hold
0813A	TEMP	70-300 in 30 min. with 60 min. hold
0815A	TEMP	70-300 in 30 min. with 60 min. hold
0815B	LAMP %	4.6% 90 min. duration
0816A	LAMP %	4.6% 90 min. duration
0826A	LAMP %	4.6% 90 min. duration
1003A	LAMP %	4.6% 90 min. duration
1009A	LAMP %	4.6% 90 min. duration
1011A	LAMP %	5% 90 min. duration
1025A	LAMP %	5% 90 min. duration
1029A	LAMP %	6% 90 min. duration
1030A	LAMP %	7% 90 min. duration
1101A	LAMP %	8% 90 min. duration
1105A	LAMP %	8% 90 min. duration
1105A	LAMP %	8% 90 min. duration
1106A	LAMP %	8% 90 min. duration
1106B	LAMP %	9% 90 min. duration
1107A	LAMP %	10% 90 min. duration
1108A	LAMP %	11% 90 min. duration
1112A	LAMP %	12% 90 min. duration
1113A	LAMP %	13% 90 min. duration
1114A	LAMP %	14% 90 min. duration
1115A	LAMP %	15% 90 min. duration
1119A	LAMP %	20% until TCs reach 750 F
1119B	LAMP %	25% until TCs reach 750 F
1119C	LAMP %	30% until TCs reach 750 F
1120A	LAMP %	35% until TCs reach 750 F
1120B	LAMP %	40% until TCs reach 750 F
1121A	LAMP %	45% until TCs reach 750 F
1121B	LAMP %	50% until TCs reach 750 F
1121C	LAMP %	75% until TCs reach 750 F
1122A	LAMP %	100% for 196 sec.

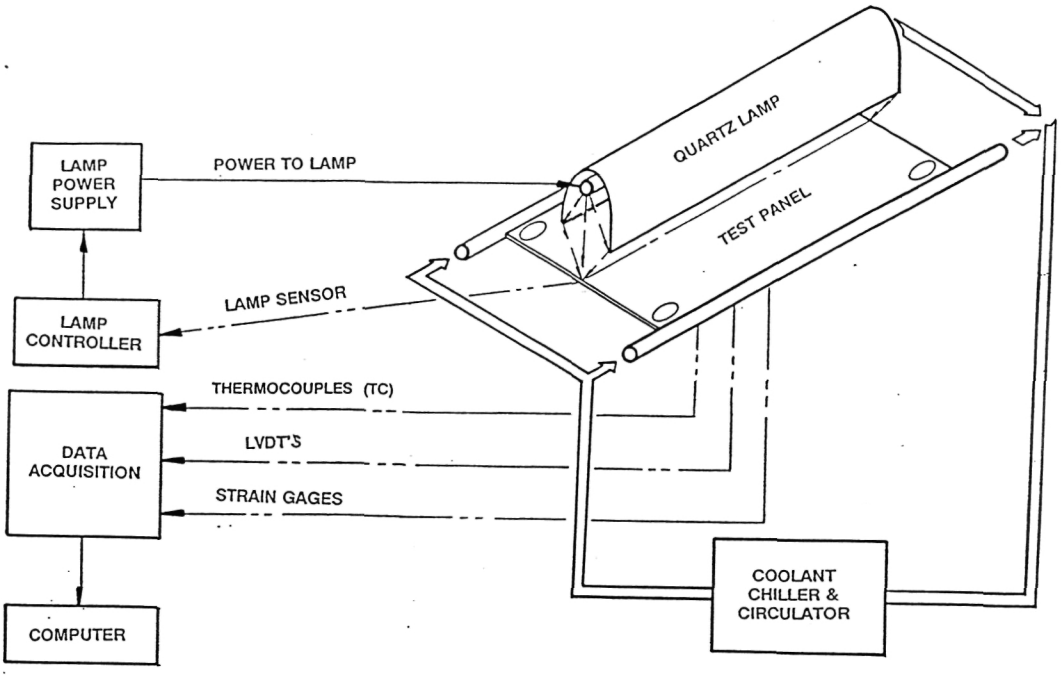

Figure 1: Schematic For Thermal-Structural Test of Panels

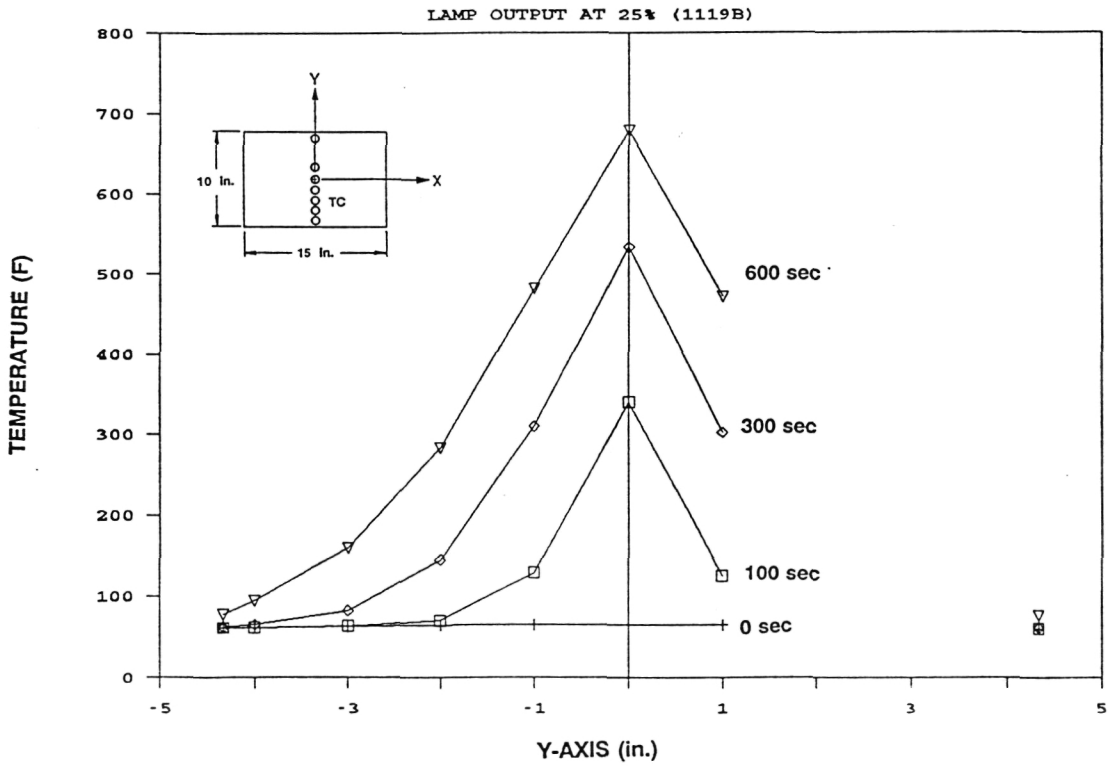

Figure 2: Panel Temperature Along the Y-Axis

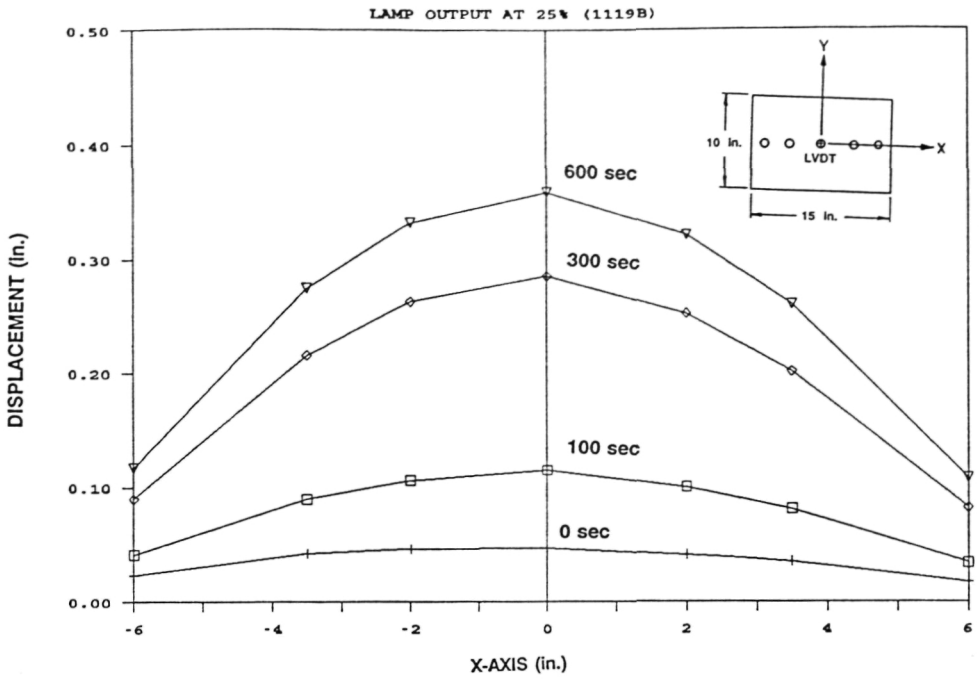

Figure: 3 Panel Displacement Along the X-Axis

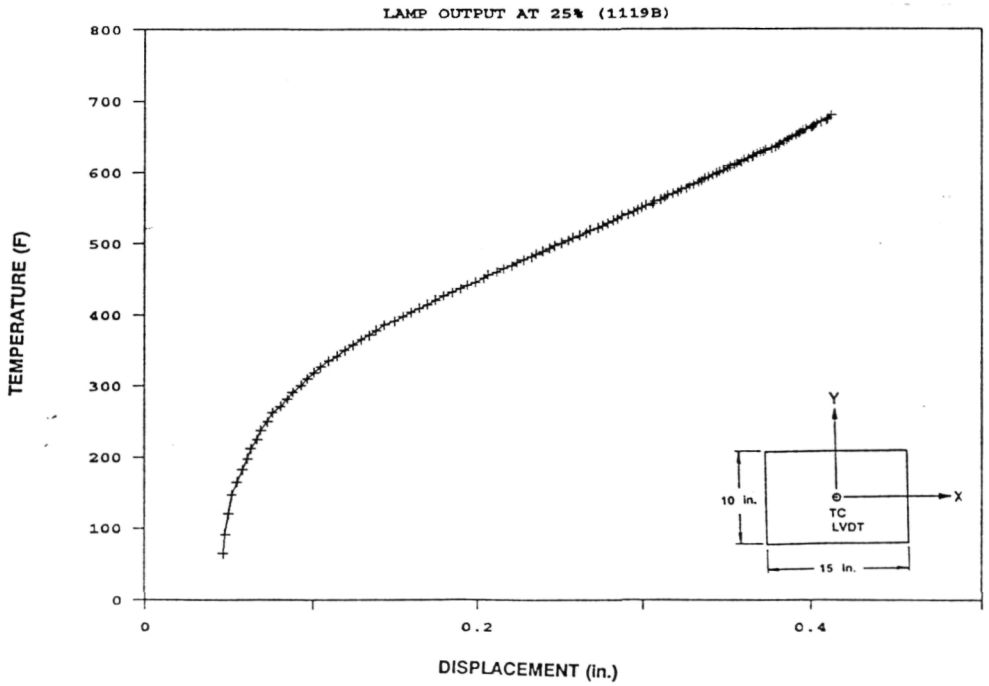

Figure 4: **Panel Temperature versus Displacement Response at the Center**

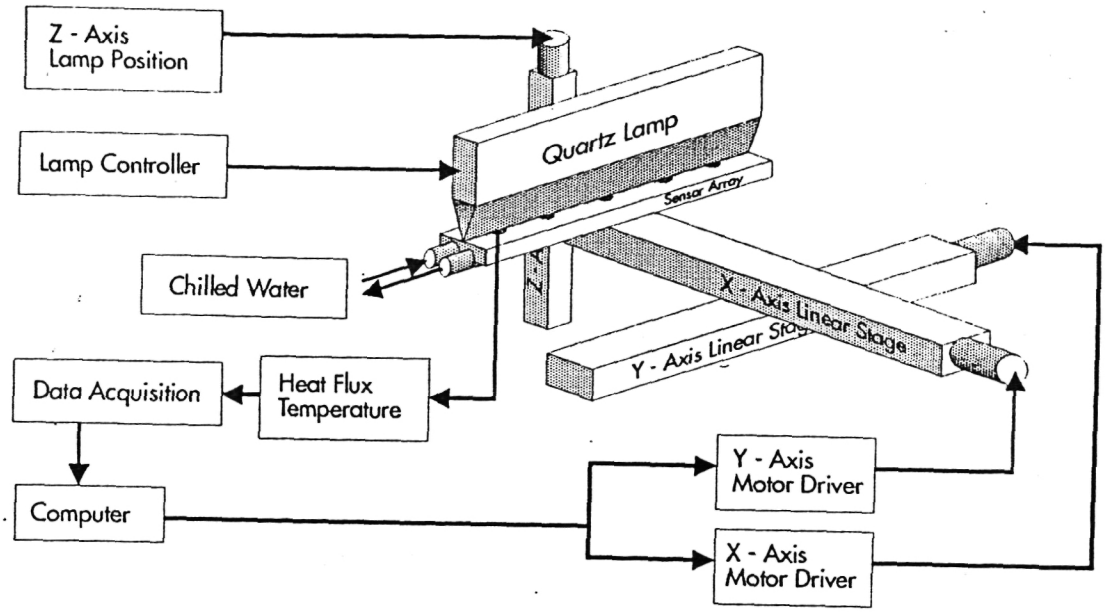

Figure 5. Heat Lamp Test Fixture Schematic

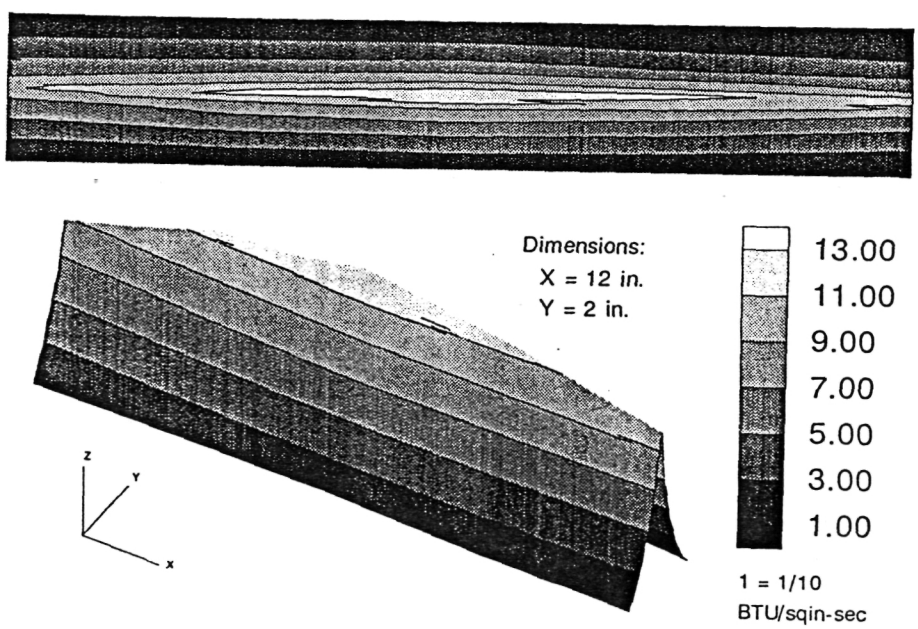

Figure 6. Quartz Lamp Heat Flux Measurements
50% Output at Z = 2 in.

Project 16 **Experimental Study of the Nonlinear Viscoplastic Response of High Temperature Structures**

Mark A. Rawley and E.A. Thornton

Introduction

An important aspect of understanding the inelastic behavior of structural components under severe heating is having a fundamental knowledge of the material behavior at elevated temperatures. To support the research funded by the Aircraft Structures Branch under Project 16 a material characterization project was initiated in the summer of 1991. The project involves close cooperation between the faculty and graduate students in the Mechanical and Aerospace Engineering and Materials Science and Engineering Departments. The experiments are being conducted using testing facilities in the Materials Science Department.

At present, Mr. Mark A. Rawley, an M.S. graduate student in the MAE Department, is being supported by the UVA Academic Enhancement Program through the Center of Light Thermal Structures. The availability of NASA funds for undergraduate research has enabled the Light Thermal Structures Center to support this project. Undergraduate participation in the material characterization project is expected to grow now that the project has been initiated.

Objective

The objective of this research is to characterize the viscoplastic behavior of materials that are being used in the thermal buckling tests. The approach has been divided into three tasks. The first task is to obtain accurate tensile data for materials of interest from which model parameters for the Bodner-Partom viscoplasticity model may be obtained. The second is to develop procedures for obtaining the constitutive model parameters from the tensile data. The third task of this research project is to obtain and validate the model parameters that provide an accurate modeling of the test materials.

Approach and Method

K.S. Chan, S.R. Bodner, and U.S. Lindholm demonstrated[1] that nickel based superalloys can be accurately modeled using a unified viscoplasticity constitutive model

developed by Bodner and Partom.[2] This model, summarized in Figures 1 and 2, implements the Prandtl-Reuss flow law, a kinetic equation relating the invariants of plastic strain rate and stress, and evolution equations for hardening.

A combined program of experimental and analytic procedures is used in developing the model parameters.[1] Previous research efforts by Chan et al.[1] showed that uniaxial tensile data are sufficient to develop a complete model over the temperature range of interest in the present buckling tests. Plastic work rate can be derived from the tensile data and used as the hardening measure. The model parameters are obtained through an iterative procedure involving calculations that incorporate saturation stresses, plastic strain rates, plastic work rates, and estimations of the yield stresses for each set of tensile data. An outline for the procedure for obtaining the Bodner-Partom Constants is as follows[1]:

1. Conduct a series of uniaxial tensile tests at several strain rates and temperatures.
2. Obtain a polynomial that approximates σ versus ϵ_p.
3. Using the polynomial data, generate a plot of γ versus σ, were $\gamma = (1/\sigma)(d\sigma/d\epsilon_p)$.
4. Obtain m_1 and m_2 from the slopes of γ versus σ.
5. Set D_0 (usually taken to be 1×10^4 sec^{-1}).
6. Obtain n from saturation stress, σ_s, versus strain rate.
7. Calculate the sum of Z_1 and Z_3 from σ_s, n, and ϵ_p.
8. Obtain Z_0 from the 0.2% offset yield stress; set $Z_2=Z_0$.
9. Calculate Z_1 from σ_{yield} and σ_s; obtain Z_3.

Research Progress

Computer Program Development A thorough investigation of the Bodner Partom viscoplasticity model was undertaken to gain familiarity with the model. A study of the experimental procedure developed by Chan, et al.[1] proved to be very useful. Results for B1900 + Hf were used in developing a working computer code that could expedite the procedure for obtaining the model constants from tensile data.

Experimental Work The experimental procedure involves a program of tests over a range of temperatures and strain rates. The first material being studied is Hastelloy-X (Ni-bal, Cr-21.7%, Fe-19.1%, Mo-9.13%, Co-1.31%, other < 1.5%), a nickel based, austenitic, solid solution strengthened alloy. Twenty-two test samples were cut from a sheet of Hastelloy-X in dog-bone geometry with a gauge length of one inch and cross sectional

areas of the gauge section of 0.025 in^2 (tolerance of +/- 0.0005 in^2). These samples were mounted in ATS 713C grips and secured with wedges made from the same high temperature material. The 18 tests shown in the test schedule for Hastelloy-X (Table 1) have been completed. These isothermal uniaxial tension tests were conducted at four temperatures ranging from 77°F (25°C) to 1000°F (538°C). The tests were performed on a screw driven Instron load frame with a load cell range up to 2000 kg. For elevated temperature tests, the samples were heated with an ATS split tube furnace to the desired temperature and allowed to soak for thirty minutes. Strain data were collected using a Capacitec HAX extensometer at strain rates of 3.28×10^{-4} in/min and 3.28×10^{-3} in/min and stored on an IBM PC with the load data. Figure 3 depicts the characteristic effects of reduced modulus and yield strength at elevated temperatures.

Future Work

Data Analysis Following the outline provided above, the experimentally determined tensile data are to be processed using the Fortran code previously mentioned. The model constants are to be optimized for the range of test conditions using an iterative procedure.

Tests of Other Materials Following the successful development of the constitutive model for Hastelloy-X, the intention is to use the procedures developed here to obtain material characteristics for other materials using the Bodner-Partom viscoplasticity model. Among others, the materials to be tested include 8009 Al and possibly NARloy (a copper alloy). The 8009 aluminum alloy is a candidate material for the High Speed Civil Transport, and NARloy is being considered for the cowl leading edge for the NASP.

References

1. Chan, K.S., Bodner, S.R., and Lindholm, U.S., "Phenomenological Modeling of Hardening and Thermal Recovery in Metals," Journal of Engineering Materials and Technology, Vol. 110, Jan. 1988.

2. Miller, A.K., Unified Constitutive Equations for Creep and Plasticity, Elsevier Applied Science, New York, NY, 1987.

3. Chan, K.S., Lindholm, U.S., and Bodner, S.R., Constitutive Modeling for Isotropic Materials (HOST) Third Annual Report, NASA-CR 174980, 1986.

4. Thornton, E.A., and Kolenski, J.D., Viscoplastic Response of Structures with Intense Local Heating, AIAA Paper No. 91-1149, April 1991.

5. ATEK Metals Center Inc., Specification Sheet for Hastelloy-X, Cincinnati, OH, May 1990.

Test Schedule for Hastelloy-X

		STRAIN RATE		
		3.28E-4 Long Trans	3.28E-3 Long Trans	3.28E-4 Short Trans
TEMPERATURE	77F (25C)	2	2	1
	400F (204C)	2	2	1
	700F (371C)	2	2	0
	1000F (537C)	2	2	0

22 Specimens Provided
18 Tests Completed

TABLE 1

ESSENTIAL EQUATIONS FOR THE UNI-DIRECTIONAL BODNER-PARTOM CONSTITUTIVE MODEL

1. Flow Law

$$\varepsilon_t = \varepsilon_e + \varepsilon_p$$

2. Kinetic Equation

$$\varepsilon_p = (2//3)D_0\{\sigma/|\sigma|\}\exp\{-.5(Z/\sigma)^{2n}\}$$

3. Evolution Equations

$$Z = Z_I + Z_D$$

$$Z_I = m_1(Z_1 - Z_I)W_p - A_1 Z_1\{(Z_I - Z_2)/Z_1\}^{r_1}$$

$$Z_D = m_2(Z_3 - Z_D)W_p - A_2 Z_1\{Z_D/Z_1\}^{r_2}$$

6. Rate of Plastic Work

$$W_p = \sigma(\varepsilon_p)$$

FIGURE 1

MATERIAL CONSTANTS IN THE BODNER-PARTOM CONSTITUTIVE MODEL

TEMP. INDEPENDENT

- D_0 Limiting Shear Strain Rate [sec^1]
- Z_1 Limiting (maximum) value of Z_I [psi]
- Z_3 Limiting (maximum) value of Z_D [psi]
- m_1 Hardening Rate Coeff. of Z_D [psi^{-1}]
- m_2 Hardening Rate Coeff. of Z_I [psi^{-1}]

TEMP. DEPENDENT

- Z_0 Initial Value of Isotropic Hardening Variable [psi]
- Z_2 Fully Recovered (minimum) value of Z_I [psi]
- n Kinetic parameter
- A_1 Recovery Coeff. for Z_I
- A_2 Recovery Coeff. for Z_D
- r_1 Recovery Exponent for Z_D
- r_2 Recovery Exponent for Z_I

FIGURE 2

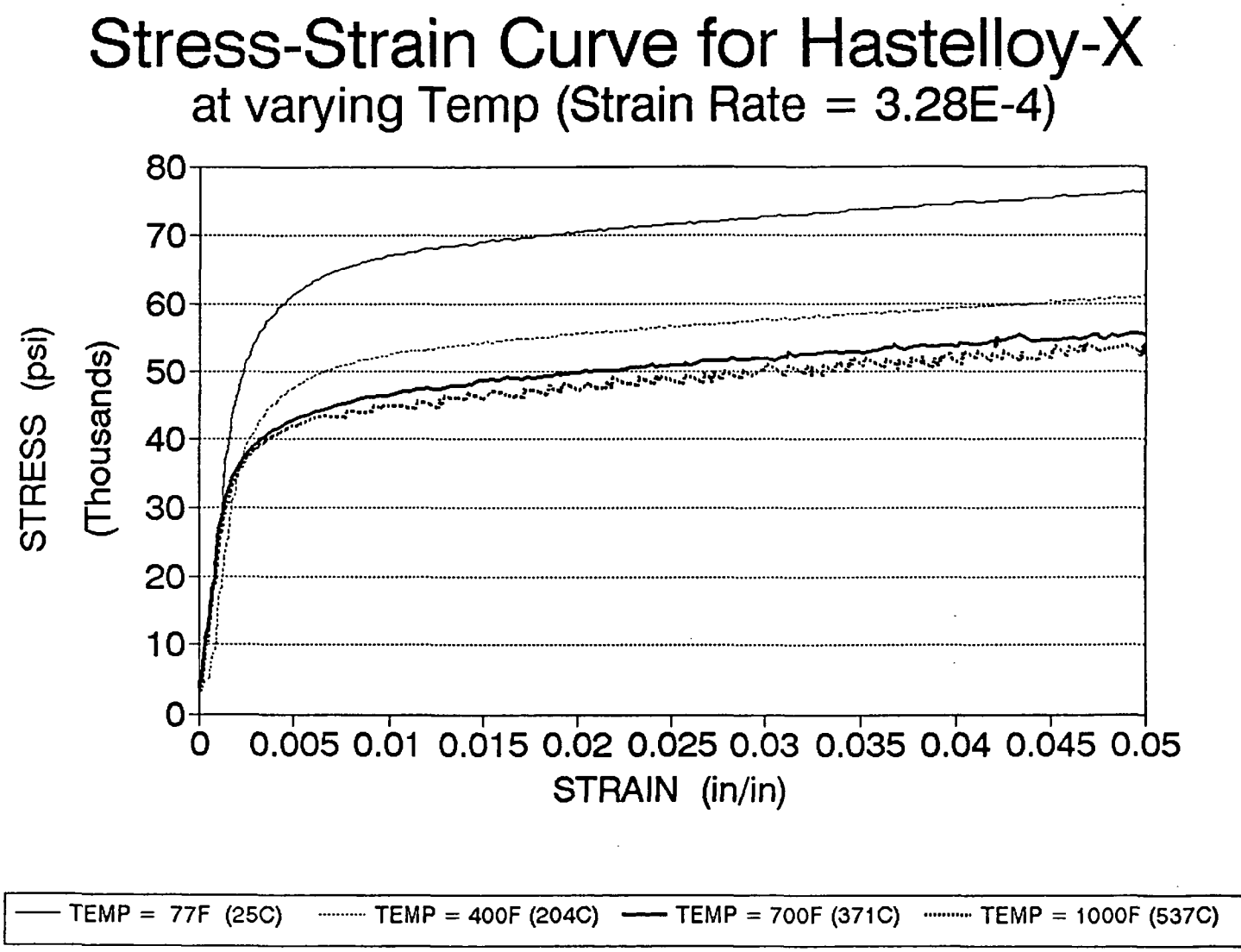
Stress-Strain Curve for Hastelloy-X
at varying Temp (Strain Rate = 3.28E-4)
STRESS (psi)
(Thousands)
80
70
60
50
40
30
20
10
0
0
0.005
0.01
0.015
0.02
0.025
0.03
0.035
0.04
0.045
0.05
STRAIN (in/in)
TEMP = 77F (25C)
TEMP = 400F (204C)
TEMP = 700F (371C)
TEMP = 1000F (537C)

FIGURE 3

APPENDIX I: GRANT PUBLICATIONS (January 1 to December 31, 1991)

1. R.P. Gangloff, R.S. Piascik, D.L. Dicus and J.C. Newman, "Fatigue Crack Propagation in Aerospace Aluminum Alloys", Journal of Aircraft, in review (1991).

2. R.P. Gangloff, D.C. Slavik, R.S. Piascik and R.H. Van Stone, "Direct Current Electrical Potential Measurement of the Growth of Small Fatigue Cracks", in Small Crack Test Methods, ASTM STP 1149, J.M. Larsen and J.E. Allison, eds., ASTM, Philadelphia, PA, in press (1991).

3. W.C. Porr, Jr., Anthony Reynolds, Yang Leng and R.P. Gangloff, "Elevated Temperature Cracking of RSP Aluminum Alloy 8009: Characterization of the Environmental Effect", Scripta Metallurgica et Materialia, Vol. 25, pp. 2627-2632 (1991).

4. R.S. Piascik and R.P. Gangloff, "Environmental Fatigue of an Al-Li-Cu Alloy: Part I - Intrinsic Crack Propagation Kinetics in Hydrogenous Environments", Metall. Trans. A, Vol. 22A, pp. 2415-2428 (1991).

5. W.C. Porr, Jr., Y. Leng, and R.P. Gangloff, "Elevated Temperature Fracture Toughness of P/M Al-Fe-V-Si", in Low Density, High Temperature Powder Metallurgy Alloys, W.E. Frazier, M.J. Koczak, and P.W. Lee, eds., TMS-AIME, Warrendale, PA, pp. 129-155 (1991).

6. Yang Leng, W.C. Porr, Jr. and R.P. Gangloff, "Time Dependent Crack Growth in P/M Al-Fe-V-Si at Elevated Temperatures", Scripta Metallurgica et Materialia, Vol. 25, pp. 895-900 (1991).

7. R.G. Buchheit, Jr., F.D. Wall, G.E. Stoner, and J.P. Moran, "The Role of Anodic Dissolution in the Stress Corrosion Cracking of Al-Li-Cu Alloy 2090," Proceedings of the First International Symposium on Environmental Degradation of Advanced Materials, San Diego, CA, June 1991, in press, July, 1991.

8. R.G. Buchheit, Jr., "Mechanisms of Localized Aqueous Corrosion in Aluminum-Lithium-Copper Alloys," Ph.D. Dissertation, University of Virginia, January, 1991.

9. R.G. Buchheit, Jr., J.P. Moran, F.D. Wall, and G.E. Stoner, "Rapid Anodic Dissolution Based SCC of 2090 (Al-Li-Cu) by Isolated Pit Solutions," Proceedings, Parkins Symposium on Stress Corrosion Cracking, TMS-AIME, Warrendale, PA, in press, October, 1991.

10. R.G. Buchheit, Jr., C.M. Moore, and G.E. Stoner, "Localized Corrosion of an Al-Li-Cu Alloy in Na_2SO_4 Solutions," to be submitted to Corrosion, November, 1991.

11. R.G. Buchheit, Jr., M.D. Bode, and G.E. Stoner, "Substitute Conversion Coatings on Aluminum for Waste Minimization," Conference Proceedings of the 17th Department of Energy Conference on Compatibility, Aging and Service Life, in press, October, 1991.

12. R.J. Kilmer and G.E. Stoner, "Effect of Zn Additions on Precipitation During Aging of Alloy 8090", Scripta Met., vol. 25, pp. 243-248 (1991).

13. R.J. Kilmer, T.J. Witters and G.E. Stoner, "Effect of Zn Additions on the Precipitation Events and Implications to Stress Corrosion Cracking Behavior in Al-Li-Cu-Mg-Zn Alloys", Proceedings of the Sixth International Al-Li Conference, October, 1991.

14. R.J. Kilmer and G.E. Stoner, "The Effect of Trace Additions of Zn on the Precipitation Behavior of Alloy 8090 During Artificial Aging", Proceedings, Light Weight Alloys for Aerospace Applications II, E.W. Lee, Editor, TMS-AIME, Warrendale, PA, pp. 3-15, 1991.

15. R.G. Buchheit, Jr., F.D. Wall, and G.E. Stoner, "The Effect of Applied Potential in Static Load SCC Testing of 2090 in Cl^- and Cl^-/CrO_4^{2-} Environments," Proceedings of the Electrochemical Society-Environmentally Enhanced Fracture Symposium, Fall Meeting, 1990, Seattle, WA, ECS, Pennington, NJ, 1991.

16. R.G. Buchheit, Jr., F.D. Wall, G.E. Stoner, and J.P. Moran, "Stress Corrosion Cracking of Al-Li-Cu-Zr Alloys 2090 in Aqueous Cl^- and Mixed Cl^-/CO_3^{2-} Environments," CORROSION/91, Cincinnati, OH, Paper No. 99, March, 1991.

17. C.J. Lissenden, M-J. Pindera, and C.T. Herakovich, "Stiffness Degradation of SiC/Ti Tubes Subjected to Biaxial Loading with Damage", **Int. J. Composites Science and Technology**, (invited paper to appear in a special issue of the journal).

18. C.J. Lissenden, M-J. Pindera, and C.T. Herakovich, "Response of SiC/Ti Tubes Subjected to Biaxial Loading in the Presence of Damage", (invited paper to appear in a symposium volume of AMSE Applied Mechanics Division, WAM 1992).

19. J. Aboudi, J.S. Hidde and C.T. Herakovich, "Thermo-mechanical Response Predictions for Metal Matrix Composites", in Mechanics of Composites at Elevated and Cryogenic Temperatures, S.N. Singhal, W.F. Jones and C.T. Herakovich, eds., ASME AMD, Vol. 118, pp. 1-18 (1991).

20. C.T. Herakovich and J.S. Hidde, "Response of Metal Matrix Composites with Imperfect Bonding", (accepted for publication in **Ultramicroscopy**). Published in Workshop Proceedings, Arizona State University, Jan., 1991.

21. E.A. Thornton, E.A. Starke, Jr., and C.T. Herakovich, "Materials and Light Thermal Structures Research for Advanced Space Exploration", AIAA paper No. 91-3431, AIAA/NASA/OAI Conference on Advanced SEI Technologies, Sept, 1991.

22. E.A. Thornton and J.D. Kolenski, "Viscoplastic Response of Structures with Intense Local Heating", AIAA Paper No. 91-1149, 32nd Structures, Structural Dynamics and Materials Conference, AIAA/ASME/ASCE/AHS/ASC, Baltimore, MD (1991). Submitted to the Journal of Aerospace Engineering.

23. E.A. Thornton, M.F. Coyle and R.N. McLeod, "Experimental Study of Plate Buckling Induced by Spatial Temperature Gradients", AIAA Paper No. 92-2540 accepted for presentation at the AIAA/ASME/ASCE/ASH/ASC Structural and Dynamics and Material Conference, Dallas, TX, April, 1992

APPENDIX II: GRANT PRESENTATIONS (January 1 to December 31, 1991)

1. R.P. Gangloff, W.C. Porr, Jr. and Yang Leng, "Elevated Temperature Crack Growth in Advanced PM Aluminum Alloys", ASTM E24.04 Meeting on Research on Subcritical Crack Growth, Indianapolis, IN, May, 1991.

2. W.C. Porr Jr., "Elevated Temperature Fracture of Advanced Aluminum Alloys", Virginia Academy of Science Annual Meeting, VPI, Blacksburg, VA, May, 1991.

3. R.S. Piascik and R.P. Gangloff, "Process Zone Modelling of Environmental Fatigue", Parkins Symposium, TMS-AIME, Cincinnati, OH, October, 1991.

4. W.C. Porr and R.P. Gangloff, "Elevated Temperature Fracture of RS/PM Aluminum Alloy 8009", Allied Signal Inc., Morristown, NJ, November, 1991.

5. R.P. Gangloff, "Elevated Temperature Fracture of RS/PM Aluminum Alloys", Department of Materials Science and Engineering, Lehigh University, Bethlehem, PA, November, 1991.

6. R.P. Gangloff, "Great Failures in Materials Science", Eastern Virginia Chapter of ASM International, Hampton, VA, November, 1991.

7 R.G. Buchheit, Jr., F.D. Wall, G.E. Stoner, and J.P. Moran, "Stress Corrosion Cracking of Al-Li-Cu-Zr Alloys 2090 in Aqueous Cl^- and Mixed Cl^-/CO_3^{2-} Environments," CORROSION/91, Cincinnati, OH, March, 1991.

8. R.G. Buchheit, Jr., F.D. Wall, G.E. Stoner, and J.P. Moran, "The Role of Anodic Dissolution in the Stress Corrosion Cracking of Al-Li-Cu Alloy 2090," First International Symposium on Environmental Degradation of Advanced Materials, San Diego, CA, June, 1991.

9. J.P. Moran, R.G. Buchheit, Jr., and G.E. Stoner, "Mechanisms of SCC of Alloy 2090 (Al-Li-Cu)", Parkins Symposium on Stress Corrosion Cracking, Fall TMS-AIME Meeting, Cincinnati, OH, October, 1991.

10. R.G. Buchheit, Jr., M.D. Bode, and G.E. Stoner, "Substitute Conversion Coatings on Aluminum for Waste Minimization," 17th Department of Energy Conference on Compatibility, Aging and Service Life, October, 1991.

11. R.J. Kilmer, T.J. Witters and G.E. Stoner, "Effect of Zn Additions on the Precipitation Events and Implications to Stress Corrosion Cracking Behavior in Al-Li-Cu-Mg-Zn Alloys", Sixth International Al-Li Conference, October, 1991, Garmisch, FRG.

12. R.J. Kilmer and G.E. Stoner, "The Effect of Trace Additions of Zn on the Precipitation Behavior of Alloy 8090 During Artificial Aging", TMS Symposium on Light Weight Alloys for Aerospace Applications II, New Orleans, Louisiana, February, 1991.

13. C.T. Herakovich, Arizona State Univ. NSF National Center for High Resolution Electron Microscopy Winter Workshop on the Structure and Properties of Interfaces, January, 1991

14. J. Aboudi, J.S. Hidde and C.T. Herakovich, "Thermo-mechanical Response Predictions for Metal Matrix Composites", 1991 ASME Summer Conference, Ohio State University, June, 1991.

15. E.A. Thornton and J.D. Kolenski, "Viscoplastic Response of Structures with Intense Local Heating", 32nd Structures, Structural Dynamics and Materials Conference, AIAA/ASME/ASCE/AHS/ASC, Baltimore, MD, April, 1991.

APPENDIX III: ABSTRACTS OF GRANT PUBLICATIONS

ELEVATED TEMPERATURE FRACTURE TOUGHNESS OF P/M Al-Fe-V-Si

William C. Porr, Jr., Yang Leng, and Richard P. Gangloff

Department of Materials Science
University of Virginia
Charlottesville, VA 22903

Abstract

The effects of temperature and loading rate on the crack initiation and growth fracture toughnesses of powder metallurgy Al-8.5Fe-1.7Si-1.3V (wt%) were investigated by an elastic-plastic J-integral method with electric potential difference crack monitoring. At 25°C the ultra-fine grained P/M alloy exhibits high crack initiation toughness (K_{IC} = 36.6 MPa$\sqrt{m}$) and crack growth resistance ($T_R = [E/\sigma_o^2][dJ/da]$ = 20.6) in the LT orientation compared to the behavior of ingot metallurgy alloy 2618 (K_{IC} = 21 MPa$\sqrt{m}$ and T_R = 0.5). While the toughness of the I/M alloy is constant (K_{IC}) or increases mildly (T_R) with temperature to the aging level of 199°C, both measures of toughness for the P/M alloy decrease between 25°C and 316°C, with minima in K_{IC} and T_R at 200°C. K_{IC} decreases and T_R increases mildly with increasing temperature for FVS0812 tested in the TL orientation. K_{IC} and T_R decrease with decreasing applied load line displacement rate for LT FVS0812 at 175°C, with crack growth resistance exhibiting a minimum. The mode of fracture is microvoid coalescence in all cases, however, the origins and evolution of damage are unclear. The TL toughness of FVS0812 is generally low because of prior particle boundary oxides oriented parallel to the fracture path. The behavior of LT FVS0812 is explained by a complex interaction of prior particle boundary delamination, perpendicular to the main crack front to promote plane stress "thin sheet toughening", and several possible intrinsic fracture mechanisms. Speculatively, intrinsic toughness decreases with increasing temperature and loading time because of dynamic strain aging from solid solution Fe or environmental hydrogen embrittlement.

Low Density, High Temperature Powder Metallurgy Alloys
Edited by William E. Frazier, Michael J. Koczak and Peter W. Lee
The Minerals, Metals & Materials Society, 1991

DIRECT CURRENT ELECTRICAL POTENTIAL MEASUREMENT OF THE GROWTH OF SMALL FATIGUE CRACKS

Richard P. Gangloff and Donald C. Slavik[1]
Department of Materials Science and Engineering
University of Virginia
Charlottesville, VA 22903

Robert S. Piascik[2]
Mechanics of Materials Branch
NASA-Langley Research Center
Hampton, VA 23665

Robert H. Van Stone[3]
General Electric Aircraft Engines
Cincinnati, Ohio 45215

ABSTRACT

This paper demonstrates the successful application of the direct current electrical potential difference method for continuous *in situ* monitoring of the growth of short (50 to 5000 μm) fatigue cracks in a variety of metallic alloys exposed to various environments. Crack initiation site and crack shape must be known *a priori*. Instrumentation includes a constant current power supply, relay circuit, 10^4 gain amplifier and computer analog to digital board with controlling software. A closed form analytical model accurately relates crack size to measured potential, as a function of crack shape and probe position local to the growing crack. Analytical calibrations are experimentally confirmed for small through-thickness edge cracks, surface semielliptical and semicircular cracks, and corner cracks in steels, nickel-based superalloys, titanium and aluminum alloys. Micron-level average crack advance resolution, long term stability, continuous measurement, simplicity, compatibility with aggressive environments, and programmed stress intensity loading are attributes of the electrical potential method. Crack length versus load cycles and growth rate versus stress intensity range data demonstrate the power of this method for studies of the effects of microstructure, environment (elevated temperature, high purity gases, vacuum and aqueous solutions) and loading variables on the growth kinetics of small and short fatigue cracks. Additional work is required for electrical potential monitoring of fatigue cracks sized below 75 μm, cracking not associated with a defined initiation site and thermal-mechanical fatigue.

FATIGUE CRACK PROPAGATION IN AEROSPACE ALUMINUM ALLOYS

R.P. Gangloff[1], R.S. Piascik[2], D.L. Dicus[3] and J.C. Newman, Jr.[4]

Abstract

This paper reviews fracture mechanics based, damage tolerant characterizations and predictions of fatigue crack growth in aerospace aluminum alloys. The results of laboratory experimentation and modeling are summarized in the areas of: (a) fatigue crack closure, (b) the wide range crack growth rate response of conventional aluminum alloys, (c) the fatigue behavior of advanced monolithic aluminum alloys and metal matrix composites, (d) the short crack problem, (e) environmental fatigue and (f) variable amplitude loading. Remaining uncertainties and necessary research are identified. This work provides a foundation for the development of fatigue resistant alloys and composites, next generation life prediction codes for new structural designs and extreme environments, and to counter the problem of aging components.

I. Introduction

The fracture mechanics approach to fatigue crack propagation quantitatively couples laboratory studies on alloy performance and fatigue mechanisms with damage tolerant life prediction methods through the concept of growth rate similitude. This method, illustrated in Figure 1, is traceable to the seminal results of Paris and coworkers for the case of moist air environments[1] and is outlined in current textbooks[2]. Subcritical fatigue crack propagation is measured in precracked laboratory specimens according to standardized methods[3]. Crack length (a) versus load cycles (N) data are analyzed to yield a material property; averaged fatigue crack growth rate (da/dN) as a function of the applied stress intensity range, ΔK. ΔK is the difference between maximum (K_{max}) and minimum (K_{min}) stress intensity values during a load cycle. Paris experimentally demonstrated the principle of similitude; that is, equal fatigue crack growth rates are produced for equal applied stress intensity ranges, independent of load, crack size and component or specimen geometry[1]. Wei and coworkers extended this concept to describe corrosion fatigue crack propagation in aggressive gas and liquid environments[4].

The similitude principle enables an integration of laboratory da/dN-ΔK data to predict component fatigue

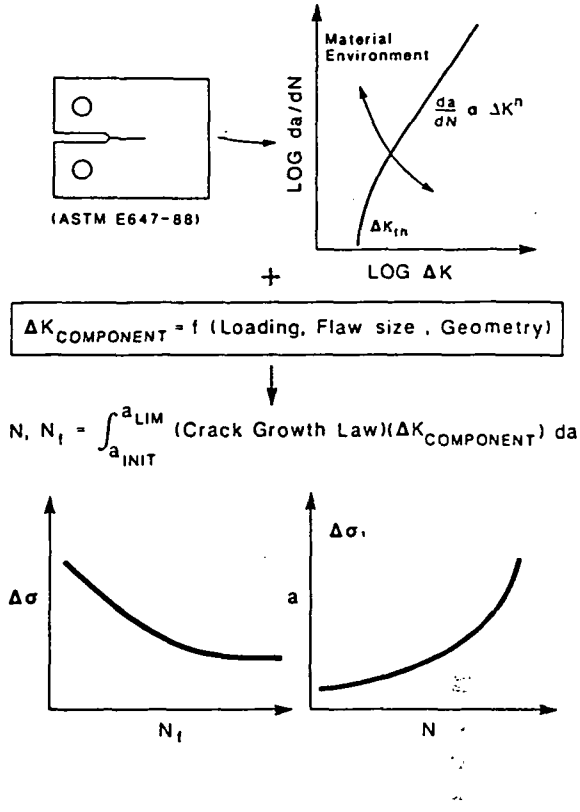

Figure 1. *Fracture mechanics approach to fatigue crack growth: material characterization and component life prediction.*

behavior, in terms of either applied stress range ($\Delta\sigma$) versus total life (N_f) or crack length (a) versus load cycles (N), for any initial defect size and component configuration. These calculations require component loading and stress analyses, initial crack size and shape, and a component stress intensity solution. This method has been developed for complex structural applications in the energy, petrochemical and

[1] Department of Materials Science, School of Engineering and Applied Science, University of Virginia, Charlottesville, VA, 22901.

[2] Formerly, Graduate Student, Department of Materials Science, University of Virginia; Currently, Mechanics of Materials Branch, Materials Division, NASA Langley Research Center, Hampton, VA, 23665.

[3] Metallic Materials Branch, Materials Division, NASA Langley Research Center, Hampton, VA, 23665.

[4] Mechanics of Materials Branch, Materials Division, NASA Langley Research Center, Hampton, VA, 23665.

Environmental Fatigue of an Al-Li-Cu Alloy: Part I. Intrinsic Crack Propagation Kinetics in Hydrogenous Environments

ROBERT S. PIASCIK and RICHARD P. GANGLOFF

Deleterious environmental effects on steady-state, intrinsic fatigue crack propagation (FCP) rates (da/dN) in peak-aged Al-Li-Cu alloy 2090 are established by electrical potential monitoring of short cracks with programmed constant ΔK and K_{max} loading. Such rates are equally unaffected by vacuum, purified helium, and oxygen but are accelerated in order of decreasing effectiveness by aqueous 1 pct NaCl with anodic polarization, pure water vapor, moist air, and NaCl with cathodic polarization. While da/dN depend on $\Delta K^{4.0}$ for the inert gases, water vapor and chloride induce multiple power laws and a transition growth rate "plateau." Environmental effects are strongest at low ΔK. Crack tip damage is ascribed to hydrogen embrittlement because of accelerated da/dN due to parts-per-million (ppm) levels of H_2O without condensation, impeded molecular flow model predictions of the measured water vapor pressure dependence of da/dN as affected by mean crack opening, the lack of an effect of film-forming O_2, the likelihood for crack tip hydrogen production in NaCl, and the environmental and ΔK-process zone volume dependencies of the microscopic cracking modes. For NaCl, growth rates decrease with decreasing loading frequency, with the addition of passivating Li_2CO_3 and upon cathodic polarization. These variables increase crack surface film stability to reduce hydrogen entry efficiency. Small crack effects are not observed for 2090; such cracks do not grow at abnormally high rates in single grains or in NaCl and are not arrested at grain boundaries. The hydrogen environmental FCP resistance of 2090 is similar to other 2000 series alloys and is better than 7075.

I. INTRODUCTION

PRECIPITATION-hardened Al-Li-Cu-based alloys are of considerable interest for aerospace applications because of low density, high stiffness, superior fatigue crack growth resistance, and high cryogenic toughness.[1-5] Research has concentrated on improving those properties controlled by high-angle grain boundaries, including low short-transverse fracture toughness,[6-9] localized aqueous corrosion,[10-13] and intergranular stress corrosion cracking.[14,15,16] In contrast, studies are lacking regarding environmental effects on fatigue crack growth and associated damage mechanisms.

The outstanding fatigue crack propagation (FCP) resistance of Al-Li alloys in moist air is controlled by two factors: increased extrinsic shielding by crack closure and reduced environmental embrittlement compared to other high-strength aluminum alloys.[17,18] Increased elastic modulus may provide some improvement in cracking resistance. The strong effect of closure on FCP is traceable to the highly localized planar and reversible character of slip in under- to peak-aged Al-Li microstructures hardened by ordered coherent precipitates.[19,20,21] Such deformation exacerbates roughness-induced closure by producing microscopic crack deflections, highly faceted fatigue crack surfaces, and mode II displacements. The mechanical and microstructural factors which affect crack closure in Al-Li alloys are reviewed elsewhere.[18]

Aluminum alloys are prone to cracking in water vapor or halogen-bearing electrolytes and under monotonic or cyclic loading.[22,23] Extensive environmental FCP rate (da/dN) studies have been conducted on conventional 2000 and 7000 series aluminum alloys.[23] This work identified the effects of important variables including: stress intensity range ($\Delta K = K_{max} - K_{min}$),[24] stress ratio ($R = K_{min}/K_{max}$),[25,26] water vapor pressure,[27,28,29] oxygen partial pressure,[30] electrode potential,[31,32,33] loading frequency,[26-28,32,34] alloy composition,[35] and deformation mode.[36] The preeminent mechanisms for environmental cracking of aluminum alloys include: hydrogen environment embrittlement,[27,32,37-40] passive film formation/rupture/anodic dissolution,[41] and surface film effects on plastic deformation.[31,42]

Uncertainties exist regarding environmental fatigue in aluminum alloys. While hydrogen embrittlement is established for 2000 and 7000 series alloys in water vapor, cracking mechanisms for aqueous solutions are controversial because of the simultaneous action of hydrogen production, metal dissolution, and surface film formation.[27,37] Quantitative models for da/dN-ΔK were developed for specific chemical processes but do not adequately describe interactive chemical and mechanical crack tip damage.[23,40] Environmental effects on near-threshold (ΔK_{th}) crack propagation* have not been extensively studied, despite the effort on mechanical fatigue threshold concepts.[43] Crack closure-environment and small crack-environment interactions have not been examined for aluminum alloys.[29,44]

Understanding of environmental FCP in Al-Li-based

*Near-threshold is defined as fatigue crack propagation at rates below 10^{-6} mm/cycle.

ROBERT S. PIASCIK, formerly Graduate Student, Department of Materials Science, University of Virginia, is Scientist, Mechanics of Materials Branch, NASA-Langley Research Center, Hampton, VA 23665. RICHARD P. GANGLOFF, Professor, is with the Department of Materials Science, University of Virginia, Charlottesville, VA 22903.

Manuscript submitted August 1, 1990.

Scripta METALLURGICA et MATERIALIA Vol. 25, pp. 2627-2632, 1991 Printed in the U.S.A.

ELEVATED TEMPERATURE CRACKING OF RSP ALUMINUM ALLOY 8009: CHARACTERIZATION OF THE ENVIRONMENTAL INFLUENCE

William C. Porr, Jr.*, Anthony Reynolds**, Yang Leng* and Richard P. Gangloff*

*Department of Materials Science and Engineering
University of Virginia
Charlottesville, VA 22903-2442

**NRC Postdoctoral Research Associate
NASA-Langley Research Center
Hampton, VA 23665

(Received July 22, 1991)

Introduction

Dispersion strengthened, ultrafine grain size aluminum alloys, produced by rapid solidification or mechanical alloying and powder processing, are candidate materials for next generation aerospace structures, particularly for applications at temperatures between 100 and 350°C. The planar flow casting, thermomechanical processing, elevated temperature strength and microstructural stability of a particular material, alloy 8009, are well established (1).

Alloy 8009, like others of this class, is prone to "intermediate temperature embrittlement", specifically tensile ductility and fracture toughness reductions (2-5), subcritical "creep" crack growth (6), and time dependent enhanced fatigue crack propagation rates (7,8) at temperatures between 150 and 325°C. Speculative mechanisms for this behavior include: (a) dynamic strain aging due to nonequilibrium solute such as iron (2-4,9), (b) reduced extrinsic delamination toughening associated with prior ribbon boundaries (2,10), (c) environmental hydrogen or oxygen embrittlement due to water vapor or O_2 reactions with aluminum (2,7,11), (d) embrittlement by dissolved hydrogen from decomposition of hydrated oxides entrained on ribbon particle surfaces (12), and localized deformation unique to submicron grain size alloys with a high volume fraction of fine dispersoids (2).

The objective of this study is to define the roles of the moist air environment and predissolved hydrogen in degrading the elevated temperature fatigue and fracture resistance of alloy 8009. Fracture mechanics characterizations of initiation (K_{IC}) and propagation (K-Δa resistance curve) fracture toughnesses during rising load, sustained load crack growth rates (da/dt-K) and fatigue crack propagation kinetics (da/dN-ΔK) were conducted at 175°C in moist air and high vacuum with both as-processed and vacuum heat treated specimens. The results show that intermediate temperature cracking is equivalent for each loading mode in moist air and vacuum, and is unaffected by vacuum heat treatment prior to loading.

Experimental Procedure

Ribbon cast, comminuted and compacted alloy 8009 (Al-8.5Fe-1.3V-1.7Si by wt%) was provided by Allied-Signal Inc. in the forms of 10 mm thick extrusion and 6.4 mm thick cross-rolled plate. Each rapidly solidified microstructure contained 25 volume percent of $Al_{12}(Fe,V)_3Si$ dispersoids, sized less than 100 nm in diameter, an ultrafine grain size of less than 500 nm, and excess solute (Fe, Si and V) in solid solution (1-4). Extruded material contained oxide decorated prior particle boundaries (1000 x 200 x 20 μm) that were largely randomized by cross rolling.

Fracture mechanics experimental procedures are detailed elsewhere (2,6). All specimens were machined in the LT orientation. Side grooved compact tension specimens (width = 38.1 mm, gross thickness = 7.6 mm or 6.0 mm, and net thickness = 6.4 mm or 5.0 mm, for extrusion and plate, respectively) were employed for fracture toughness and sustained load crack growth experiments. Fully rotating single edge cracked tension specimens (width = 38.1 and thickness = 5.5 mm) and compact tension specimens (width = 38.1 mm and

Scripta METALLURGICA et MATERIALIA
Vol. 25, pp. 895-900, 1991
Printed in the U.S.A.

TIME DEPENDENT CRACK GROWTH IN P/M Al-Fe-V-Si AT ELEVATED TEMPERATURES

Yang Leng, William C. Porr, Jr. and Richard P. Gangloff

Department of Materials Science and Engineering
University of Virginia
Charlottesville, Virginia 22903

(Received January 23, 1991)
(Revised February 11, 1991)

Introduction

Time dependent subcritical crack growth can be an important fracture mode which affects the damage tolerance of structural materials in elevated temperature service [1,2]. While referred to as "creep crack growth" (CCG), the causal micromechanism may include creep deformation, microstructural instability and environmental embrittlement due to oxygen or hydrogen.

It is critical, from both the life prediction and mechanistic perspectives, to determine the correct continuum fracture mechanics parameter which describes the governing crack tip stress, strain and strain rate fields [1,2]. For creep ductile materials (e.g. alloy steels), time dependent crack growth is reasonably characterized by the C^*-integral under steady-state creep conditions and by C_t under small scale creep (SSC) and transient creep (TC) conditions [1,2]. For creep brittle materials (e.g. Ni and Ti alloys), time dependent crack growth is governed by time independent parameters such as the small scale yielding stress intensity (K) or the elastic-plastic J-integral [3,4].

Elevated temperature crack growth occurs in aluminum alloys; however, such behavior has not been broadly defined, particularly for advanced materials with thermally stable ultra-fine grain size microstructures [5-7]. For the latter, recent results indicate loading rate dependent fracture toughness, suggesting that time dependent subcritical crack growth is important [8]. This report presents observations of time dependent crack growth in rapidly solidified alloy 8009 (previously called FVS0812) designed for elevated temperature applications [9]. The applicability of several fracture mechanics parameters (viz. C^*, C_t, K and J) to correlate crack growth kinetics is investigated.

Experimental Procedure

Powder processed, hot extruded 8009 (Al-8.5Fe-1.3V-1.7Si (wt%)) plate was supplied by Allied-Signal, Inc. Rapid solidification processing produces a microstructure with ultra fine $Al_{12}(Fe,V)_3Si$ dispersoids (less than 0.1 μm in size) distributed in the aluminum matrix of grain size less than 1 μm [8,9].

Sidegrooved compact tension (CT) specimens in the L-T orientation (width (W) = 38.1 mm, gross thickness = 7.62 mm, net thickness = 6.35 mm) were used for crack growth experiments. Experiments were conducted with a servo-electric mechanical testing system. Specimens were instrumented to measure load (P), front-face crack mouth opening displacement (CMOD), crack length (a) from electrical potential and temperature, as described in Ref. 8. Specimens, fatigue precracked to an a/W of 0.5, were tested at 175, 250 and 316°C under constant load. Load levels were chosen to be approximately 40% of the load at which the "fast loading rate" K_{IC} is defined [8]. Crack growth rate was determined from crack length versus time measurements. The minimum crack extension between successive data points was about 0.02 mm and the secant method was used to obtain the crack growth rate (da/dt). A JEOL JXA-840A scanning electron microscope (SEM) and a Phillips EM 400T transmission electron microscope (TEM) were used for fractography and microstructural examinations. To determine power-law creep constants, tensile creep deformation tests were conducted at 175, 250 and 316°C in a dead weight creep machine. The round bar specimens were 5.7 mm in diameter. The tensile strain was measured with a high temperature Capacitec extensometer over a gage length of 25.4 mm.

Results and Discussion

Experimental observations indicate that 8009 exhibits substantial time-dependent subcritical crack growth at each of the test temperatures, with the rates varying between 0.003 and 0.2 mm/hour. Crack growth occurs

Proceedings

Sixth International Aluminium-Lithium Conference.
October 7-11, 1991 in Garmisch-Partenkirchen (FRG)

Effect of Zn Additions on the Precipitation Events and Implications to Stress Corrosion Cracking Behavior in Al-Li-Cu-Mg-Zr Alloys

R.J. Kilmer, J.J. Witters*, G.E. Stoner, Center for Electrochemical Sciences and Engineering, Department of Materials Science, University of Virginia, Charlottesville, Virginia, USA
*Alcoa Technical Center, Pittsburgh, Pennsylvania, USA

Introduction

The four principle design criteria typically considered when developing or evaluating an aluminum alloy for aerospace application are strength, density, toughness and resistance to environmental fracture. As with most conventional aluminum aerospace alloys, Al-Li alloys may become susceptible to stress corrosion cracking (SCC). SCC is the phenomenon whereby an environmentally induced crack grows under the application of a static tensile stress. This stress may be residual or externally applied. There is general agreement that SCC occurs in aluminum alloys via a discontinuous process following two principle stages: initiation and propagation.

In the initiation stage, localized corrosion occurs either intergranularly or at a constituent particle forming a pit or notch in the material. An example of SCC initiation at a constituent particle pit in alloy 2090 (Al-Li-Cu-Zr) was given in a recent paper by Buchheit, Moran and Stoner (1). A stress concentration then develops at the base of the notch. Propagation involves two substages. Initially, local deformation occurs at the notch or crack tip which violates the integrity of the oxide film and the crack propagates along a grain or subgrain boundary. Propagation may be significantly aided by hydrogen embrittlement within or ahead of the crack tip in many alloys. Once the crack propagates, newly exposed anodic material rapidly corrodes until reformation of a passive oxide or film occurs. These events are cyclic and increase in frequency as the stress intensity increases with increasing effective crack length. These processes occur until the critical crack length is achieved and the component fails by tensile overload. Pure metals are generally considered immune to SCC, and in general, the SCC process is governed by alloy chemistry and alloy microstructure.

In commercial Al-Li-Cu-Mg-Zr alloys, SCC is generally associated with an anodic dissolution based process along or adjacent to grain and subgrain boundaries (2,3,4). Zn additions to these alloys have been shown to result in materials of greatly improved SCC resistance most notably in 8090 or near 8090 compositions (5). It also has been demonstrated that Zn additions can have a marked effect upon the systems' precipitation events (6,7). The emphasis of this paper is focussed on the correlation of Zn content with the resultant microstructure, specifically precipitation during artificial aging. Furthermore, the interrelation between specific microstructural changes and their possible effect on SCC, most notably SCC propagation, will be discussed.

Light-Weight Alloys for Aerospace Applications II

Proceedings of a symposium sponsored by the
TMS Nonferrous Metals Committee,
held during the 1991 TMS Annual Meeting,
New Orleans, Louisiana, February 17–21, 1991.

Edited by

Eui W. Lee
Code 6063
Naval Air Development Center
Warminster, PA 18974

and

Nack J. Kim
POSTECH
P. O. Box 125
Pohang, Korea

A Publication of
TMS
Minerals · Metals · Materials

THE EFFECT OF TRACE ADDITIONS OF Zn ON THE PRECIPITATION BEHAVIOR OF ALLOY 8090 DURING ARTIFICIAL AGING

R.J. Kilmer, G.E. Stoner
Center for Electrochemical Sciences and Engineering
Department of Materials Science
University of Virginia
Charlottesville, VA 22903-2442

Abstract

The effect(s) of trace additions of Zn to the artificial aging behavior of alloy 8090 (Al-Li-Cu-Mg-Zr) was investigated in the approximate composition range 0 - 1 wt-% Zn. Trace Zn additions were found to delay aging and under equivalent aging treatments (100 hrs at 160C) the alloy without Zn and the 1.07 wt-% Zn alloy developed δ'-free zones along subgrain boundaries, while the alloys of 0.21 and 0.58 wt-% Zn did not. DSC analysis indicated that Zn was being incorporated into the δ', shifting it's exotherm to higher temperatures, while having little if any effect on its associated endotherm making it unlikely that it is an artifact of a solvus shift. In the 8090 + 1.07 wt-% Zn alloy, coarse precipitates were found to reside on subgrain boundaries and EDS indicated that they were rich in Cu and Zn. It was also noted that in the Zn containing 8090 varients, the S' precipitates were more coarse in size than the baseline 8090.

Introduction

The potential for Al-Li base alloys in aerospace applications is well documented [1-5]. The Soviet Union, since the early 1960's has centered its

Light Weight Alloys for Aerospace Applications II
Edited by Eui W. Lee and Nack J. Kim
The Minerals, Metals & Materials Society, 1991

Scripta METALLURGICA et MATERIALIA
Vol. 25, pp. 243-248, 1991
Printed in the U.S.A.

EFFECT OF Zn ADDITIONS ON PRECIPITATION DURING AGING OF ALLOY 8090

R.J. Kilmer, G.E. Stoner
Center for Electrochemical Sciences and Engineering
Department of Materials Science
University of Virginia
Charlottesville, VA 22903-2442

(Received August 3, 1990)
(Revised November 7, 1990)

Introduction

Al-Li base alloys have received considerable attention as potential lightweight replacements for conventional Al-base alloys in aerospace applications. The low density and high stiffness of alloy 8090 (Al-Li-Cu-Mg) earmarks it as an especially attractive candidate. Alloy 8090 derives its strength from the co-precipitation of Al_3Li (δ'), Al_2CuMg (S') and Al_2CuLi (T_1) during artificial aging. Stretching prior to aging enhances the heterogeneous precipitation of S' and T_1, greatly improving the fracture toughness properties in Al-Li-Cu-(Mg) alloys (1). In applications where a pre-aging stretch is not feasible, additions of Zn to the Al-Li-Cu-Mg system have been investigated as a means to improve toughness.(2)

The present paper reports the precipitation events of three stretched alloys whose compositions fall within the 8090 composition window and contain varying amounts of Zn additions up to 1.07 wt %. The alloys were examined under two different aging conditions using transmission electron microscopy (TEM) and the results were compared with those of alloy 8090 employed as a baseline. Differential scanning calorimetry (DSC) was employed to provide further insight into the effects that varying the Zn content has on the precipitation events.

RAPID ANODIC DISSOLUTION BASED SCC OF 2090 (Al-Li-Cu) BY ISOLATED PIT SOLUTIONS

R.G. Buchheit, Jr.[1], J.P. Moran[2], F.D. Wall[3], G.E. Stoner[3]

[1]Sandia National Laboratories
P.O. Box 5800
Albuquerque, New Mexico 87185

[2]Aluminum Company of America
Alcoa Technical Center
Alcoa Center, Pennsylvania 15069

[3] Center for Electrochemical Sciences and Engineering
Department of Materials Science
University of Virginia
Charlottesville, Virginia 22903

Abstract

Pre-exposure induced stress corrosion cracking of 2090 (Al-Li-Cu) was studied using a variety of test techniques. Results from time to failure SCC testing in a simulated isolated pit solution and electrochemical corrosion rate data obtained for individual phases in the subgrain boundary region are combined with existing data on the crevice chemistry of isolated pits in Al-Li alloys and X-ray diffraction studies of solid corrosion products formed in crevice environments to propose a model for pre-exposure induced cracking based on anodic dissolution along subgrain boundaries. Key features of the model are selective dissolution of subgrain boundary T_1 (Al_2CuLi) at the crack tip and passivation of crack walls by the formation of an $Li_2[Al_2(OH)_6]_2{\cdot}CO_3{\cdot}nH_2O$ barrier film.

(Submitted for review to the Parkins Symposium on Fundamental Aspects of Stress Corrosion Cracking, TMS/ASM Fall '91 Meeting, Cincinnati, OH.)

MECHANISMS OF SCC OF ALLOY 2090 (Al-Li-Cu) - A COMPARISON OF INTERPRETATIONS FROM STATIC AND SLOW-STRAIN-RATE TECHNIQUES

J. P. Moran[1], R.G. Buchheit[2], and G.E. Stoner

Center for Electrochemical Sciences and Engineering
Department of Materials Science
The University of Virginia
Charlottesville, VA 22901

Abstract

The SCC behavior of alloy 2090 was investigated using three techniques. These included both constant immersion and alternate immersion static time-to-failure (TTF) experiments, and a slow-strain-rate (SSRT) technique (all using smooth-bar tensile specimens). Experiments were performed in 0.6M NaCl with and without additions of Li_2CO_3. It is illustrated that a mechanistic interpretation of the data from both static and dynamic techniques are corroborative, suggesting a consistent mechanism for SCC. Based on the experimental evidence, a mechanism for intergranular SCC is proposed incorporating two key steps: anodic dissolution of active precipitates at the crack tip and passivation of crack walls by a hydrotalcite-based film. In addition, the importance of crack wall passivity, as interpreteted from all three techniques, will be discussed.

(Submitted for review to the Parkins Symposium on Fundamental Aspects of Stress Corrosion Cracking, TMS/ASM Fall '91 Meeting, Cincinnati, OH.)

---

[1] Present address : Alcoa Technical Center, Alcoa Center, PA 15068
[2] Present address : Sandia National Laboratories, Albuquerque, NM 87185

(This work was supported by an Alcoa Fellowship (E.L. Colvin & S.C. Byrne), with additional support from NASA-Langely (W.B. Lisagor & D.L. Dicus) and the Virginia Center for Innovative Technology.)

CORROSION 91

The NACE Annual Conference and Corrosion Show

March 11-15, 1991 • Cincinnati Convention Center • Cincinnati, Ohio

PAPER NUMBER

99

STRESS CORROSION CRACKING OF AL-LI-CU-ZR ALLOY 2090 IN AQUEOUS Cl^- AND MIXED CO_3^{2-}/Cl^- ENVIRONMENTS

R.G. Buchheit
Sandia National Laboratories
P.O. Box 5800
Albuquerque, NM 87185

F.D. Wall, G.E. Stoner
Center for Electrochemical Sciences and Engineering
Department of Materials Science
University of Virginia
Charlottesville, VA 22903

J.P. Moran
National Institute for Standards and Technology
Gaithersburg, MD 20879

ABSTRACT

A comparison of the short-tranverse SCC behavior of 2090 in pH 5.5 Cl^- and alkaline CO_3^{2-}/Cl^- solutions using a static load smooth bar SCC technique was made. In the alkaline CO_3^{2-}/Cl^- solutions, E_{br} for the α-Al matrix phase was 0.130 V more positive than the E_{br} of the subgrain boundary T_1 phase. In this environment, stress corrosion cracking test specimens subjected to potentials in the window defined by the two breakaway potentials failed along an intersubgranular path in less than an hour. In the Cl^- environment, the E_{br} values for the two phases were nearly equal and this rapid SCC condition could not be satisfied; accordingly SCC failures were not observed.

Rapid SCC failure of 2090 in CO_3^{2-}/Cl^- in our static load, constant immersion experiments appear to be related to recently reported "pre-exposure embrittlement" failures induced by immersing stressed specimens removed into ambient laboratory air after immersion in aerated NaCl solution for 7 days. In those experiments, specimens failed in less than 24 hours after removal from solution. Our polarization experiments have shown that the corrosion behavior of T_1, residing at the crack tip, is relatively unaffected by the alkaline CO_3^{2-}/Cl^- environments, but the α-Al phase crack walls, is rapidly passivated.

Abstract submitted for NACE Student Poster Session, to be held at CORROSION/92

HYDROGEN INTERACTIONS IN ALUMINUM LITHIUM ALLOYS

Stephen W. Smith
University of Virginia
Center for Electrochemical Sciences and Engineering
Dept. of Materials Science and Engineering
School of Engineering and Applied Sciences
Charlottesville, VA 22903

Al-Li-Cu-X alloys are being studied for use in aerospace applications, due to the improved stiffness and strength to weight ratio in comparison to conventional aluminum alloys. It has been documented in the literature that under appropriate circumstances these alloys may be susceptible to environmentally assisted cracking (EAC).[1] Although it has been shown that hydrogen production can occur at the tip of a crack in aluminum lithium alloys, when exposed to moist air or many aqueous environments, the exact role hydrogen plays in the EAC process of these alloys has not been clearly distinguished from aqueous dissolution effects. This project is being performed to aid in understanding the effects dissolved and trapped hydrogen have on the mechanical properties of selected Al-Li alloys. The objectives of this work are three fold; 1) distinguish hydrogen induced EAC from aqueous dissolution controlled EAC, 2) correlate hydrogen induced EAC with mobile and trapped hydrogen concentrations, and 3) identify significant trap sites and hydride phases (if any). Progress in answering these questions for Al-Li alloys has been impeded by several experimental factors. These include, the propensity for inter-subgranular fracture in Al-Li alloys when tested in the short-transverse (S-T) orientation in air or vacuum. This compromises the ability to readily detect hydrogen induced fracture based on straight forward changes in fractography. Hydrogen detection and measurement is complicated by the inherently low hydrogen diffusivity and solubility

in Al alloys and is further compounded by a native oxide which acts as a hydrogen permeation barrier. Finally, hydrogen effects may be masked by rapid dissolution of T_1 (Al_2CuLi) precipitates, or pitting adjacent to constituent particles which complicate mechanical testing in aqueous solutions. We are applying several novel approaches to existing tests, including continuous extension rate testing, breaking load, hydrogen analysis by thermal desorption spectroscopy (TDS), and hydrogen permeation which makes it possible to circumvent these experimental barriers. With the aid of several analytical methods such as TDS and differential scanning calorimetry (DSC) we hope to determine exactly how hydrogen is incorporated in Al-Li alloys. This information can then be used in conjunction with results from mechanical testing to obtain correlations between hydrogen interactions and mechanical properties. In addition to studying the effects of hydrogen on commercial alloys, we are also examining how hydrogen is incorporated into constituent phases inherent in these alloys. The experimental approaches, as well as the results to date will be reviewed in this presentation.

REFERENCES

1. T.D. Burleigh, Corrosion, Vol. 47, pp. 89-98 (1991).

ACKNOWLEDGEMENTS

I would like to note the efforts of my advisor John R. Scully. I also wish to thank NASA - Langley Research Center and the Virginia Center for Innovative Technology for their help in funding this project, and Alcoa Technical Center for supplying materials.

Thermo-Mechanical Response Predictions for Metal Matrix Composite Laminates

by

J. Aboudi,[1] J. S. Hidde,[1] C. T. Herakovich

University of Virginia
Charlottesville, VA 22903

ABSTRACT

An analytical, micromechanical model is employed for prediction of the stress-strain response of metal matrix composite laminates subjected to thermo-mechanical loading. The predicted behavior of laminates is based upon knowledge of the thermo-mechanical response of the transversely isotropic, elastic fibers and the elastic-viscoplastic, work-hardening matrix.

The method is applied to study the behavior of silicon carbide/titanium metal matrix composite laminates. The response of laminates is compared with that of unidirectional lamina. The results demonstrate the effect of cooling from a stress-free temperature and the mismatch of thermal and mechanical properties of the constituent phases on the laminate's subsequent mechanical response. Typical results are presented for a variety of laminates subjected to monotonic tension, monotonic shear and cyclic tensile/compressive loadings.

---

[1]Visiting from Tel Aviv University, Tel Aviv, Israel
[1]Now with Michelin Americas Research & Development, Greenville, S.C.

RESPONSE OF METAL MATRIX COMPOSITES WITH IMPERFECT BONDING[1]

Carl T. Herakovich

Jeffrey S. Hidde[2]

University of Virginia
Charlottesville, VA 22903-2442

ABSTRACT

The method of cells is employed to study the micromechanical response of metal matrix composites as a function of variable bonding parameters. Elastic constants and nonlinear stress-strain responses are predicted as functions of normal and tangential displacement discontinuities between the fiber and the matrix. Typical results are presented for axial, transverse and shear loading of unidirectional silicon-carbide/titanium. It is shown that imperfect bonding can degrade both the elastic constants and nonlinear response of composites with the degree of degradation dependent upon the type and degree of imperfect bond.

[1]Proceedings of the Workshop on Structure and Properties of Interfaces, Arizona State University, Jan., 1991.

[2]Now with Michelin Americas Research & Development, Greenville, S.C.

Response of SiC/Ti Tubes Under Bi-axial Loading in the Presence of Damage

by

C. J. Lissenden, M-J. Pindera, and C. T. Herakovich

Abstract

This paper presents the results of an experimental investigation of the nonlinear response of unidirectional [0] and angle-ply $[\pm 45]_s$ tubes subjected to axial, torsional and combined axial/torsional loading. The tubes were made from SCS-6 silicon carbide fibers in Ti-15-3 titanium matrix. The test program consisted of a series of axial or torsion tests to sequentially higher load levels. At each load level, both the axial and torsional stiffnesses were measured. This procedure provided an assessment of inelastic response due to both matrix plasticity and micro-level fiber/matrix damage. The use of tubes in a combined load environment also provided insight into the influence of a given damage state on axial and torsional response. The results of the experimental investigation were compared with predictions of the method of cells micromechanics model. The micromechanics model included inelastic (plastic) response of the matrix as well as imperfect bonding between fiber and matrix. The results of the investigation show good correlation between theory and experiment prior to the development of fiber/matrix damage. Further, the imperfect bonding feature of the micromechanics model was capable of predicting some features of the actual response after damage development.

VISCOPLASTIC RESPONSE OF STRUCTURES FOR INTENSE LOCAL HEATING

Earl A. Thornton* and J. D. Kolenski**
University of Virginia
Charlottesville, Virginia 22903

Abstract

A thermoviscoplastic finite element method employing the Bodner-Partom constitutive model is used to investigate the response of simplified thermal-structural models to intense local heating. With rapid rises of temperature, the nickel alloy structures display initially higher yield stresses due to strain rate effects. As temperatures approach elevated values, yield stress and stiffness degrade rapidly and pronounced plastic deformation occurs.

Introduction

As hypersonic vehicles accelerate at high speeds in the atmosphere, shocks sweep across the vehicle interacting with local shocks and boundary layers. These interactions expose structural surfaces to severe local pressures and heat fluxes. One example is leading edges of integrated engine structures which experience intense, highly localized aerothermal loads (Fig. 1). Reference 1 studies issues relevant to the thermal-structural response of hydrogen cooled, super thermal-conducting leading edges subject to intense aerodynamic heating. A thermo-structural analysis with experimental verification[2] of a cowl lip design demonstrated that inelastic effects occur and may be significant.

Until recent years the study of structural response at elevated temperatures due to dynamic loads was not possible because of an inability to model inelastic material behavior. Over the last twenty years, unified viscoplastic constitutive models have evolved to meet this need. These constitutive models provide a means for representing a material's response from the elastic through the plastic range including strain-rate dependent plastic flow, creep and stress relaxation. Rate-dependent plasticity effects are known to be important at elevated temperatures. The first multidimensional formulations of viscoplastic constitutive relations was due to Bodner and Partom. Since then, a number of constitutive models have been developed; many of these theories, including the model of Bodner and Partom, are summarized in review articles that appear in reference 3.

---

*Director, Center for Light Thermal Structures, Associate Fellow, AIAA
**Graduate Research Assistant, Department of Mechanical and Aerospace Engineering

Unified constitutive models implemented in finite element programs provide an important simulation capability. Finite element analysis with unified constitutive models have been under development for about 15 years. Reference 4 describes these efforts and presents a thermoviscoplastic finite element computational method for hypersonic structures. Applications of the approach to convectively cooled hypersonic structures illustrate the effectiveness of the approach and provide insight into the transient viscoplastic behavior at elevated temperatures. A recent paper[5] uses the computational method presented in reference 4 to perform quasi-static finite element thermo-viscoplastic analysis of aerospace structures including a convectively-cooled engine cowl leading edge subjected to aerodynamic shock interference heating. A study [6] of dynamic effects in thermoviscoplastic vibrations shows that inelastic strains introduces significant damping.

There is a need for further computational thermoviscoplastic studies to: (1) understand the phenomena that occur in the viscoplastic response of structures for intense local heating, (2) investigate the finite element modeling techniques required to represent thermoviscoplastic behavior, (3) assist in planning thermal-structural experiments to validate computational methods, and (4) aid in understanding the high-temperature behavior of difficult design problems such as leading edges of hypersonic vehicles.

The purpose of this paper is to describe recent studies that address the first three needs. The paper begins with a description of quasi-static thermoviscoplastic structural analysis. The initial value viscoplasticity problem statement is presented, the Bodner-Partom constitutive model is described, the finite element formulation is outlined, and the viscoplastic solution method is detailed. Computational studies of thermoviscoplastic behavior of two thermal structural applications are then presented. An appendix presents thermal and structural data for materials used in the numerical computations.

Thermo-Viscoplastic Structural Analysis

The behavior of a thermo-viscoplastic structure subjected to intense heating is analyzed assuming that: (1) thermo-mechanical coupling in the conservation of energy equation can be neglected, (2) the structural response is quasi-static, and

APPENDIX IV: GRANT PROGRESS REPORTS (January, 1988 to December, 1991)

1. R.P. Gangloff, G.E. Stoner and R.E. Swanson, "Environment Assisted Degradation Mechanisms in Al-Li Alloys", University of Virginia, Report No. UVA/528266/MS88/101, January, 1988.

2. R.P. Gangloff, G.E. Stoner and R.E. Swanson, "Environment Assisted Degradation Mechanisms in Advanced Light Metals", University of Virginia, Report No. UVA/528266/MS88/102, June, 1988.

3. R.P. Gangloff, G.E. Stoner and R.E. Swanson, "Environment Assisted Degradation Mechanisms in Advanced Light Metals", University of Virginia, Report No. UVA/528266/MS89/103, January, 1989.

4. R.P. Gangloff, "NASA-UVa Light Aerospace Alloy and Structures Technology Program", UVa Report No. UVA/528266/MS90/104, August, 1989.

5. R.P. Gangloff, "NASA-UVa Light Aerospace Alloy and Structures Technology Program", UVa Report No. UVA/528266/MS90/105, December, 1989.

6. R.P. Gangloff, "NASA-UVa Light Aerospace Alloy and Structures Technology Program", UVa Report No. UVA/528266/MS90/106, June, 1990.

7. R.P. Gangloff, "NASA-UVa Light Aerospace Alloy and Structures Technology Program", UVa Report No. UVA/528266/MS91/107, January, 1991.

8. R.P. Gangloff, "NASA-UVa Light Aerospace Alloy and Structures Technology Program", UVa Report No. UVA/528266/MS91/108, July, 1991.

9. R.P. Gangloff, "NASA-UVa Light Aerospace Alloy and Structures Technology Program", UVa Report No. UVA/528266/MS92/109, January, 1992.

DISTRIBUTION LIST

1 - 2	Mr. D. L. Dicus Contract Monitor Metallic Materials Branch, MS 188A NASA Langley Research Center Hampton, VA 23665
3 - 4*	NASA Scientific and Technical Information Facility P. O. Box 8757 Baltimore/Washington International Airport Baltimore, MD 21240
5	Mr. Richard J. Siebels Grants Officer, M/S 126 NASA Langley Research Center Hampton, VA 23665
6	Dr. Darrel R. Tenney Materials Division NASA Langley Research Center Hampton, VA 23665
7	Dr. Charles E. Harris Mechanics of Materials Branch NASA Langley Research Center Hampton, VA 23665
8	Mr. W. Barry Lisagor Metallic Materials Branch NASA Langley Research Center Hampton, VA 23665
9	Mr. T.W. Crooker Code RM NASA Headquarters Washington, DC 20546
10	Dr. Robert S. Piascik Mechanics of Materials Branch NASA Langley Research Center Hampton, VA 23665
11	Mr. W. Brewer Metallic Materials Branch, MS 188A NASA Langley Research Center Hampton, VA 23665

12 Mr. Thomas Bayles
Metallic Materials Branch, MS 188A
NASA Langley Research Center
Hampton, VA 23665

13 Dr. W.S. Johnson
Mechanics of Materials Branch
NASA Langley Research Center
Hampton, VA 23665

14 Dr. M.J. Shuart
Aircraft Structures Branch
NASA Langley Research Center
Hampton, VA 23665

15 Dr. James H. Starnes, Jr.
Aircraft Structures Branch
NASA Langley Research Center
Hampton, VA 23665

16 Mr. Dana Ward
Northrop Corporation
1 Northrop Avenue
Mail Zone 3872562
Hawthorne, CA 90250-3277

17 Dr. Santosh K. Das
Senior Manager
Metals and Ceramics Laboratory
Allied-Signal, Inc.
P. O. Box 1021
Morristown, NJ 07960

18 Dr. Michael Zedalis
Metals and Ceramics Laboratory
Allied-Signal, Inc.
P. O. Box 1021
Morristown, NJ 07960

19-20 Mr. E.A. Colvin
Alcoa Technical Center
Route 780, 7th Street Road
Alcoa Center, PA 15069

21 Mr. Fred Casey
Space Transportation Systems Division
Rockwell International
Dept. 289 MC/AC56
12214 Lakewood Blvd.
Downey, CA 90241

22 Mr. Stephen G. Moran
Lockheed Aeronautical Systems Company
Georgia Division; Dept. 73-71
Zone 0160
86 South Cobb Dr.
Marietta, GA 30063

23 Dr. J. Andrew Walker
Advanced Composite Materials Corporation
1525 South Buncombe Road
Greer, SC 29651

24 E.A. Starke, Jr.; UVA

25-27 R.P. Gangloff; MS&E

28 G.E. Stoner; MS&E

29 J.A. Wert; MS&E

30 F.E. Wawner; MS&E

31 W.A. Jesser; MS&E

32 J.R. Scully; MS&E

33 W.D. Pilkey; MAE

34 E.A. Thornton; MAE

35 C.T. Herakovich; CE/Applied Mechanics

36-37 E.H. Pancake; Clark Hall

38 SEAS Preaward Administration Files

39 Mr. Gwyn Faile
Code ED 24
Marshall Space Flight Center
Huntsville, AL 35812

40 Mr. Brian McPherson
Code ED 24
Marshall Space Flight Center
Huntsville, AL 35812

41 Dr. Ken Garr
Rocketdyne Division, Rockwell International
6633 Canoga Ave.
Canoga Park, CA 91303

42 Mr. Michael Falugi
WRDC/FIBAA
Wright Patterson Air Force Base, OH 45433-6553

43 Mr. Peter Rimbos
Boeing Aerospace and Electronics
Aerospace Group
Seattle, WA 98124

44 Mr. James Learned
Boeing Military Aircraft
Organization L-7109
Aerospace Group
Seattle, WA 98124

45 Dr. Howard G. Nelson
NASA-Ames Research Center
EEM: 213-3
Moffett Field, CA 94035

46 Dr. R.G. Forman
Mail Code ES-5
NASA-L.B. Johnson Space Flight Center
Houston, TX 77058

47 Professor A.K. Noor
Center for Computational Structures Technology
NASA Langley Research Center .
Hampton, VA 23665

48 Dr. M.J. Luton
Exxon Research and Engineering Company
Clinton Township, Route 22 East
Annandale, NJ 08801